Durham E-Theses

Clay minerals and their gallery guests: an ab initio investigation into their interactions.

GEATCHES, DAWN,LESLEY

How to cite:

Use policy

Clay Minerals and their Gallery Guests: an *ab initio* investigation into their interactions.

Dawn L. Geatches

A Thesis presented for the degree of
Doctor of Philosophy

Supervised by Prof. S. J. Clark[a],

co-supervised by Dr. H. C. Greenwell[b]
Departments of Physics[a] and Earth Sciences[b]
University of Durham
England

January 2011

Clay Minerals and their Gallery Guests: an *ab initio* investigation into their interactions.

Dawn L. Geatches

Submitted for the degree of Doctor of Philosophy

January 2011

Abstract

Clay minerals are ubiquitous and readily accessible in the natural environment and consequently have become an essential ingredient in the development of Western Society. Their structural properties are responsible for many of their uses, their layered-leaf composition enables the absorption of water and other solutes, for example. In this thesis, the focus of interest lies primarily in the chemical properties of the clay minerals, which is due to the large surface areas of varying atomistic environments comprising the mineral layers. Clay minerals offer a challenge to the electronic structure modeller as their atomistic composition is non-exact, consequently a number of constraints are automatically applied during the modelling process, the first being the choice of composition of the model. There are currently few examples of density functional theory studies using planewaves and the pseudopotential approximation, and the available experimental data is not necessarily directly applicable to theoretical data due in part, to the inexactness of the clay mineral composition. Consequently, in the studies presented in this thesis, as much time has been spent in considering the modelling methods as on the results obtained and the implication of these in the modelling environment chosen.

This thesis records investigations into the decarboxylation of a fatty acid into an alkane and CO_2 with the modelling of a catalytic environment of an aluminium-bearing clay mineral; the identification of a transition state of this reaction pathway using lattice dynamics and finally, the mechanism of reduction within iron-bearing

clay minerals.

Declaration

The work in this thesis is based on research carried out under the supervision of Prof. S. J. Clark, in the Department of Physics, University of Durham, England. No part of this thesis has been submitted elsewhere for any other degree or qualification and it is all my own work unless referenced to the contrary in the text.

Acknowledgements

Publications

The following list details the publications from this thesis. Apart from those listed, there is work concerning another category of clay, which will contribute as the theory to an experimental paper but has not been recorded in this thesis, to maintain continuity of subject matter.

Geatches D.L.; Clark S. J.; Greenwell H. C. Role of Clay Minerals in Oil-Forming reactions. *J. Phys. Chem. A.*, 114:3569-3575, 2010.

Geatches D.L.; Greenwell H. C.; Clark S. J. *Ab initio* Transition State Searching in Complex Systems: Fatty Acid Decarboxylation in Minerals. In publication with *J. Phys. Chem. A.*.

Geatches D.L.; Greenwell H. C.; Clark S. J. Iron Reduction in Minerals: Modelling a Complex System. In submission.

Contents

Contents vii

List of Figures

List of Tables

1

Introduction

The term 'clay' will be recognised by many with an association to a mud-like substance found in garden soil. Clay becomes heavy and sticky when wet and hard and dry when exposed to heat. This swelling and shrinking property (a source of irritation to many gardeners) is thought to be a causative factor in the origins of chirality i.e. left or right handedness of molecules [1] in biological life [2], [3]. This adsorbent property is responsible for the use of clay minerals in products as diverse as cat litter and cosmetics and arises, in part, from the structure of the clay minerals comprising the clay. 'Clay' describes a rock or an ore containing one or more clay minerals as components [4]. 'Clay mineral' describes one of a category of aluminium, silicon and oxygen (alumino-silicate) compounds, which are bonded within a plane where the planes are layered [5]. The layers of the clay minerals are separated by an interlayer space, which is inhabitable by molecules such as amino acids — pertinent to the origins of chirality, or water — pertinent to such uses of clay minerals as adsorbents

in, for example, cat litter [6] and cosmetics [7]. If the clay mineral absorbs water plus other molecules, and subsequently dries out, the molecules may become trapped and concentrated between the layers [8]. These trapped interlayer molecules are exposed to a large surface area of varying, potentially catalytic, atomic environments resembling mini laboratories, where such reactions as the formation of long-chain molecules [8], the addition of specific chemical groups to molecules [9] and the conversion of molecules into another species e.g. by the removal of a specific group, [10] can take place. The structure of clay minerals, the variable composition of the layers and that of the interlayer species endows the clay minerals with an ambiguous identity that is difficult to classify experimentally [11]. Consequently, the number of permutations possible between structure, composition, interlayer species and type of interaction provides the computationalist with an embarrass de richesses with regard to the choice of theoretical investigation to support and inform experimental results.

The choice of investigations presented in this thesis were motivated by the desire to extend the application of density functional theory (DFT) with planewaves and within the pseudopotential approximation, to larger, heterogeneous systems. That is, if a homogeneous environment describes for example, a silicon crystal, a heterogeneous environment describes a system consisting of slab layers with surfaces, vacuum space and interlayer, gas-phase like molecules. As well as acquiring the modelling techniques specific to clay minerals, further motivation lay in addressing unanswered questions concerning in particular, catalytic reactivity of aluminium-bearing clay minerals and the mechanism of the acquisition of electrons, i.e. reduction, in iron-bearing clay minerals.

The *ab initio* investigation of the electronic structure of clay models such as those included in this work, has only relatively recently become possible with the development of efficient computational algorithms and the availability of high performance parallel computing facilities. Even so, results are not quickly gained in comparison to those of standard condensed matter subjects undergoing the same investigations. Consequently, modelling techniques which may be used ubiquitously

with more 'standard' systems cannot always be applied to the clay mineral models indiscriminately. Therefore, this work concentrates as much on the techniques of modelling clay minerals, as on the reactions and interactions of interest and also on the interpretation of the results in the context of the models and methods used.

The investigation of modelling techniques and catalytic reactivity begins in Chapter 3, which, in Section 3.2 investigates aluminium-bearing clay minerals. The motivation behind the study is to determine the catalytic role of the clay in a decarboxylation reaction, a role first hypothesised by Almon and Johns [10] in 1975 from their experimental results. They were investigating the part clay minerals play in the formation of fossil oil from biologically-derived fatty acids, i.e. how the conversion of dead sea life into fossil oil occurs. An optimum modelling environment is determined, which is used in Section 3.6 as the template for an investigation into the same reaction, but within iron-bearing clay minerals, employing two different density functional approximations.

The exploration of modelling and analytical techniques continues in Chapter 4 where the investigation into the decarboxylation reaction recommences with the optimum modelling environment obtained in Chapter 3. This is used to locate an intermediate in the reaction pathway from first principles, which is then followed by its identification as a transition state using lattice dynamics.

The subject of appropriate modelling techniques continues in Chapter 5 where the question of reduction in iron-bearing clays is addressed. The issues involved include, how to represent reduction in static models; how to ensure that modelling artefacts are kept to a minimum and how to interpret the results in the context of the techniques employed. This chapter concludes with an adjunct study designed to isolate reduction in a specific environment of the clay mineral.

Each investigation has its own introduction and conclusion and there is a brief chapter of closing comments in Chapter 6. However, before the investigations be-

gin, the following chapter provides the theory and methods behind the computations employed throughout this thesis.

2

Theory and Methods

This chapter outlines the route from a many-body Schrödinger equation to its re-casting as many, single-particle equations each dependent on a common electron density. It then proceeds to methods of its solution including some specific implementations within CASTEP with particular reference to the clay mineral models. This is by no means a comprehensive description of either the theory or methods as there are many in-depth works covering both these aspects, particularly Payne *et al's* work for an all-encompassing description of the evolution and implementation of density functional theory (DFT) [12]. An excellent guide for the novice practitioner of DFT is provided by the work of Mattsson *et al* [13]. For a more focussed examination of particular aspects of electronic structure theory, consult the books of Martin [14] and Ashcroft and Mermin [15].

Quantum mechanics describes the wave behaviour and properties of particles.

The Hamiltonian operator of a quantum mechanical system acting on a wavefunction, comprises the right-hand side of the following time-dependent Schrödinger equation

$$i\hbar\frac{\partial\Psi}{\partial t}(\mathbf{r},t) = -\frac{\hbar^2}{2m}\frac{\partial^2\Psi}{\partial r^2}(\mathbf{r},t) + V(\mathbf{r},t)\Psi(\mathbf{r},t) \quad , \tag{2.1}$$

presenting the kinetic and potential energy of a one-particle system described by state $\Psi(\mathbf{r},t)$, where $V(\mathbf{r},t)$ is a time-dependent potential. The wavefunctions of the solution to the Schrödinger equation contain all the information of a system, however, obtaining that information becomes the problem as highlighted by Dirac [16], *"The fundamental laws necessary for the mathematical treatment of a large part of physics and the whole of chemistry are thus completely known, and the difficulty lies only in the fact that application of these laws leads to equations that are too complex to be solved."* This is certainly the case for the many-body, time-dependent Schrödinger equation with the implication that, to be at all useful, it needs simplifying.

Although solutions can be readily found for a one-particle system, a many-body system renders an exact solution within a 'reasonable' time, impossible. The complexity arises in the first instance, from the interdependence of distance (x) and momentum (p) encapsulated by Heisenberg's Uncertainty Principle:

$$\Delta(x)\Delta(p_x) \geq \frac{\hbar}{2} \quad , \tag{2.2}$$

itself arising from the non-commutation of conjugate operators. Consequently the x-, y- and z- axes are no longer independent, and the simplifications possible as a result of this independence in classical mechanics, are not possible in the quantum sphere. Further complexity is added when considering a system of interacting electrons due to the nature of the electrons themselves, properties embodied by Pauli's exclusion principle

$$\Psi(\mathbf{r_1},\mathbf{r_2}) = -\Psi(\mathbf{r_2},\mathbf{r_1}) \quad , \tag{2.3}$$

satisfying the condition of allowed, non-zero wavefunctions only, considering the

antisymmetric wavefunctions of a two-particle (electron) system

$$\Psi(\mathbf{r_1}, \mathbf{r_2}) = \frac{1}{\sqrt{2}} [\Psi_A(\mathbf{r_1})\Psi_B(\mathbf{r_2}) - \Psi_A(\mathbf{r_2})\Psi_B(\mathbf{r_1})] \quad,$$

$$\Psi(\mathbf{r_2}, \mathbf{r_1}) = \frac{1}{\sqrt{2}} [\Psi_A(\mathbf{r_2})\Psi_B(\mathbf{r_1}) - \Psi_A(\mathbf{r_1})\Psi_B(\mathbf{r_2})] \quad,$$

where states Ψ_A and Ψ_B are functions of all four quantum numbers, n, l, m, s and $\mathbf{r_1}, \mathbf{r_2}$ are the spatial vectors for each particle.

Pauli's exclusion principle says that two fermionic particles cannot have identical quantum states. The consequence of this, in the case of electrons, is that they interact with one another. Two electrons of the same spin have a greater separation distance than two of opposite spin, consequently their Coulomb energies are different. The former has a lower Coulomb energy than the latter and when this energy difference due to antisymmetry is included as a property of the system, it is known as the *exchange energy* of a Hartree-Fock approximation.[1] The Coulomb energy of a system can be lower still if the electrons with opposite spin are also separated, however, this increases their kinetic energy. This is correlation i.e. where electrons of opposite spins are separated, reducing the Coulomb energy at the expense of increasing their kinetic energy. The difference in energy between the Hartree-Fock approximation and that of a many-body system is the *correlation energy*, and, in combination with the exchange energy, will be re-encountered as the exchange-correlation energy later in this chapter. As a consequence of the spin property of electrons, both the kinetic energy and the potential terms of Equation 2.1 are no longer simple and the Hamiltonian of a time-independent system of interacting nuclei (position vector $\mathbf{R}$) and electrons (position vector $\mathbf{r}$) is given by the Hamiltonian

$$\hat{H}\Psi(\mathbf{r}_i, \mathbf{R}_j) = E\Psi(\mathbf{r}_i, \mathbf{R}_j) \quad,$$

---

[1]The Hartree-Fock approximation is historical in the development of DFT and has been generally superceded by more recent approximations. It is discussed briefly in Section 2.1.4

where

$$
\hat{H} = -\frac{\hbar^2}{2m_e} \sum_i \nabla_i^2 - \frac{\hbar^2}{2M_n} \sum_j \nabla_j^2 \tag{2.4}
$$
$$
- \frac{1}{4\pi\epsilon_0} \sum_i \sum_j \frac{eZ_j}{|\mathbf{r}_i - \mathbf{R}_j|} + \frac{1}{2} \sum_i \sum_{j\neq i} \frac{e^2}{|\mathbf{r}_i - \mathbf{r}_j|} + \frac{1}{2} \sum_i \sum_{j\neq i} \frac{Z_iZ_j}{|\mathbf{R}_i - \mathbf{R}_j|} \quad .
$$

Equation 2.4 describes, term-by-term the kinetic energy of the electrons and the nuclei, the Coulomb potentials of the electrons and nuclei, electron-electron and finally the nuclei-nuclei.[2] The prefactor of $\frac{1}{2}$ for the latter two potentials is to correct for double-counting where the differences between particles i and j is counted as well as the difference between j and i. The only simplifications made so far are the non-relativistic framework and the adoption of time-independence, which has had little impact on the solvability of a many-body Hamiltonian; an analytic solution is still intractable. The electron interactions described in the preceding paragraph are, for the moment, encapsulated in the words describing this many-body interacting Hamiltonian rather than in any explicit maths. For any progress to be made, further simplifications were necessary, the first of which was density functional theory (DFT); its development forms the subject of the following section.

2.1 Towards Tractability

2.1.1 Born-Oppenheimer

The first important simplification to the many-body Schrödinger equation began with the Born-Oppenheimer approximation, where the masses of the nuclei, being approximately two thousand times greater than those of the electrons, renders them relatively immobile. The electrons effectively move instantaneously in response to the nuclei and hence the nuclei have relatively zero kinetic energy, removing the second term of Equation 2.4 and decoupling the wavefunction, $\Psi(\mathbf{r}_i, \mathbf{R}_j)$ into

---

[2]From this point onwards, Hartree atomic units are used, $\hbar = m_e = e = 4\pi/\epsilon_0 = 1$ unless otherwise stated.

$\psi(\mathbf{r}_i)\phi(\mathbf{R}_j)$.

2.1.2 Hohenberg-Kohn

Following the Born-Oppenheimer fixed nuclei approximation came two pivotal theorems in the history of DFT posited by Hohenberg and Kohn [17]. Firstly, they said that for any system of interacting particles in an external potential, $V_{\text{ext}}(\mathbf{r})$, i.e. a potential external to the electrons, there is a unique (apart from an additive constant) ground state density, $(n_0(\mathbf{r}))$. And secondly, that for any external potential, $V_{\text{ext}}(\mathbf{r})$, it is possible to define the total energy, E as a functional of the density, i.e. $E[n(\mathbf{r})]$. Furthermore, for any $V_{\text{ext}}(\mathbf{r})$, the groundstate density, $(n_0(\mathbf{r}))$ is found at the global minimum of $E[n(\mathbf{r})]$.

2.1.3 Kohn-Sham — Part 1

The next simplification was made by Kohn and Sham [18] who said that, a system of $N-$ interacting particles can be replaced by N non-interacting particle systems, with an interacting density and a background potential due to all other electrons moving in a potential of fixed nuclei. In light of the simplifications and approximations made so far, Equation 2.4 can be re-written as the Kohn-Sham energy functional of the charge density $(n(\mathbf{r}))$ for a fixed array of nuclei,

$$E[n(\mathbf{r})] = \int V_{\text{ion}}(\mathbf{r})n(\mathbf{r})d\mathbf{r} + \frac{1}{2}\int\int \frac{n(\mathbf{r})n(\mathbf{r}')}{|\mathbf{r}-\mathbf{r}'|}d\mathbf{r}d\mathbf{r}' + G[n(\mathbf{r})] \quad , \tag{2.5}$$

where the first term is the total electron/ion potential the second the Coulomb interaction or Hartree potential between the electrons. The last term is given by

$$G[n(\mathbf{r})] = T[n(\mathbf{r})] + E_{xc}[n(\mathbf{r})] \quad , \tag{2.6}$$

and describes the non-interacting kinetic energy of the electrons and the exchange-correlation energy of their interactions respectively. This latter term embodies the

non-classical interactions between electrons that were introduced in Section 2. A necessary condition for the Kohn-Sham (K-S) energy functional is for any variation of the charge density to leave the particle number (N) unchanged, given that $N = \int n(\mathbf{r})d\mathbf{r}$, this condition is fulfilled by $\int \delta n(\mathbf{r})d\mathbf{r} = 0$.

2.1.4 An Historical Interlude —- Hartree and Hartree-Fock approximation

The Hartree potential of Equation 2.5 contains a self-interaction, due to the spatial spread of the electron. This is an artefact of the Coulomb potential which was addressed by the Hartree-Fock approximation (HFA). The HFA includes exchange by employing the Hartree potential and enforcing antisymmetry of the electron wavefunctions. This is achieved by creating a many-body wavefunction which is the determinant of a matrix of single-particle, orthogonal, spin orbitals. The determinant of this Slater matrix includes direct and exchange terms, which cancel exactly. However, two main problems with the HFA are the size of the Slater matrix, it scales as the square of the number of wavefunctions, and the absence of correlation. Consequently HFA has been overtaken by DFT where the self-interaction of the Hartree potential is counteracted by the $E_{xc}[n(\mathbf{r})]$ term which creates an exchange hole around a region of electron density, which is re-encountered in Section 2.1.5. Further details of HFA can be found in reference [14].

2.1.5 Kohn-Sham — Part 2

Returning to the Kohn-Sham Hamiltonian. The single-particle Kohn-Sham Hamiltonian is given by

$$\left[-\frac{\hbar^2}{2m}\nabla^2 + V_{\text{ion}}\left(\mathbf{r}\right) + V_H(\mathbf{r}) + V_{XC}(\mathbf{r}) \right] \psi_i(\mathbf{r}) = \varepsilon_i \psi_i(\mathbf{r}) \quad , \tag{2.7}$$

respectively describing the kinetic energy of non-interacting electrons; the electron-ion (pseudo)potential; the electron-electron Hartree potential and the exchange-correlation potential. ψ_i are the eigenstates and ε_i the eigenvalues of the

Kohn-Sham Hamiltonian. They are the single-particle wavefunctions. A sketch of the simplifications made so far can be seen in Figure 2.1.

The wavefunction of Equation 2.4, $\Psi(\mathbf{r}_i, \mathbf{R}_j) = \Psi(\mathbf{r}_1, \mathbf{r}_2, ..., \mathbf{r}_n, \mathbf{R}_1, \mathbf{R}_2, ..., \mathbf{R}_n)$ has become $\psi_1(\mathbf{r})\phi(\mathbf{R}), \psi_2(\mathbf{r})\phi(\mathbf{R}), ...\psi_n(\mathbf{r})\phi(\mathbf{R})$ where $\phi(\mathbf{R})$ is effectively a constant as it is the ion-ion potential due to an array of fixed nuclei described by the Ewald term — see Section 2.4. The total electron density is given by the sum of the amplitudes of the Kohn-Sham orbitals for both spin-up and spin-down occupied states, but for simplicity of notation, spin is subsequently not differentiated unless otherwise stated. The charge density is given by

$$n(\mathbf{r}) = \sum_i \mid \psi_i(\mathbf{r}) \mid^2 \quad, \tag{2.8}$$

where the wavefunctions are orthonormalised

$$\int_V \psi_i^*(\mathbf{r})\psi_j(\mathbf{r})dV = \delta_{ij} \quad \text{for} \quad \delta_{ij} = \begin{cases} 1 & \text{if } i = j \\ 0 & \text{if } i \neq j \end{cases} \quad \text{and} \quad \int n(\mathbf{r})d\mathbf{r} = N \quad,$$

where N is the total number of electrons.

Figure 2.1: Cartoon of many-body system, with two nuclei, N and two electrons, e^- (LHS). 'KE' is kinetic energy and all other labels are as detailed in Equation 2.7. After the Hohenberg-Kohn and Kohn-Sham simplifications focussing on one of the two electrons. The yellow cloud represents the term $G[n(\mathbf{r})]$ in Equation 2.5.

Taking each term of Equation 2.7: the kinetic energy term is that of the non-interacting electrons and the portion due to their interaction is encapsulated by the

exchange-correlation potential. The potential term, $V_{\text{ion}}(\mathbf{r})$ is the pseudopotential term and is discussed in greater depth later in this chapter, but for now suffice it to say that it simplifies the nuclear region from the perspective of the valence electrons. The Hartree term, $V_H(\mathbf{r})$ describes the Coulomb interaction between electrons without their spin effects. The exchange-correlation potential, V_{XC} takes account of the kinetic energy difference due to interacting electrons and their interacting spin effects as discussed at the beginning of this Chapter, and is given by

$$V_{XC}(\mathbf{r}) = \frac{\delta E_{xc}[n(\mathbf{r})]}{\delta n(\mathbf{r})} \quad . \tag{2.9}$$

Can it be said that any progress has been made in finding a solution? How is this term any more accessible than its forbears? Well, if Equation 2.9 is re-written as

$$\frac{\delta E_{xc}[n(\mathbf{r})]}{\delta n(\mathbf{r})} = \frac{\partial [n(\mathbf{r})\varepsilon_{XC}(\mathbf{r})]}{\partial n(\mathbf{r})} \quad , \tag{2.10}$$

$$\text{with} \quad \varepsilon_{XC}(\mathbf{r}) = \epsilon_{XC}^{\text{hom}}(\mathbf{r}) \quad , \tag{2.11}$$

then a possible route to a solution is glimpsed through Equation 2.11 which says that, in a Kohn-Sham system of non-interacting particles, at position $\mathbf{r}$ with a density $n(\mathbf{r}_{ks})$, the exchange-correlation energy is given by the exchange-correlation energy at position $\mathbf{r}$ with the same density, $n(\mathbf{r}_{ks})$ in a homogeneous electron gas. This is a local density approximation (LDA) [18] of the exchange-correlation energy and was formulated in 1965, and in 1981 was parameterised by Perdew and Zunger [19] based on Ceperley and Alder's Monte Carlo computations, which worked out the exchange-correlation energy of a locally homogeneous gas at various densities [20]. This is local because a small volume around the point $\mathbf{r}$ is assumed to have the same density as that at the point $\mathbf{r}$. The sum of the individual ϵ_{XC} gives the total exchange-correlation energy of an interacting system [14]

$$E_{XC}^{LSDA}[n^{\uparrow}, n^{\downarrow}] = \int n(\mathbf{r})\epsilon_{xc}^{\text{hom}} \left(n^{\uparrow}(\mathbf{r})n^{\downarrow}(\mathbf{r}) \right) d^3r \quad . \tag{2.12}$$

The LDA described here includes the spin (S) densities and is referred to as LSDA.

Where there is an explicit inclusion of spin, the spin charge density is given by

$$n^\sigma(\mathbf{r}) = \sum_i |\psi_i^\sigma(\mathbf{r})|^2 \quad \text{and the total density by} \quad n(\mathbf{r}) = \sum_\sigma n^\sigma(\mathbf{r}) \quad , \qquad (2.13)$$

consequently there could be two energy minima that minimise $E[n^\sigma(\mathbf{r})]$. This spin polarisation effect (with respect to the GGA exchange-correlation functional) is discussed in Chapter 5 with reference to iron.

In spite of inaccuracies in the density due to ignoring local inhomogeneities in the electron density around position $\mathbf{r}$, the LDA is a successful approximation. This is due to obeying the sum rule for an exchange-correlation hole. Exchange and correlation effects cause a decrease in classical electron density at position $\mathbf{r_1}$ due to the presence of an electron at position $\mathbf{r_2}$ and vice versa. This depleted area or hole has electron density given by $n_{xc}(\mathbf{r_1}, \mathbf{r_2})$, which satisfies the normalisation condition or sum rule, $\int n_{xc}(\mathbf{r_1}, \mathbf{r_2})d\mathbf{r_2} = -1$. Consequently, the total entity of an electron plus its volume of electron-depleted space, i.e. exchange-correlation hole, constitute a neutral entity. This exchange-correlation hole exactly cancels the self-interaction term of the Hartree potential.

Subsequent exchange-correlation approximations involve the first and higher orders of the density gradient at $\mathbf{r}$. This hierarchy forms a Jacob's ladder of density functional approximations designed with the intention to achieve ever greater accuracy. The next rung on the ladder up from LDA is the generalised gradient approximation (GGA). The GGA is semi-local as it depends on the gradient of the density at point $\mathbf{r}$, i.e. Equation 2.12 becomes

$$E_{xc}^{GGA}[n^\uparrow, n^\downarrow] = \int n(\mathbf{r})\epsilon_{xc}\left(n^\uparrow, n^\downarrow, |\nabla n^\uparrow|, |\nabla n^\downarrow|...\right) dr^3 \quad . \qquad (2.14)$$

The generalised gradient approximation of Perdew, Burke and Ernzerhof i.e the GGA-PBE [21] is the density functional of choice in the clay mineral studies because it is better able to describe molecular bonding than the LDA due to its gradient parameter [22]. That is, molecules tend to be inhomogeneous in their electron den-

sity, which the LDA cannot describe very well as it is essentially a local functional. Molecular systems tend to have rapidly varying densities, environments ill-suited to a functional originating from a smoothly varying electron density. However, with regard to band gaps, LDA fares better than the GGA due to gradient discontinuities at the band gap with the latter approximation. Hence, whereas LDA overestimates binding energies and thus underestimates bond lengths, GGA underestimates band gaps. Higher-order approximations are variations on the gradient theme where in the meta-GGA's, $\nabla^2 n(\mathbf{r})$ is used. The density functionals will not be described in greater detail here; the interested reader is referred to reference [23] for an in-depth comparative study of these functionals.

To re-cap: at this point, the many-body Schrödinger is now tractable due to the approximations of Born-Oppenheimer, Hohenberg-Kohn and Kohn-Sham plus the employment of density functional theory. There still remains the question of how the strong potential of the core electrons should be addressed, how physical systems can be modelled and how the computations can be carried out to optimum efficiency.

2.2 Modelling Systems — the essential ingredients

Density functional theory casts a many-body problem in terms of a single parameter, electron density, which is the sum of the amplitudes of occupied spin-up and spin-down Kohn-Sham orbitals. The modelling of these orbitals requires a basis set for their mathematical representation. Within CASTEP the basis set of choice is planewaves and the bulk of a material is modelled by periodic cells.

2.2.1 Periodic Cells

Modelling the bulk of a material involves a unit cell containing an atomic basis, such that an infinite repetition of this cell throughout space reproduces the bulk material. A unit cell of the lowest order symmetry — the primitive cell — is preferable to minimise computational time. In the atomic basis of the periodic cell, electrons comprise regions of charge density and, as expressed by Equation 2.8, this charge density is readily calculated from the amplitude of wavefunctions.

2.2.2 Planewaves

The set of wavefunctions used to described the electron density within a DFT formalism is known as a 'basis set'. The basis functions of choice within CASTEP are planewaves. As quantum mechanics is a linear theory, the principle of linear superposition applies, which, for planewaves [3] can be described by the following: if $f = e^{-i\theta}$ and $g = e^{-i\phi}$ then $f + g = e^{-i\theta} + e^{-i\phi}$.

Planewaves also have the following properties:

Completeness: any continuous function satisfying periodic boundary conditions can be described by a set of planewaves. The set of planewaves describing the function forms a complete set, e.g. if a function $f(x)$ satisifies the boundary conditions $f(0) = 0, f(L) = 0$ then the set of sine functions, $\sin(n\pi x/L), n = 1, 2, 3....$ forms a complete set of functions for the expansion of $f(x)$.

Orthonormality: pairs of member functions of complete sets are orthogonal and planewaves are normalizable, i.e. for a pair of wavefunctions, orthonormality is described by $\int_0^{2\pi} \phi_i(x)\phi_j(x) = 2\pi\delta_{ij}$, where δ_{ij} is the Kronecker delta.

These properties allow for the description of the energy surface of a many-body system within DFT formalism in the form of a Fourier series of planewaves. One computational drawback is that they describe all of the volume of a periodic cell, including the vacuum space. The series of planewaves comprise a wavefunction at

---

[3]the exponential expression for planewaves is used ubiquitously throughout this chapter, where $e^{i\theta} = \cos\theta + i\sin\theta$

position $\mathbf{r}$, i.e.

$$\psi(\mathbf{r}) = \sum_{\mathbf{G}_{\text{max}}} C_G e^{i(\mathbf{G} \cdot \mathbf{r})} \quad , \tag{2.15}$$

where C_G is the coefficient per planewave up to an arbitrary wavevector $\mathbf{G_{max}}$, where $\mathbf{G}$ is a reciprocal space lattice vector — more of this in the following section. Without a pseudopotential approximation,[4] the size of the maximum wavevector, $\mathbf{G}$ and hence the size of the basis set are determined by the strong Coulomb interaction between the core electrons and the nuclei. The kinetic energy of these electrons is high, hence they have a relatively high number of oscillations, which require a large number of planewaves for their description. This is ameliorated by the pseudopotential approximation, which reduces the size of the basis set required but remains the determining factor in its size. (Properties of pseudopotentials will be described in greater depth later in this chapter.) Within the pseudopotential approximation, the basis set size for a computation is determined by testing the kinetic energy cut-off via the relation between the kinetic energy (E_{KE}) and $G_{\text{max}} = |\mathbf{G}_{max}|$ i.e.

$$E_{KE} = \frac{\hbar^2 G_{\text{max}}}{2m} \quad , \tag{2.16}$$

where, in order to form a complete set, $G_x = 2\pi n/x, G_y = 2\pi n/y, G_z = 2\pi n/z, n = 1, 2, 3....$ where x, y, z are the lengths of reciprocal space vectors containing the wavefunction $\psi(\mathbf{r})$.

2.2.3 Reciprocal Space

Reciprocal/wave or $k-$ space is a more appropriate environment in which to describe wave properties than is real space. An example of this is wavenumber, which in non-wave or 'real' space has units cm^{-1} whereas in $k-$space it is a number representing the number of nodes per cm. It is simple to deduce from this and from Figure 2.2 the inverse relationship between wavelength, λ and wavenumber, k consequently the

---

[4]This is an approximation that replaces an all-electron model for the core and valence electrons with a smoother potential. There is a detailed description in Section 2.3, suffice it to say for now that the number of planewaves required is reduced by several orders of magnitude by using this approximation.

$$\lambda = 2\pi/k$$

1 node,
k = 1

λ_A

8 nodes,
k = 8

$\lambda_B = \lambda_A/8$
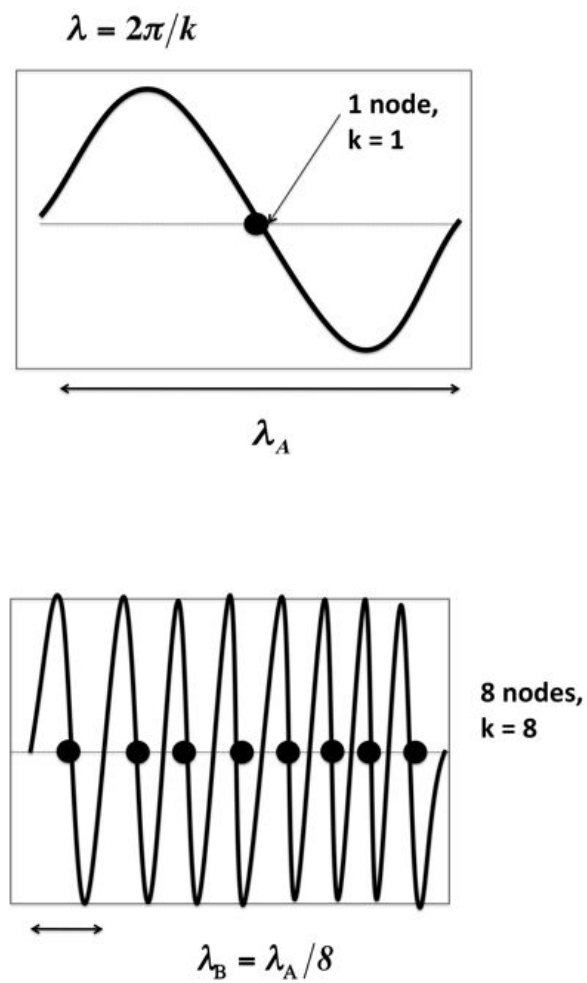
Figure 2.2: Illustrating the relationship between wavelength and wavenumber.

smaller the value of k, the larger the value of λ.

The replication of the periodic unit cell in real space produces a Bravais lattice in reciprocal space. As an electron's wavefunction given by Equation 2.15 evolves throughout the lattice, it will be affected by an infinite number of other wavefunctions and potentials, i.e. it will experience diffraction. This leads to interference between a wavefunction and its periodic image, producing wavefunctions that are out of phase with one another. Formulating the effect of phase variance on the wavefunction evolving from the single unit cell, is achievable by including a phase factor per term of the Fourier series, which is simpler to see using trigonometric functions. If a complex wave is represented by $\cos\theta + i\sin\theta$ then a phase shift of ϕ is given by $\cos(\theta + \phi) + i\sin(\theta + \phi)$, which is the same as $e^{i\theta}e^{i\phi} = e^{i(\theta+\phi)}$. Hence multiplying the periodic wavefunction of Equation 2.15 by a second wavefunction induces a phase shift per term of the Fourier series

$$\psi_{\mathbf{k},\mathbf{G}}(\mathbf{r}) = \sum_{\mathbf{k}} C_k e^{i(\mathbf{k}\cdot\mathbf{r})} \sum_{\mathbf{G}} C_G e^{i(\mathbf{G}\cdot\mathbf{r})} \quad , \tag{2.17}$$

where $k_x = 2\pi n/x, k_y = 2\pi n/y, k_z = 2\pi n/z, n = 1, 2, 3....$ and x, y, z are reciprocal lengths of the unit cell. k-points are the positions described by the $\mathbf{k}$ vector and either term will be used to suit the context. Equation 2.17 now describes the evolution of a wavefunction throughout an infinite bulk and satisfies Bloch's Theorem described in the following section.

2.2.4 Bloch's Theorem

For a periodic potential given by

$$U(\mathbf{r} + \mathbf{R}) = U(\mathbf{r}) \quad , \tag{2.18}$$

where $\mathbf{R}$ is a Bravais lattice vector and the potential is a function of the charge density, it follows that the charge density is also periodic. However, this does not

require the wavefunctions to be periodic as the charge density, being the sum of the amplitudes of the wavefunctions, does not include any information about their phases, which can be anything. The scale of the periodic potential is usually 10^{-8}cm, the same order of magnitude as the de Broglie wavelength of free electrons. Thus, electrons are susceptible to diffraction and their total wavefunction is given by a superposition of wavefunctions of the periodic potential. Now, the wavefunction obtained so far is periodic in that it is defined by the boundary conditions of the unit cell and is the basis set required for the energy surface description, i.e.

$$u_{\mathbf{G}}(\mathbf{r}) = \psi(\mathbf{r}_{\mathbf{G}}) = \sum_{\mathbf{G}} C_G e^{i(\mathbf{G}\cdot\mathbf{r})} \quad , \tag{2.19}$$

and, including a phase factor, this term describes Bloch's Theorem

$$\psi_{\mathbf{k},\mathbf{G}}(\mathbf{r}) = e^{i\mathbf{k}\cdot\mathbf{r}} u_{\mathbf{G}}(\mathbf{r}) \quad , \tag{2.20}$$

where $\mathbf{k}$ is the Bloch wavevector, which is, in general, any complex vector. This is exactly the form of Equation 2.17 obtained in the previous section on considering the effect of diffraction on the phase of a wavefunction. So, for any Bravais lattice vector $\mathbf{R}$, the wavefunction is given by

$$\psi_{\mathbf{k},\mathbf{G}}(\mathbf{r} + \mathbf{R}) = e^{i(\mathbf{k}\cdot\mathbf{R})} \psi_{\mathbf{k},\mathbf{G}}(\mathbf{r}) \quad . \tag{2.21}$$

(Comprehensive proof of Bloch's Theorem can be found in references [15], [24]). Bloch's Theorem maps the problem of an infinite number of wavefunctions onto an infinite number of phases within the original unit cell. The choice of the cut-off energy defined by G_{max} results in a finite basis set at an infinite number of phases or k-points.

The discussion so far has concentrated on periodicity and its use to replicate a bulk system, an obvious question arises concerning aperiodic systems and surfaces, is it possible to model these with periodic cells? The answer is yes it is, by using supercells.

2.2.5   Supercells

Aperiodic systems such as those containing a defect or those with a surface, are modelled using supercells, which effectively isolate the defect or the surface. If a defect is within the bulk of a material, surrounding the defect with sufficient non-defective bulk renders the defect a relatively singular event. If the defect is charged, careful consideration must be paid to its long-range Coulombic field and periodic interactions. Although the clay mineral models do not contain defects, the same considerations apply to their charged species, which is covered in detail in Chapter 5. Modelling a surface involves including sufficient vacuum space within a large cell (hence the term 'supercell') to separate adjacent surfaces sufficiently to minimise their interactions. All of the clay minerals described in this study are composed of a three-tier layer of atoms, which has two surfaces and, in some models, the surfaces are charged.

2.3   Pseudopotentials

Substituting Equation 2.17 into the Kohn-Sham Hamiltonian of Equation 2.7 produces a dominant kinetic energy term given by

$$-\sum_{k,G} |\mathbf{k} + \mathbf{G}|^2 C_{k,G} e^{i(\mathbf{k}+\mathbf{G})\cdot\mathbf{r}} \quad . \tag{2.22}$$

This determines the size of the Hamiltonian matrix of the K-S Hamiltonian. To include the high kinetic energy of the core and valence electron interactions would require a large cut-off energy, which has been established is dependent on $|\mathbf{G}_{\mathrm{max}}|$. A larger $|\mathbf{G}_{\mathrm{max}}|$ equates with a larger basis set and consequently a Hamiltonian matrix growing by a factor of n^2 where n is the number of terms in the basis set. The computations would become unfeasibly large for most day-to-day requirements, consequently all-electron models are not employed without justification.

The core electrons have less effect on the physical properties of solids than the valence electrons, due to their tight binding to the nuclear region. As the core region requires high kinetic energy oscillations for its description, an approximation to smooth out this region became an important step in the feasibility of modelling using planewaves. The advent of this pseudopotential approximation reduced the size of the K-S Hamiltonian matrix by replacing the highly oscillatory core region of electrons with a smoother pseudo-core region, while reproducing the pertinent properties of the core region beyond a cut-off radius. As the valence electrons are screened from the bare nuclear Coulomb potential by the core electrons, they experience a much smoother potential than might have been initially anticipated, thus the pseudopotential approximation is entirely appropriate from the perspective of the valence electrons. Two of the types of pseudopotentials used in the clay mineral studies are norm-conserving and ultrasoft and between them, they reproduce the following properties:

1. The eigenvalues of the pseudo-valence (PP) electrons are the same as those of the electrons in an all-electron (AE) calculation i.e $\varepsilon_i^{PP} = \varepsilon_i^{AE}$.

2. There are no discontinuities in the wavefunctions at the core radius cut-off.

3. There are no discontinuities in the logarithmic derivatives of the wave functions at the core radius cut-off.

4. The first energy derivative of the logarithmic derivatives of the pseudo- and 'real' wave functions agree at the core radius cut-off.

5. The integrated charge for each wavefunction agrees within the radius cut-off. (Applies to norm-conserving potentials only.)

Property one ensures that the correct energy bands are maintained; property two is a physical and mathematical necessity; properties three and four ensure the correct scattering properties of the core region are reproduced; property five is optional depending on whether the approximation is norm-conserving or ultrasoft. The general construction of the two types is similar in that there is a local part depending on
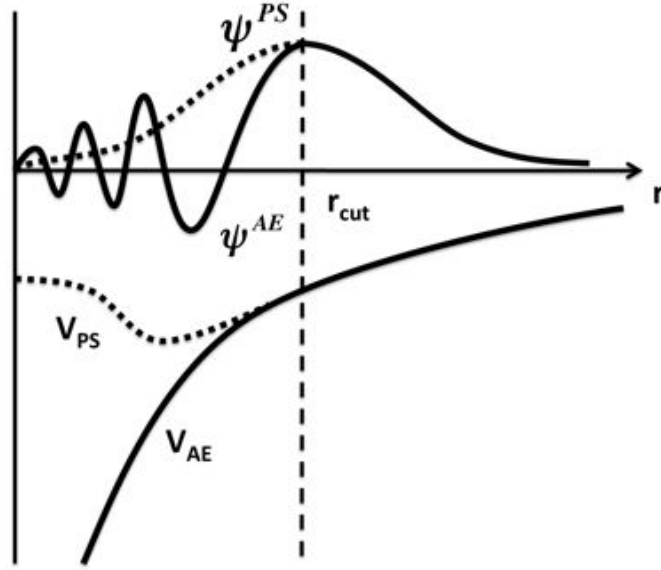
Figure 2.3: Schematic of the smoothing effect of the pseudo-wavefunction ψ^{PS} and potential V^{PS}, compared to the all-electron (AE) versions. Note how they agree at r_{cut} [12].

radial distance only and a non-local part depending on angular momentum channel projectors, which are necessary to reproduce the correct scattering properties.

$$V^{PP} = V(\mathbf{r}) + \sum_i |\chi_l\rangle V_l \langle \chi_l| \quad . \tag{2.23}$$

The all-electron and pseudo-wavefunctions are identical beyond the cut-off radius, r_{cut}. The total ionic psuedopotential of a system is given by [12]

$$V_{\text{ion}}(\mathbf{G}) = \sum_\alpha S_\alpha(\mathbf{G}) v_\alpha(\mathbf{G}) \quad , \tag{2.24}$$

where v_α is the pseudopotential of species α and $S(\mathbf{G})$ is the structure factor of a periodic position of ions (R_I) of that species i.e. $S(\mathbf{G}) = \sum_I e^{i(\mathbf{G} \cdot \mathbf{R}_I)}$.

2.3.1 Norm-conserving

Within this approximation, the charge density of the all-electron core is reproduced within the cut-off radius, which tends to be relatively short. Therefore, the kinetic

energy is still high and hence a large number of planewaves are required to describe the potential experienced by the valence electrons. Norm-conserving pseudopotentials were designed by Hamann, Schlüter and Chiang [25] in 1979 and further developed by Kleinman and Bylander [26]. The charge conservation property of norm-conserving pseudopotentials confers greater transferability than that of the ultrasofts, which, according to Goedecker and Maschke [27] is due to an inert region of charge density surrounding the core. If the r_{cut} lies within the inert region, a pseudopotential is transferable to any chemical environment, if, however, it falls outside of this region, the transferability is reduced, which can be the case in the ultrasoft approximation.

As the exchange-correlation energy is non-linear, in some cases the charge density in the core region overlaps with the valence density causing an underestimation of the exchange-correlation energy in the valence region. To remedy this, a fraction of the core charge is added to the valence charge in this area of overlap. Both the norm-conserving and ultrasoft pseudopotentials for iron contain this non-linear core correction [28] and will be encountered in Chapter 3, Section 3.6.

2.3.2 Ultrasoft

Within this approximation, the norm-conserving constraint is relaxed and r_{cut} can be larger than in the norm-conserving case. Consequently, the kinetic energy is reduced, the valence electrons experience a smoother potential and the number of planewaves required for its description decreases. This is the main advantage of ultrasofts, which were developed by Vanderbilt [29] and has lead to the application of *ab initio* molecular dynamics to a wider class of systems than with norm-conserving PP. The increase in r_{cut} decreases the transferability of ultrasofts to some extent, although Laasonen demonstrated good transferability between small oxygen molecules [30], a notoriously demanding element. Relaxing the charge constraint allows the pseudo-and the all-electron wavefunctions to be matched independently at r_{cut}. As a direct result, the pseudopotential must be self-consistently updated

but this extra computational expense is outweighed by the reduction in the number of planewaves required. If the integrated charge density in the pseudo-core region does not match that in the all-electron core, an augmentation charge is added.

Their construction begins by introducing non-local overlap operators, where (as in the norm-conserving model) the β projectors are per angular momentum channel: [29], [14], [31]

$$\hat{\mathbf{S}} = \hat{\mathbf{I}} + \sum_{nml} q_{nm} |\beta_n^l\rangle\langle\beta_m^l| \quad \text{where} \quad q_{nm} = \int_0^r Q_{nm}(r)dr \quad , \tag{2.25}$$

and $Q_{nm} = 0$ is the norm-conserving constraint. The charge density is now given by:

$$n(\mathbf{r}) = \sum_i \phi_i^*(\mathbf{r})\hat{\mathbf{S}}\phi_i(\mathbf{r})$$

$$= \sum_i \left[|\phi_i(\mathbf{r})|^2 + \sum_{nml} Q_{nm}^i(\mathbf{r})\langle\phi_i|\beta_n^l\rangle\langle\beta_m^l|\phi_i\rangle \right] \quad , \tag{2.26}$$

where the term $\sum_{nml} Q_{nm}^i(\mathbf{r})$ describes the quantity of augmentation charge. The ultrasoft potential can be written as

$$V^{PP} = V_{loc}(\mathbf{r}) + \sum_{nml} D_{nm}^0 |\beta_n^l\rangle\langle\beta_m^l| \quad , \tag{2.27}$$

$$\text{where} \quad D_{nm}^l = D_{nm}^0 + \int V_{\text{ion}}(\mathbf{r})Q_{nm}^l d\mathbf{r} \quad . \tag{2.28}$$

D_{nm}^0 are the coefficients characterizing the pseudopotential, differing with the atomic species and the index l refers to an atomic site. Equations 2.25 to 2.28 are reproduced here to illustrate the difference between norm-conserving and ultrasoft construction, that, although the latter requires fewer planewaves, its structure is complicated by the introduction of the tensor and its overlap operator, $\hat{S}$. The self-consistent Hamiltonian becomes $\hat{H}|\psi_i\rangle = \epsilon_i\hat{S}|\psi_i\rangle$, the total energy is now $E = \sum_{ij}\langle\psi_i|\hat{H}|\psi_j\rangle$ and the wavefunctions of the smooth potential are S-orthogonal, i.e. $\langle\psi_i^{PP}|\hat{\mathbf{S}}|\psi_j^{PP}\rangle = \delta_{ij}$. The implications of this are that although ultrasoft PP require a more complex pre-

conditioner[5] than norm-conserving PP, this is outweighed by the reduced number of planewaves required for their description. Further details can be found in Hasnip and Pickard's work [32].

The potential artefacts on creating pseudopotentials in general, are ghost states arising within the core region, due to the addition of augmented charge with too many nodes, which creates an unphysical phenomenon. Gonze [33] describes a method of eliminating these ghost states should they arise.

Both norm-conserving and ultrasoft pseudopotentials are constructed by removing an electron and inverting the Schrödinger equation to determine the potential experienced by a valence electron. As this is done within a particular density functional, e.g. LDA, it is important to match the pseudopotential with the density functional computation. The investigations of the following chapters use the GGA exchange-correlation functional with ultrasoft PBE and norm-conserving pseudopotentials.

Since the formulation of the K-S Hamiltonian, there has been no reference to the ion-ion interactions. The following section addresses this term.

2.4 Ion-Ion interaction

The brief description of the ion-ion (Ewald) term that follows, serves more as recognition of its existence than an in-depth exploration of its theory. If the latter is required, the references within this section should be consulted.

The interactions between the nuclei are long-range Coulomb forces in real and reciprocal space. Ewald cast the problem in the form of a nucleus at position $\mathbf{R}_1$

---

[5]This term is explained in Section 2.5.3 but for now, in its most general sense, describes the stabilisation of an ill-conditioned system to enable numerical convergence of a minimisation algorithm.

interacting with an array of atoms at points $\mathbf{R}_1 + \mathbf{l}$ where $\mathbf{l}$ is a lattice vector and split the problem into a real space and reciprocal space part. The contribution to the total energy at $\mathbf{G} = \mathbf{0}$ from the Hartree, pseudopotential and ion-ion terms exactly cancel but Ewald's real space/reciprocal space splitting excluded this term from the reciprocal space contribution. This was later remedied by Yin and Cohen [34] so that the correct form for the Ewald energy is [12]

$$E_{R-R} = \frac{1}{2} \sum_{I,J} Z_I Z_J e^2 \left\{ \sum_{\mathbf{l}} \frac{\mathrm{erfc}(\eta|\mathbf{R}_1 + \mathbf{l} - \mathbf{R}_2|)}{|\mathbf{R}_1 + \mathbf{l} - \mathbf{R}_2|} - \frac{2\eta}{\sqrt{\rho}} \delta_{IJ} \right\} +$$

$$\frac{1}{2} \sum_{I,J} Z_I Z_J e^2 \left\{ \frac{4\pi}{\Omega} \sum_{\mathbf{G} \neq \mathbf{0}} \frac{1}{|\mathbf{G}|^2} \exp\left[-\frac{|\mathbf{G}|^2}{4\eta^2} \right] \cos\left[(\mathbf{R}_1 - \mathbf{R}_2) \cdot \mathbf{G} \right] - \frac{\pi}{\eta^2 \Omega} \right\} \quad , \quad (2.29)$$

where Z_I, Z_J are the valences of ions I and J, erfc is the complementary error function, $\mathbf{l}, \mathbf{R}$ are the real and reciprocal space lattice vectors respectively, Ω is the volume of the unit cell, η is a number and ρ is the charge density.

2.5 Computational Methods

The second half of this chapter concerns the computations supporting the theory of the first half, including the algorithmic routines involved in finding a self-consistent solution to the K-S Hamiltonian. All computations were carried out using CASTEP [35], an *ab initio* DFT, total energy, planewave pseudopotential code written in Fortran 90. Some procedures specific to CASTEP are mentioned and some with particular reference to the clay mineral models. It begins with a description of how the Born-Oppenheimer energy surface of a system is sampled.

2.5.1 K-point Sampling

In reciprocal space, the phases are nodes or points in the unit cell, which are described by sampling the Brillouin zone (BZ). The BZ describes the unique region of space closest to the $\mathbf{G} = \mathbf{0}$ point onto which all other points can be mapped by periodicity, therefore by sampling the BZ, the entirety of the bulk is sampled. The

change in energy when sampling $k-$points determines how many of them need to be sampled, that is, an energy convergence test (or other property of interest) is carried out using an increasing number of $k-$points, in a similar method to the cut-off energy convergence testing described in Section 2.5.10. (There is a detailed description of the variation in the average energy per k-point per volume of k-space, for a particular bandstructure of GaAs, in reference [36].) In crystals of high symmetry, the number of k-points is reduced by symmetry operations where grids of sampling points such as the Monkhurst-Pack grid, are formulated by the generation of periodic functions based on point group symmetries [37], [38]. Efficient k-point sampling reduces the computational time required as it reduces the number of computations, therefore it is highly beneficial to determine the symmetry of the unit cell to produce a primitive cell and thus the smallest number of k-points. Unfortunately, the clay mineral models are asymmetric due to the guest species in the interlayer, however, they are sufficiently large in the $z-$direction to require only gamma point sampling, i.e. sampling at $k = 0$, in that direction. k-point sampling of the clay mineral models is described in Chapter 3, which also includes an example of a primitive cell of wüstite.

2.5.2 Locating the Groundstate Energy

Hohenberg and Kohn established that there is a unique correspondence between the groundstate density of a system and its potential. From this groundstate density, many properties of the system can be determined such as equilibrium crystal structure, elastic constants, dielectric and magnetic susceptibility etc.. Total energy differences between systems are used in this study to identify the potential reactivity of particular configurations where, for example, a lower total energy implies greater stability than a system containing the same constituent atoms in a different configuration. How is this groundstate density reached, given that the K-S potential depends on the density which depends on the wavefunctions which are shaped by the potential? The answer is that the initial wavefunctions are guessed, which then allows for a self-consistent iterative minimisation of the K-S energy, towards the groundstate density. The previous section established the theory behind the

construction of the Kohn-Sham Hamiltonian and this section now proceeds with a self-consistent determination of the groundstate charge density, $n_0(\mathbf{r})$.
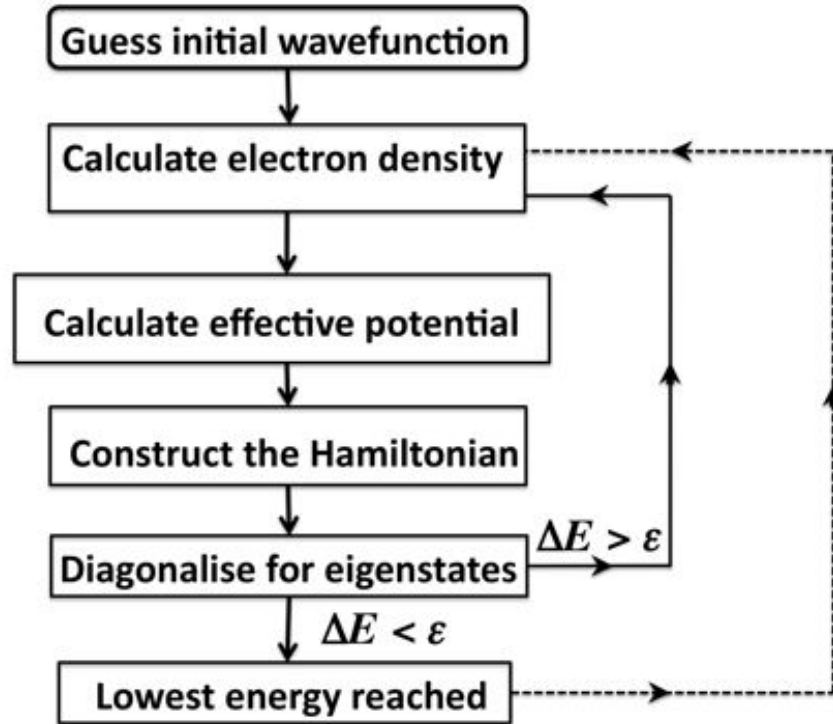
Figure 2.4: Outline of the algorithm for identifying the groundstate charge density for a single self-consistent field (SCF) cycle. ΔE is the energy difference between successive SCF iterations and ε is the energy tolerance criteria. The outermost dashed line refers to geometry optimisation, which proceeds from the lowest energy by moving the atoms and then repeating the entire cycle with the inclusion of the atomic positions and a force tolerance criteria. This is explained in greater detail in Section 2.5.4.

Figure 2.4 illustrates the iterative self-consistent cycle leading towards finding the groundstate density of a system. Initially the trial wavefunctions $\psi_i(\mathbf{r})$ for a single k-point are guessed, from which the charge density is calculated via $n(\mathbf{r}) = \sum_i |\psi_i(\mathbf{r})|^2$. This is then fed into the K-S Hamiltonian to obtain the effective (total) potential and the Hamiltonian matrix. In principle the next step is to directly diagonalise the Hamiltonian, but, in reality, this is unfeasible for any but the smallest systems due to the cubic scaling with the number of planewaves. So, rather than matrix decomposition, a self-consistent minimisation (the charge density is updated

iteratively) of the K-S Hamiltonian is performed. The K-S energy functional can be successfully, directly minimised as it has a well-defined minimum providing a stable platform for minimisation routines. Iterative diagonalisation methods are employed to obtain the lowest (i.e. the occupied) eigenstates of the K-S matrix, beginning with a steepest descent step.

2.5.3 Minimisation Algorithms

Steepest Descent

The steepest descent algorithm finds the largest negative derivative of the energy with respect to the wavefunctions and uses this as the search direction to locate the minimum of the electronic energy surface. The principle is given by

$$\mathbf{h^1} = -\frac{\partial \mathbf{E}}{\partial \psi}\big|_{\psi=\psi^1} \quad , \tag{2.30}$$

where $\mathbf{h^1}$ is the first steepest descent direction. Alternatively, in terms of the steepest descent direction for a single band

$$\zeta_i^m = -(H - \lambda_i^m)\psi_i^m \quad ,$$
$$\text{where} \quad \lambda_i^m = \langle \psi_i^m | H | \psi_i^m \rangle \quad , \tag{2.31}$$

where i is the band, H is the Hamiltonian and m the iteration index.

To reduce $\mathbf{E}(\psi)$ a move from ψ^1 to $\psi^1 + \phi^1 \mathbf{h^1}$ is required. This is sampling along a line or line minimisation to determine the value of ϕ^1 that minimizes $\mathbf{E}(\psi^1 + \phi^1 h^1)$. A line minimisation follows a steepest descent step.

The drawback with the steepest descent method occurs when the energy surface is long and shallow and the initial search direction is perpendicular to the long-axis of the surface, the subsequent orthogonal search direction would then lie along the long axis of the shallow valley. In such an instance, the minimisation process be-

comes inefficient. An improvement of the steepest descent is the conjugate gradients algorithm.

Conjugate Gradients
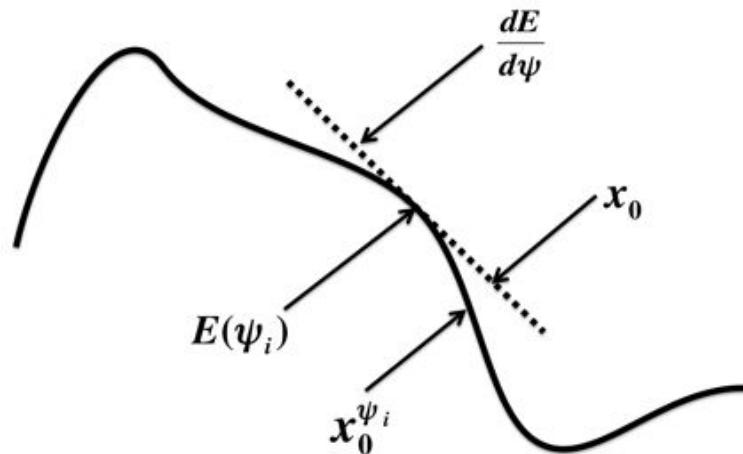
Fit $E(\psi)$, $\frac{dE}{d\psi}$, x_0 to $y = ax^2 + bx + c$ at $\frac{dy}{dx} = 0$ i.e. $2ax_0 + b = 0$.
Then, check $x_0 - x_0^{\psi_i} >$ tolerance?
If no, minimum found.
If yes, then fit a cubic and repeat check.

Figure 2.5: Schematic of the principles of line minimisation. There is an implicit assumption in the check illustrated that the length of the step taken from $E(\psi)$ to x_0 is optimal. The check is repeated until the tolerance criteria are met, which may involve extending the algorithm to fitting a quartic function.

Conjugate gradients is an improvement over steepest descent as, for a quadratic function, convergence is guaranteed for a system of $n-$dimensions, within n steps. (Not proven here). This is true in theory, but in practice depends on a perfect line search. Conjugate gradient iterations converge in proportion to $\sqrt{\epsilon_{max}/\epsilon_{min}}$ i.e. to a ratio of the maximum and minimum eigenvalues of the basis states [32]. Gradients

are conjugate to one another if they obey the following condition:

$$\mathbf{d^n} \cdot H \cdot \mathbf{d^m} = 0 \,; \ \text{for } n \neq m \quad n, m \ \text{are integers,} \tag{2.32}$$

where $\mathbf{d^n}$ and $\mathbf{d^m}$ are the minimization directions; H and $\mathbf{h}$ are as previously defined.

$$\mathbf{d^m} = \mathbf{h^m} + \gamma^m \mathbf{d^{m-1}} \ \text{where} \ \gamma^m = \frac{\mathbf{h}^m \cdot \mathbf{h}^m}{\mathbf{h^{m-1}} \cdot \mathbf{h^{m-1}}} \quad . \tag{2.33}$$

Equations 2.32 and 2.33 show that each subsequent search direction contains information about the previous search directions. This, together with the conjugacy condition, ensures that all n-dimensions of a system are searched, thus guaranteeing the location of a minimum. Each complete and minimised conjugate gradients iteration proceeds with a line minimisation as outlined earlier in this section. Figure 2.5 illustrates a simple line minimisation using a quadratic fit. Although these algorithms are efficient, the K-S Hamiltonian matrix is, as it has been described, ill-conditioned. Therefore there is room for improvement in the minimisation methods, which can be achieved by preconditioning.

Preconditioning

The dominance of the kinetic energy terms in the Hamiltonian matrix with the increasing size of the coefficents of the wavefunctions can be seen by substituting the following

$$\psi_i(\mathbf{r}) = \sum_{\mathbf{k},\mathbf{G}} C_{k,G} e^{i(\mathbf{k}+\mathbf{G})\cdot\mathbf{r}} \quad , \tag{2.34}$$

into the K-S Hamiltonian (Equation 2.7). This produces

$$\sum_{\mathbf{G'}} \left[\frac{\hbar^2}{2m} |\mathbf{k}+\mathbf{G}|^2 \delta_{\mathbf{G}\mathbf{G'}} + V_{\text{ion}}(\mathbf{G}-\mathbf{G'}) + V_H(\mathbf{G}-\mathbf{G'}) \right.$$
$$\left. + V_{XC}(\mathbf{G}-\mathbf{G'}) \right] c_{i,\mathbf{k}+\mathbf{G'}} = \epsilon_i c_{i,\mathbf{k}+\mathbf{G}} \quad , \tag{2.35}$$

an ill-conditioned Hamiltonian matrix [39], which, for kinetic energies is a diagonal matrix of the form

$$\frac{1}{2} \begin{pmatrix} (k+G_1)^2 & 0 & 0 & \cdots & 0 \\ 0 & (k+G_2)^2 & 0 & \cdots & 0 \\ & & \cdots\cdots\cdots\cdots\cdots & & \\ 0 & 0 & 0 & \cdots & (k+G_{\mathrm{max}})^2 \end{pmatrix}$$

whose larger coefficients on the descending diagonal leads to the imbalance shown in Figure 2.6 In comparison to G_n, k is small.

Figure 2.6: Illustrating the relative magnitude of the increase in kinetic energy along the diagonal of the Hamiltonian matrix.

Now, the current wavevectors have produced an error in the total energy because they do not solve $H\psi_i = \epsilon_i \psi_i$. The error in the wavevectors and the steepest descent direction are related by [12]:

$$\xi_i = -\sum_\alpha (\varepsilon_\alpha - \lambda_i) c_{i,\alpha} \xi_\alpha \quad , \tag{2.36}$$

as the error in the wavevectors is given by $\delta\psi_i = \sum_\alpha c_{i,\alpha} \xi_\alpha$, where ε_α is the eigenvalue of the eigenstate ξ_α, $\lambda_i^m = \langle \psi_i^m | H | \psi_i^m \rangle$, i is the band index and m the iteration number. Thus, if the unoccupied states (those with the higher kinetic energies) were degenerate then the steepest descent vector, ξ_i would become a multiple of the error vector, $\delta\psi_i$ thus shortening the route to the wavevectors solving $H\psi_i = \epsilon_i \psi_i$. This is preconditioning i.e producing a steepest descent vector that is close to the error vector.

The eigenstates with the higher kinetic energies have these kinetic energies lying close to their eigenvalues due to the dominance of the kinetic energy over the potential energy term. The eigenstates with lower kinetic energies have a more equal contribution from the kinetic and potential energy terms producing a range of energies in the basis states. Pre-multiplying the Hamiltonian by a preconditioning matrix, K re-balances the system to effectively produce degenerate eigenvalues, hence the steepest descent vector becomes a simple multiple of the error vector as desired for the optimum rate of convergence. K consists of a polynomial which removes the effect of high kinetic energy while leaving the lower kinetic energy terms relatively unaffected. The preconditioning matrix $\mathbf{K}$ has elements $K_{G,G'}$ which are a function of x i.e. $K_{G,G'} = \delta_{G,G'} f(x)$ where

$$x = \frac{(\hbar^2 |\mathbf{k} + \mathbf{G}|^2)/2m}{\langle \psi_i^m |(-\hbar^2/2m)\nabla^2|\psi_i^m\rangle} \quad . \tag{2.37}$$

A key point in reducing the computational expense, is to ensure that ψ_i are constrained to be orthogonal allowing for a band-by-band update of the charge density. Orthogonalising the steepest descent vector to all other bands fulfils this constraint on the wavefunctions and is achieved by adapting Equation 2.31 to become

$$\zeta_i^m = \zeta_i^m - \sum_{j \neq i} \langle \psi_j | \zeta_i^m | \psi_j \rangle \quad . \tag{2.38}$$

The preconditioned steepest descent vector is now [12] $\eta_i^m = \mathbf{K}\zeta_i^m$. The next step is to produce the preconditioned conjugate gradient direction based on Equation 2.33 and detailed in reference [12], then continue as described in Section 2.5.3.

Proceeding with the minimisation band-by-band, that is, within a band, repeating the cycles until the total energy changes by less than a particular value, then moving on to the next band and repeating the process, ensures that all bands are updated gradually towards the convergence criteria before ψ_i and hence $n(\mathbf{r})$ are updated. This is the general procedure; there are a couple of variations on this

implemented within CASTEP, in the form of density mixing (DM) and ensemble density functional theory (EDFT).

Density Mixing and Ensemble Density Functional Theory

Density mixing in general produces a new estimated charge density at each step from a linear combination of the input charge densities from a previous history of densities [40]. The advantage of this is that the trial wavefunctions do not have to be updated after each band optimisation, which saves time, but has the potential to introduce charge oscillation or 'sloshing' in successive iterations. If the trial wavefunctions are not updated after each band partial-convergence, an error, particularly in the Hartree potential is introduced, which grows with system size as the wavenumber, k decreases. Disparities are then created in the wavefunction/potential interaction which produces charge sloshing in successive iterations. There are various tuneable parameters to control the sloshing and improve the reliability of convergence and this is discussed in depth with respect to the clay mineral models in Chapter 5. Generally speaking, DM is reliable for 'reasonably sized' insulators where there is a well-defined band gap, which effectively stabilises orbital occupancy.

EDFT is useful where the band gap is small and for metallic systems where the Fermi level of the Brillouin zone is comprised of orbitals with varying occupancy. The EDFT algorithm depends on the creation of a projected functional that depends only on the orbitals rather than their occupancies [41]. The evolution of the orbitals towards the groundstate is decoupled from their occupancy while maintaining orthogonality and conserving charge. The updated charge density then recombines the occupancies with the wavefunctions, which is then followed by updating the potentials. Thus, for every iteration, $n(\mathbf{r})$, ψ_i and all potentials are updated creating a very tight self consistency between all elements of the Kohn-Sham Hamiltonian, thus, EDFT is an extremely robust minimisation method. It is also variational unlike DM, which is not. The reliability of EDFT comes at a cost of increased computational time, nevertheless, it became the minimisation method of choice in the clay mineral studies, for reasons discussed in-depth in Chapter 5.

2.5.4   Beyond the groundstate charge density

It is important that the range of trial wavefunctions encompasses those of the groundstate wavefunction or the true groundstate will not be located. For this reason the coefficients of the initial trial ψ_i are randomly generated. Also, even in systems where there is a band gap, it is advisable to include some empty bands in the model to ensure the groundstate is fully spanned.

Each iteration updates the charge density and the cycle continues until conceptually, $\mathbf{H}\psi_{i(r_{\text{new}})}(\mathbf{r}) = \varepsilon_i \psi_{i(r_{\text{old}})}(\mathbf{r})$; computationally the limiting factor is $E_n - E_{n-1} \leq \Delta\epsilon$ i.e. where the energy difference between two successive iterations is no larger than the energy convergence criteria, $\Delta\epsilon$. When the convergence criteria has been met for two to three SCF cycles, the final charge density is the groundstate density for that particular configuration of atoms.

2.5.5   Geometry Optimisation

Locating the groundstate of a system where the ions and electrons are in their minimum energy configuration, is a straightforward matter of geometry optimisation. The SCF iterations are repeated following a shift in the atomic positions. The convergence criteria for the electronic groundstate still apply per SCF iteration, as well as convergence criteria applicable to the geometry per SCF cycle, which are often energy and force tolerances.

The Hellman-Feynman (H-F) Force Theorem provides the directional guide for the change in ionic positions and the calculated force on the nuclei [42]. The force on an ion is given by the derivative of the total energy with respect to the position of the ion i.e.

$$F_I = -\frac{dE}{d\mathbf{R}_I} \quad , \tag{2.39}$$

providing the wavefunctions are eigenstates of the Kohn-Sham Hamiltonian, i.e.

$$F_I = \frac{\partial E}{\partial \mathbf{R}_I} - \sum_i \frac{\partial E}{\partial \psi_i} \frac{d\psi_i}{d\mathbf{R}_I} - \sum_i \frac{\partial E}{\partial \psi_i^*} \frac{d\psi_i^*}{d\mathbf{R}_I} \quad . \tag{2.40}$$

In a fixed ionic configuration, the electronic structure is relaxed to its groundstate — where the ψ_i are the eigenstates — and *then* the forces on the ions are calculated. The ions are then moved along the directions of the H-F forces and the electronic structure is relaxed to its groundstate for the new configuration, beginning the new SCF cycle with the wavefunctions obtained from the previous ionic configuration. This cycle continues until the residual forces on all atoms are less than a specified tolerance. As the forces are sensitive to first order errors in ψ_i, it is more difficult to calculate accurate forces than energies, which are sensitive to second order errors in ψ_i. Consequently, the force convergence criteria used in the clay mineral studies is four orders of magnitude higher than that used for the electronic structure energy convergence and three orders of magnitude higher than that used for the geometry energy tolerance.

Using planewaves has the advantage that Pulay forces do not have to be considered. They are a mathematical artefact of the method of self-consistent solutions, arising due to a change in the basis set on relaxation of the ions. The difference in the potentials caused by a change in ionic configuration from one iteration to the next creates an additional term in Equation 2.40, which is the derivative of the basis set with respect to the position of the ions. This term causes an instability in the variational force, which is corrected by the frozen cores of the pseudopotential approximation and, as was shown by Scheffler, Vigneron and Bacheret [43], by the basis set including its own derivatives, a criteria fulfilled by a planewave basis set.

2.5.6 Calculating Stresses

If the lattice parameters as well as the positions of the ions are allowed to relax, the shape of the unit cell is able to change; the extent to which this affects the total

energy of the system is contained within the stress tensor. Stress is an internal bulk property caused by external pressure and is calculated by considering the strain on a system. If the lattice vectors $\mathbf{a}, \mathbf{b}, \mathbf{c}$ are written in terms of the identity matrix, $\mathbf{I}$ and a matrix $\mathbf{X}$ then the effect of an applied strain ε on the shape of the unit cell is given by

$$\mathbf{X}' = (\mathbf{I} + \varepsilon)\mathbf{X} \quad . \tag{2.41}$$

The stress tensor, $\sigma_{\alpha\beta}$ is then given by

$$\sigma_{\alpha\beta} = \frac{1}{\Omega}\frac{\partial E}{\partial \varepsilon_{\alpha\beta}} \quad , \tag{2.42}$$

where α, β are the labels for the x, y, z directions and $\Omega = \mathbf{a} \cdot (\mathbf{b} \times \mathbf{c})$ [44], i.e. the volume of a unit cell. The paragraph describing artefactual Pulay forces also applies to artefactual Pulay stresses, i.e. when using a planewave basis set, they are non-existent.

2.5.7 Geometry Optimiser

Geometry optimisation uses the stress and strain calculations in its minimisation routine. When the lattice parameters are allowed to relax, it is the enthalpy of the system that is minimised where the enthalpy is given by $\mathcal{H} = E + p\Omega$ where E is the total energy, p is the applied pressure and Ω is the volume of a unit cell as described above. If $\mathbf{X}$ describes a position vector, then the force vector is given by [45]

$$F = -\frac{\partial \mathcal{H}}{\partial X}\Big|_p \quad , \tag{2.43}$$

whose strain components, ε are

$$f^{(\varepsilon)} = -(\sigma + p\Omega)(1 + \varepsilon^T)^{-1} \quad , \tag{2.44}$$

where σ is the stress at X

$$\sigma = \left(\frac{\partial E((1+\varepsilon')h)}{\partial \varepsilon'}\right)_{\varepsilon'=0} \quad , \tag{2.45}$$

where the strain tensor stretches a reference configuration h_0 onto $h = (1 + \varepsilon)h_0$. The remaining $3N$ components of F are given by

$$F = (f^{(\varepsilon)}, gf_1, \ldots, gf_N)^T \quad , \tag{2.46}$$

where $g = h^T h$ and N is the number of atoms in the unit cell. Essentially, F is a multivariable function whose minima can be found by a quasi-Newton minimisation method such as Broyden-Fletcher-Goldfarb-Shanno (BFGS), which is the geometry optimiser of choice for all of the calculations in this thesis. For small displacements from the minimum, the energy surface is quadratic and can be described by the second derivatives of the energy (the Hessian, $\mathbf{A}$) with respect to small displacements i.e. $\delta\mathcal{H} = \frac{1}{2}(\mathbf{X} - \mathbf{X_{min}}) \cdot \mathbf{A}(\mathbf{X} - \mathbf{X_{min}})$. $\mathbf{A}$ is not known, so, after an initial guess successive iterations approach $\mathbf{X_{min}}$ according to

$$\mathbf{X}_{i+1} = \mathbf{X}_i + \lambda\mathbf{\Delta X}_i \tag{2.47}$$

$$\mathbf{\Delta X}_i = \mathbf{H}_i\mathbf{F}_i \quad , \tag{2.48}$$

for $\mathbf{H} = \mathbf{A}^{-1}$; λ is the step length determined by an approximate line minimisation along step direction $\mathbf{\Delta X}_i$. Further details can be found in reference [45].

As the size and shape of the unit cell changes during geometry optimisation, errors can be introduced into the computations due to the effect on the size of the planewave basis set. This basis set size is dependent on the reciprocal lattice length via the boundary conditions established in Section 2.2.3, hence a change in lattice length introduced during the relaxation of the lattice can change the size of the planewave basis set. This can be addressed by either keeping the number of planewaves fixed in which case the variational principle still applies and the minimum sought is the minimum enthalpy, however, the cut-off energy varies. The other

alternative is to fix the cut-off energy allowing the number of planewaves to vary, which breaks the variational principle and looks instead for zero force and stress rather than minimum enthalpy. All of the calculations in this thesis have used the latter method on variable cell optimisations as this retains consistency between models, i.e. the upper bound on the degree of description applies to each, due to the employment of the same cut-off energy.

2.5.8 Convergence in General

When investigating a system it is important to decide which are the features of interest, in order to converge computations with respect to these features. In the clay mineral models, the energies are important in so far as the energy differences between like-configuration models are used to discriminate between relative states, e.g. a lower relative energy indicates greater stability. Absolute energies of systems are absolutely meaningless in this study. Another important feature of the clay mineral models is relative, minimum energy configurations to determine the reactant and product systems of a chemical reaction. For this feature, the forces, as well as the energies are converged. By comparing like-systems, many of the potential errors due to 'poor' convergence criteria are cancelled out, as long as the systems are investigated consistently. 'Poor' in this context can adopt any meaning from too low a cut-off energy, to the forces being too lax. This method of comparing similar systems is especially important when working in relatively unexplored territory, such as that inhabited by the clay mineral models. There are so few of these particular DFT studies in existence for guidance, that, some other method of comparison is required, hence the comprehensive adoption of this 'like-models' method.

2.5.9 Fast Fourier Transforms

Fast Fourier Transforms (FFT) are used within CASTEP to switch between reciprocal and real space to optimise calculations in their physical representations. The

kinetic energy, Hartree potential and local pseudopotential have diagonal representations in reciprocal space, therefore it is most efficient for them to be minimised in this space, whereas the exchange-correlation operator is diagonal in real space. FFT allows for efficient, computationally inexpensive switching between the two optimal environments.

2.5.10 Energy Cut-off Convergence

An energy cut-off is used to fix the number of planewaves in the basis set, rather than a straightforward option of choosing the number of planewaves as the former method ensures the reproduction of the optimal number of nodes when the cell size changes, such as during a total-cell relaxation. The energy cut-off for planewave systems is usually tested by examining the convergence of energy differences between two like-systems. The method for the clay mineral models is described in Chapter 3. The theory behind this method is robust because energy differences between systems mainly arise due to different chemical bonding, which is external to ion core regions. An increase in cut-off energy will increase the number of planewaves, which will increase the accuracy of the description of the ion cores. As long as an increase in the number of planewaves does not increase the charge density in the bonding region, an additional number of planewaves increases the energy per atom of the systems by a constant amount, hence the energy differences remain the same.

Within CASTEP there is a standard grid size used to determine the points at vectors $\mathbf{r}$ where the wavefunction is evaluated when the cut-off energy is chosen. These points coincide with the Fourier coefficients of the wavefunction. To calculate the charge density, which is the sum of the square of the wavefunctions, a grid size of half the spacing of the standard grid is used and is called the coarse grid. The charge density for ultrasoft potentials is composed of two parts, a softer part which is the sum of the square of the wavefunction amplitudes and a harder part, which describes the augmentation charge and is 'harder' as the wavefunctions are more oscillatory. The coarse grid describes the soft density and, practically has spacing

1/1.75 of that of the standard grid due to ignoring some of the contribution from the small, high-frequency components of the soft density.

The description of the augmentation charge of the ultrasoft pseudopotentials requires a finer grid (in real space) due to its high-frequency components. This grid is the fine grid and by default has the same scaling as the coarse grid. The GGA exchange-correlation functional also has high-frequency components even in the norm-conserving pseudopotentials, so it is possible that some adjustment of grid scale may be required in this case as well as within the ultrasoft approximation. It is possible that using a closer grid spacing, which corresponds to including more Fourier terms of a wavefunction, can reduce the cut-off energy requirement. In the clay mineral studies, the default coarse grid of 1.75 was found to be adequate for the study of Chapter 3 and of 2.0 for Chapters 4 and 5. An investigation not recorded in this dissertation, involving a different ultrasoft pseudopotential, showed an improvement in convergence to a greater number of decimal places when the coarse and fine grid scales were adjusted. This implies that it is a very useful auxiliary convergence parameter and the time spent investigating it could reduce the cut-off energy and hence increase overall computational efficiency.

2.5.11   Mulliken analysis

Throughout the clay mineral studies, a means of comparing valence charge and spin was required, to determine trends such as the population of particular atoms and how this changes in various environments. The analytical tool of choice is Mullikens population analysis, a method of calculating charges based on the population of linear combined atomic orbitals (LCAO) bases [46], [47], [48], [49]. As planewaves and not LCAO are the choice of basis set in CASTEP, a means of projecting the eigenstates onto atomic orbitals was required. This was implemented in CASTEP by Segall *et al* [50] based on the method of Sanchez-Portal [51].

Sanchez-Portal provided the link between methods using LCAO and those us-

ing planewaves. Where planewaves are essentially delocalized, atomic orbitals are localised and allow for the quantification of atomic charge, orbital population, bond charge and charge transfer via population analysis. Planewaves offer a means of providing a well optimised basis set through the pseudo-atomic orbitals generated from the pseudopotentials. However, these atomic orbitals form a non-orthogonal basis set, inferring greater transferability between environments. Essentially the eigenstates of the Kohn-Sham Hamiltonian are projected onto the pseudo-atomic orbitals. The quality of this projection is measured by the spilling parameter given by [51]

$$ S = \frac{1}{N_{\mathbf{k}}} \frac{1}{N_\alpha} \sum_{\mathbf{k}}^{N_{\mathbf{k}}} \sum_{\alpha=1}^{N_\alpha} \langle \psi_\alpha(\mathbf{k}) | (1 - P(\mathbf{k})) | \psi_\alpha(\mathbf{k}) \rangle \quad , \tag{2.49} $$

where $N_{\mathbf{k}}$ and N_α are the number of calculated points in the Brillouin zone and the number of bands respectively; $\psi_\alpha(\mathbf{k})$ are the K-S Hamiltonian eigenstates; $P(\mathbf{k})$ is the projector operator. Further details can be found in Sanchez-Portal's work [51]. The essence of the projector method is that the spilling parameter, S measures the difference between the eigenstates of the K-S Hamiltonian and their projection onto the atomic basis. S varies between 0 and 1 where 0 is a perfect projection and 1 describes orthogonality between the pseudo-atomic orbitals and the K-S eigenstates. For groundstate properties such as the total energy, geometry and electron density describing bonding, all properties studied in the clay mineral models, occupied eigenstates are required. Excited and optical properties require an inclusion of some of the lowest unoccupied states.

The Mulliken analysis which turns the projection of the planewaves onto the pseudo-atomic orbitals, into quantified charges per atom, proceeds as described in Mulliken's work [46], [47], [48], [49]. Essentially the charge per atom is obtained from the weighted total of the product of the density and overlap matrices and the interested reader is advised to consult the aforementioned references for further details.

Mulliken analysis is a very quick post-processing calculation as it uses information already obtained in the energy minimisation. It is widely acknowledged that

Mulliken population analysis cannot provide physically meaningful absolute magnitudes of atomic charges, due to the sensitivity of the results to the choice of basis set. However, Mulliken analysis is very useful when considering relative values, as demonstrated by Sanchez-Portal [52] in examination of the '... redistribution of charge and bonds ...'. This is exactly the application of Mulliken analysis in the clay mineral studies, where charge and spin comparisons have been made between like-systems. This, together with relaxed geometries and the occupation of the Fermi levels are used to draw conclusions about the relative chemical states of reactant, products and intermediates in Chapters 3 and 4 and relative reduction in Chapter 5.

Although within the studies presented in this thesis, the Mulliken charge partitioning was deemed suitable for analysis, if, in future studies '...meaningful charges that conform to chemical experience..' [53] are sought, the Hirshfeld partitioning scheme [54] would be more appropriate. This is based on electron density rather than the spatial extent of basis sets, as in the Mulliken scheme. Hirshfeld measures the flow of electron density from an initial state to the final SCF converged molecule, measuring changes of charge density or deformations, with respect to an initial charge density of a 'promolecule'. As it is the deformation density that is important, the exact shape and size of atomic regions are not critical. Given that the deformation density is the difference between the molecular and the unrelaxed atomic charge densities, careful consideration would need to be given to the initial configurations of unrelaxed, like-models. That is, it would be important to determine how much the deformation density depends on the state of 'unrelaxedness' of the initial configuration. This would be an interesting investigation, but unfortunately time has not allowed for it in this thesis.

2.5.12 Parallel Computing

All of the calculations done for this thesis were processed on either of the following parallel computers.

HECToR — UK's high-end computing resource, funded by the UK Research Coun-

cils. It has 44000 cores, each at 2.1GHz, 1.3Gb per core.

Hamilton — Durham's ITS High Performance Computing cluster. It has 1792 cores, each at 2.4GHz, 448 cores at 6Gb per core and a further 1344 cores at 3Gb per core.
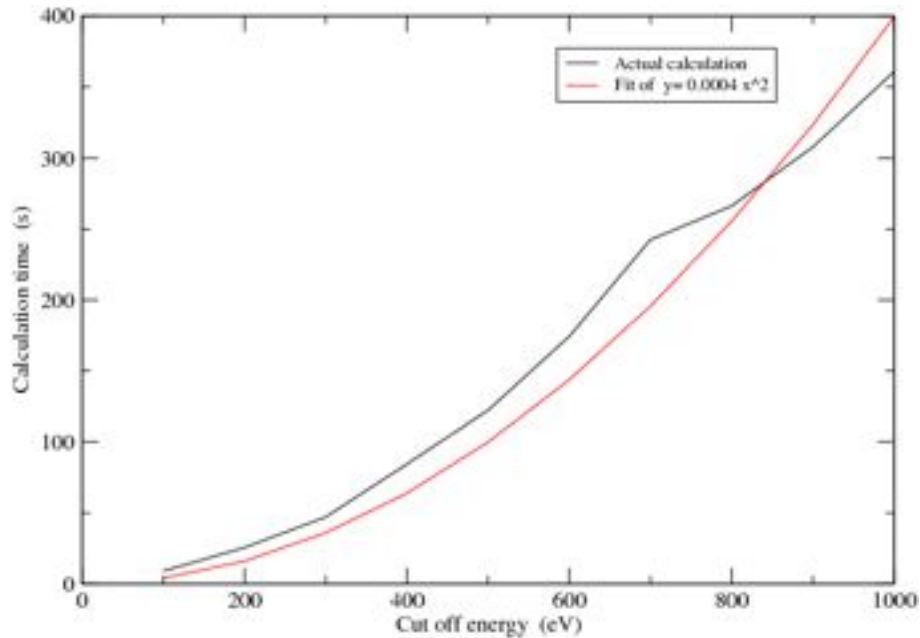
Figure 2.7: Calculation time with cut-off energy.

Each computation in the following chapters (apart from the wüstite study in Chapter 3) used at least sixteen cores as this was found to be the lower bound for optimum speed. As can be seen in Figure 2.7 the computational time grows as the square of the cut-off energy. Figure 2.8 illustrates the relationship between the number of k-points, symmetry and calculation time. Almost all of the models within this thesis do not require more than two k-points and have no symmetry operations other than the trivial identity, consequently there are few examples of k-point tests recorded. However, in cases (other than within this thesis) where more than two k-points are required, it is often most efficient to use the number of cores corresponding to the highest common factor of k-points and cores per node. For example, for nodes containing 4 cores where 15 $k$points are required, the optimum choice for k-point parallelisation would be for 15 cores distributed over 4 nodes. This is assuming that the communication saturation time between the cores has not
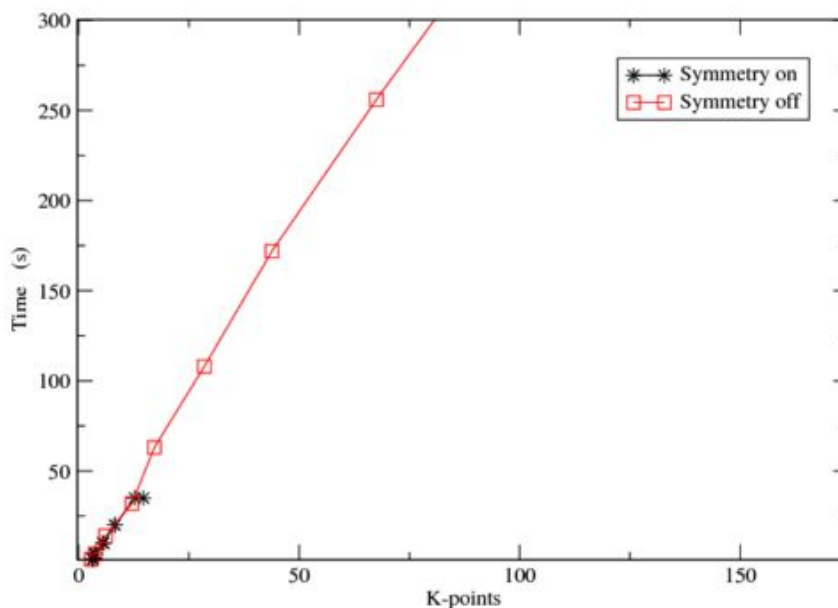
Figure 2.8: Calculation time with number of k-points for a silicon crystal, where symmetry operations were applicable, reducing the calculation time by an order of magnitude.

been reached. If it has, then either 5 or 3 cores would be more efficient, i.e. the number of cores matching the factors of the number of k-points. This is assuming that the memory requirements per node are within their limits.

The aim of this chapter was to provide some background theory and methodology used in the investigation of the electronic structure of materials. It is far from exhaustive in its breadth and depth but the references contained within, should provide sufficient guidance as to where further theory can be found.

The following chapter is the first of three investigations into clay mineral models and their gallery guests and begins with a description of the clay models and their specific terminology.

3

The Role of Clay Minerals in Oil Forming Reactions

3.1 Introducing Clay Minerals

Before launching into the study itself, a brief introduction is required concerning some aspects of the materials modelled and the terminology used to describe them. As mentioned in Chapter 1, clay minerals are the focus of all of the electronic structure investigations described in this thesis, and, although probably everyone would know in general terms what is meant by the word 'clay', fewer people would be familiar with specific clay mineral terminology. Therefore, this brief introduction is designed to equip the reader with the necessary background information required for the easy digestion of the remainder of this work.
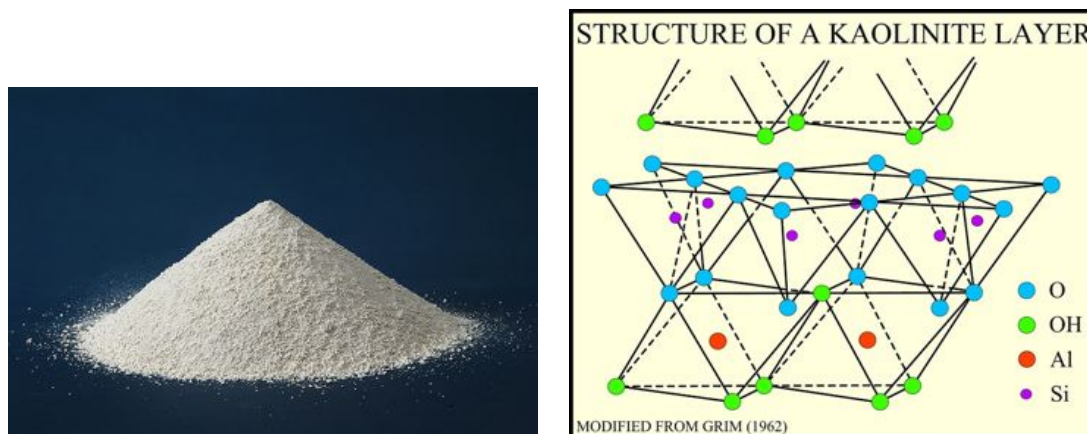
Figure 3.1: Left — Bulk kaolinite [55], right — atomic structure of kaolinite layer [56], [57].

Clays are the products of weathered and decomposed igneous rocks [58], where 'igneous' describes one of the three types of rocks on Earth. Clays contain clay minerals of several groups such as kaolin [5], illite [5] and smectite [5] where these terms describe particular properties of the clay minerals. An example of a clay mineral in its bulk form [55] and its atomic structure [56], [57] are shown in Figure 3.1. The clay minerals of focus in this manuscript are smectites — from the Greek word *smectos* for 'soap' — which includes montmorillonite, pyrophillite and nontronite to name a few. The smectite group encompasses clay minerals that are composed of layered, planar sheets of silicates, which is silicon occupying a tetrahedral environment surrounded by oxygen, forming hexagonal siloxane rings [5]. 'Layered silicates' is given the one word description 'phyllosilicates', where 'phyllo' is from the Greek word *phyllon* for leaf, as clay minerals are composed of many stacked layers or leaves.
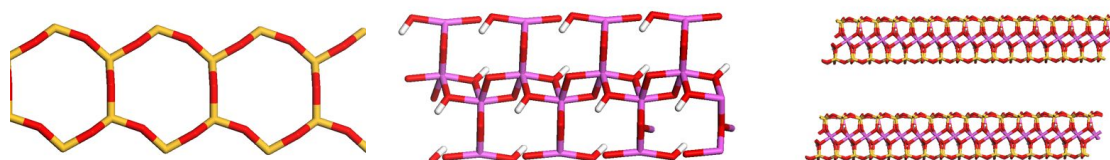
Figure 3.2: Far left: octahedral sheet of siloxane; centre: tetrahedral sheet of aluminium oxide; right: two clay mineral layers comprised of 2:1 combination of the siloxane and aluminium oxide shown to the left. Colour scheme: red: oxygen; yellow: silicon; pink: aluminium; white: hydrogen.

The tetrahedral phyllosilicate sheets conjoin an octahedrally coordinated metal oxide sheet to form a clay mineral layer. The ratio of tetrahedral to octahedral describes this coordination e.g. pyrophillite is a 2:1 dioctahedral phyllosilicate, which means there is one octahedral metal oxide sheet sandwiched between two tetrahedrally coordinated silicate sheets, as seen in Figure 3.2. There are often isomorphic ('same shape') substitutions of the metal atoms in either or both sheets leading to an overall negative charge on the layer. This attracts charge-balancing cations such as Na^+ or Ca^{2+} into the space between the layers i.e. into the 'interlayer space' or 'gallery'. The interlayer cations or 'gallery guests' are exchangeable cations as they may trade places with other cations in the layer, increasing the difficulties of definitively identifying a clay mineral's constituent atoms.

The layered nature of clay minerals is responsible for their swelling property as the interlayer space can increase and decrease without loss of integrity of the layers. The large surface area of the layers provides extended, potentially chemically reactive environments and consequently a wealth of subject material for any interested researcher. The focus of this study is the catalytic nature of the clay mineral, pyrophillite in a reaction describing the removal of carbon dioxide, i.e. decarboxylation, in the context of the formation of fossil oil. The following section is a summary and overview of the study to provide the reader with a general picture before becoming immersed in the details.

3.1.1 Synopsis

Mineral catalysed decarboxylation reactions are important in both crude oil formation and, increasingly, biofuel production. In this study decarboxylation reactions of a model fatty acid, propionic acid, C_2H_5COOH to an alkane, C_2H_6 were examined in an aluminosilicate model of pyrophillite with an isomorphic substitution of aluminium in the tetrahedral sheet. The choice of clay mineral was driven by the experiments of Almon and Johns in the 1970s, who published their work on decarboxylation within clay minerals [10], which described a theoretical, radical,

decarboxylation pathway based on their experimental results. To date, this theory has not been either definitively confirmed or refuted and yet the potential benefits from identifying this pathway resonate today in, for example, the biofuel industry as will be explained in the Section 3.2. Thus an attempt was made to investigate decarboxylation from a DFT-planewave perspective as the nature of the clay material lends itself very well to periodic representation in two of its three dimensions.

The aim of the DFT study was to determine a suitable environment in which decarboxylation would be possible, based on the experimental data recorded by Almon and Johns and where 'suitable' means feasible at atomistic and computational levels. So, the model itself needed to be large enough to be representative of the clay mineral and to accommodate an appropriate interlayer species but not so large that computations became unfeasible. The exact nature of the catalytic environment within clay minerals had to be determined as did the atomistic representation of a dynamic decarboxylation reaction. Added to this were other modelling considerations such as how best to represent the addition of a charged species in the interlayer space and what constitutes an intermediate in a chemical reaction? The outcome was the creation of five stages of a decarboxylation reaction, interpreted from those hypothesised by Almon and Johns, which were allowed to relax in different clay mineral environments.

Conclusions were drawn from the results of energy differences between models post geometry optimisation together with analysis of relaxed structures and the relative occupancies of the frontier/Fermi level orbitals. When the optimum catalytic environment had been identified, it was used as the basis to look at two varieties of iron-bearing or ferruginous clay minerals, variations of a type of clay mineral investigated by Almon and Johns and believed to be promoters of radical reactions. The inclusion of iron into the models brought with it further electronic structure modelling considerations, which lead to the investigation of the Hubbard parameter by way of a simple case study of wüstite (FeO). This informed an appropriate Hubbard value for use with the GGA functional under which the ferruginous models

were relaxed and the results examined and compared to those obtained from the aluminosilicate models.

The study begins with a wide-ranging introduction bringing together the essential ingredients, namely clays, their role in the conversion of organic matter to fossil oil and a comparison of the constituents of fossil oil with those of biofuel crops and finally, the role DFT has played so far in investigating some of these key ingredients of decarboxylation.

3.2   Introduction

Both clays and petroleum have played important roles in the development of Western society from the production of bricks, tiles and pottery to pet litter, drug delivery agents and catalysts from clays [11] and a carbon-based economy from petroleum. The wide-ranging use of clays is due to their molecular properties (e.g. molecular sieve catalysts [59]) and phyllosilicate structure (e.g. adsorbents) where sheets of aluminosilicate of octahedral (Al) and tetrahedral (Si) coordination are interleaved. The general form of the octahedral sheet is $Al_4O_8(OH)_4$ and of the tetrahedral, Si_4O_6. Isomorphic substitution often occurs in both the octahedral and tetrahedral sheets [60] with an ion such as Mg for Al in the octahedral sheet and Al for Si in the tetrahedral sheet. Substitution by Mg or Al, produces a negatively charged sheet which attracts cations, if these are hydrated, the clay is a cationic clay e.g. montmorillonite. The hydroxyl groups in the octahedral sheet are one of the sources of Brønsted acid sites and the aluminums which are exposed at the broken edges of crystals, Lewis acid sites [61]. Although it is widely reported that crystal edges are sites of greater reactivity than the basal plane [62], the initial choice was to investigate basal surface reactivity as this is the simpler site to model and has a larger area for the catalysis of a decarboxylation reaction. The issue of edge versus lateral site reactivity has been removed by using a comparative study of four similar, basal plane, clay environments.

The presence of catalytic sites in clays is an important property in the formation of fossil oil. The layered leaf structure of clay allows the adsorption of organic matter [63]; during kerogenization decarboxylation is catalyzed, producing the hydrocarbons [64] of petroleum.

Petroleum has played a major role in western society since the 1850s from the first stages of oil and gas exploration [65] to our current state of dependency. Oil exploration peaked in the 1960s and 1970s with the aid of experimental data which helped in the identification of oil reservoirs and improved the extraction process [65]. At the same time, experimenters were identifying the possible origins of petroleum and an examination of fatty acids (RCOOH) and hydrocarbons such as alkanes (of general formula C_nH_{2n+2}) showed the chemical and structural similarity between biologically derived organic material (fatty acids) and petroleum (paraffins/alkanes/hydrocarbons) [66]. There are several different routes by which a fatty acid can become deoxygenated to an alkane:- decarboxylation, decarbonylation and hydrogenation. Decarboxylation involves the release of carbon dioxide, decarbonylation involves the release of carbon monoxide and hydrogenation typically involves saturation with hydrogen atoms, which removes oxygen as water. Further experiments indicated the formation of fossil petroleum from biologically derived fats and fatty acids (RCOOH) involves a conversion to a reactive intermediate before conversion into hydrocarbons [66]. Geological evidence suggested the conversion of organic matter into petroleum occurs in marine environments at temperatures conducive to decarboxylation of fatty acids via a reactive intermediate [67]. In 1975, Almon and Johns [10] theorized a decarboxylation pathway based on experimental results and came to the conclusion that there is an organic free radical intermediate. It is this hypothesis that forms the basis of our investigation.

The age of near sole reliance on fossil fuels to meet most of our energy needs may be drawing to a close by dint of climate change, dwindling supplies of high quality, 'easily' accessible sources and worldwide energy security issues [68]. The

release of fossil bound carbon dioxide into the atmosphere as a result of using fossil derived oil is strongly correlated with climate change and, at the same time as oil reserves are diminishing, the threat to energy supplies by global geopolitics is increasing. One of the solutions to both of these problems is to locally grow vegetable oil bearing biofuel crops such as rapeseed, soybean and algae. The fatty acids in these crops, usually in the form of triglycerides, closely resemble the alkanes of fossil oil, consequently, there is potential for their conversion into high grade biofuel.

The biofuels in current use are mostly first generation using feedstock such as sugar and starch to produce bioethanol, which can be used as a petrol substitute or blended with it, and oils from, for example, rapeseed and sunflower crops [69] to produce biodiesel. Biodiesel can be used as a direct replacement for diesel-type fuels although the lipids usually undergo transesterification into fatty acid methyl esters (FAMEs) producing oxygenated 'biodiesel' which can be integrated with fossil diesel but only to a concentration of 5% [69] before engine modifications are required for long term use at higher biofuel concentrations. As these crops are competing for the same land as food crops, these biofuels do not offer a viable replacement for fossil fuels. Another drawback of using FAMEs is their use of methanol, itself a fossil-derived chemical, in as, at best, a ratio of 6 : 1 methanol : sunflower [68]. As reported in the King review, [70] the complete life cycle of potential fuels from origins to use must be considered when calculating carbon impact.

Second generation biofuels that produce ethanol, such as Switchgrass and other tall perennial grasses, are currently under investigation [69] as they have the potential to address some of the problems of the first generation biofuels. For instance, they can be grown in areas of soil erosion [69] and the whole plant can be used in several different processes resulting in an overall positive fossil fuel energy balance. A further development applicable to both the first and second generation fuels that produce lipids, such as soybean and algae respectively, is to deoxygenate them to produce green diesel. The triglycerides and fatty acids are upgraded to have a carbon number and molecular weight similar to the molecules found in fossil fuels [71]

and therefore are a direct replacement for fossil-derived diesel.

One of the processes of upgrading to produce green diesel is hydrodeoxygenation, and yet, using hydrogen to produce biofuels is somewhat counterproductive as the hydrogen itself is derived from fossil fuels. Therefore, to be able to control the deoxygenation process in the guise of decarboxylation is important industrially for a variety of reasons [72]. Furthermore, to improve the efficiency of green diesel production, a detailed understanding of the catalysts and their properties is essential as this would enable the control of catalyst selectivity and hence task specificity [73], [74].

Just as the experiments and tests of petroleum's properties in the early days of oil exploration lead to a deeper understanding of the location of oil reserves [65], so a thorough examination of the conversion process of the precursors of hydrocarbons into petroleum will enable the efficient production of alternative sources of diesel-like biofuels. Such an examination infers an understanding at the atomic level of deoxygenation pathways, in particular decarboxylation. Coincidentally, computational processing capacity along with improved algorithmic and theoretical methods are currently such that it is possible to carry out first principles investigations of ever larger systems. This now allows for a thorough investigation of the conversion of a fatty acid into a hydrocarbon chain involving electronic processes and hence quantum activity, by an *ab initio*, electronic structure simulation of decarboxylation in a periodic system.

Previous DFT studies involving clays and/or fatty acids have looked at the structure of clays [75], the catalytic activity of anionic clays [76], the vibrational and conformational properties of fatty acid methyl esters (FAMEs) using the B3LYP density functional [77], the attachment of the COOH group of fatty acids on metallic monolayers [78] or, using a Gaussian 3 variation, the combustion pathway of methyl butanoate to find a CO_2 production pathway [79]. At the time of writing, the most recent DFT study of clays [80] investigating the adsorption of volatile molecules on clays, acknowledges the current deficit of quantum-chemical, periodic

cell studies of clays and molecules in general, other than those involving cluster models [11], peptides [81], [82] or amino acids [83].

In this study of a bulk, periodic system, the interaction between a clay catalyst and a fatty acid in a decarboxylation reaction is investigated; with the aim of addressing various general aspects of a clay mineral model such as: how can a non-dynamic simulation investigate decarboxylation? What is the nature of the catalyst? How does the electronic structure representation of the clay surface affect the results? How does the role of charge, ionic substitution and counter ions affect the catalytic properties of clay? The following sections of this chapter proceed by introducing the simulation methods and models used, examining the results, discussing their implications and drawing conclusions from these. There then follows a section on ferruginous clay minerals, how these models necessitate the use of GGA+U [84] and the difference this functional makes to the computational results.

3.3 Computational Details

Pyrophillite is a 2 : 1, dioctahedral, uncharged, aluminosilicate clay. A unit cell of pyrophillite $(Al_2Si_4O_{10}(OH)_2)_2$, space group P$\bar{1}$ — see Appendix A for lattice dimensions and atomic coordinates — was constructed by removing the potassiums from muscovite, adding four coordinated hydrogens to form hydroxyl groups in the octahedral sheet and substituting an aluminium for a silicon on the tetrahedral sheet surface, see Figure 3.3. The aluminium substitution is thought to be the site of catalytic activity as it has the potential to be an electron-accepting site [85].

The CASTEP [35] code was employed, with a planewave basis set within the density functional theory (DFT) formalism [18], [86]. Convergence testing for kinetic energy cut-off energy was done by creating two small sample models of pyrophillite, that is, two cells containing a representative sample of pyrophillite, plus propionic acid and sodium where the samples differed only in the position of Na. This ensured
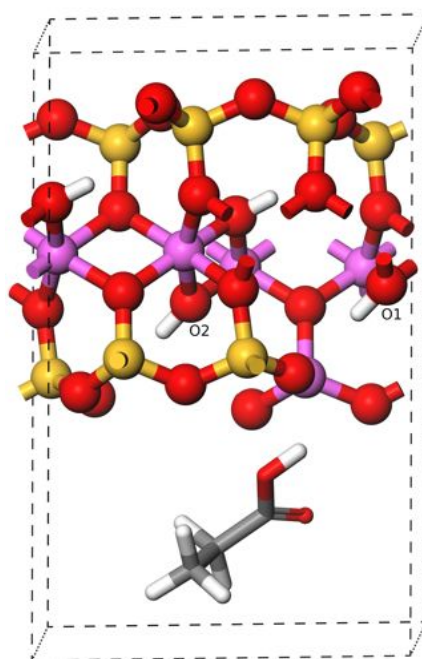
Figure 3.3: A single unit cell of pyrophillite with an aluminium substitution in the tetrahedral sheet and guest molecule of a simple model fatty acid, propionic acid. See Table 3.3 for geometry optimized dimensions. Oxygen:red; hydrogen:white; aluminum:pink; carbon:grey; silicon:yellow. This colour scheme, where relevant, applies to all subsequent figures in this chapter. The oxygens of two of the hydroxyl bonds are numbered for later reference. The dashed line is the periodic boundary of a unit cell.

that the pseudopotentials of all species were tested against basis set size. The point where the energy differences between the two samples converged to within the chosen convergence criteria, indicated the optimal kinetic energy cut-off as illustrated in the example shown in Figure 3.4. 550eV gave an energy difference in total energies of less than 0.04eV per unit cell for higher cut-offs.

A unit cell was then tested for k-point convergence ranging from one k-point at the gamma point (0, 0, 0) to five k-points varying with respect to $(\frac{1}{3}, \frac{1}{3}, 0)$ with the z-direction fixed at zero as this was the largest dimension of the unit cell. The Brillouin zone integrations were performed on a grid containing two k-points giving an energy difference of 0.03eV per unit cell between two and four or five k-points as shown in the example shown in Figure 3.5 and, as this is within the energy cut-off criteria, two k-points were adequate to converge the calculation at a volume appropriate for these simulations.

Cross-boundary, periodic effects were tested using supercells containing one molecule of the reactant (propionic acid) and separately, the product (C_2H_6 alkane plus CO_2), in supercells up to four unit cells wide in the y-direction. This showed that the greatest energy difference between a single unit cell and an nth-sized supercell was 0.01eV, again within the cut-off energy bound, hence a single cell was used throughout this study. The question of cross-boundary effects for sodium were more difficult to tackle because chemically, Na is attracted by the Al substitution in the tetrahedral sheet, so, if a unit cell contains one Al substitution and one Na, does a 2-cell supercell contain two Al substitutions and two Na? If it does, then the Coulomb interaction between the Na ions may be affecting the results; this interaction might be larger than that between periodic images of the guest species. However, lying between neighbouring Na in the supercells is the guest species, which, in this instance reduced the Coulomb effect between Na, resulting in the conclusion that a single unit cell was sufficient to produce results converged to 0.01eV. The subject of the interaction between periodic images of Na ions in the absence of other gallery guests, is revisited in Chapter 5.
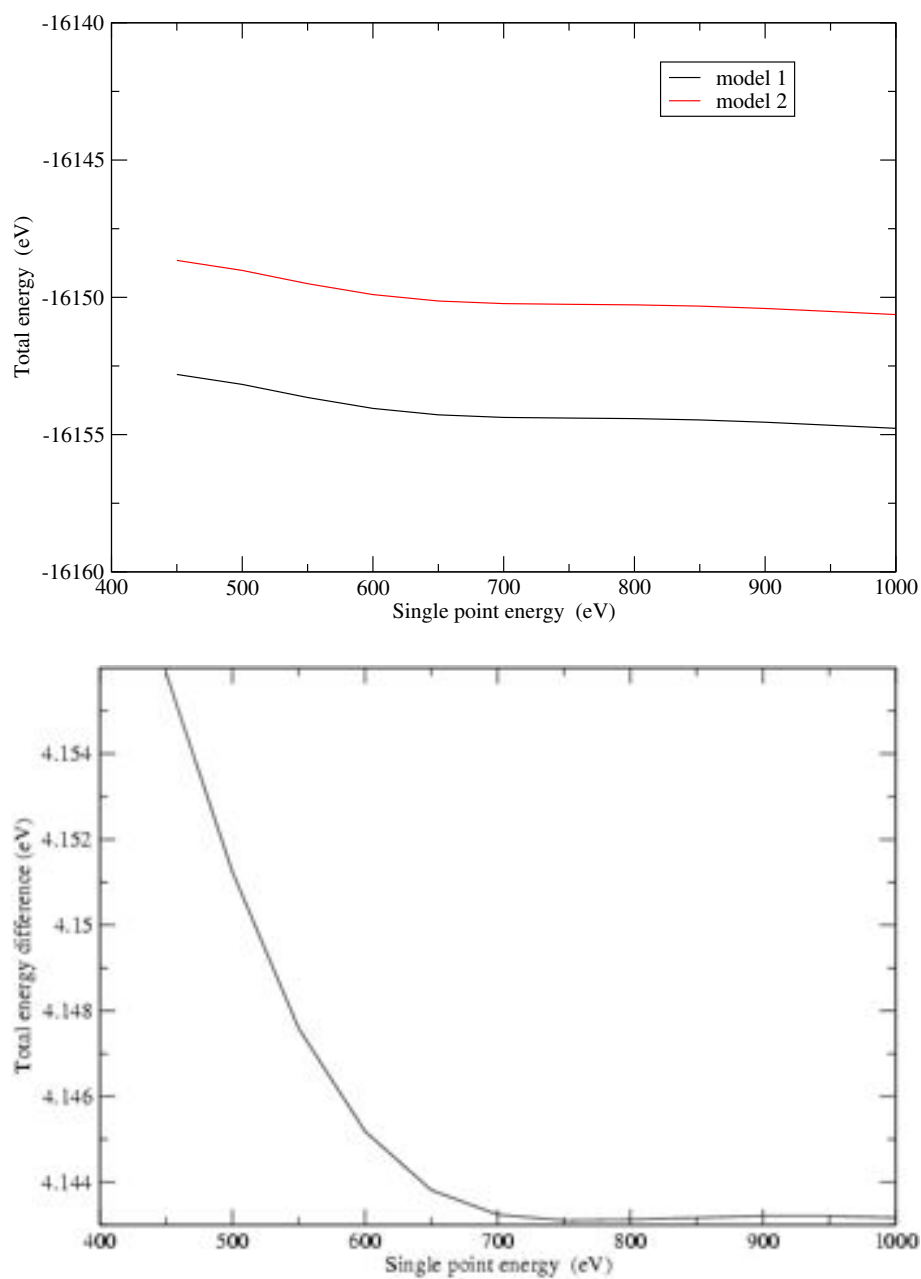
Figure 3.4: Example of pseudopotential convergence testing to obtain the kinetic energy cut-off. Top shows the total energies calculated after single point energy calculations for two models which differ in the atomic coordinates of one atom. Bottom shows the convergence of the energy difference between these two models.
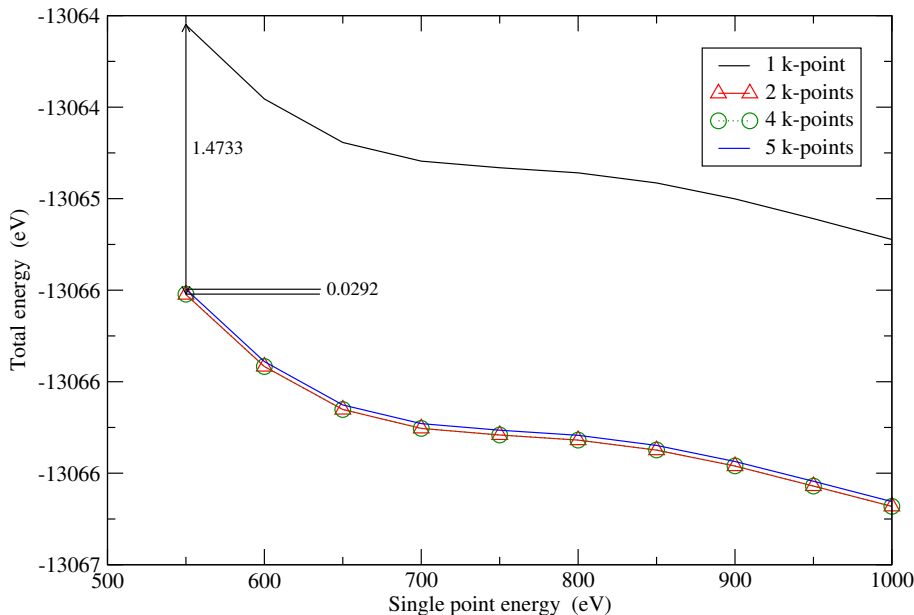
Figure 3.5: Example of converging the number of k-points with a range of single point energy calculations.

The density functional used was the generalized gradient approximation (GGA), specifically that of Perdew, Burke and Ernzerhof (PBE) [21] as this describes molecular bonding to a greater accuracy [22] than does the local density approximation (LDA), due to the difference in electron density within a molecular environment. Molecules have regions of low electron density which LDA struggles to describe well, as explained in Chapter 2. Also, the electron density of molecules can vary rapidly, which is an environment ill-suited to an LDA description as it originates from a smoothly varying density. PBE ultrasoft pseudopotentials [29] were used as these are consistent with the PBE exchange functional and their configurations are shown in Table 3.1. The (geometry) optimizer was Broyden-Fletcher-Goldfarb-Shanno (BFGS) and the electronic method was ensemble density functional theory (EDFT) [41]. Further convergence details per BFGS iteration are as follows: electronic energy tolerance: $\leq 10^{-6}$ eV per atom; geometry optimisation:- energy change per ion: dE/ion $\leq 10^{-5}$eV; maximum force: $|F|$max ≤ 0.04 eV/$\mathring{A}$; change in distance: $|dR| \leq 0.001\mathring{A}$.

The cell and contents were geometry optimized under an external anisotropic

Element	Configuration
Al	$3s^2 3p^1$
C	$2s^2 2p^2$
H	$1s^1$
Na	$2s^2 2p^6 3s^1$
O	$2s^2 2p^4$
Si	$3s^2 3p^2$

Table 3.1: Electronic structure of the ultrasoft pseudopotentials (GGA-PBE).

pressure of 0.05GPa, which was applied in the z-direction only. It is important to use a small, non-zero pressure when relaxing the cell to prevent unbounded cell expansion in the z-direction, due to the ultimate groundstate being for the clay layers to be sufficiently separated such that effectively zero potential exists between them. This would have occurred because the important van der Waals interaction, which is the source of attraction between the clay layers in physical clay systems, was not available in CASTEP at the time the investigations were carried out.

Both the fatty acid and the alkane plus CO_2 were optimised as isolated molecules to gauge the volume of space they required to achieve relaxed configurations. This helped when expanding the optimised pyrophillite cell in the z-direction for inclusion of the gallery guests, plus, as the latter were already optimised structures, added to computational efficiency. Cell parameters a and b and all angles were then constrained allowing only the c-parameter and cell contents to relax, with the inclusion of a molecule of propionic acid, positioned as illustrated in Figure 3.3. The c-parameter converged to $14.5\mathring{A}$ and all lattice parameters were then fixed throughout the remainder of the study, allowing the relaxation of the contents only.

According to Almon and Johns [10] a general fatty acid is converted to a hydrocarbon and a carbon dioxide molecule within a phyllosilicate; for this study, the fatty acid chosen was a simple model with a short hydrocarbon chain, propionic acid. Longer hydrocarbon backbones dissipate charge along their length [87], [88] as shown for two molecules, C_2H_5COOH and $C_5H_{11}COOH$ in Figure 3.6. A longer hydrocarbon chain molecule would require a larger unit cell to accommodate it. Also,

as the carboxyl head is a reactive site in decarboxylation, concentration of electron density should produce optimal conditions for a reaction as well as optimising computational efficiency, hence, a short chain length was used.

To determine the catalytic effects of different surfaces (see Table 3.2) on decarboxylation, the total energy obtained after geometry optimisation was taken as a guide, where the product was expected to have a lower energy than the reactants if decarboxylation was favoured, as the lower total energy of a system indicates greater stability at zero temperature.

Model Set	Description
1	Al substitution with zero applied charge
1a	Al substitution with range of applied charge
2	Al substitution with −1e applied charge
3	No Al substitution with no applied charge
4	Na ion added to Al substitution with no applied charge

Table 3.2: Model Sets as illustrated in Figures 3.7 and 3.8

The first consideration when investigating the clay/reactant and the clay/product reactions was the effect of charge on the system. It is feasible to consider that the negative charge on the clay layer created in the tetrahedral sheet by the substitution of Al^{3+} for Si^{4+}, is dissipated by a counter ion which may partially or wholly counterbalance the negative charge per periodic cell, as the counter ion may not be close to the substitution site but may exist somewhere in the clay so that the net charge of the bulk system is zero. This is the chemical interpretation of the effect of a counter ion. The electronic structure interpretation is that a counter ion donates an electron to the clay layer due to the tetrahedral sheet Al^{3+}/Si^{4+} substitution. This donation can be effected in two ways, by adding a counter atom to the periodic cell or by adding charge to the parameter input file. An applied charge of −1.0e represents the presence of one counter ion per isomorphic substitution per periodic cell, whereas an applied charge of 0e represents the counter ion's absence. The difference between an input of charge compared to a counter ion being present, is that in the latter scenario the source of electron donation is localised. Where charge is
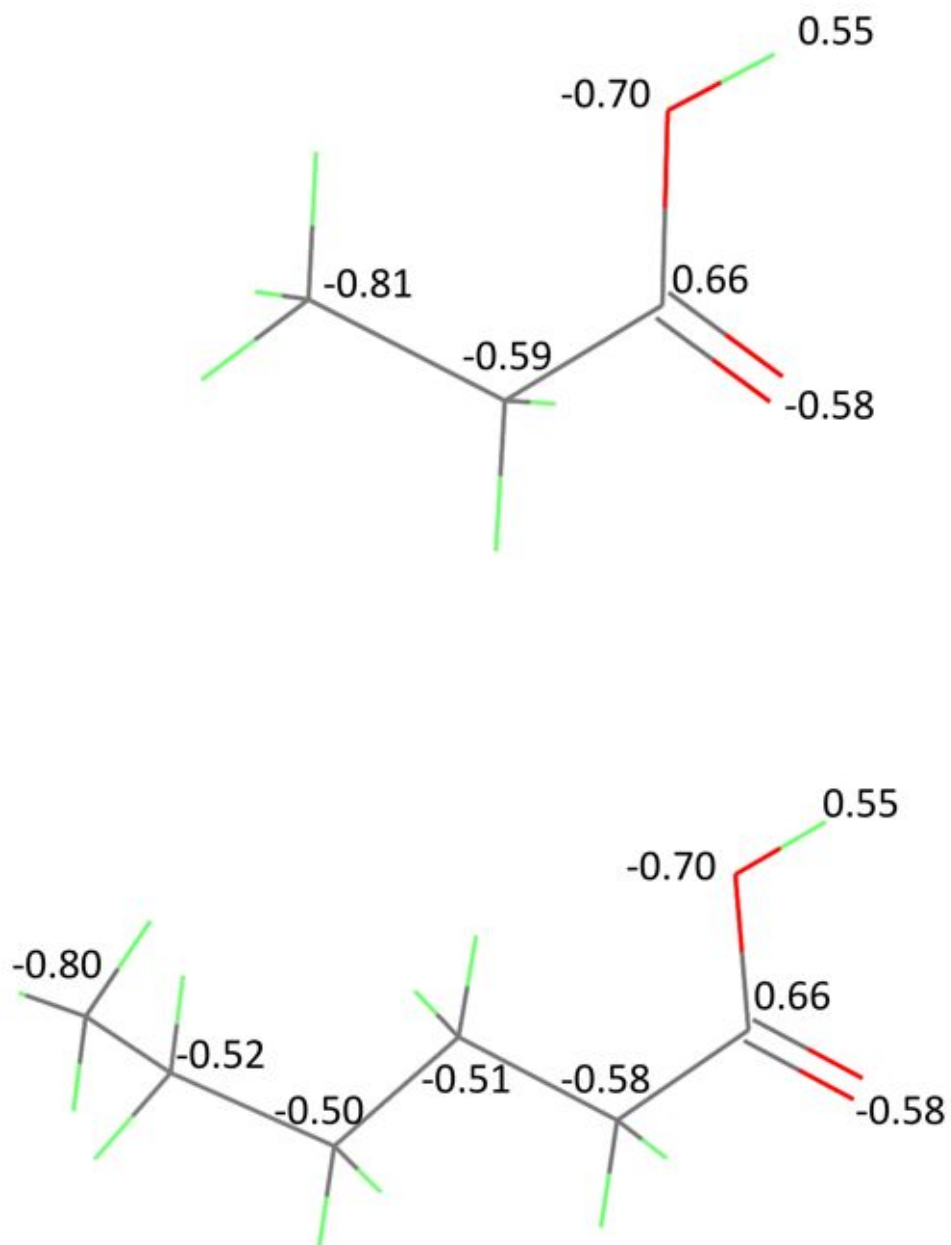
Figure 3.6: Example of the dissipation of charge along the backbone of a hydrocarbon with increasing chain length. For clarity, hydrogen is green for this figure only.

applied, it is a uniform background charge and is non-site specific.

The sets of models investigated are shown in Table 3.2. Each Model Set (apart from 1a, which involved the reactant and product models only) is based on Figure 3.7 where there are three intermediate stages between the reactant and product as postulated by Almon and Johns [10]. The DFT perspective is that, if the three intermediate stages were transition states in a decarboxylation reaction pathway, then, as the energy surface of a transition state contains a minimum at the saddle point, these initial configurations would relax to their groundstate geometries, which would be configurationally equivalent to the initial stages.

Model Set 1 has no counter ion to determine whether its presence is required for catalysis of decarboxylation. Set 1a involves the reactant and product models only, with charge applied from -0.25e to -1.0e in steps of 0.25e, to determine the effect of an increase in electron density. Fractional charge represents the presence of a counter ion somewhere in the bulk, for example, an added charge of -0.5e describes one counter ion 'shared' between two unit cells. Model Set 2 is the same as Model Set 1 with the addition of -1.0e to all stages, representing the presence of one counter ion donating one electron per unit cell. Model Set 3 is where there is no aluminium substitution, to determine if decarboxylation has any dependency on tetrahedral sheet substitution. This model is akin to an experimental control. Model Set 4 includes a sodium ion positioned over the SiO_3 ring in the tetrahedral sheet [5] as shown in Figure 3.8, where the sodium ion is close to the aluminum substitution and external to the clay surface [89]. The physical presence of a counter ion is, as previously discussed, the alternative to the addition of charge. Although studies show that sodium is hydrated [90] pyrophillite is generally considered hydrophobic on its (001) surface [91], hence water has not been included in this hypothetical model to decrease modelling complexity and consequently computational time.

All of the models in each set were geometry optimized using the same convergence criteria described in this section. This was followed by an evaluation of the band
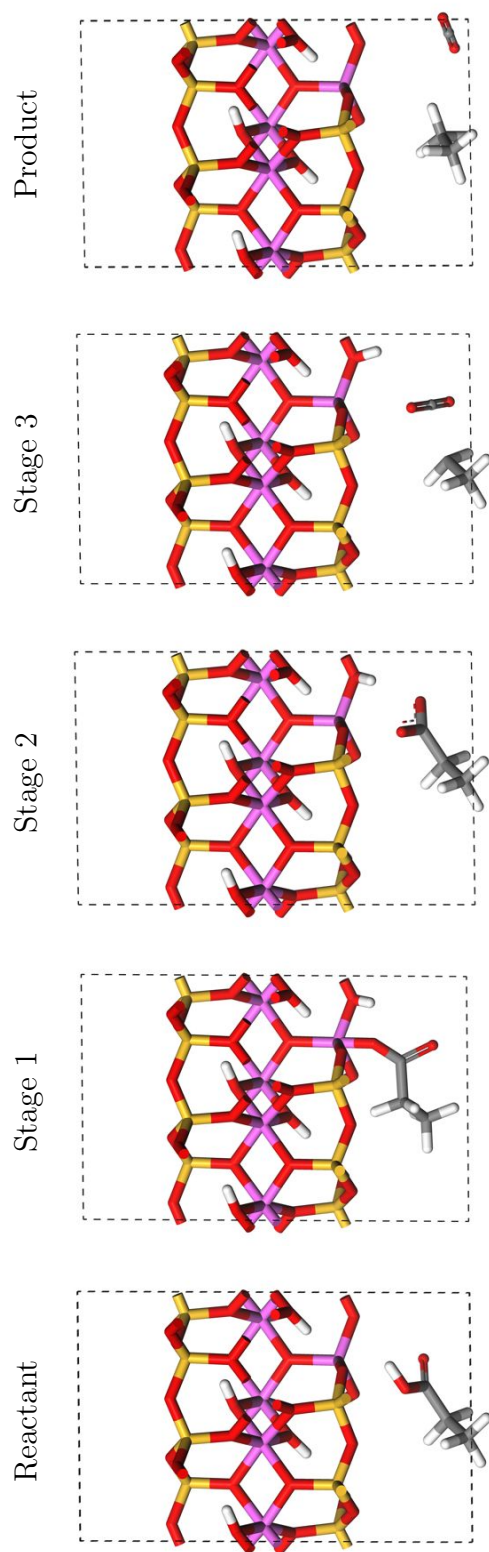
Figure 3.7: Schematic of the intermediate stages in a decarboxylation of a model fatty acid, as theorized by Almon. The 'R' in the Almon and Johns paper is CH_3 here. Each of the four Model Sets in this study were geometry optimized from these initial configurations, with the relevant substitution of Si for Al and the addition of Na as described in the text.

structure of the relaxed system for examination of the Kohn-Sham orbitals, which described where the electrons were positioned which were most likely to be involved in a reaction, on the application of energy. The results from these calculations are reported and discussed in the following section.

3.4 Results and Discussion

3.4.1 Clay Structure

Table 3.3 shows the structural parameters of the clay as determined by the electronic structure calculations, after geometry optimization and without a reactant or product molecule. They are in very close agreement with experiment (1%) [92] and another DFT study (1%) [93]. The subsequent calculations use these lattice parameters apart from the c length which was allowed to relax when a molecule of propionic acid was included in the model and subsequently fixed at an optimum length of $14.5\mathring{A}$, as this met the BFGS convergence criteria for the pyrophillite model plus gallery guest, as well as for the isolated gallery guest species.

This study DFT (PBE)		Experiment [92]		Other DFT (PB86[a]) [93]	
$a = 5.22$	$\alpha = 90.87$	$a = 5.18$	$\alpha = 90.00$	$a = 5.119$	$\alpha = 90.77$
$b = 9.07$	$\beta = 100.00$	$b = 8.96$	$\beta = 99.9$	$b = 8.911$	$\beta = 100.96$
$c = 9.73$	$\gamma = 89.65$	$c = 9.97$	$\gamma = 90.0$	$c = 9.065$	$\gamma = 89.91$

a: A semi-empirical functional with a fitted parameter for the exchange part.

Table 3.3: Lattice parameters of a unit cell of pyrophillite. Lengths are in $\mathring{A}$ and angles in degrees.

3.4.2 Effect of charge

The results shown in Table 3.4 indicate that decarboxylation is not likely to occur for Model Set 1, (this is equivalent to the system with zero charge in Model Set 1a) as the product energy is higher than the reactant energy by 0.08eV which, at room temperature with an available k_BT of 0.025eV, suggests 100% conversion from the product to the reactant. The products become lower in energy than the reactants

for charges of -0.75e and -1.0e suggesting that the larger the negative charge of the system and hence the higher the electron density, the more stable the product becomes, thus increasing the feasibility of a decarboxylation reaction. The total energy of the *in vacuo* models decreased with an increasingly negative applied charge but there was no spontaneous decarboxylation indicating the requirement of a catalyst for this reaction. That is, on relaxation of the atomic coordinates, the reactant did not relax to the product configuration. Based on the original assertion that the relative energies of the reactant and product models would indicate the probability of decarboxylation within a Model Set, these results initially suggest that the presence of the negative charge in the aluminium substituted system is necessary for decarboxylation to occur.

The five postulated stages of decarboxylation as illustrated in Figure 3.7 for Model Set 2 — where there is an Al substitution — were geometry optimized with a uniform, non-site specific charge of -1.0e to model the addition of an electron, which represents the presence of a counter ion somewhere in the bulk material. That is, the counter ion has donated its electron but the electron-deficient ionic species is not actually in the same unit cell. The application of charge is throughout the periodic cell, similar to a jellium model [20]. In each of the intermediate stages, the initial configurations relaxed to variations of the reactant model although the relaxed, interlayer species indicate interaction with the clay layer, as seen in Figure 3.8 and in Table 3.5.

Charge (e)	$E_{product} - E_{reactant}$	*in vacuo* Reactant
0.00	0.084	0.000
-0.25	0.018	-0.088
-0.50	-0.043	-0.194
-0.75	-0.100	-0.354
-1.00	-0.102	-0.557

Table 3.4: Energy differences (eV) after geometry optimisation of charged aluminium systems (Model Set 1a). The values for the *in vacuo* (reactant only) models are relative to zero charge.

The three intermediate stages, as shown in Figure 3.7 further examined the effect

of charge by investigating possible interactions between the guest molecules and the clay. In Model Set 3, where there is no charge addition and no chemical charge deficit in the tetrahedral sheet i.e. there is no Al substitution, the intermediate stages (1–3) reverted to the fatty acid with the COOH group lying almost parallel to the (001) clay surface, see Figure 3.8 and Table 3.5. The optimized results (Figure 3.8) show the guest molecules positioned halfway between the opposite surfaces of the clay, indicative of a balanced interaction between neighbouring surfaces, but this does not lead to any catalysed interaction between the guest and clay host. This adds further evidence to the assertion that the presence of a tetrahedral sheet, Al substitution, plus a source of additional electron density are pre-requisites for decarboxylation.

	COOH $\angle$ (001) Angle [0]				
Model Set	Reactant	Stage 1	Stage 2	Stage 3	Product
1	25	29	39	46	N/A
2	−12	36	42	53	N/A
3	6	−28	7	−6	N/A
4	30	−7	58	42	N/A

Table 3.5: Relative orientations of the plane of the COO(H) groups to the (001) surface of the clay where a positive angle is towards the surface and a negative angle away from the surface; refer to Table 3.2 for description of Model Sets.

3.4.3 Effect of aluminium substitution and counter ions

To test whether the presence of the Al is important for catalysis, the Al ion in the tetrahedral sheet was substituted for silicon for reactant, intermediate stages and product models and the atomic positions were allowed to relax to the convergence criteria detailed in Section 3.3. The results from this, shown in Table 3.6 show that no-Al substitution lowers the product energy compared to the reactant energy by 0.22eV, showing that the product is more stable than the reactant in an all-silicon (tetrahedral sheet) phyllosilicate. However, this is not sufficient information to definitively state that decarboxylation could happen within these models, as the findings detailed in Section 3.4.2 attest, where it was seen that the relaxed, interlayer species in the all-Si models were not interacting with the clay layer. An examina-

Figure 3.8: Structures after geometry optimisation. Model Sets 1–4: Al no charge; Al charged; no Al; Al plus Na counter ion (orange). Each Model Set shows the structural results after geometry optimisation of the five stages shown in Figure 3.7. The colour scheme used is the same as that in Figure 3.3.

tion of the Kohn-Sham orbitals in Section 3.4.4 will provide the electronic structure detail necessary to draw firmer conclusions, but before this, a brief analysis of the effect of the presence of a counter ion is examined.

Models	$E_{s1} - E_r$	$E_{s2} - E_r$	$E_{s3} - E_r$	$E_p - E_r$
1	-0.151	0.206	0.059	0.084
2	0.021	0.031	-0.006	-0.102
3	-0.054	-0.098	-0.109	-0.223
4	0.136	-0.413	-0.025	-0.159

Table 3.6: Total energy differences (eV) to three significant figures, after geometry optimisation of various models; refer to Table 3.2 for a description of model sets. $E_{s1,2,3}$ is the energy of stage one, two, three and $E_{r,p}$ is the energy of the reactant or product.

The addition of a counter ion in Model Set 4, tests the effect of the presence of a cation to counteract the chemically charged Al site. Na is used here as it donates its 3s electron, leaving Na^{+1} to exactly balance the chemical ^-1e charge deficit due to the Al substitution in the tetrahedral sheet. Sodium is a commonly occurring cation within phyllosilicate clays [11]. In this case, the clay/product system is lower in energy than the clay/reactant system by 0.16eV hence decarboxylation resulting in a stable product, can occur. An examination of the Mulliken charges on Na in the following environments: clay-only (i.e. no organic species); clay/reactant; clay/product; gives values of 1.10e; 1.36e; 1.45e; respectively, illustrating how, in the presence of the clay layer and organic species, Na increases in charge due to the donation of electron density.

Table 3.7 shows the difference in the angles of the hydroxyl bonds involving oxygens 1 and 2, (see Figure 3.3) for the four different systems. The all-silicon system (Model Set 3) hydroxyl bond angles are consistent throughout the five stages due to the non-interaction between the surface and the guests. The O2-H bond angles for the charged, Al-substituted system (Model Set 2) are the largest, due to the distribution of the applied $-1.0e$ charge. There is a difference of over 20° for O2-H between each of the stages for Model Sets 1 and 4, two Al-substituted models where the former has no balancing counter ion, but the latter contains Na as the counter

| Model set | COOH $\angle$ (001) Angle ^{0} | | | | | | | | | | | | | | | |
| | Reactants | | Stage 1 | | Stage 2 | | Stage 3 | | Products | |
	O1H	O2H	O1H	O2H	O1H	O2H	O1H	O2H	O1H	O2H
1	25.66	23.32	22.84	28.10	22.13	31.63	21.11	22.13	25.92	25.32
2	27.85	51.15	25.37	59.46	26.19	65.46	26.82	61.85	27.54	63.80
3	14.43	13.12	11.29	10.68	14.10	13.85	14.51	13.49	14.66	14.60
4	20.87	1.20	21.98	0.68	22.25	5.53	21.49	1.73	21.66	2.52

Table 3.7: Angles between the (001) surface and the hydroxyl bonds, O1-H and O2-H

ion. Although the O1-H bond angles are very similar for the four systems, there is a marked difference in the O2-H bond angles, due to the presence of the Na counter ion. This effect should be observable in a Fourier transform infra red (FTIR) [94] spectroscopy analysis of the OH frequency mode. Therefore these results from the addition of the interlayer cation have the potential to add to the work done on vibrational frequencies seen in cluster models [95].

3.4.4   Analysis of Kohn-Sham orbitals

The analysis so far, of the relaxed structures and energy differences has highlighted that these are insufficient to draw any firm conclusions about the probability of decarboxylation. A higher resolution of the analysis tool is required, a call met by the facility to visualise the Kohn-Sham orbitals as these describe the location of the Fermi level electrons i.e. those electrons in the frontier orbitals — or highest occupied molecular orbitals (HOMO), which, if energy is applied to the system, are the most likely to react. Hence, the presence of Fermi level electrons — visualised as blue orbitals in Figure 3.9 indicate a relative instability compared to regions devoid of these orbitals. In this section each Model Set is examined in turn.

In Model Set 1, the hydrogen of the fatty acid remained attached to the clay surface after geometry optimisation in stages 1–3 as it acted as a counter ion to the chemically charge -deficient Al substitution. The angle between the plane of the COO^- group and the (001) surface as shown in Figure 3.8 show that throughout system 1, the COO^- group is oriented towards this hydrogen. An examination of the frontier orbitals (Figure 3.9) show that for the reactant, the occupied Fermi levels reside in the clay surface whereas for the product, the occupied Fermi levels are in the hydrocarbon and the oxygens in the tetrahedral sheet of the clay forming a ring around the hydrocarbon, explaining why the product has a higher total energy than the reactant and is less stable.

In Model Set 2, the addition of the $-1.0e$ charge, which was distributed through-

Model
Sets   Reactants   Products
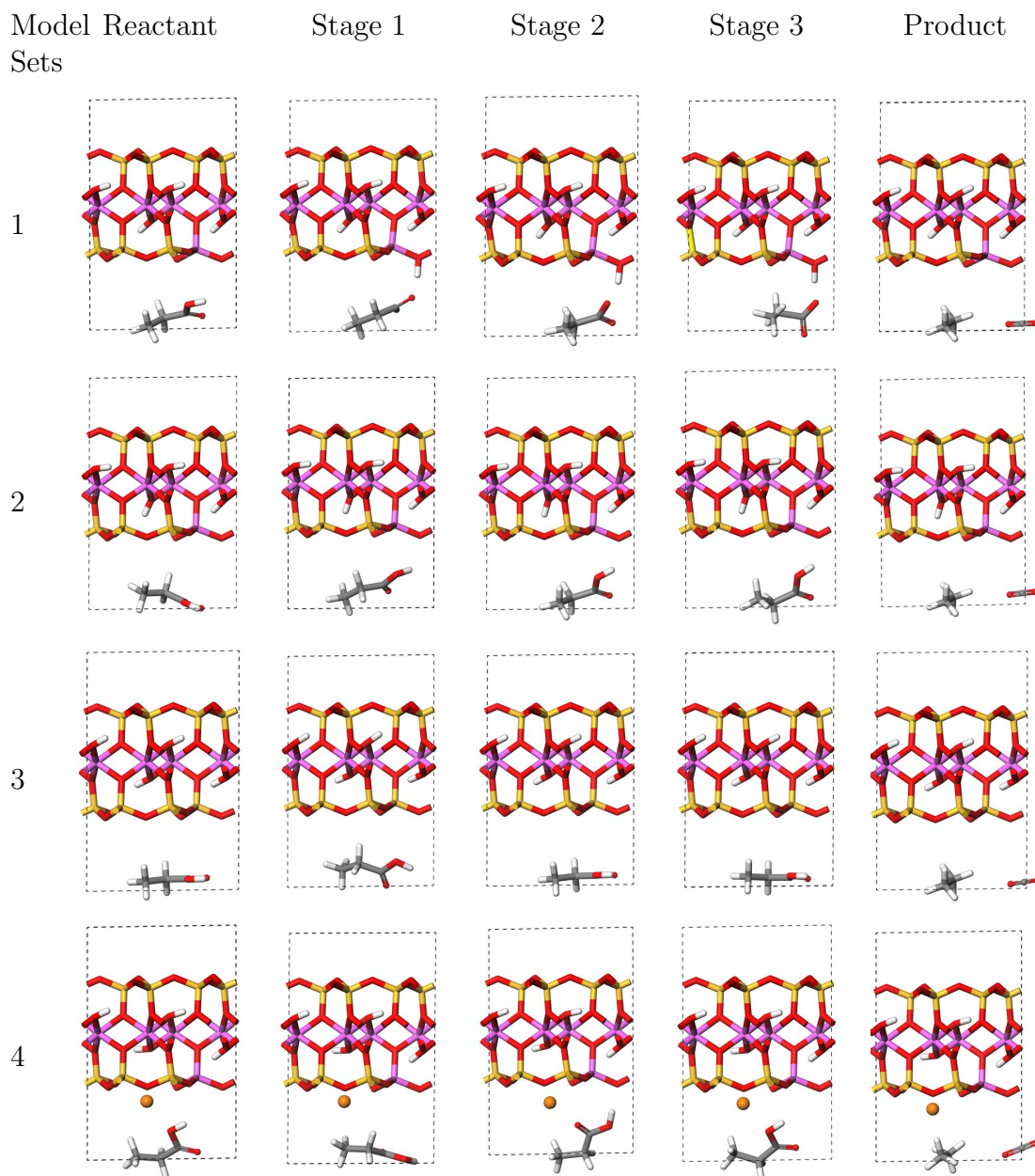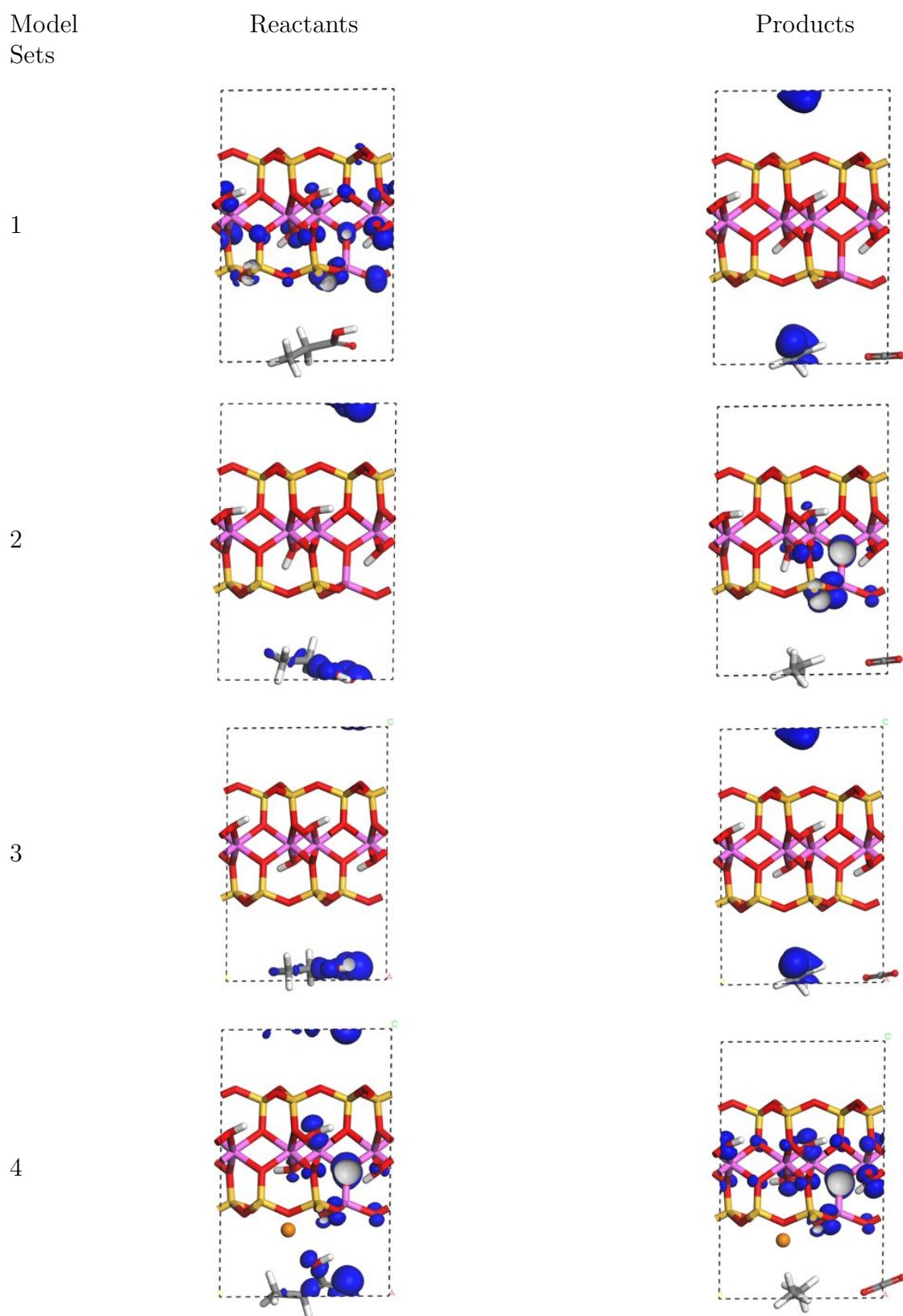

Figure 3.9: Fermi level orbitals (blue shells) of the reactants and products after geometry optimisation. Model Sets 1–4: Al no charge; Al charged; no Al; Al plus Na counter ion (orange). The colour scheme used is the same as that in Figure 3.3.

out the model as a background charge, shows the occupied Fermi level orbitals are on the C-COOH portion of the fatty acid hence the negative orientation away from the clay. Although, the intermediate stages also have the Fermi level π-orbitals on the guest molecules but their COOH groups are oriented towards the clay which may indicate local energy minima. In the product model, the occupied Fermi levels are in the clay thus lowering the energy of the product and stabilizing it relative to the reactant.

In Model Set 3, the Fermi level, π-orbitals are located solely over the guest molecules in each of the reactant and intermediate stages and over the hydrocarbon in the product stage, suggesting that there is no interaction between the clay and the guest molecules. The product energy is lower than the reactant by 0.22eV, hence the product has greater stability than the reactant within this system, however, the intermediate orbitals analysis shows the clay and variously oriented guest cannot interact hence a decarboxylation reaction will not occur.

In Model Set 4, the Fermi level π-orbitals are on the fatty acid and the clay, whereas in the product model they are solely in the clay with increased occupancy. The electron from the sodium atom is transferred to the fatty acid and clay and is then dissipated within the clay layer in the presence of the hydrocarbon and CO_2. Although there is no bonding between the guest and clay in the intermediate stages there is a transfer of charge which stabilises the product by 0.16eV relative to the reactant. This is the most feasible model for decarboxylation because the product has a lower total energy than the reactant and there is electron transfer involving Na, the fatty acid, the clay layer and the product.

Although the optimal environment for decarboxylation has been determined, the reaction pathway has not, and the results from the relaxed intermediate stages suggest it is probably not as hypothesised by Almon and Johns [10].

3.5 Conclusion

In this study four different model systems of a decarboxylation reaction have been studied to determine how the application of charge, ionic substitution and the inclusion of counter ions affects the catalytic properties of pyrophillite clay. It has been shown that applying charge to an Al-substituted system appears to produce favourable conditions for a decarboxylation reaction, but examination of the Kohn-Sham orbitals shows that the physical presence of a counter ion in an Al-substituted system produces the optimal decarboxylation environment. This shows that the theoretical presence of a counter ion (-1.0e applied charge) is not equivalent at the level of orbital occupancy, to the inclusion of the actual counter ion, which has implications when using cluster models. Application of charge is often adopted in cluster models for computational convenience. However, this study shows that electronic structure detail is different in the counter ion and charge scenarios, hence careful thought should be given to the effect this may have on the aspect being investigated.

The nature of the catalyst has been determined to be an aluminium substitution in the tetrahedral sheet, which attracts a counter ion that donates its electron to the reactant guest and clay. An examination of the Mulliken charges on the sodium ion shows a relative increase in positive charge from a sodium/clay system — no guest molecule — to the clay/reactant system to a smaller increase for the clay/product system, indicating the dissipation of electron charge from the sodium ion to the clay in the presence of a guest molecule. In this way a decarboxylation reaction is favoured.

The three-fold analysis of structure, relative energy differences between reactant and product and examination of the Kohn Sham orbitals lends confidence to the assertion that the Al-substituted system incorporating the counter ion accurately describes an environment conducive to decarboxylating a fatty acid. This can be used as the basis to build more realistic models, which eventually will provide information for the efficient production of biofuels. Therefore, the next step using this model would be to look for transition states between the sodium clay/reactant and

clay/product models as the identification of transition states is key to determining a reaction pathway. Within CASTEP there are synchronous transition state searching functionalities [96], and the implementation of these forms the first part of Chapter 4.

An alternative approach, which forms the remainder of this chapter, is to investigate another type of clay mineral used by Almon and Johns in their experiment. Their theoretical pathway involved a radical species, and iron-bearing clay minerals are important in radical reactions [97], [98], therefore it is a logical step to recreate the optimum decarboxylation environment using ferruginous clay minerals. Will the inclusion of radical-promoting Fe change the intermediate stage configurations on relaxation? Are there any different modelling considerations on the introduction of Fe? These questions are considered and addressed in Section 3.6.

There are many more approaches possible, using the optimum environment as the starting point, for example, repeating the calculations using geologically relevant temperature and pressure; including a hydrated sodium ion; investigating the effect of other cations such as potassium and calcium and so on. However, limited time focusses resources and interests, so that unfortunately these approaches must be held in reserve for the time being.

3.6 Ferruginous Clay Minerals

3.6.1 Introduction

The abundance of iron-bearing clay minerals in the Earth makes it highly probable that these clays were hosts to fossil oil formation and hence decarboxlyation. Almon and Johns were of the same opinion, as an iron-bearing clay mineral nontronite, was one of their experimental materials. It is possible that the Fe content of clay minerals promotes radical reactions, which is the category of reaction pathway of decarboxylation hypothesised by Almon and Johns. Therefore, it would be informative to repeat the investigation of the five stages applied to ferruginous models to see how this compares with the results from the study on pyrophillite.

Ferruginous smectite is called nontronite and contains a dioctahedral sheet of Fe^{3+}. The nontronites with a $\frac{1}{8}$ substitution of Fe^{3+} in the tetrahedral sheet are type NG-1 and those with Al^{3+} in the tetrahedral sheet replacing Si^{4+} are type Ideal; these terms will be used for the remainder of this chapter. The size of the unit cell used so far in this chapter allows for a $\frac{1}{4}$ substitution so, the potential catalytic effect of the substitution is optimised without loss of generality, that is, if the site of the substitution in the tetrahedral sheet, together with the cation, is important for a reaction to occur, then the environment modelled by a single unit cell will exist within the double cell without loss of any detail.

The following sections are shorter than those preceding as much of the computational details have been covered in-depth in describing the main study. Consequently, the differences in methods will be pointed out where relevant rather than repetition of all of the computational details.

3.6.2 Method and Computational Details

The optimised reactant models from the main study with a tetrahedral substitution of Al for Si, were used as the templates for the ferruginous models. Two varieties were made, both of which contained only Na in the interlayer space and all octahedral Al were substituted by Fe and in one labelled Ideal, the Al substitution in the tetrahedral sheet remained, in the second, labelled NG-1, the tetrahedral Al was also substituted by Fe. The introduction of the new Fe pseudopotential required the re-convergence of cut-off energy as previously described in this chapter. The energy differences between the two models converged to 4meV at a cut-off of 550eV hence this was used as the cut-off energy. All other convergence criteria are as previously described. The Fe pseudopotential was constructed using the PBE exchange-correlation functional with core corrections [28]. This allows for the inclusion of spin density in the exchange-correlation term. To allow for the spin of the d-electrons of Fe, all subsequent calculations were spin polarised. This is explained in greater depth in Chapter 5.

The Ideal and NG-1 models were allowed to completely relax, including both the cell and contents after which the c-length was extended to $14.5\mathring{A}$ to allow for the inclusion of a gallery guest, see Figure 3.10.

Ideal   NG-1

$a = 5.20, \alpha = 93.80$ $a = 5.21, \alpha = 94.29$
$b = 9.09, \beta = 101.73$ $b = 9.04, \beta = 101.73$
$c = 14.50, \gamma = 89.65$ $c = 14.50, \gamma = 89.65$
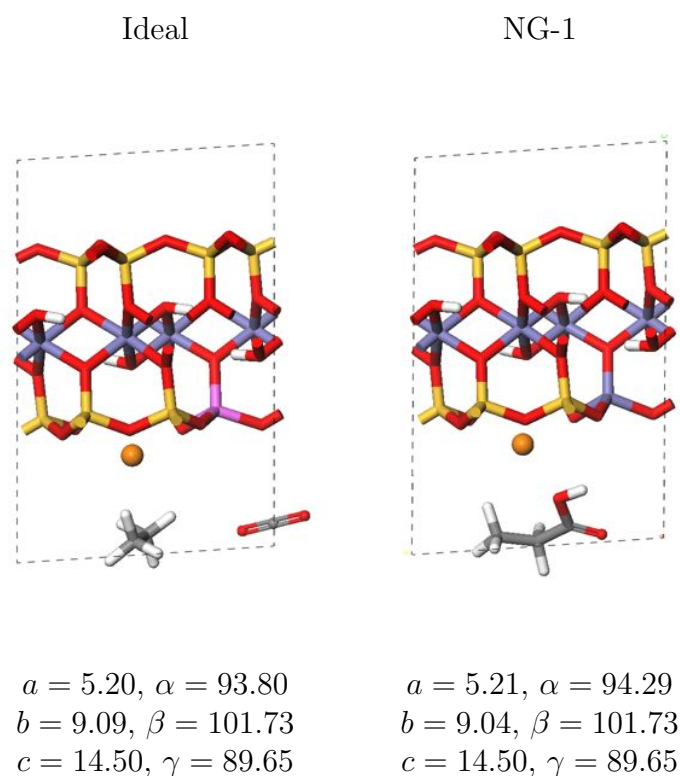
Figure 3.10: On the left is a single unit cell of Ideal containing the product and on the right, a single unit cell of NG-1 containing the reactant. The following colour scheme is used throughout the remainder of this chapter: Oxygen: red; hydrogen: white; aluminium: pink; silicon: yellow; iron: blue; sodium: orange. The dashed line is the periodic boundary of a unit cell.

The optimised Ideal and NG-1 models were used to produce the five configurations as shown in Figure 3.7, with the same intention as in the main study, that is, if any of the postulated intermediates were transition states then, allowing them to relax would result in the reproduction of the initial configuration. All of the cell contents were allowed to relax with the lattice parameters held fixed, with the same convergence criteria as that detailed in the main study. A post-processing band structure calculation to determine the Fermi level orbital occupancies, completed the computations.

3.7 Results and Discussion

Figure 3.11 shows the relaxed configurations and the Fermi level occupancies of Ideal and NG-1. The relaxed configurations for both Ideal and NG-1 have all assumed the reactant configuration, hence, within these ferruginous clay mineral models, no transition state has been found. All five model stages in both cases appear similar to each other and to the stages of Model Set 4 (shown in Figure 3.8) apart from Stage 1 where, in the Ideal and NG-1 sets, the carboxyl head is oriented towards the tetrahedral sheet rather than away from it, as is the case in Model set 4. Where configurations contain a carboxyl end group, its orientation is towards the tetrahedral sheet, Al or Fe substitution, apart from in Model Set 4 where it points away, indicating the existence of at least two local minima resulting from relaxation of the same initial configurations.

Models	$E_{s1} - E_r$	$E_{s2} - E_r$	$E_{s3} - E_r$	$E_p - E_r$
Ideal	0.483	-0.310	-0.065	-0.136
NG-1	0.551	-0.722	0.206	-0.168

Table 3.8: Total energy differences (eV) to three significant figures, after geometry optimisation of ferruginous models. $E_{s1,2,3}$ is the energy of stage one, two, three and $E_{r,p}$ is the energy of the reactant or product.

The energy differences shown in Table 3.8 provide information about the relative orientations of the fatty acid to the clay layer. In both Ideal and NG-1, stage one, where the carboxyl head has relaxed to point away from the layer, the difference in energy between this orientation and that of the reactant is positive, hence the reactant model is closer to the global minimum for this system. This is important information because it emphasises the dependence of the outcome of a geometry optimisation on the configuration of the initial input. If this 'falling into local minima' were of concern, then by testing a few orientations, an energy/orientation picture would emerge. In the sets presented here, stage two in both Ideal and NG-1 is closer to the global minimum than the original reactant models. Although this does not
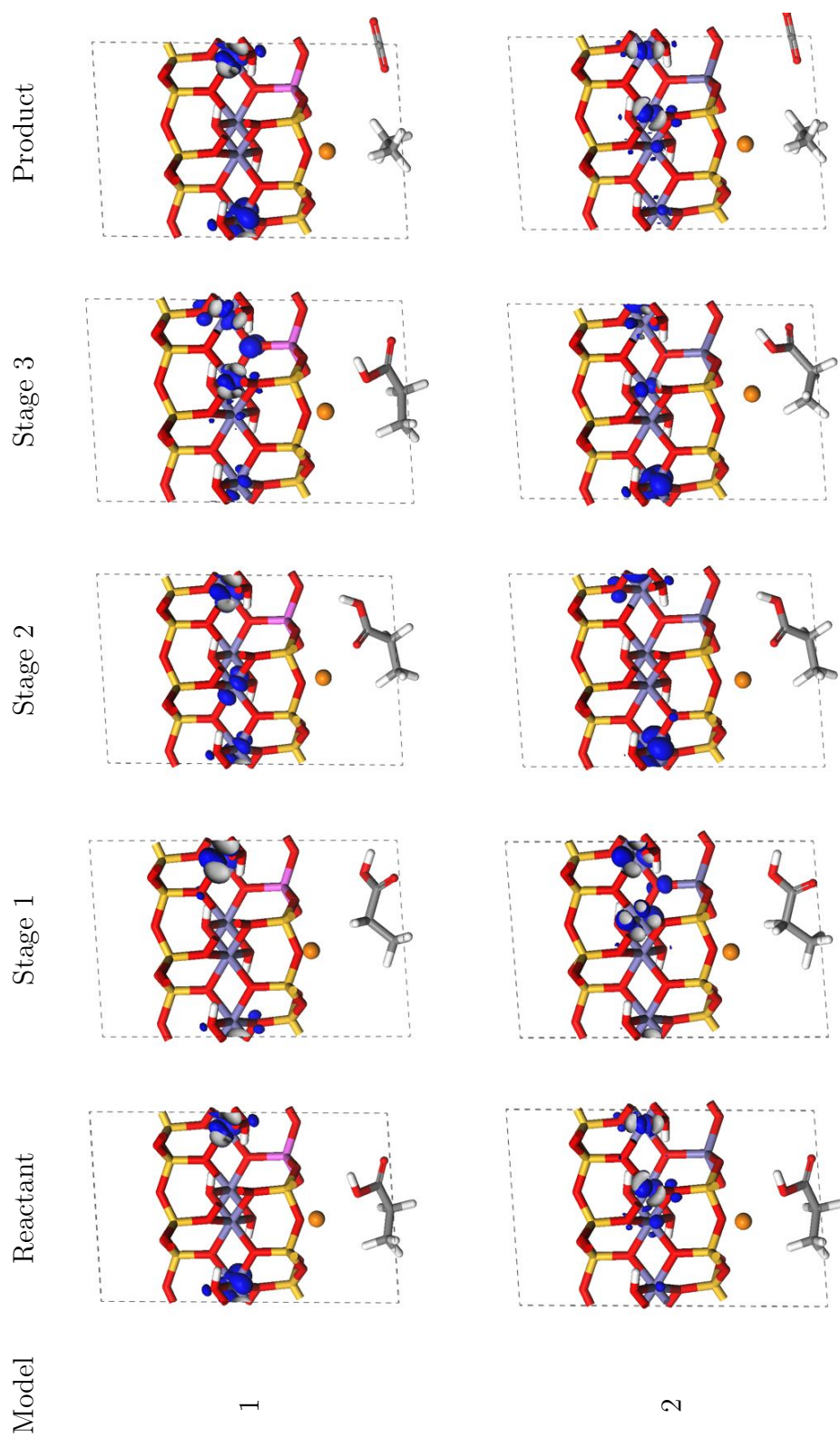
Figure 3.11: Configurations of 1: Ideal and 2: NG-1 models after geometry optimisation. The blue shells are the Fermi level orbitals.

affect the conclusion drawn from the results of these geometry optimisations, insofar as none of the initial configurations are transition states as they relaxed away from their starting configurations, this orientation information could be used in, for example, the search for a transition state where the Reactant model[1] would be that of stage two as this has the lowest energy of the reactant configurations shown here.

The product models for Ideal and NG-1 are both lower in energy than their respective reactant models and the energy differences are an order of magnitude larger than the tolerance criteria, hence the conversion from reactant to product is possible. An examination of the Fermi level orbitals should provide the information required to draw a firm conclusion as to the feasibility of decarboxylation within ferruginous clays.

Scrutiny of the Fermi level orbitals (Figure 3.11) shows a marked difference from the non-ferruginous models in that in every scenario, the occupied orbitals are those of the iron within the octahedral sheet, apart form Stage 3 of Ideal and Stage 1 of NG-1 where there is involvement of the oxygen in the octahedral sheet lying above the substitution in the tetrahedral sheet. Particularly striking is the total lack of involvement of the fatty acid and alkane, which indicates that, on application of energy, their electrons would not be the first to react, hence a decarboxylation reaction is not likely within these clays. However, is this a 'real' result or is it an artefact of the approximations used?

Iron is a transition metal of electronic structure $[Ar]4s^2 3d^6$ where the unpaired electrons in five of the d-orbitals are able to interact as can be seen in Figure 3.12 where d-electrons with different angular momentum vary in their proximity to each other depending on their d-orbital. Consequently there is a complex interplay of Coulomb and exchange interactions between the 3-d electrons, which the GGA functional is not able to capture as it cannot split the triply degenerate d_{zx}, d_{yz} and d_{xy},

---

[1]The two end configurations of a reaction pathway in a transition state search implemented in CASTEP, are called the 'Reactant' and 'Product'.

i.e. the t_{2g} bands [99]. Consequently, an iron oxide bearing insulator for example, could be described as metallic within the GGA approximation. Table 3.9 illustrates this phenomenon very well, showing that the band gap of the ferruginous models is an order of magnitude less than that of the aluminosilicates. Apparently GGA has reduced the band gap and interpreted the iron models as more metallic than insulating, thus, the results obtained for these models are not 'real' results but are artefacts of the GGA approximation.
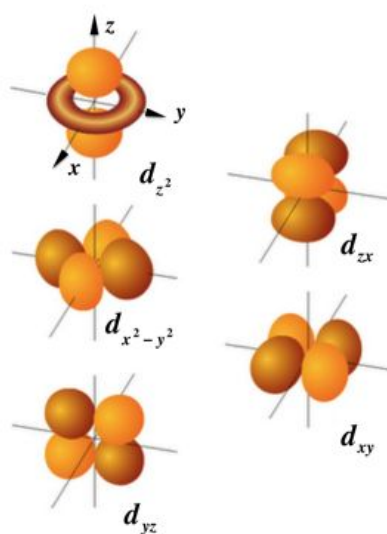
Figure 3.12: Five 3d-orbitals of Fe where light orange represents the bonding and dark orange the anti-bonding orbitals. The d_{z^2} and $d_{x^2-y^2}$ are centred on the z-, x- and y- axes respectively and form the symmetry group e_g, whereas d_{zx}, d_{yz} and d_{xy} are centred between the axes, comprising the symmetry group t_{2g}.

Model	Reactant	Stage 1	Stage 2	Stage 3	Product
4	5.10	5.07	5.33	5.11	5.54
Ideal	0.26	0.20	0.19	1.57	0.26
NG-1	1.18	0.16	0.25	0.10	1.10

Table 3.9: Band gaps (eV) of the relaxed clay models where '4' refers to the main study i.e. the sodium models with the Al substitution in the tetrahedral sheet.

Fortunately, there is a potential solution to this seemingly artificial reduction in the band gaps; it is the Hubbard parameter, which is used with GGA (or LDA). The theory behind it plus its application to the ferruginous models forms the subject of

the following section.

3.8   LDA $+ U$

The following description concerns the LDA approximation but in principle also applies to the GGA and higher functionals as the aim of the Hubbard parameter is to separate the d-orbitals to introduce Coulomb and exchange terms between the d-electrons. Describing LDA $+U$ captures the essential theory without becoming swamped by the larger number of mathematical terms used in GGA and higher functionals.

The transition metals in the middle of the periodic table contain partially filled d- or f-orbitals displaying properties that depend on these orbital occupancies. LDA cannot describe these localized interactions [84] as this functional represents the one electron, delocalized exchange-correlation potential of a homogeneous electron gas. Consequently, under the LDA the d-bands are described as being partially filled with non-local electrons, somewhat in the manner of the electronic structure of a metal and the material falls into the category of a Mott insulator. This occurs when the (d-/f-) orbital-dependent Coulomb and exchange interactions are larger in energy than the bandwidth of the sum of the (d-/f-) orbitals.

To describe the interactions between the electrons in the d-orbitals, an additional term, the Hubbard or U value, is added to the energy; the following is a simplified version of it: [84]

$$E = E_{LDA} - \frac{UN(N-1)}{2} + \frac{1}{2}\sum_{i \neq j} n_i n_j \quad , \qquad (3.1)$$

where the first term is the usual LDA describing the delocalised s and p orbitals; the second term is the Coulomb energy of d-d electrons, which is a function of the total number, N of d-electrons; the third term is the additional Hubbard term, which depends on the orbital occupancies n_i. Taking the derivative of E with respect to

n_i gives:

$$\epsilon_i = \frac{\partial E}{\partial n_i} = \epsilon_{LDA} + U\left(\frac{1}{2} - n_i\right) \quad, \tag{3.2}$$

in the orbital energy, i.e. if there is occupation, $n_i = 1$ hence $\epsilon_i = \epsilon_{LDA} - \frac{U}{2}$ and if not, $n_i = 0$ hence $\epsilon_i = \epsilon_{LDA} + \frac{U}{2}$.

As the potential of the orbitals is given by $V_i(r) = \frac{\delta E}{\delta n_i(r)}$, which describes the change in charge density of a specific orbital, information which GGA alone was not able to capture, then

$$V_i(r) = V_{LDA}(r) + U\left(\frac{1}{2} - n_i\right) \quad, \tag{3.3}$$

and a mathematical description of the correct physics of Mott insulators is achievable that is, their strong electron-electron interactions are correctly described hence theoretically, as well as physically, they are insulators. In some Hubbard approximations [84], the term describing exchange is described separately to the Coulomb term and is proportional to $\frac{1}{2}J[n \uparrow (N \uparrow -1) + [n \downarrow (N \downarrow -1)]$ where J is the exchange parameter and $n \downarrow$ is the number of spin down electrons (for example). In CASTEP the U and J parameters are combined into a single 'U' number. As well as Coulomb interactions between the d-electrons, there are also screening effects between each other and with electrons in the s- and p-orbitals. In fact, separation of the d-orbitals in the planewave approximation appears to be an advantage over local orbitals basis sets as, within the planewave approximation the screening effects are well reproduced, that is, when the d-orbitals are separated they are decoupled from the whole environment, bestowing the d-electrons with their own identity, thus allowing for Coulomb, exchange and screening interactions with their environment. This lack of basis-set dependency is an advantage over a local orbitals basis such as Gaussians, where each partial orbital decoupling results in an over-screened scenario [100], which then leads to the introduction of s- and p-hybridization to ameliorate this effect.

The Hubbard parameter U, is a number whose value depends on the local environment, e.g. for the d-electrons of Ni, $U = 2.5$eV whereas for the f-electrons of La, $U = 6.0$eV [31]. The environment of interest here contains Fe, O, Si, H, C and Al where only Fe has d-electrons but there is a high proportion of Fe-O bonding. Documented U values for Fe range from U= 4 to 7eV [99], [100] and the optical band gap for FeO is 2.4eV [101]. However, the band gap obtained from an excited state does not represent the same exchange-correlation environment as that within the groundstate. Is it a reasonable value when the optical excitation promotes a 3d electron to the 4s orbital and yet the band gap describes the separation of the d-orbitals? Perhaps not, but then perhaps the exchange-correlation approximation is able to absorb potential discrepancies between an actual band gap and that obtained experimentally. The following section is a short study on a simple system, FeO to show the effect of varying U and to determine the value of U which gives a band gap of 2.4eV.

3.8.1 Wüstite — FeO

The ferruginous smectites described in this chapter are heterogeneous systems, containing infinite slabs of clay separated by vacuum which itself contains isolated molecules. Compared to the usual condensed matter material such as crystals of silicon, the computations are time consuming, so, in order to illustrate the effect of increasing the Hubbard parameter, a simpler system, namely wüstite, FeO, has been chosen as the subject. This system is relevant to the ferruginous clays as there are also FeO environments within them and hence the results from the study will be somewhat transferable as well as illustrative.

Wüstite is a paramagnetic crystal of Fe and O with the structure of NaCl and cubic symmetry [102]. It has the relative coordination Fe_xO where x varies between 0.85 and 0.95 [103], [104] displaying a high concentration of defects, hence a pure crystal is difficult to obtain, which explains the scanty band gap data. In its antiferromagnetic state, FeO has a slightly distorted rhombohedral structure [102]

($\alpha < 60^o$) where the spins of the Fe in the planes parallel to the (111) axis, are able to align as shown in Figure 3.13.
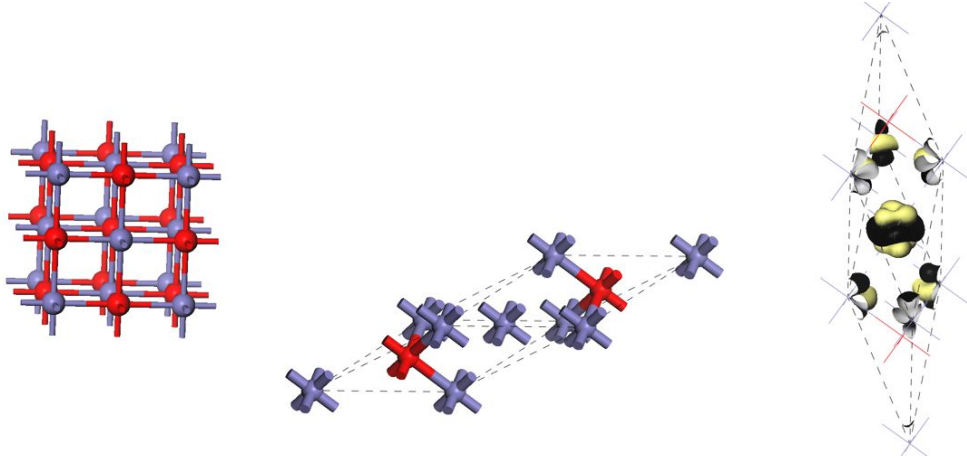
Figure 3.13: Cubic structure of paramagnetic wüstite shown on the left; antiferro-magnetic, rhombohedral crystal of FeO in the middle and with spin density (black and yellow shells) on the right. Blue: Fe; red: O.

The model crystal made for this study was a double-sized, rhombohedral super-cell (to allow for the antiferromagnetism) of $a = 5.31\mathring{A} = b = c$, $\alpha = 33.56^o = \beta = \gamma$. The same cut-off energy of 550eV as was used in the Ideal/NG-1 study, was used as the ultrasoft pseudopotentials were for Fe and O, two of the same species used in the clay studies. A k-point grid of $6 \times 6 \times 6$ was used to sample the Brillouin zone, which, with symmetry operations, reduced this to 28 points. This produced energy-differences convergence within the criteria detailed in Section 3.3 i.e. to less than 40meV per unit cell. The exchange-correlation function was GGA PBE be-cause this is the functional used in all of the clay models, and hence the results from the wüstite study would be transferable to the clay models. The minimiser was EDFT as density mixing does not easily converge in the presence of the Hubbard parameter, possibly due to the charge sloshing and mixing of spin histories required in the algorithm — density mixing is explained in greater depth in Chapter 5.

The Hubbard values ranged from 2.0eV to 6.0eV and the crystal was allowed to completely relax. Figure 3.14 shows the linear relationship between the band gap and Hubbard value in the range 2.0eV to 5.5eV; at the value 6.0eV there is a sharp

increase in the gradient indicating this value is an upper bound of the Hubbard value. The U value corresponding to a band gap of 2.4eV is approximately 5.0eV. The shifting of the d-orbitals shown in Figure 3.14 illustrates how, in increasing the band gap, the d-orbitals in the conduction band are squashed, which if continued, becomes increasingly unphysical.

The conclusion from this is that increasing the Hubbard value increases the band gap as was expected. It does so within the d-orbitals as explained previously. A Hubbard value of $U = 5.0$ reproduces the reported band gap of wüstite of 2.4eV and so, as the ferruginous clays Ideal and NG-1 also contain FeO environments in their octahedral sheets, $U = 5.0$ will be used to re-optimise the reactant, product and three intermediate stages to determine whether this changes the computed catalytic properties of these clay minerals.

3.8.2 Ideal and NG-1 revisited with GGA + U

The five initial configurations shown in Figure 3.7 were geometry optimised with the inclusion of $U = 5.0$ in the cell file for Ideal and NG-1. For the latter model Fe in the tetrahedral sheet was given the same U value as the octahedral sheet Fe, although this is an approximation, it was to ensure simplicity of modelling. All convergence criteria were the same as described in this chapter for each previous optimisation.

Results and Discussion

There are two sets of results in this section which are not converged to the same precision as the rest due to time constraints and lengthy BFGS cycles — in some cycles over 150 SCF iterations were required to reach the electronic groundstate. These are Ideal, Stage 3 and NG-1, Stage 2 and the convergence details are in Table 3.10. However, their progress was monitored at various intervals and their inclusion in the results is representative of their converged results and where it is thought that total convergence will make a difference, reference is made to this in the text.
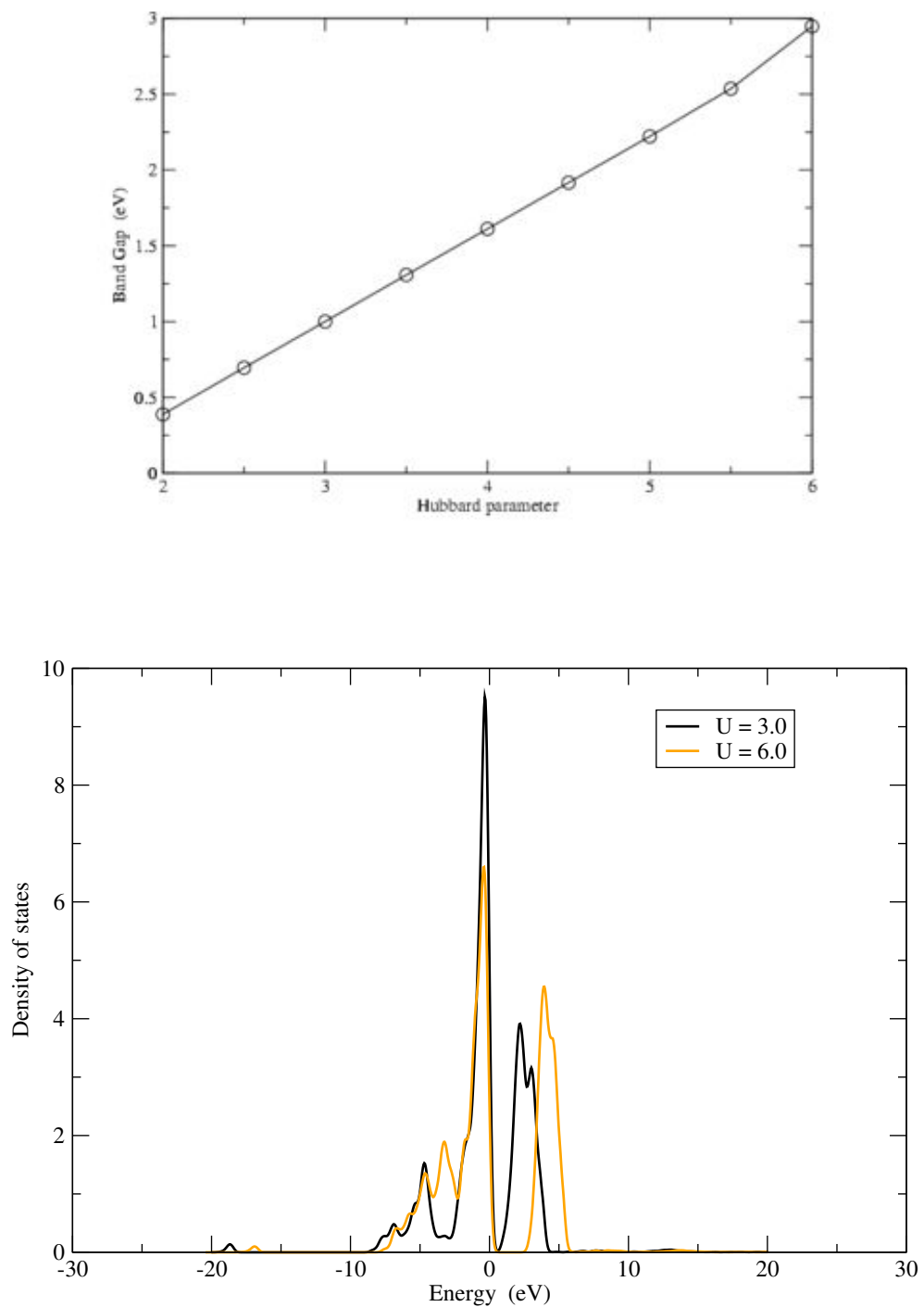
Figure 3.14: Illustrating the linear increase in the band gap of FeO (top), and the density of states for the d-electrons of Fe with two different Hubbard values.

	dE/ion (eV)	$|F|$max (eV/$\mathring{A}$)	$|dR|$max ($\mathring{A}$)
Convergence criteria	1.000 x 10^{-5}	3.000 x 10^{-2}	1.000 x 10^{-3}
Ideal — Stage 3	1.096 x 10^{-4}	2.510 x 10^{-1}	4.923 x 10^{-2}
NG-1 — Stage 2	5.913 x 10^{-6}	7.571 x 10^{-2}	1.654 x 10^{-2}

Table 3.10: Top row describes the convergence criteria achieved by all models apart from the two listed below.

(a) Band Gap

Table 3.11 shows that a Hubbard value of 5.0 has increased the band gaps of every configuration apart from Stage 3 of Ideal where there has been an order of magnitude decrease.

Model	Reactant	Stage 1	Stage 2	Stage 3	Product
Ideal	2.17	N/A	2.13	0.05	2.26
NG-1	1.69	N/A	1.53	1.47	1.67

Table 3.11: Band gaps of the relaxed clay models within the GGA+U approximation with $U = 5.0$.

There is no data available for Stage 1 as there was a problem during its relaxation, the BFGS algorithm ran out of search directions declaring that it was going to begin looking uphill which meant a probable deviation away from the original minimum into another, not based on the starting configuration. This happened for both Ideal and NG-1 and an examination of the forces showed that they were ridiculously high (> 100eV/$\mathring{A}$) for some atoms. This implied that the starting configuration was so far removed from an energy minimum, that the results, if the ground state was eventually reached, would have little bearing on the relevance of Stage 1's initial configuration and how close this was to a possible transition state. It could be said that the problem with Stage 1 indicates the unlikelihood of it being a transition state, however, exactly the same configurations had no problem converging in the absence of the Hubbard value, hence there was something happening due to the Hubbard term, which was interfering with geometry optimisation for this configuration. One way to determine whether the Hubbard parameter was causing the problem, would be to use a range of Hubbard values for this Stage. Perhaps the increase in band

gap is responsible for creating large Coulomb forces between some of the atoms; again, this could be monitored with increasing U and conclusions drawn as to the potential for Stage 1 being a transition state. For example, perhaps a Hubbard value of 1.0 would allow relaxation of this Stage to its ground state and hence appropriate analysis could be applied.

Stage 3 of Ideal and NG-1 have the smallest band gaps where, in the former case, the band gap is almost non-existent and has decreased from 1.57 in the same model without the inclusion of the Hubbard parameter, whereas the band gap of NG-1 has increased from 0.10. This may be an artefact of convergence and an examination of the energy differences and structures of the relaxed geometries should illuminate the results further.

(b) Relaxed Geometries

Models	$E_{s2} - E_r$	$E_{s3} - E_r$	$E_p - E_r$
Ideal	-0.355	0.833	-0.130
NG-1	-0.323	-0.596	-0.153

Table 3.12: Total energy differences (eV) to three significant figures, after geometry optimisation of ferruginous models. $E_{s1,2,3}$ is the energy of stage one, two, three and $E_{r,p}$ is the energy of the reactant or product.

The energy differences shown in Table 3.12 imply that the reactant and product models in Ideal and NG-1 are contenders for investigating transition states as the product has a lower energy than the reactant in both cases. As Stage 2 in Ideal and NG-1 and Stage 3 of NG-1 have lower energies than the reactant, they could not be transition states. The higher energy of Ideal, Stage 3 is possibly due to its convergence as discussed and at this point cannot be seen as a potential transition state.

Figure 3.15 shows how, with a Hubbard value of 5.0, three new configurations have appeared; Stage 3 of Ideal and Stages 2 and 3 of NG-1. In Stage 3 of Ideal, the hydrogen has remained attached to the tetrahedral surface and the CO_2 has attached to CH_3CH_2 to form the species CH_3CH_2COO. This latter species is the
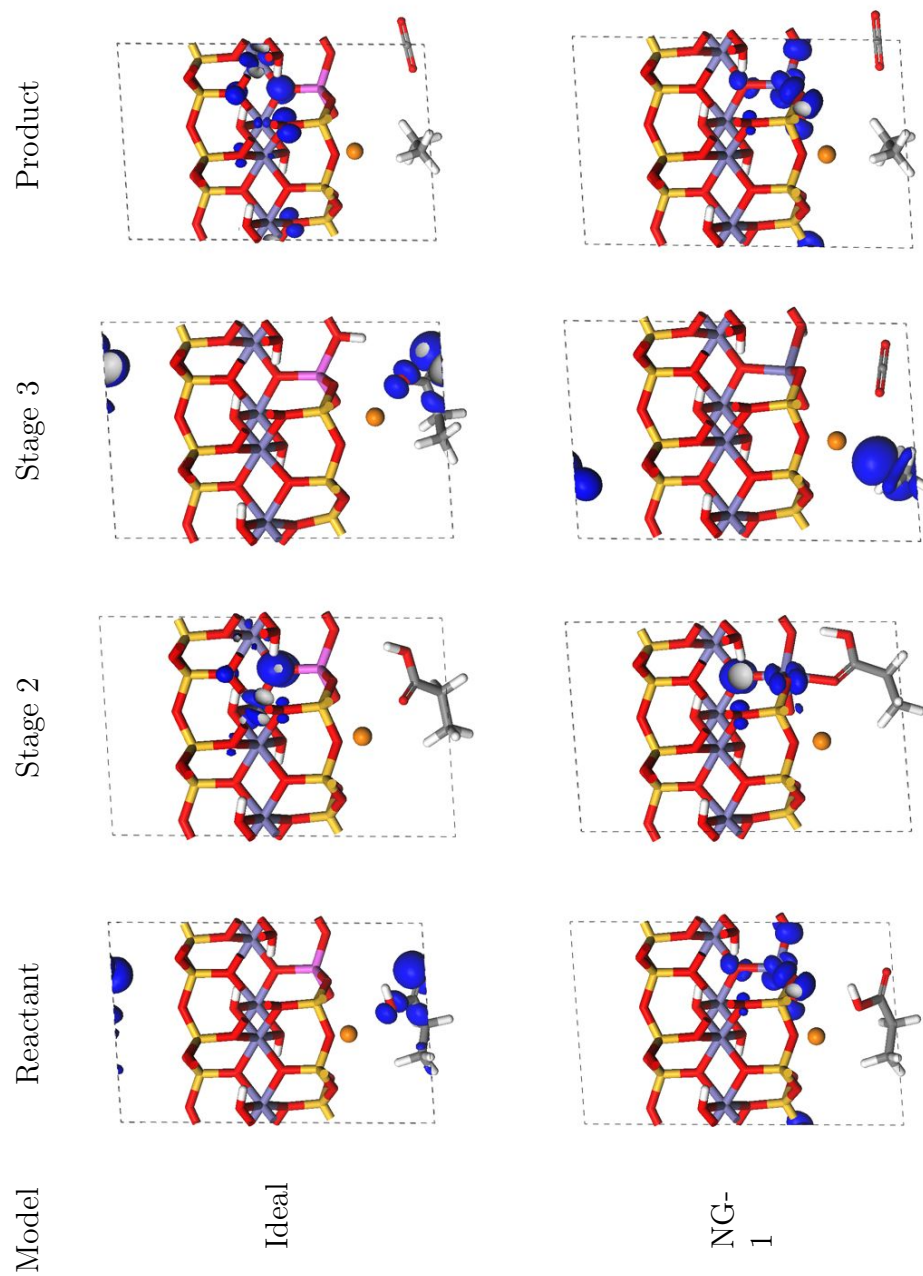
Figure 3.15: Relaxed geometries within the GGA+U approximation where $U = 5.0$. NG-1, Stage 3 is shown at an angle to highlight the position of the hydrogen attached to the tetrahedral surface of the clay layer.

initial species of each Stage 2, based on Almon and Johns hypothesis where it is attached to the tetrahedral substituted atom, which implies that it is potentially a transition state and hence an intermediate in decarboxylation. An examination of the distance between the hydrogen atom attached to the tetrahedral surface and the doubly-bonded oxygen of CH_3CH_2COO at increasing levels of convergence shows an increase from $3.56\mathring{A}$ to $3.70\mathring{A}$, strongly implying that the CH_3CH_2COO species would not move back towards the hydrogen on further convergence. Thus, a new species has been located, furthermore, it has a higher energy than the reactant and hence could be a new transition state.

The relaxed geometry of NG-1, Stage 2 is similar to the initial configuration for this stage, except that the species, CH_3CH_2COO has moved sufficiently close to the tetrahedral Fe, that a bond is forming between it and an oxygen. An examination of the relaxed configuration at increasing levels of convergence showed that, at lower convergence the hydrogen of the fatty acid remained attached to the tetrahedral surface. Further convergence has resulted in the re-attachment of this hydrogen to form the fatty acid and an increase in the bond length between the Fe on the tetrahedral surface and the oxygen of the fatty acid, from $2.16\mathring{A}$ to $2.19\mathring{A}$. Thus, in this case, further convergence will probably result in the fatty acid detaching from the tetrahedral surface and becoming a variation on the reactant model configuration, hence it is not a potential transition state as the energy differences intimated.

The relaxed configuration of NG-1, Stage 3 is new to this study and is a variant of a stage hypothesised by Almon and Johns. The energy difference between it and the reactant is negative and is the largest in magnitude of that between the reactant and all other models, which would not appear to indicate that it is a transition state between the NG-1 reactant and product. The results analysed so far, lead to contradictory conclusions, perhaps an examination of the orbitals of the potentially most reactive electrons will clarify the picture.

(c) Fermi Level Occupancies

The addition of the Hubbard parameter has changed the Fermi level orbital occupancies as can be seen by comparing Figures 3.11 and 3.15. In the case of Ideal, GGA+U results in occupation of the Fermi level orbitals of the fatty acid in the reactant model, which is one of the factors used in the aluminosilicate study to identify the correct reactant environment. Although in the ferruginous case, there is no involvement of the clay layer. In Stage 3, Ideal, the potentially most reactive electrons are on the carboxyl head of the 'new' species, possibly indicating its transitory nature, although again there is no involvement of the clay layer. In the product model of Ideal, the Fermi level electrons are within the clay, which was previously used as an indicator of the relative stability of the product, hence the ferruginous GGA+U product model conforms to this description.

For the NG-1 reactant model, the Hubbard parameter has changed the area of occupation of the Fermi level orbitals in the clay layer, where prior to GGA+U there was dissipation within the layer, there is now concentration around the tetrahedral Fe and the adjacent oxygens. The degree of confidence with which this environment could be described as a suitable reactant model has decreased. For Stages 2 the Fermi level electrons are localised within the clay layer, around the tetrahedral Fe. If, as suggested in a previous paragraph, further convergence results in separation of the fatty acid from the clay layer, then it is probable the Fermi level occupation remains within the clay. In Stage 3, the highest energy electrons are of the species CH_3CH_2, suggesting this species is transitory and yet the energy difference between it and the reactant is the largest within these model sets. This says that, if it is a transition state, it will not become the reactant or product (models of this study) as it moves away from its saddle point and into a minimum. For the product model, there is occupation of the clay layer with concentration around the tetrahedral Fe, so, within the previously stated definitions of 'relative stability', the product model is acceptable as being representative of a product environment.

Can any firm conclusions be drawn from this analysis? The following section addresses this and discusses what should come next.

3.8.3 Conclusion

The ferruginous models were initially investigated in the same manner as the aluminosilicate models but the results attained were artefactual due to the inability of the GGA functional to correctly describe the relationships between the strongly correlated, d-electrons of Fe. To remedy this, the GGA+U functional was employed where the Hubbard parameter was gauged from a trial study on the FeO environment comprising wüstite. The ferruginous clay mineral results gained using this functional were ambiguous and somewhat contradictory in their implications.

The Hubbard parameter increased the band gaps in all but one case but the new band gaps were less than half those of the aluminosilicate models. This phenomenon has been reported in another first principles study where the introduction of Fe into aluminosilicate nanotubes reduced the band gap from 4.7eV to 1.4eV [105] but the author does not describe how the strongly correlated electrons were modelled, so a direct comparison between results is unreliable. There is a lack of experimental data on the band gaps of clay minerals, consequently it is difficult to say whether the difference in band gaps between the aluminosilicate and the ferruginous clays is representative of reality. However, what is real, is that the inclusion of the Hubbard parameter changed the band gaps as well as the relaxed structures and the Fermi level occupancies.

The aim of this part of the study was to determine if the inclusion of the Hubbard parameter would change the results. The conclusion is that yes, indeed it has. The question of the reliability of these results is worthy of a separate study due to the number of issues raised. For example, the choice of the U value was somewhat arbitrary even though it was obtained from a study investigating an environment that exists within the ferruginous clays. This value was used for *all* Fe, including the tetrahedral Fe in NG-1, with no justification other than for modelling simplicity. In a stand alone study, a range of Hubbard values could be applied to the models with a different value for the tetrahedral Fe, which would test the effect on the band gap, structural and orbital results and whether a different value for tetrahedral Fe

made any significant difference to these results.

The slow convergence of Ideal Stage 3 and NG-1 Stage 2 raised an interesting modelling question, as a result of checking on their convergence and the effect this had on their structures and orbital occupancies. In the course of the relaxation from the initial structure of NG-1, Stage 2, the interlayer species passed through Stage 1 where it moved towards the tetrahedral surface to 'collect' the hydrogen before moving away again to form the reactant model. The question this raises is, could the course of geometry relaxation of a structure be representative of a chemical reaction, given a viable i.e. chemically feasible starting configuration? This would require the initial configuration to be a chemically feasible intermediate not a transition state[2] nor a minimum energy configuration, although the relaxed structure could be either of these.

A second modelling issue raised is that of convergence, when is a structure in its ground state and what does this mean with regard to experimental conditions? Although, to some extent using sets of models by-passes these issues, in that there is always a relative comparison possible and hence error cancellation, can this be compared to experimental conditions? For example, if a species existing in a higher energy state requires less energy to metamorphose than a species of a lower energy state, should the same convergence criteria be applied to the two configurations? For the electronic structure, without the implementation of excited state methodology, then yes, but, for the geometry, perhaps not. Perhaps, by enforcing the same convergence criteria on all models, potential reaction pathways are being lost. An interesting investigation would be to begin with relatively low convergence criteria for all models, gradually increasing it and analysing the results.

Clearly, the introduction of the GGA+U has raised more questions than it has

---

[2]An intermediate in this investigation is a species identified during geometry optimisation, which may or may not exist physically during a chemical reaction and does not have the potential energy surface of a saddle point. A transition state is a species formed from the reactants or products, is separated from them by a positive energy barrier and has the potential energy surface of a saddle point with the expectation of chemical significance.

answered. In spite of it having affected the results, the investigation needs to be extended to determine how 'real' these results are. This would be one way forward, especially worthwhile given the potential new species the ferruginous models with the GGA+U functional have uncovered. However, that particular investigation will have to be revisited at some point in the future, as the alternative step forward was explored. And that was, to attempt to find a transition state between the reactant and product models of the aluminosilicate models, in an effort to identify the reaction pathway of the decarboxylation of a fatty acid within a smectite clay mineral. It is this that forms the substance of the following chapter.

4

Ab initio Transition State Searching in Complex Systems: Fatty Acid Decarboxylation in Minerals

4.1   Synopsis

This chapter continues from the point reached in the last chapter, concerning the identification of an appropriate model to investigate decarboxylation in the aluminosilicate, pyrophillite. In the previous study, none of the intermediates hypothesised by Almon and Johns were found to be potential transition states, so in this chapter, an *ab initio* approach to identifying a transition state is taken. This involves the reactant and product models only, in linear and quadratic synchronous transition searches, two techniques which will be explained in the chapter. These

searches were semi-automatic in that CASTEP was able to carry them out to a limited convergence but required user-input to reach tighter convergence criteria. The reasons for this are examined and a potential solution mooted.

The semi-automatic transition state search found a species different from both the reactant and product but its transition state nature was in question, therefore a means of identifying a transition state was required. Lattice dynamics (i.e. phonon calculations) were used because a phonon calculation will produce imaginary eigen-frequencies for transition states, the theory behind this is described in this chapter.

Employing a phonon calculation required a change of pseudopotential, from ultrasoft to norm-conserving which brought to light several modelling considerations; the decisions taken and their consequences are discussed at length.

The layout of this chapter is somewhat in the manner of a standalone study, hence there is some brief repetition from the previous chapter, which has been kept as a reminder of the essential elements of this investigation.

4.2 Introduction

Chapter 3 introduced clay minerals and the importance they played in the development of Western society from, for example, the production of bricks, tiles and pottery to pet litter, drug delivery agents and catalysts, [11] and in particular their potential catalytic role in the production of biofuels. To this end, a 1975 experimental paper by Almon and Johns [10] was used as the basis for the DFT modelling of a decarboxylation environment within a phyllosilicate clay, pyrophyllite. The investigation presented in this chapter is a continuation from that DFT study, which described the optimum decarboxylation environment catalysed within pyrophyllite, involving a short chain fatty acid, propionic acid (reactant) and ethane plus carbon dioxide (product). The aim of the present study is to locate an intermediate between

the reactant and product and to verify it as a transition state using vibrational analysis.

In chemical terms, transition states are short-lived intermediates between reactants and products; they are found at a stationary point on a chemical reaction pathway and describe the activation energy of a chemical reaction and the relative stability of the product. Their location is important in identifying the pathway of a chemical reaction, such as in research into enzymes [106], [107] and the production of enzyme inhibitors [108], to calculating reliable rate coefficients [109]. Transition states can be located by various means such as eigenvector following [110], nudged elastic band [111], string method [112] and statistical transition path sampling [113], although for large systems there is no obvious way to predict the efficiency of one method over another [114]. In this investigation linear and quadratic synchronous transition state (LST/QST) searches [115] are employed, which bear a resemblance to a practised method that involves the identification of intermediates (see reference [116] for more details), although that particular method relies on chemical intuition or *a priori* knowledge of the reaction pathway and does not need the reactant and product configurations. In contrast, LST/QST uses the reactant and product geometries and assumes nothing about the decarboxylation reaction pathway, hence it could be described as an *ab initio* transition state search.

An examination of the current literature shows that DFT and the B3LYP functional have been used to study the kinetics of decarboxylation [117] and to identify transition states by vibrational analysis [118], [119]. These and other DFT investigations have mostly been carried out on cluster models [11] and isolated molecules in the gas phase [120], which contrasts with this study where periodic models are used to represent an extended clay surface. As well as investigating decarboxylation, DFT has been used extensively to determine the structure of clays [75] and their vibrational properties [121], [122] and structural defects [123] as well as examining the catalytic activity of anionic clays [76].

This study brings together several facets of the above in an uncommon, if not unique, combination. Linear response density functional perturbation theory (DFPT) (which will be described in detail) is used to calculate the vibrational frequencies of a periodic clay system containing a gas phase-like molecule in the interlayer space, in order to identify an intermediate of a decarboxylation reaction and verify it as a transition state, with the aim of gaining insight into the chemical pathway of clay-catalysed decarboxylation.

As previously stated, the location of a transition state would ultimately help identify the chemical pathway of this form of fossil oil production. This is of particular relevance today as the fatty acids in biofuel crops are of a similar type to those modelled in this reaction [66], [71] hence the investigation of this reaction and the insight gained into the catalytic conversion of fatty acids into high-grade fuel, offers the potential to contribute to the efficient production of biofuels.

This chapter proceeds with a description of the method of searching for transition states together with the theory of linear and quadratic synchronous searches.

4.3 Method

4.3.1 Structures

A unit cell of pyrophillite $(Al_2Si_4O_{10}(OH)_2)_2$, space group $P\bar{1}$ was constructed as detailed in Chapter 3, Section 3.3. The reactant model is comprised of a unit cell of pyrophillite plus propionic acid and the product model a unit cell of pyrophillite plus the alkane C_2H_6 and CO_2 as shown in Figure 4.1; the cell dimensions are shown in Table 4.1. From this point onwards the terms 'reactant' and 'product' are used respectively to describe these models. The optimal reactant and product models were found to incorporate an aluminum substitution in the tetrahedral sheet which is thought to be the site of catalytic activity [10] plus a sodium atom which counterbalances the charge generated by this and enables electron transfer between the

guest organic molecule and the clay. These reactant and product models provided the end points for the transition state search detailed in the following section.

Reactant

Product
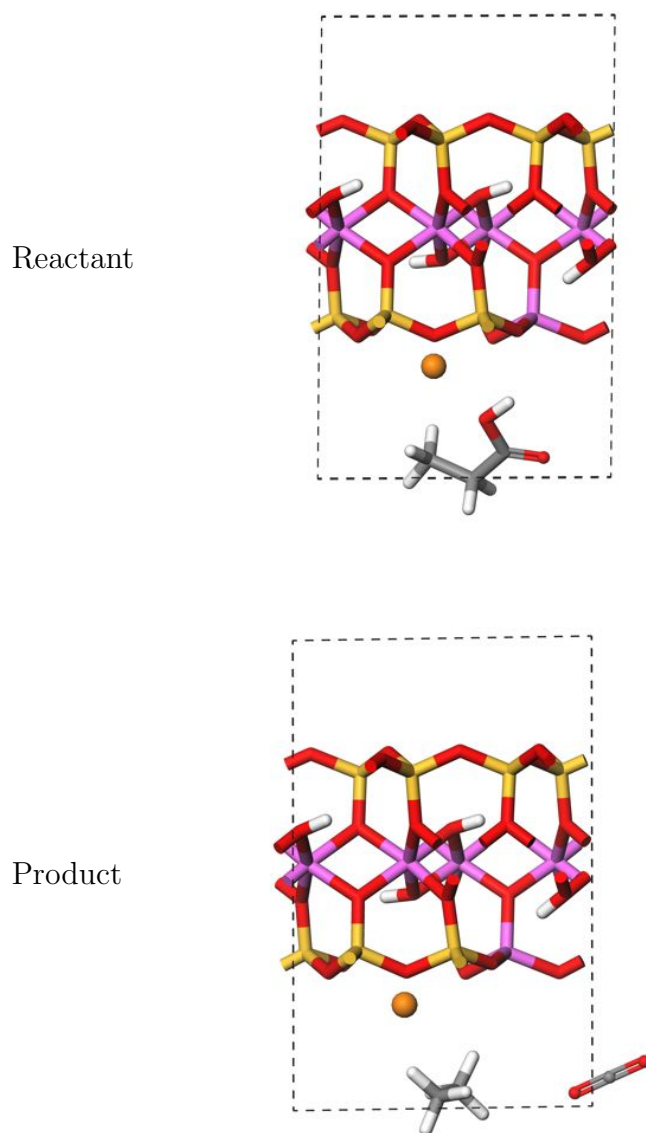
Figure 4.1: A single unit cell of pyrophillite (with an aluminum substitution in the tetrahedral sheet) and guest molecule of one of the simpler model fatty acids, propionic acid within the interlayer space of the reactant model and ethane plus carbon dioxide in the product model. See Table 4.1 for initial geometry optimized dimensions. Oxygen: red; hydrogen: white; aluminum: pink; carbon: grey; silicon: yellow; sodium: orange The dashed line is the periodic boundary of a unit cell. All subsequent figures use the same colour scheme.

DFT (PBE) [124]		Experiment [92]		Other DFT (PB86^a) [93]	
a = 5.22	$\alpha = 90.87$	a = 5.18	$\alpha = 90.00$	a = 5.119	$\alpha = 90.77$
b = 9.07	$\beta = 100.00$	b = 8.96	$\beta = 99.9$	b = 8.911	$\beta = 100.96$
c = 9.73	$\gamma = 89.65$	c = 9.97	$\gamma = 90.0$	c = 9.065	$\gamma = 89.91$

a: A semi-empirical functional with a fitted parameter for the exchange part.

Table 4.1: Lattice parameters of a unit cell of pyrophillite after geometry optimisation. The first column reproduces the results from our previous paper with no interlayer molecules; the c-length in our previous study converged to $14.5\mathring{A}$ on the inclusion of a molecule of propionic acid, hence the same extension was used in this study. Lengths are in $\mathring{A}$ and angles in degrees.

4.3.2 Computational details

The computations were carried out using the CASTEP code [35], with a planewave basis set within the DFT formalism [18], [86]. Convergence testing from the previous study described in Chapter 3 showed that a planewave basis represented by a kinetic energy cut-off of 550eV gave an energy difference in total energies of less than 0.04eV per unit cell for higher cut-offs and the Brillouin zone integrations were optimal using a grid containing two k-points to converge the calculation at a volume appropriate for these simulations [124].

The generalized gradient approximation (GGA) density functional, specifically Perdew, Burke and Ernzerhof (PBE) [21] was used as this describes molecular bonding to a greater accuracy than does the local density approximation (LDA) [23]. PBE ultrasoft pseudopotentials [29] were used which are consistent with the PBE exchange functional. The (geometry) optimizer was Broyden-Fletcher-Goldfarb-Shanno (BFGS) and the electronic method was ensemble density functional theory (EDFT) [41]. As a transition state search as implemented in CASTEP requires force tolerance criteria of less than 0.1 eV/$\mathring{A}$, the geometries of the reactant and product models were relaxed to the following criteria: electronic energy tolerance: $\leq 10^{-10}$ eV; geometry optimisation:- energy change per ion: $\leq 10^{-8}$eV; maximum force: ≤ 0.025 eV/$\mathring{A}$; change in distance: $\leq 0.0005\mathring{A}$. All calculations were carried out without spin polarization, as in the aluminosilicate models, there was an even number of electrons.

4.3.3 Searching for Transition States

CASTEP has automatic transition state searching functionality in the guise of linear synchronous transitions (LST) and quadratic synchronous transitions (QST) [96] and with the help of visualising software such as Materials Studio, [31] is a seemingly straightforward procedure and indeed, may well prove to be so for more homogeneous models than the clay minerals. Transition state searches require the identification of two configurations comprising the end points of a reaction pathway, the transition state lies between them. In the CASTEP set-up, the two end models on the reaction pathway are identified as the Reactant and Product which, in this study coincided with the reactant and product models, that is, a Reactant and or Product could be any configuration on the reaction pathway, it is entirely up to the user to determine which part of a reaction pathway is under scrutiny. The next step, if using Materials Studio, is to map atoms between the Reactant and Product and therein lies the first potential source of error. For example, in reference to Figure 4.1, for part of the carboxyl head of the fatty acid in the reactant model to become CO_2, a decision has to be made about which oxygen of COOH becomes which oxygen in CO_2. The general guideline is that the least distance moved by each constituent atom on transforming from the Reactant to the Product, is the most probable, which in its most general sense is known as the Principle of Least Motion (PLM) [125]. However, as can be seen in Figure 4.1, this is not always clear, fortunately, in this case there are only two possibilities so both were attempted. In more complex models, this problem might be ameliorated by choosing different orientations for the Reactant and Product models where possible, as some relative orientations might lend themselves to more obvious atom-atom mappings. This suggests a use for the various reactant configurations found in Chapter 3 on relaxation of the Almon and Johns intermediates, where the reactants contained the same species but in varying orientations with respect to the tetrahedral surface.

With the Reactant and Product models identified along with their atom-atom mappings, the LST commences. The LST and QST are searches based only on the geometries of the Reactant and Product models, there is no chemical intuition

introduced nor is there any dependence on energy to obtain the reaction interme-
diates. LST is 'linear' because the extrapolation equation used to find an initial
intermediate is a linear equation, similarly for QST being quadratic. Equation 4.1
describes the internuclear distance between atoms a and b (shown in Figure 4.2) of
the interpolated intermediate, $r_{ab}(i)$ defined by an addition of a proportion of the
internuclear distance between a and b in the reactant, r_{ab}^R and the product, r_{ab}^P.
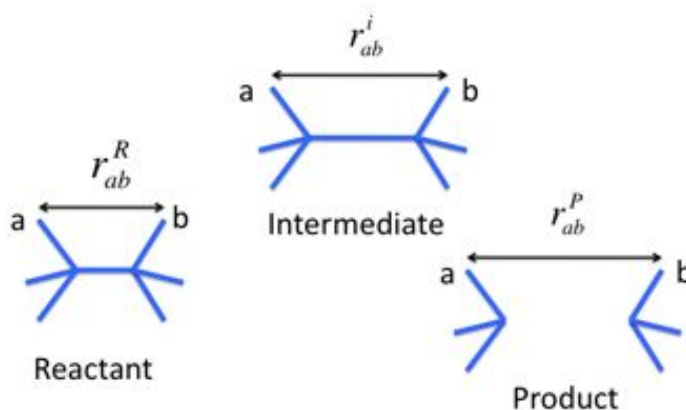
Figure 4.2: Schematic defining the variables used in Equation 4.1 where a and b
are labels for the same two atoms in each molecule and the intermediate is an
interpolated configuration between the Reactant and Product.

$$r_{ab}(i) = (1 - f)r_{ab}^R + fr_{ab}^P \qquad 0 \leq f \leq 1 \quad . \tag{4.1}$$

The proportion parameter, f, minimizes the following equation

$$S(f) = \frac{1}{2} \sum_{a \neq b}^{N} \frac{[r_{ab}(c) - r_{ab}^i(f)]^2}{[r_{ab}^i(f)]^4} + 10^{-6} \sum_{\zeta = x,y,z} \sum_a^N [\zeta_a(c) - \zeta_a^i(f)]^2 \quad , \tag{4.2}$$

where $r_{ab}(c)$ is the calculated and $r_{ab}^i(f)$ the interpolated internuclear distances be-
tween atoms a and b; similarly for the calculated ($\zeta_a(c)$) and interpolated ($\zeta_a^i(f)$)
Cartesian coordinates per atom; N is the number of atoms. The first term's weight-
ing of r^{-4} guarantees the close reproduction of important distances between bonded
atoms while the second term weighted by 10^{-6} minimises rigid translations and ro-

tations [126] in the manner of maximum coincidence [125]. The result of this is a 'loose' intermediate configuration between the Reactant and Product species which can be further refined according to the following

$$p = \frac{d_R}{(d_R + d_P)} \quad , \tag{4.3}$$

where p defines the relative distance from path-limiting geometries and

$$d_R = \left[\frac{1}{N} \sum_{\zeta=x,y,z} \sum_a^N (\zeta_a - \zeta_a^R)^2 \right]^{1/2} \quad , \tag{4.4}$$

and similarly for d_P and previous definitions of variables apply.

The application of this algorithm in CASTEP has been modified to apply to periodic systems, where the function $S(f)$ is subject to a cut-off radius that includes a few unit cells [96]. The LST with maximum energy becomes the upper bound on the geometry of the intermediate such that subsequent structures are determined by altering the internal coordinates while maintaining the p value. The constraint enforced on p ensures that the relative distance from path-limiting geometries is maintained in subsequent structures.

There then follows a conjugate gradient and line minimisation refinement in the same manner as that discussed in Chapter 2 where the tangent to the LST trajectory at the LST maximum becomes the initial search direction $\mathbf{s}_0$. If this minimisation fails to produce a transition state structure, a QST search commences using the 'best guess' [96] from the conjugate gradient algorithm. The QST search is based on the following equations.

$$r_{ab}(i) = \alpha + \beta f + \gamma f^2 \quad , \tag{4.5}$$

$$\text{given} \quad r_{ab}(i) = r_{ab}^R \quad \text{for} \quad f = 0 \quad \text{and} \quad r_{ab}(i) = r_{ab}^P \quad \text{for} \quad f = 1$$

where

$$r_{ab}(i) = (1 - f)r_{ab}^R + fr_{ab}^P + \gamma f(1 - f) \quad , \tag{4.6}$$

and γ is defined through

$$\gamma = \frac{[r_{ab} - (1 - p)r_{ab}^R - pr_{ab}^P]}{[p(p - 1)]} \quad , \tag{4.7}$$

As with the LST maximum, the geometry corresponding to the QST maximum is refined using conjugate gradients and line minimisations where the tangent to the QST energy maximum is the new $\mathbf{s}_0$. In theory, conjugate gradient refinement will locate the negative gradient direction of a saddle point as it searches every direction orthogonal to $\mathbf{s}_0$, so, if the algorithmic assumption is that the transition state has been found, then $\mathbf{s}_0$ is negative and no subsequent search directions will also be negative. Now, if the energy surface of the saddle point is n-dimensionally quadratic then two vectors $\mathbf{s}_i$ and $\mathbf{s}_j$ in this surface with Hessian $\mathbf{G}$ are conjugate providing

$$\mathbf{s}_i^T \mathbf{G} \mathbf{s}_j = 0, \qquad i \neq j \quad , \tag{4.8}$$

and a conjugate refinement will complete in n iterations. In reality, the energy surface is not perfectly quadratic and lack of precision in the line searches requires the introduction of a monitor, based on ratios of search directions relative to $\mathbf{s}_0$ as there could be a tendency for the gradient in the $\mathbf{s}_0$ direction to become too large. A new cycle of QST optimisation then begins and is considered converged when the residual forces fall below a user-input tolerance.

For the reactant and product model of this study, the LST was successful and found the structure shown in Figure 4.3. The QST search output described how the search was 'falling off the ridge', a description of the conjugate gradients algorithm falling into a minimum close to the saddle point. This meant another QST maximum was located and the conjugate refinement began again. However, after several attempts of adjusting the force tolerance criteria, no transition state was located. During some QST conjugate refinements the line minimizer had failed. On examination of the code, it was seen that the step-size for the conjugate gradients was too
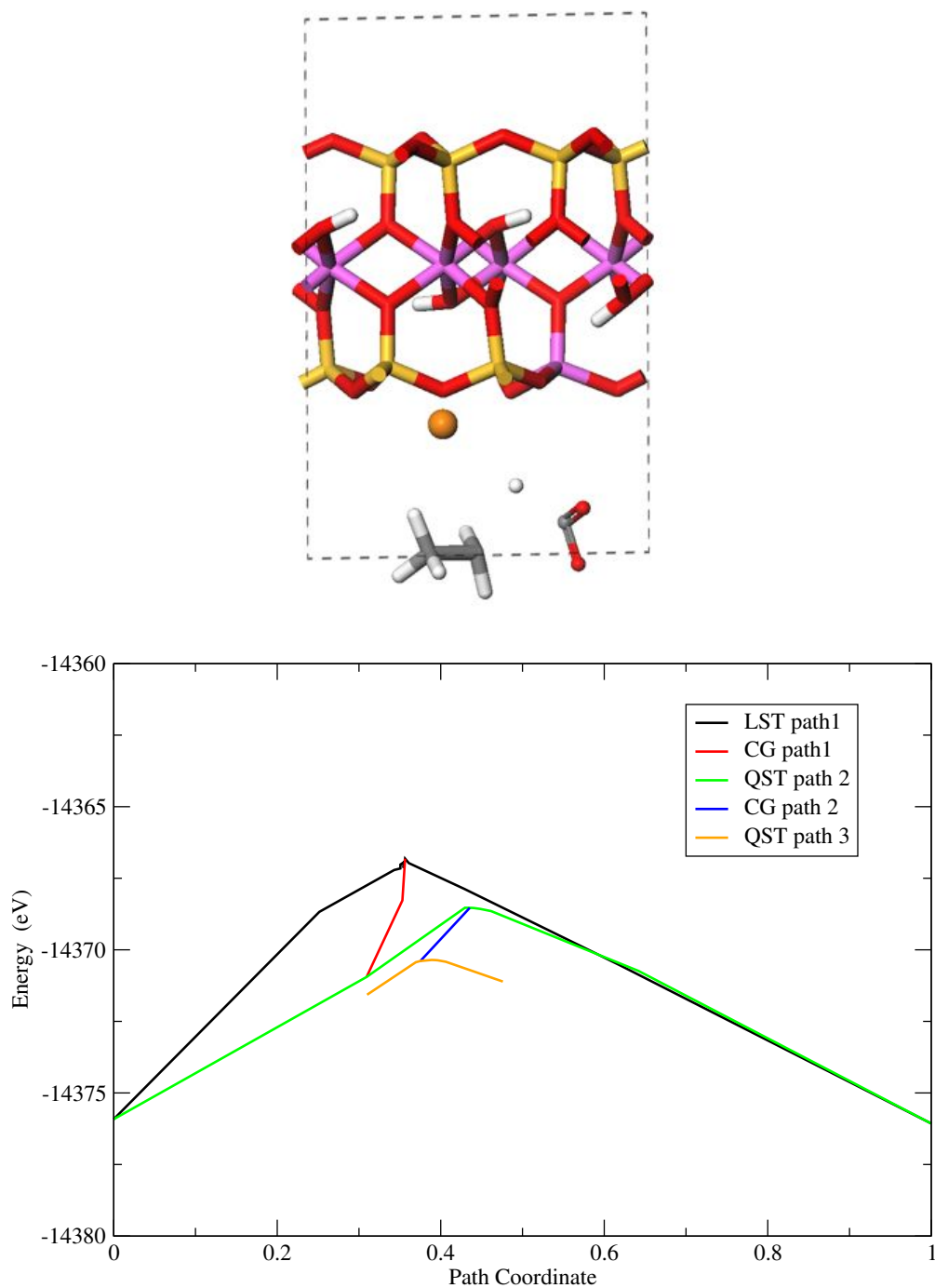
Figure 4.3: Top — the LST maximum corresponding to the LST maximum at the apex of the black line, on the chart at the bottom. (CG is conjugate gradients.)

large and the check on predicted energy compared to calculated energy, too coarse. Also, the line minimizer extended to a cubic but there was no check imposed and no quartic extrapolation, which would increase the accuracy of the minimisation. These were inherent problems with the code, which, if time allowed could have been repaired and tested. However, a different approach was taken.

Although the algorithm had failed to find a transition state, it had identified some structures different to both the reactant and product, new geometries with the potential to be transition states, two examples of which are shown in Figure 4.4. If these geometries were potential transition states, relaxing them to their ground states would allow them to fulfil this potential, although this would require strict convergence criteria as the slightest noise in the computations would cause a transition state to relax to a reactant or product. As the convergence criteria used for the transition state algorithm involved strict convergences, the same geometry optimisation criteria described in Section 4.3.2 were used to relax the QST maxima. The relaxed geometries show that one fell into the product configuration and hence was not a potential transition state but more of an intermediate on the route to becoming a product — this is purely geometrical and has no chemical significance. One of the QST maxima relaxed into a completely new configuration, implying that a new minimum on the potential energy surface had been reached. At this point there was no way of differentiating between a true minimum and the minimum of a saddle point.

The energy landscape of a transition state is a saddle point, such that there is an increase in energy in traversing the saddle in all directions but one, and a decrease in the other. The mathematical description of this is a single imaginary eigenfrequency identifying the direction of decreasing energy. This eigenfrequency can be detected as a vibrational mode and hence lattice dynamics calculations can be used to identify transition states. The following section describes this procedure.
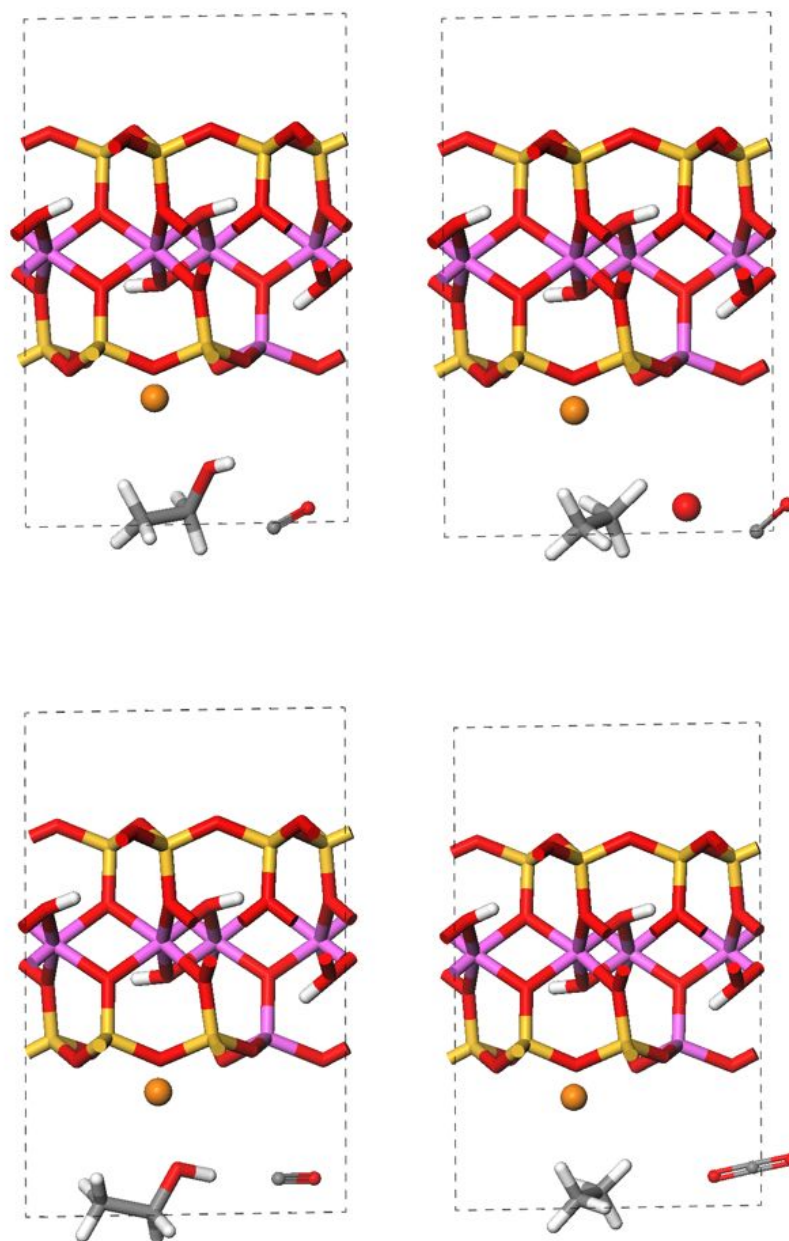
Figure 4.4: Two of the QST maximum configurations before relaxation (top row) and after relaxation (bottom row).

4.3.4 Lattice dynamics

Vibrational analysis via lattice dynamical calculations, is the examination of atomic motion within a bulk material under an applied electromagnetic field. The theory behind this is essentially simple but when applied from first principles is computationally complex. In light of this, this section introduces the simple theory progressing to an increasingly complex model, during the course of which, the convergence of the classical and the quantum in experimental spectroscopy is highlighted. There then follows an introduction to the *ab initio* implementation of linear response lattice dynamics in the form of density functional perturbation theory (DFPT). Concluding this section is the description of some of the restrictions necessary for its successful implementation within CASTEP.

1-D Basic Model

In classical mechanics the motion of a collection of masses is modelled by representing the masses as point particles joined by springs with their own spring constants. The resting position of the masses is considered to be the equilibrium position and any deviation away from this is the measured motion, which is simple harmonic oscillatory. This is motion that can be described by a single frequency cosine or sine function, with a constant amplitude for all time. When the masses move in a synchronised manner, that is they begin their motion and end their motion at the same instant, this is known as 'moving in phase'. In-phase motion is called a normal mode and can encompass different amplitudes. In a system of three masses, the equations of motion produce three normal mode solutions — see Figure 4.5 — one of which is the translational mode ($\lambda_n = 0$) where the centre of gravity of the whole system moves. Any general motion of this three particle system consists of a superposition of the three normal modes with its own set of amplitudes and phases [127]. This is the basic, one dimensional mathematical model behind lattice dynamical calculations.

To begin applying this simple model to more complex systems, the next step
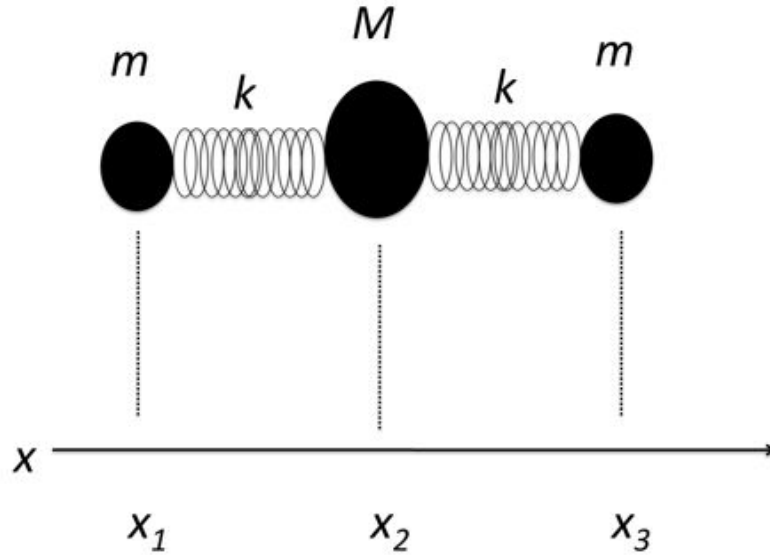
Equations of motion for masses 1, 2 and 3 respectively

$$m\ddot{x}_1 + k(x_1 - x_2) = 0;$$
$$M\ddot{x}_2 + k(2x_2 - x_1 - x_3) = 0;$$
$$m\ddot{x}_3 + k(x_3 - x_2) = 0.$$

(4.9)

Assuming a solution of the form $x_n = A_n\cos(2\pi\nu t + \phi)$ where A is the amplitude, ν the characteristic frequency of a normal mode and ϕ the phase angle, gives the secular equation of motion:

$$\begin{vmatrix} (k - m\lambda) & -k & 0 \\ -k & (2k - M\lambda) & -k \\ 0 & -k & (k - m\lambda) \end{vmatrix} = 0 \qquad \text{where} \quad \lambda = 4\pi^2\nu^2.$$

Whose solutions are: $\lambda_a = \frac{k}{m}$; $\lambda_b = \frac{k(M+2m)}{Mm}$; $\lambda_n = 0$.

Figure 4.5: Schematic of a model system of three masses (LHS) of mass M and m connected by springs with spring constant k.

is to consider a single molecule. The key to making this transition is to use the Born-Oppenheimer approximation, whereby the atomic nuclei (of a molecule) are the point masses and it is their motion that is modelled. The spring constants between the point masses are representative, in the first instance, of the chemical bonds between atoms in a molecule, where the chemical bonding is due to electrons. The intramolecular forces created by the presence of the electrons are responsible for the restoring forces, which counteract a change in internuclear distance precipitated by vibrational motion. As the molecular vibrational amplitudes are small, the simple harmonic oscillator (SHO) approximation is appropriate.

Prior to the implementation of *ab initio* lattice dynamics computations, spectroscopic data was used to gauge the strength of the intramolecular force fields. At this point, no quantum mechanics has been introduced and yet a classical mechanical model together with experimental data is informing what is essentially quantum mechanical relationships. This is because in the case of an SHO, electromagnetic radiation can only be absorbed in multiples of quantum numbers e.g. from $n = 0$ to $n = 1$, that is, where the energy levels are adjacent. Suppose two energy levels have eigenvalues W_0 and W_1, then the frequency of the radiation required for this transition (v_q) is given by the Bohr relation

$$v_q = \frac{W_0 - W_1}{h} \quad , \tag{4.10}$$

and the eigenvalue $W^{'}$ associated with wave function $\psi^{'}$ is given by

$$W^{'} = (n^{'} + \frac{1}{2})hv_c \quad , \tag{4.11}$$

where $n^{'}$ is the quantum vibrational number and v_c is the classical vibrational frequency. Substituting this into Equation 4.10 gives

$$v_q = \frac{(n^0 + \frac{1}{2})hv_c - (n^1 + \frac{1}{2})hv_c}{h} = (n^0 - n^1)v_c = v_c \quad , \tag{4.12}$$

and hence the use of radiation frequencies in spectroscopic analyses of classical me-

chanical frequencies, in order to determine the strength of internuclear force fields.

Introducing Dipoles

The dipole moment of a molecule is due to its nuclear (and electronic) configuration and hence the principle of SHO motion applies, where the normal modes are characteristic of the dipole. The energy of radiation a dipole is able to absorb to induce oscillations of the normal modes, lies in the infrared region between wave numbers 650 cm^{-1} and 4400 cm^{-1}. This frequency region spans the spectrum of energy a dipole can absorb, to effect its range of vibrational modes. In complex molecules some vibrations involve the whole molecule whereas others involve only some of the bonds or the functional groups [128]. These localized vibrations can be used as a means of identification of the functional groups as they have specific motions such as stretching, bending, rocking, twisting or wagging. Where infrared spectroscopy involves the absorption of radiation, a second technique, Raman spectroscopy, involves the detection of a change in frequency due to the scattering of incident radiation and the induction of a dipole moment. Raman will not be explored in greater depth here, suffice to say that infrared and Raman can be complementary tools of spectroscopic analysis, as some absorptions disallowed in infrared, are allowed in Raman.

Towards Quantum Mechanics

Moving on from the consideration of isolated molecules, to the consideration of a periodic array of atoms, which, by its very definition, implies that the various vibrational modes of the atoms in adjacent unit cells are strongly coupled. The phase relationships of the coupled displacements can be identified in real space using long wavelength radiation of wavevector $\mathbf{q}$ where $|\mathbf{q}| = 2\pi/\lambda_p$ where λ_p is the wavelength of the incident radiation. To examine the commensurate or in-phase vibration of the bulk, $\lambda_p = \infty$ is required which, relative to atomic spacing and bond lengths, is achieved by infrared radiation [94]. Computationally it is possible to probe the phase relationships between cells by using wavevectors of $q \neq 0$, information that

can be used to plot dispersion curves and density of states. Further elastic properties are then accessible such as the heat capacity of the bulk, thermal expansion, thermal conductivity and thermal resistivity [24].

So far the classical mechanical implementation of lattice vibrations is straightforward, but now it is time to introduce quantum mechanics into the model. Although there are several methods of implementing *ab initio* lattice dynamics such as the frozen phonon method and finite differences, the focus of this study is linear response DFPT. The vibrational change in energy of a material due to the displacement of atoms is ultimately governed by the electrons. As long as the vibrations are of a sufficiently low frequency, i.e. with longer wavelengths and lower frequency than those of the electrons, the electrons can be considered to remain in their ground-state, which evolves as a function of nuclear displacements [14]. The total energy of the material is then a function of the positions of the nuclei i.e $E = E_{\text{total}}(\mathbf{R}_I)$ and the forces on the nuclei are given by $\mathbf{F}_I = -\frac{dE}{d\mathbf{R}_I}$ where, in the SHO approximation, the forces at equilibrium are zero. The second derivatives of the energy (Hessian in matrix form) with respect to the nuclear positions, which identify stationary and saddle points, are the interatomic force constants given by

$$C_{IJ} = -\frac{d\mathbf{F}_I}{d\mathbf{R}_J} = \frac{d^2 E}{d\mathbf{R}_I d\mathbf{R}_J} \quad . \tag{4.13}$$

The force constants of C_{IJ} can be calculated from the responses of the nuclei to positional perturbations, i.e. expansions of the nuclear displacements from their equilibrium position produce displacements with vibrational modes at frequency ω, and are described by [14]

$$\mathbf{u}_I(t) = \mathbf{R}_I(t) - \mathbf{R}_I^0 \equiv \mathbf{u}_I e^{i\omega t} \quad , \tag{4.14}$$

where $\mathbf{R}_I^0$ is the equilibrium position. Given that the force on the nuclei is

$$\mathbf{F}_I(\mathbf{R}) = M_I \frac{\partial^2 \mathbf{R}_I}{\partial t^2} = -\frac{\partial}{\partial \mathbf{R}_I} E(\mathbf{R}) \quad , \tag{4.15}$$

then substituting in Equation 4.14 and combining with Equation 4.13 produces, for each I

$$-\omega^2 M_I u_I = -\sum_J C_{IJ} u_J \quad .$$
(4.16)

Add in the Born van Karman boundary conditions which imposes the Bloch theorem as detailed in Chapter 2 and the full solution to Equation 4.16 is given by

$$\det \left| \frac{1}{\sqrt{M_s M_{s'}}} C_{s,s'}(\mathbf{q}) - \omega_{i\mathbf{q}}^2 \right| = 0 \quad ,$$
(4.17)

where s refers to the sth atom, $\mathbf{q}$ is the wave vector where for $\omega_{i\mathbf{q}}, i = 1, 3s$ (3 degrees of freedom per atom). The force constant matrix for wavevector $\mathbf{q}$ is then defined as

$$C_{s,s'}(\mathbf{q}) = \sum \mathbf{T}_n e^{i\mathbf{q}\cdot\mathbf{T}_n} \frac{\partial^2 E(\mathbf{R})}{\partial \mathbf{R}_s(0) \partial \mathbf{R}_{s'}(\mathbf{T}_n)} = \frac{\partial^2 E(\mathbf{R})}{\partial \mathbf{u}_s(\mathbf{q}) \partial \mathbf{u}_{s'}(\mathbf{q})} \quad ,$$
(4.18)

where $\mathbf{T}_n$ is cell $\mathbf{T}_n$ in the bulk and $\mathbf{u}_s$ the Bloch wave function of atom s given by

$$\mathbf{u}_{s,\mathbf{T}_n} = e^{i\mathbf{q}\cdot\mathbf{T}_n} \mathbf{u}_s(\mathbf{q}) \quad .$$
(4.19)

Equation 4.17 is an analogy of the classical mechanical secular equation shown in Figure 4.5 where in the latter case, the force constant matrix is given in terms of the spring constant, k. But now, the case is quantum mechanical, explicit in its inclusion of wave functions and, as mentioned previously, the effect of the electrons is expressed in the interatomic force constants as will now be demonstrated.

The Hellman-Feynman theorem detailed in Chapter 2 gives the force expression of the Born-Oppenheimer Hamiltonian as [129]

$$\mathbf{F}_I = -\int n_{\mathbf{R}}(\mathbf{r}) \frac{\partial V_{\mathbf{R}(\mathbf{r})}}{\partial \mathbf{R}_I} d\mathbf{r} - \frac{\partial E_N(\mathbf{r})}{\partial \mathbf{R}_I} \quad ,$$
(4.20)

where $\partial E_N(\mathbf{r})$ is the electrostatic interaction between nuclei and $V_{\mathbf{R}}(\mathbf{r})$ is the electron-nucleus interaction given by

$$V_{\mathbf{R}(\mathbf{r})} = -\sum_{iI} \frac{Z_I e^2}{|\mathbf{r}_i - \mathbf{R}_I|} \quad .$$
(4.21)

Equation 4.20 explicitly shows the inclusion of the groundstate electron charge density, $n(\mathbf{r})$. To obtain the interatomic force constants, simply differentiate $\mathbf{F}$ with respect to the nuclear coordinates to obtain [129]

$$\frac{\partial^2 E(\mathbf{R})}{\partial \mathbf{R}_I \partial \mathbf{R}_J} \equiv -\frac{\partial \mathbf{F}_I}{\partial \mathbf{R}_J} = \int \frac{\partial n_{\mathbf{R}}(\mathbf{r})}{\partial \mathbf{R}_J} \frac{\partial V_{\mathbf{R}}(\mathbf{r})}{\partial \mathbf{R}_I} d\mathbf{r} + \int n_{\mathbf{R}}(\mathbf{r}) \frac{\partial^2 V_{\mathbf{R}}(\mathbf{r})}{\partial \mathbf{R}_I \partial \mathbf{R}_J} d\mathbf{r} + \frac{\partial^2 E_N(\mathbf{R})}{\partial \mathbf{R}_I \partial \mathbf{R}_J} \quad , \tag{4.22}$$

which now requires the ground state charge density and its linear response to a perturbation of the nuclear positions. The theory introduced here has served to draw parallels between classical and quantum mechanics, to emphasise that the essential idea behind the approach of lattice dynamics is that of simple harmonic oscillators. From this point, the interatomic force constant matrix is obtained by perturbing each term in Equation 4.22 according to perturbation theory, as detailed in Gonze's work [130]. Implementation of DFPT in CASTEP was refined in 2006 with the inclusion of the linear response of the GGA exchange-correlation potential, responsive to incommensurate ($q \neq 0$) wave vectors [131]. The interested reader is referred to the aforementioned references for further details as this study will not delve further into the theory behind lattice dynamic calculations apart from discussing some of its output and 'limitations' pertinent to this investigation.

The results of a DFPT calculation for N atoms in periodic boundary conditions are $3N$ phonon branches, three of which are the acoustic modes representing 3-D translations of the lattice, analogous to the 1-D case shown in Figure 4.5 where $\lambda_n = 0$. The remaining $3N - 3$ optic modes are due to the interaction of the nuclei. The output can be in the form of infrared and Raman plots as well as dispersion curves and density of states. Transition states are identifiable because the Hessian of the Born-Oppenheimer energy surface produces an imaginative frequency for a saddle point energy surface.

Another consequence of a DFPT calculation is the ability to calculate (longitudinal optic/transverse optic) LO/TO splitting. This experimentally observed phenomenon occurs due to a coupling of the long wavelength optical phonon and

the electric field due to long range Coulomb forces. As can be seen in Figure 4.6 the LO/TO splitting is dependent on the direction of wavevector $\mathbf{q} = \mathbf{0}$ relative to the direction of the Coulomb electric field, $\mathbf{E_c}$. When $\mathbf{q}$ is longitudinal/parallel to $\mathbf{E_c}$ i.e ($\mathbf{E_c} \parallel \mathbf{q}$) the degeneracy of optical modes is removed as there is no equivalent perpendicular/transverse electric field coupling ($\mathbf{E_c} \perp \mathbf{q}$). Thus there is a change in Coulomb forces created by ($\mathbf{E_c} \parallel \mathbf{q}$), which does not occur due to ($\mathbf{E_c} \perp \mathbf{q}$) hence there is a frequency difference between the LO and TO modes, detectable by spectroscopy. The strength of coupling of ($\mathbf{E_c} \parallel \mathbf{q}$) is quantified by the Born effective charges.
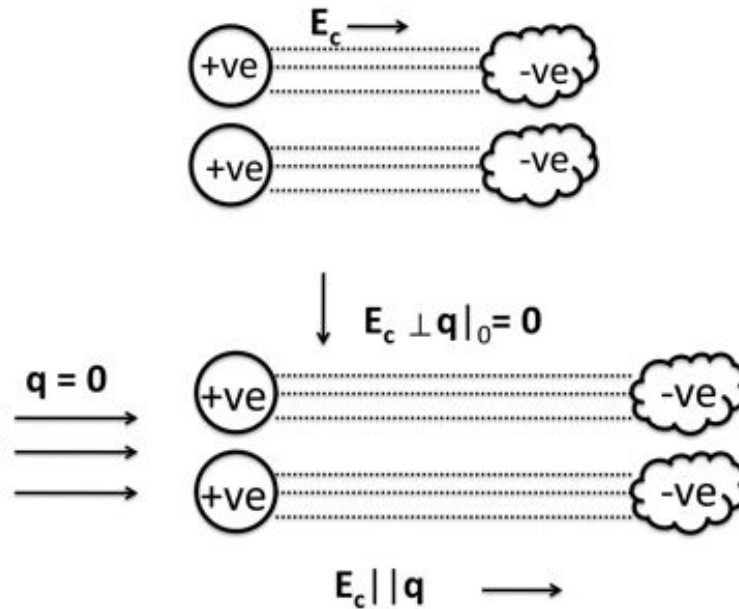
Figure 4.6: Schematic of the origins of LO/TO splitting where the change in the Coulomb forces caused by the incident longitudinal phonon, removes the degeneracy of optical modes at the gamma point. $\mathbf{E_c}$ is the electric field produced by long range Coulomb forces.

The first 'limitation' of the linear response DFPT implementation within CASTEP to date, is that it can only be applied to insulators. During a perturbation, the first order response of the Kohn Sham orbitals ($\phi^{(1)}$) is required and is given as the

solution to the Sternheimer equation

$$\left(H^{(0)} - \epsilon_m^{(0)}\right)\left|\phi_m^{(1)}\right\rangle = -P_c v^{(1)}\left|\phi_m^{(0)}\right\rangle \quad , \tag{4.23}$$

where $\phi_{\mathbf{k},\mathbf{q}}^{(1)}(\mathbf{r}) = e^{-i(\mathbf{k}+\mathbf{q})\cdot\mathbf{r}}u^{(1)}(\mathbf{r})$; $u^{(1)}(\mathbf{r})$ is the first perturbed periodic function [130]; P_c is the projection operator and the first order potential, $v^{(1)}$ includes the response of the Hartree and XC potentials [132]. The projection operator projects perturbed occupied states only onto unoccupied states because a perturbed charge density projected onto itself produces a null result [129]. Thus, a definite band gap (together with fixed orbital occupancy) is required in DFPT, which is the electronic structure definition of insulators.

The second 'limitation' is that DFPT is currently implemented in CASTEP with norm-conserving pseudopotentials (PP) only. This is because ultrasoft PP have non-orthogonal atomic orbitals and an augmentation charge and an overlap operator as detailed in Chapter 2. A varying orthogonality produces artefact forces and extra terms and derivatives are produced when calculating the Hessian of the Born-Oppenheimer energy surface, due to the augmentation charge term. Basically, the model becomes so complicated that the code has not, to date, been functionalised. Further details can be found in Paul Tulip's thesis [133]. This is a pertinent point for the study detailed in this chapter, as the norm-conserving PP requirement introduced several modelling issues, which will be discussed in due course.

In spite of the above drawbacks, which in itself is a subjective viewpoint, linear response DFPT is a powerful analytical tool. It can be computationally expensive to produce the Hessian for $\mathbf{q} \neq \mathbf{0}$ but this process is made efficient by the technique of Fourier transforming the force constant matrix to produce the dynamical matrix, $D(\mathbf{q})$, a $3N$ by $3N$ matrix at each $\mathbf{q}$

$$D(\mathbf{q}) = \frac{1}{\sqrt{M_I M_J}}\sum\left(\frac{\partial^2 E}{\partial\mathbf{u}\partial\mathbf{u}}\right)e^{-i\mathbf{q}\cdot\mathbf{R}} \quad . \tag{4.24}$$

Sub- and super- scripts have been dropped as this equation is illustrative of the

method and not the mathematical details, which can be found in reference [132]. Although the dynamical matrix is costly to produce, it can be used as the basis of an interpolation procedure, by virtue of the relatively short range of the real space forces in the force constant matrix, of the order of $\frac{1}{R^{-5}}$. This arises from the relatively short interatomic interactions in a non-polar solid or insulator [132]. From a relatively coarse calculation of $D(\mathbf{q})$, a density of states or dispersion curve can be produced at little extra computational expense.

As mentioned in the Introduction to this chapter there is a dearth of studies combining heterogeneous periodic systems, planewaves, pseudopotentials and DFPT in spite of the analytical power of the latter method of vibrational analysis. Therefore, the study outlined in this Chapter is pioneering but the potential to add to the scientific understanding of chemical reactions via the identification of transition states, is sufficient to justify this venture into uncharted territory. All that remains to be remarked on before the Results section is the convergence criteria specific to DFPT.

4.3.5 Computational Details

The linear response calculation, DFPT [130] implemented in CASTEP computes the lattice dynamic responses of a bulk material for a range of phonon wavevectors (q-values/points). DFPT is currently implemented for norm-conserving pseudopotentials [134]. All previous calculations up to this point have employed ultrasoft PP, which require a relatively low cut-off energy compared to the norm-conserving PP. If a higher energy cut-off was introduced, then all previous geometry optimisations would have to be re-done. A higher cut-off would increase the computational time, which, with these particular models was already substantial reaching several weeks for a full optimisation. However, the need for a higher cut-off was obviated by switching from a coarse grid of 1.75 to a coarse grid of 2.0. An energy-differences convergence test showed that, for a coarse and fine grid scale of 2.0, (these scales are explained in Chapter 2) an energy cut-off of 550eV produces convergence per

unit cell to 1meV - illustrated in Figures 4.7 and 4.8. This is an order of magnitude higher than was used for the ultrasoft PP, which lends confidence in the output obtained used norm-conserving PP.
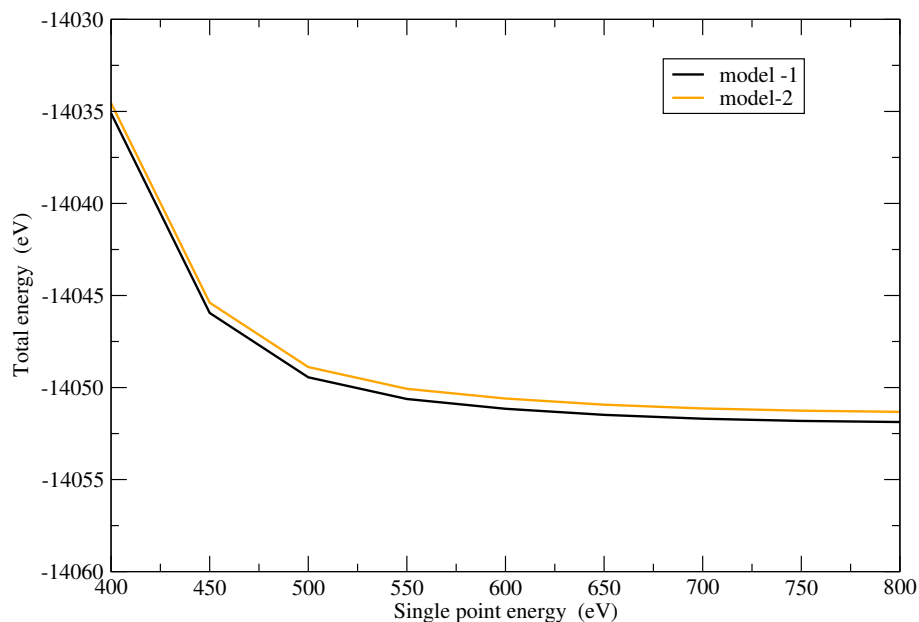
Figure 4.7: Energy cut-off convergence test for the norm-conserving pseudopotentials using two product models, which differ in the position of their sodium atom only.
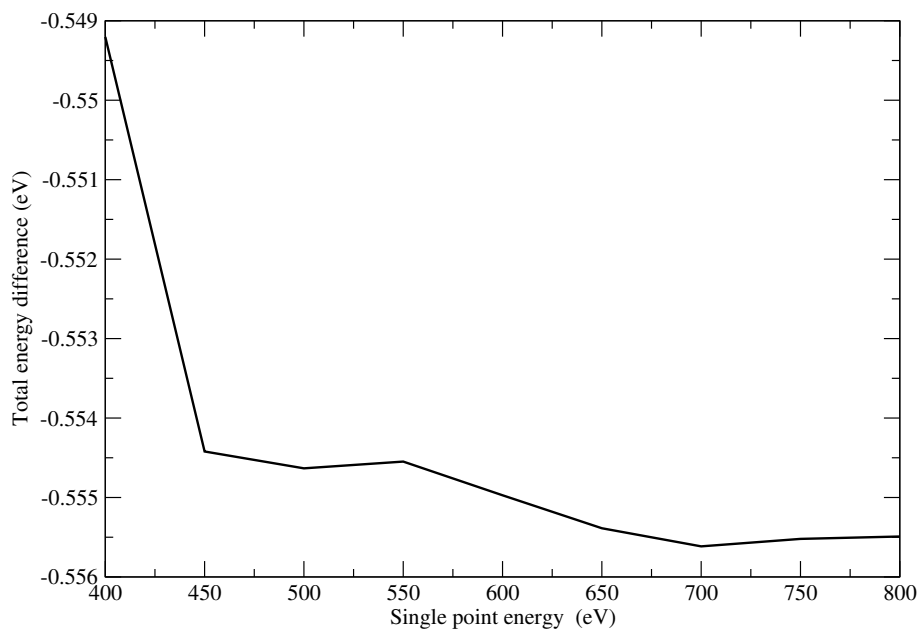
Figure 4.8: Showing the convergence of the total energy differences with cut-off energy for the norm-conserving pseudopotentials.

Consequently a pragmatic decision was made to keep the 550eV cut-off energy,

together with the relaxed lattice parameters found with the ultrasoft PP. Fixing the lattice parameters was motivated by computational efficiency and the fact that the interlayer species were contained within a vacuum-like space.

To summarise, keeping the lattice parameters fixed, and allowing only the atoms to relax, the reactant, intermediate and product models were re-optimized with the GGA-PBE exchange-correlation functional, norm-conserving pseudopotentials [31], using 550eV, two k-points, a grid scale of 2.0 and the convergence criteria previously stated in section 4.3.2, paragraph two. The additional convergence criteria used for the linear response calculation were as follows: phonon energy tolerance: $\leq 10^{-5}$eV; phonon convergence tolerance: $\leq 10^{-5}$eV/Å^2; phonon preconditioner: Teter, Payne and Allan (TPA) [39].

DFPT calculations were carried out on the optimized geometry of the intermediate at the gamma point, $q = 0$ followed by a dispersion curve based on a coarse, reciprocal space, Monkhurst Pack grid of q- points: $[10, 5, 1]$ with an interpolation of q- point spacing of 0.01. This spacing was found to be optimal as spacing less than this produced no further refinement in the results. This was repeated for the reactant, product and the clay-only model plus the full relaxation of the clay-only model including its lattice parameters. The latter two cases involved solely the clay surface without any guest molecules. The motivation for the relaxation in the latter two cases will be revealed in the following section.

4.4 Results and Discussion

4.4.1 Finding the Transition State

The LST/QST searches produced a configuration of interlayer species, consistent with a possible transition state between the reactant and product, see Figure 4.4. The intermediate is comprised of ethanol CH_3CH_2OH plus CO, which are not species hypothesised by Almon and Johns who deduced an organic free radical intermediate

or, in the absence of water, the involvement of a carbonium ion [10]. Some of the reasons for these differences will be discussed in due course.

An examination of the energy differences between the intermediate, reactant and product, Table 4.2, shows that in both PP approximations, there is a positive energy difference between the intermediate and the reactant and the intermediate and the product due to the higher energy of the intermediate, which is consistence with the characteristics of a transition state between a reactant and product. Although the two PP approximations show a difference in magnitude of the energy differences between the reactant, product and intermediate, these results were found to be acceptable within the scope of this study, as the expectation was not to obtain quantitative data about reaction rates from this simulation. Although the GGA achieves greater accuracy in calculating reaction barrier heights — in the context of the attachment of a gas-phase molecule to a surface [135] — than does the LDA, due to the overbinding of the latter, this result is being used as a guide to the feasibility of the intermediate being a transition state. Quantitative calculations of barrier heights would follow the full identification of the reaction pathway, and might require the consideration of clay layer surface–gas-phase molecule interactions, or gas-phase–gas-phase interactions depending on the configuration of the transition state(s).

(Δ_{A-B})	ultrasoft	norm-conserving
Δ_{I-R}	1.2026	0.8773
Δ_{I-P}	1.3413	1.6467
Δ_{P-R}	-0.1387	-0.7694

Table 4.2: Energy differences (Δ_{A-B}) of the optimised models using ultrasoft and norm-conserving pseudopotentials where R is reactant; I is intermediate; P is product.

Much of the initial interest in mineral mediated decarboxylation reactions arose from issues surrounding the formation of crude oil and its extraction and purification. Early work by Almon and Johns evidenced that one possible pathway for

decarboxylation, under putative reservoir conditions, involved free radical mechanisms, with increased conversion of fatty acids in the presence of radical promoters and, conversely, a decrease in reactivity in the presence of free radical inhibitors. In other work by Zhang et al [136], who used metal oxide catalysts to reduce the total acid number (caused by naphthenic acid) in crude oil, in order to increase the value of the product, cationic/anionic and concerted pathways were proposed as potential reaction mechanisms. However, the intermediate and potential transition state found in this study does not suggest a reaction pathway in agreement with any of the above mechanisms.

As previously stated, decarboxylation has become of interest through the desire to be able to produce fossil fuel-like products from plant oils, which are primarily composed of tri-acyl glycerides, based on fatty acid structures. In this present study an alcohol has been identified as a potential transition state, which is not without precedent [137]. An alcohol is involved in a hydrodeoxygenation pathway where it subsequently undergoes further reduction down to the hydrocarbon with the simultaneous formation of CO_2. Dehydration/hydrogenation reactions of fatty acids and their esters have been shown to involve alcohol intermediates in studies of biofuel production [137] as illustrated in Figure 4.9. However, in contrast to the physical hydrodeoxygenation pathway, the production of the simulated ethanol intermediate occurred without C-C bond cleavage, no hydrogen source was introduced and no water was formed.

$$H_{2n+1}C_n - COOH \xrightarrow{[+2H_2 - H_2O]} H_{2n+3}C_{n+1} - OH \xrightarrow{[-H_2O]} C_{n+1}H_{2n+2}$$
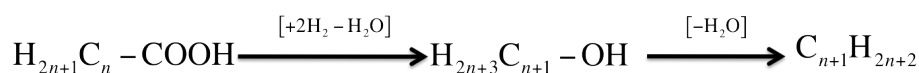
Figure 4.9: Hydrodeoxygenation reaction scheme of a fatty acid.

The difference between the intermediate found and the hypothesised reaction pathway of Almon and Johns is completely within expectations. The models used in this investigation are as minimal as possible. The approach to investigating the reaction mechanism is simplistic where only the reactant and product are defined, allowing, in the first instance, a one-configuration transition between them. If, as

is highly likely in the case of free radical reactions, multiple transition states with small energy separations exist on that pathway, this method may not uncover them in a single investigation of this type. An alternative approach, within the methodological constraints, would be to specify explicit intermediate states or, on obtaining one intermediate state, to use this as either the reactant or product and repeat the transition state search.

Additionally, it should be noted that the experimental reaction rates were rather slow, with only 2% conversion to the alkane product, even at elevated temperatures of 250°C and that Almon and Johns did state that their proposed decarboxylation mechanism probably did not 'reflect reality except in the broadest sense' [10].

Both their study and this agree that a decarboxylation reaction within a clay environment involves the transfer of electrons to the clay minerals, as will be illustrated in subsequent sections. Furthermore, the potential transition state found here opens up the possibility in future work to determine an intrinsic reaction coordinate (IRC) path [138] and to analyse the mechanics of a reaction [139] leading from the reactant to the product via this transition state and, possibly, many others. The following section describes the results obtained from vibrational analysis of the intermediate.

4.4.2 Vibrational analysis

On geometry optimisation of the intermediate configuration using norm-conserving PP and visualisation of the resulting geometry, it was found that there was a distortion in the clay layer above the position of the sodium atom, see Figure 4.10. When repeating the optimisation on the reactant, product and clay-only layer using norm-conserving PP, the same distortion of the clay layer appeared. When the lattice and atomic positions of the clay-only layer were allowed to relax, there was no distortion in the clay layer, see Figure 4.11. This implies the distortion is a direct result of using the norm-conserving PP without allowing the lattice parameters to

relax. The lattice lengths of the completely relaxed clay-only layer are within 5% of those obtained using the ultrasoft PP and although the clay layer has been distorted, a comparison of Figures 4.1, 4.4 and 4.10 shows that the configurations of the interlayer species appear similar in both PP approximations. This is probably due to the vacuum of the interlayer enabling the organic molecules to relax without the imposed lattice restraint, as anticipated in Section 4.3.5. The aim of this study is to identify a transition state configuration and, as both PP approximations have produced the same configuration when geometry optimised, this elicits the question: how much has the distortion in the clay layer affected the verification of a transition state using vibrational analysis?

The four lowest eigenfrequencies of the phonon calculation (see Table 4.3) for the commensurate $q = 0$ point, show that the intermediate has four imaginary frequencies, three of which are shared with the reactant and clay and two with the product. The three frequencies with the value $-0.02i$ cm^{-1} and $-0.03i$ cm^{-1} represent the three translational vibrations of the lattice in the x-, y- and z-directions. The difference between these values and zero is acceptable noise of the calculation in the context of a range of frequencies that extends to 3700cm^{-1}, together with the force convergence criteria of the geometry optimisation. The results for the reactant and clay models do not contain any large imaginary frequencies implying that the imaginary frequencies found in the intermediate and product are not due to using the norm-conserving PP and the effect it has had on the clay.

Reactant		Intermediate		Product		Clay	
$-0.02i$	N	$-45.35i$	Y	$-53.9i$	Y	$-0.02i$	N
$-0.02i$	N	$-0.02i$	N	$-0.03i$	N	$-0.02i$	N
$-0.02i$	N	$-0.02i$	N	$-0.02i$	N	$-0.02i$	N
38.22	Y	$-0.02i$	Y	$-0.02i$	N	55.66	Y

Table 4.3: Four lowest eigenvalues from the phonon calculation on each model where 'Y' and 'N' refer to Raman acivity, 'Yes' and 'No' respectively and units are cm^{-1}

The largest imaginary frequency of the intermediate is indicative of a transition

Reactant   Intermediate

Product   Clay
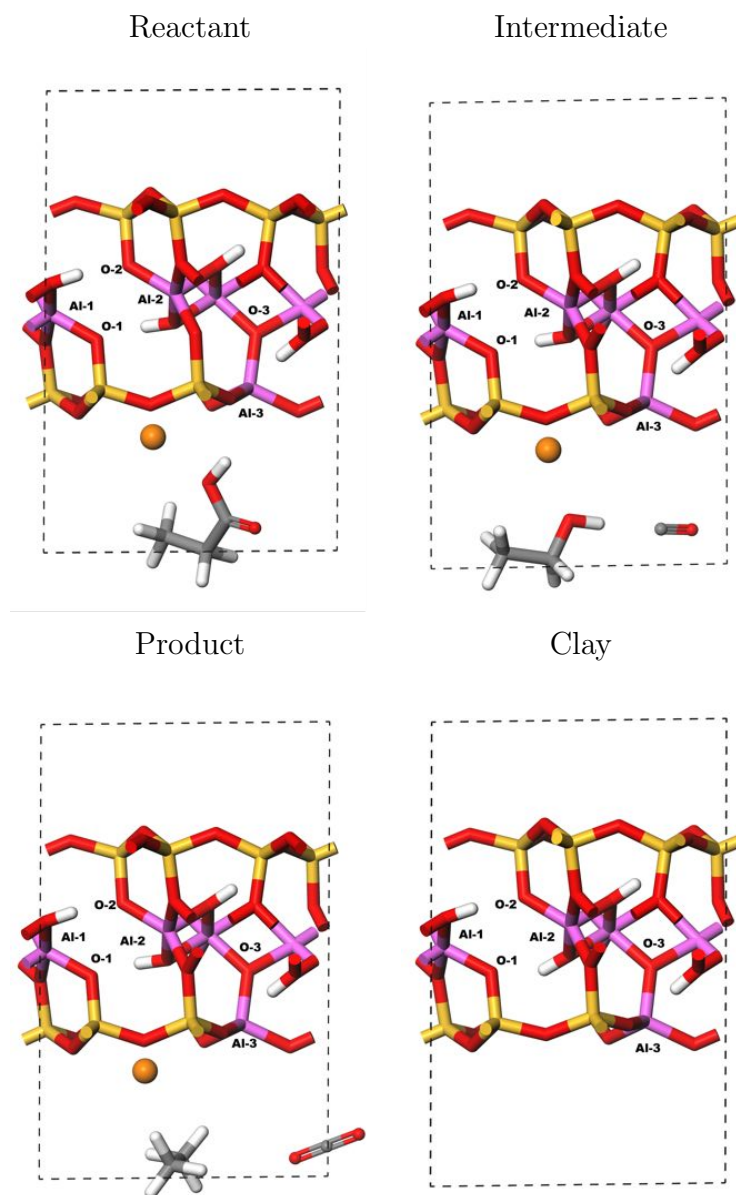
Figure 4.10: Geometry optimised models using the norm-conserving pseudopotentials. The labelled atoms are referred to in Tables 4.4 and 4.5.

state but, as can be seen in the results, the product also has a large imaginary eigenfrequency although the product was assumed to be stable. Dynamic visualisations of these imaginary modes — a facility available in Materials Studio — show for the intermediate an oscillation of the OH branch of ethanol towards CO suggesting that an application of energy would initiate a reaction between the two separate molecules of this intermediate stage, which would then form the product alkane and CO_2. Therefore this intermediate is a transition state. In contrast, visualisation of

Clay layer   Lattice dimensions

$a = 4.97 \quad \alpha = 90.09$
$b = 8.63 \quad \beta = 100.88$
$c = 9.24 \quad \gamma = 89.60$
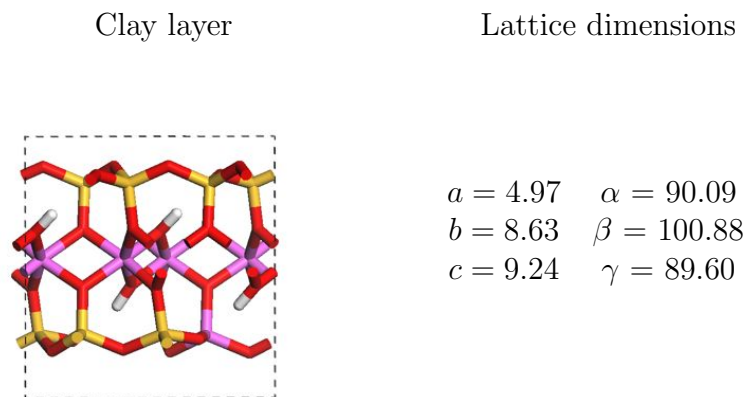
Figure 4.11: Unit cell of the clay layer (without any interlayer species) after geometry optimisation where the whole cell and contents have been allowed to relax within the norm-conserving pseudopotential approximation. Lengths are in $\mathring{A}$ and angles in degrees.

the imaginary mode of the product model shows an oscillation of the alkane in the z-direction pivoted at one end, with no feasible interaction with the local environment. As this imaginary vibrational mode does not indicate a change of configuration, it is more an indication of a mechanical instability in the system rather than a transition state. See Figure 4.12 for a static visualisation of these modes.

An analysis of other vibrational modes shows agreement with both experimental [140] and computational results [93], [141]: $O - H$ libration mode at 930cm^{-1}, $Si - O$ modes at 1100cm^{-1} and 1104cm^{-1} and $O - H$ stretching at 3644cm^{-1} and 3663cm^{-1} involving the central-cell $O - H$. This indicates that the results concerning the imaginary vibrational modes have equal validity and that the distortion caused by the norm-conserving PP has had a minimal effect on vibrational frequencies.

Table 4.4 shows the effect on the bond distances between the aluminiums of using norm-conserving PP, which provides evidence that the distortion in the clay layer in the norm-conserving PP approximation is responsible for the bond length disparities. Comparing the relaxed lattice, ultrasoft models and norm-conserving, Clay layer-2 model, there is a 6% difference in bond length which could be due to the imposed lattice constraint.
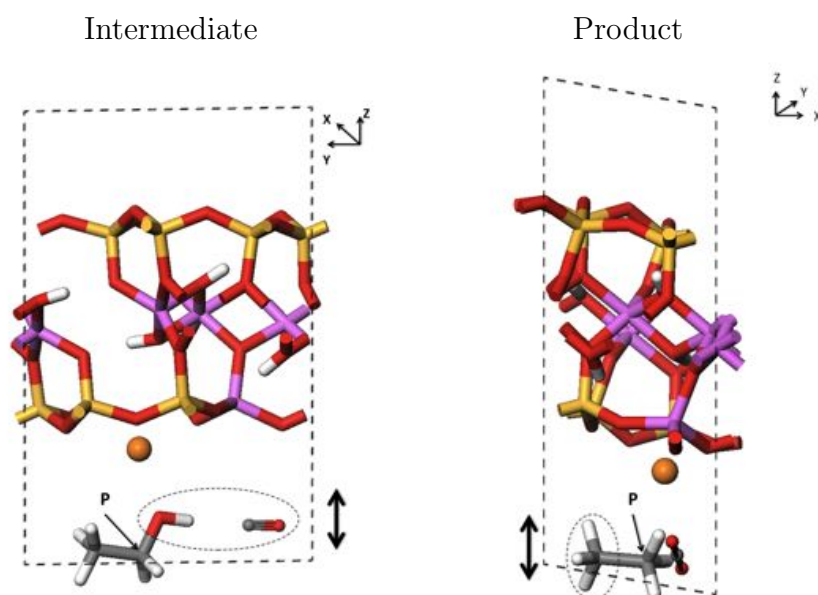
Figure 4.12: Schematic of the imaginary vibrational modes of the intermediate and the product. The area encircled by the dashed line indicates the atoms involved in the vibration. The double-headed arrow indicates the direction of vibration and the point labelled P represents the intersection of the pivotal axis with the organic molecule. In the intermediate this is the x-axis and in the product, the z-axis.

	Al-1 to Al-2 ($\mathring{A}$)	
Model	ultrasoft	norm-conserving
Reactant	3.066	3.925
Intermediate	3.070	3.926
Product	3.070	3.919
Clay layer-1	-	3.993
Clay layer-2	-	2.877

Table 4.4: Distances between the Al's marked on Figure 4.10. Clay layer-1 refers to the clay only layer without lattice relaxation and Clay layer-2 to the clay only layer with lattice relaxation.

The clay mineral models used here are anisotropic with only C-1 symmetry, hence two paths through the Brillouin zone were chosen to compare dispersion curves through the models, see Figure 4.13 for details of the paths and Figures 4.14 and 4.15 for the dispersion curves.

The short path dispersions shown in Figure 4.14 for all four models share a similar feature between [0,0,0] and [0,0,0.5], which is strong evidence of the effect of the same geometry in all four models, possibly the distortion creating an instability in the clay layer. This could be proved by running a DFPT calculation on the distortion-free, clay-only layer. The two imaginary frequencies of the transition state and the product are distinct and are representing a phenomenon that is not shared by the clay layer and the reactant models. If this is evidence for the intermediate being a transition state, then the same must be said about the product system.

Evidence of the intermediate being a transition state and the product not, is provided in Figure 4.15, which shows the dispersion graphs for the longer path through the Brillouin zone shown in Figure 4.13. The intermediate has one distinct line of imaginary frequencies compared to the product which has three. The reactant and clay-only models do not have any imaginary frequencies, which indicates that there are no inherent system instabilities along that path. Therefore, the multiple imaginary frequencies of the product model indicate an instability in that system, whereas the single imaginary frequency seen in the intermediate model is indicative of a genuine transition state.

The lattice was not re-optimized at the same time as the contents because the optimised cell agreed with previous DFT calculations and experimental results (see Table 4.1). This inspired confidence that any intermediate found in a transition state search using these optimised models, would likewise accurately reflect experimental geometries. Although a distortion was created in the clay layer, the relative configurations of the interlayer guests remained the same on the PP substitution,

a (0,0,0); b (0,0.5,0.5); c (0,0,0.5)

a (0,0,0); b (0.5,0,0); c (0.5,0.5,0.5); d (0.25,0.5,0.5); e (0.25,0.5,-0.5);

f (0.25,-0.5,-0.5); g (-0.5,-0.5,-0.5); h (-0.25,0,-0.5; i (-0.5,0,-0.5);
j (-0.5,0,0.5);
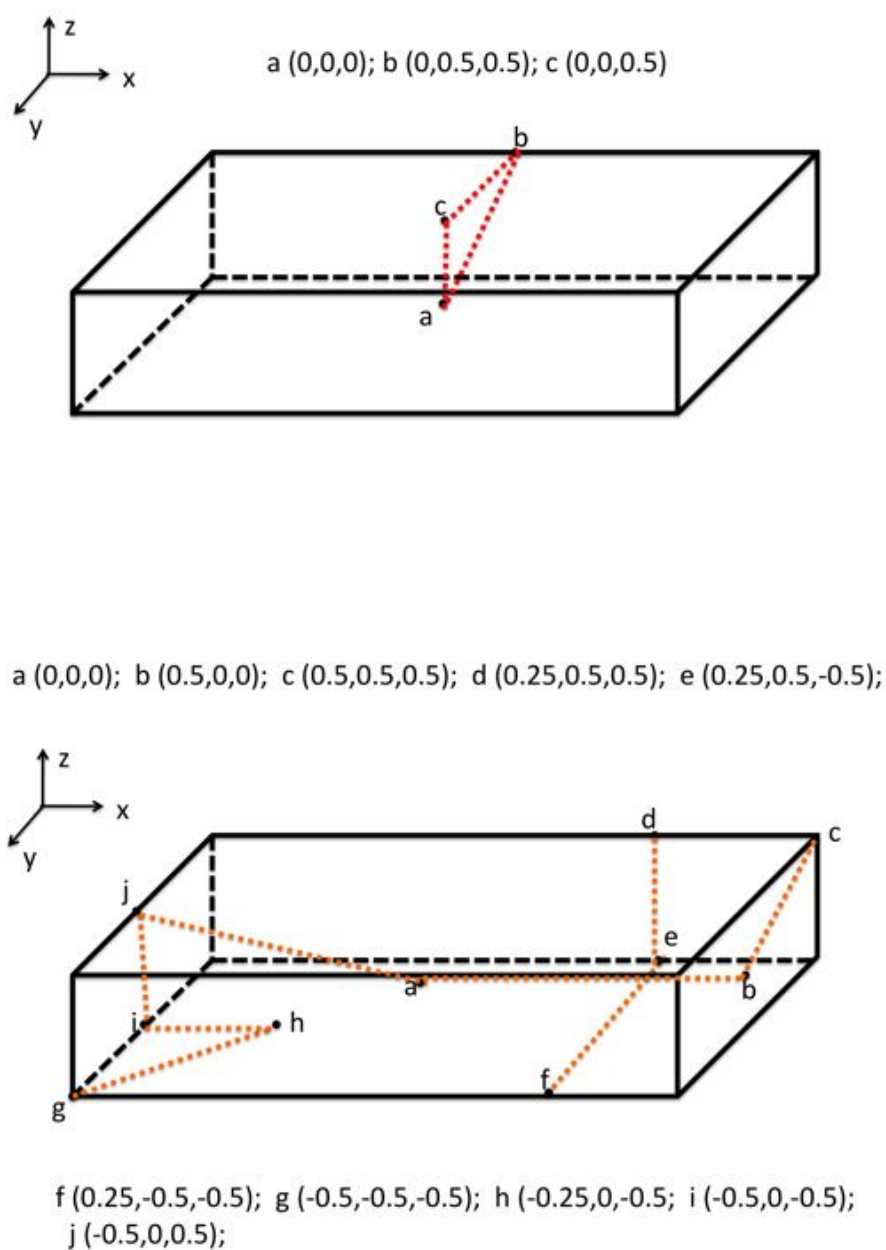
Figure 4.13: Two different paths through the Brillouin zone of the clay mineral
models. x, y, z are the reciprocal space axes.
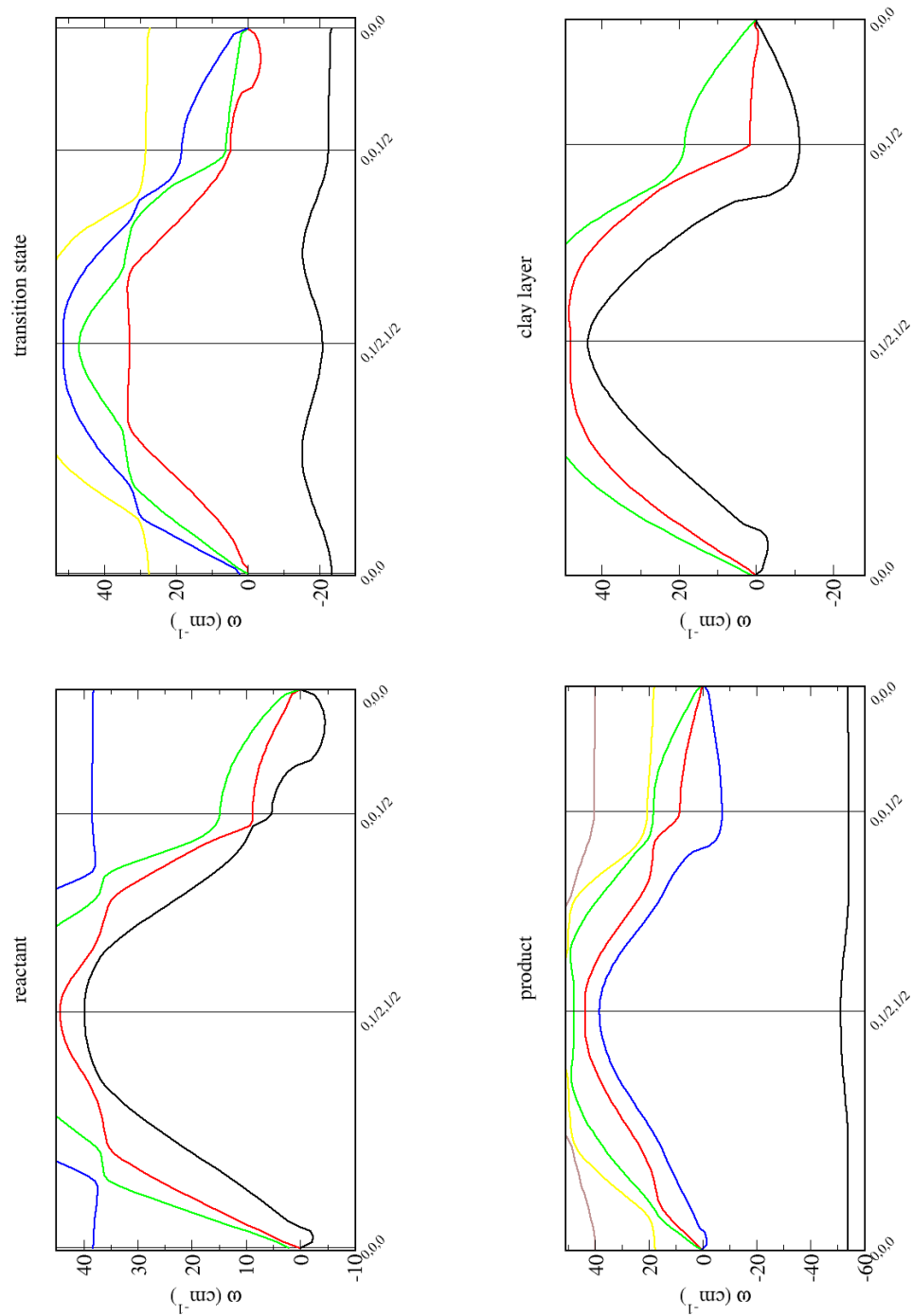
Figure 4.14: Dispersion curves following the short path shown in Figure 4.13. The negative part of the *y*-axis represents imaginary frequencies.
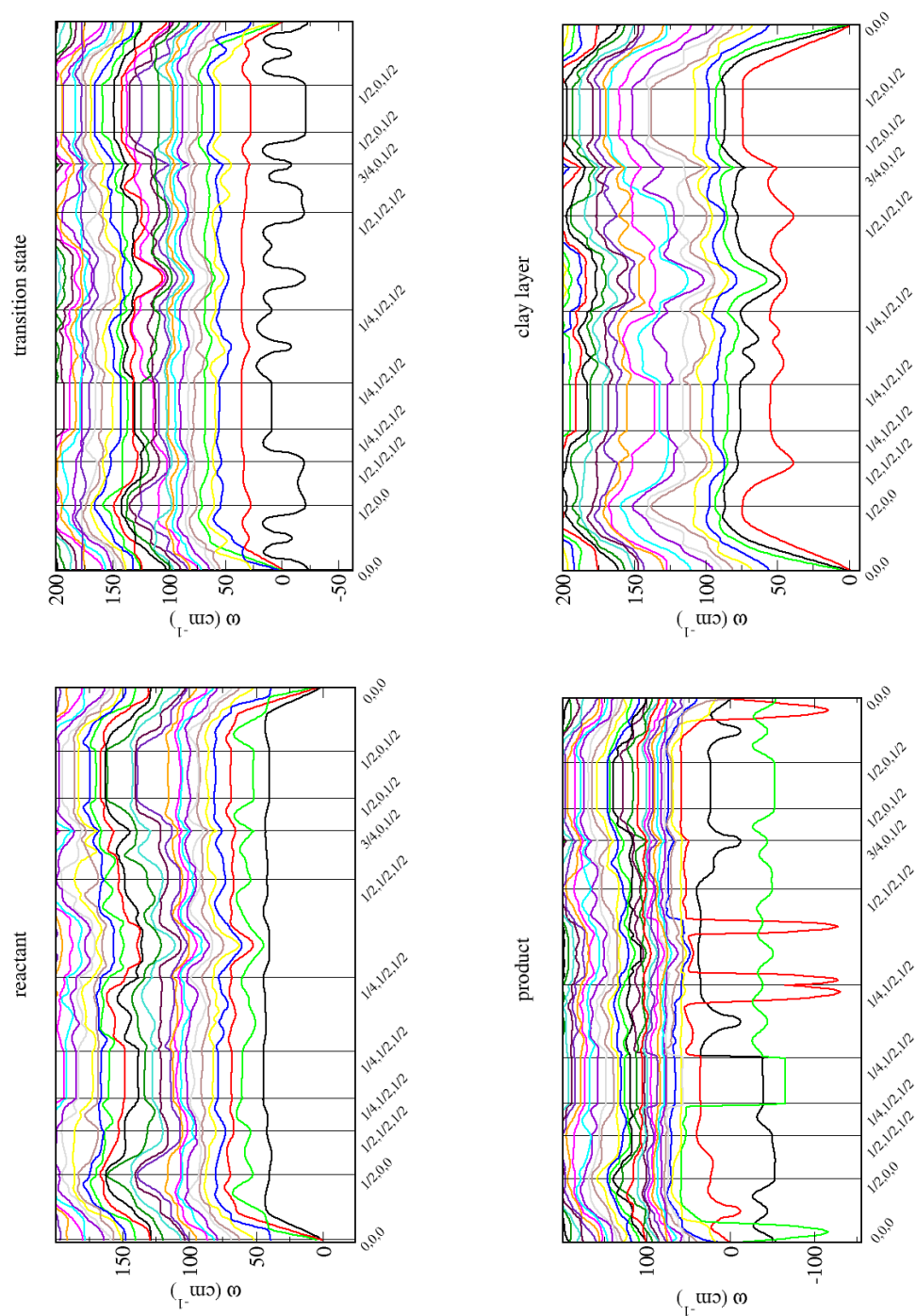
Figure 4.15: Dispersion curves following the long path shown in Figure 4.13. The negative part of the *y*-axis represents imaginary frequencies.

hence the change caused by the substitution did not detract from the main aim of this study. An examination of the Mulliken charges and Kohn Sham orbitals in the following section, will provide additional evidence to strengthen the conclusion reached in the previous paragraph.

4.4.3   Mulliken charges and Kohn-Sham orbitals

The Mulliken charges of the aluminiums and oxygens labelled in Figure 4.10 within the clay layers (see Table 4.5) show that, in the norm-conserving PP calculations, Al1 and Al2 are allocated a higher charge than in the ultrasoft calculations whereas Al3 is between 1.86 and 1.88 for both approximations for the reactant, intermediate and product. This shows that the tetrahedral sheet aluminium (Al3) has the same charge as the octahedral sheet aluminiums when the lattice has not been allowed to relax, however, when it is able to relax (model C-2) the tetrahedral sheet aluminium has a charge higher than Al1 and Al2 by 0.1e which is the same as the difference between these aluminiums within the ultrasoft approximation. The same trend in the clay-only layers, C-1 and C-2 where sodium is absent is seen in both scenarios which implies that, in spite of the lattice restraint, the absence of sodium results in a higher charge on Al3 due to the decrease in electron density. Therefore, the lattice restraint has had no effect on the mechanism of electron donation to the clay layer.

An examination of the charges on the oxygens shows that within the norm-conserving PP approximation, they range from -1.18 to -1.20e for the reactant, intermediate and product models whereas within the ultrasoft approximation they range from -1.12 to -1.18e. When the clay-only layer is allowed to relax (C-2), the charges on the oxygens within the octahedral sheet both become -1.15e and the oxygen closest to the tetrahedral aluminium becomes -1.09e. This less negative charge compared to that of O3 in the reactant (-1.19e), intermediate (-1.20e) and product (-1.20e) models appears to be due to the absence of sodium — no electron donation and hence the consequent reduction in electron density. The clay-only layer which was not allowed to relax (C-1) shows a charge of -1.16e on O3

Model	Ultrasofts				Norm-conserving				Ultrasofts			Norm-conserving		
	Al1	Al2	Al3	Na	Al1	Al2	Al3	Na	O1	O2	O3	O1	O2	O3
R	1.79	1.77	1.88	1.41	1.89	1.89	1.87	1.45	−1.12	−1.14	−1.18	−1.18	−1.19	−1.19
I	1.79	1.78	1.88	1.27	1.89	1.89	1.86	1.39	−1.12	−1.14	−1.18	−1.18	−1.19	−1.20
P	1.79	1.78	1.88	1.45	1.89	1.89	1.86	1.56	−1.12	−1.14	−1.18	−1.18	−1.20	−1.20
C-1	-	-	-	-	1.92	1.93	2.02	-	-	-	-	−1.13	−1.15	−1.16
C-2	-	-	-	-	1.87	1.88	1.98	-	-	-	-	−1.15	−1.15	−1.09

Table 4.5: Mulliken charges of the atoms marked on Figure 4.10 within the two pseudopotential approximations. Where R is Reactant, I is Intermediate, P is Product, C-1 refers to the clay only layer without lattice relaxation and C-2 to the clay only layer with lattice relaxation.

even in the absence of sodium, and could have assumed some of the negative charge from O1 which has a charge of $-1.13e$. The charges on the sodium within both PP approximations show different values but the same trend — a decrease from the reactant to intermediate then an increase to the product. The higher charges of the oxygens for C-1 and C-2 in the norm-conserving models than those of the oxygens in both PP approximations for the reactant, intermediate and product models add further evidence to the assertion that sodium is the source of electron donation.
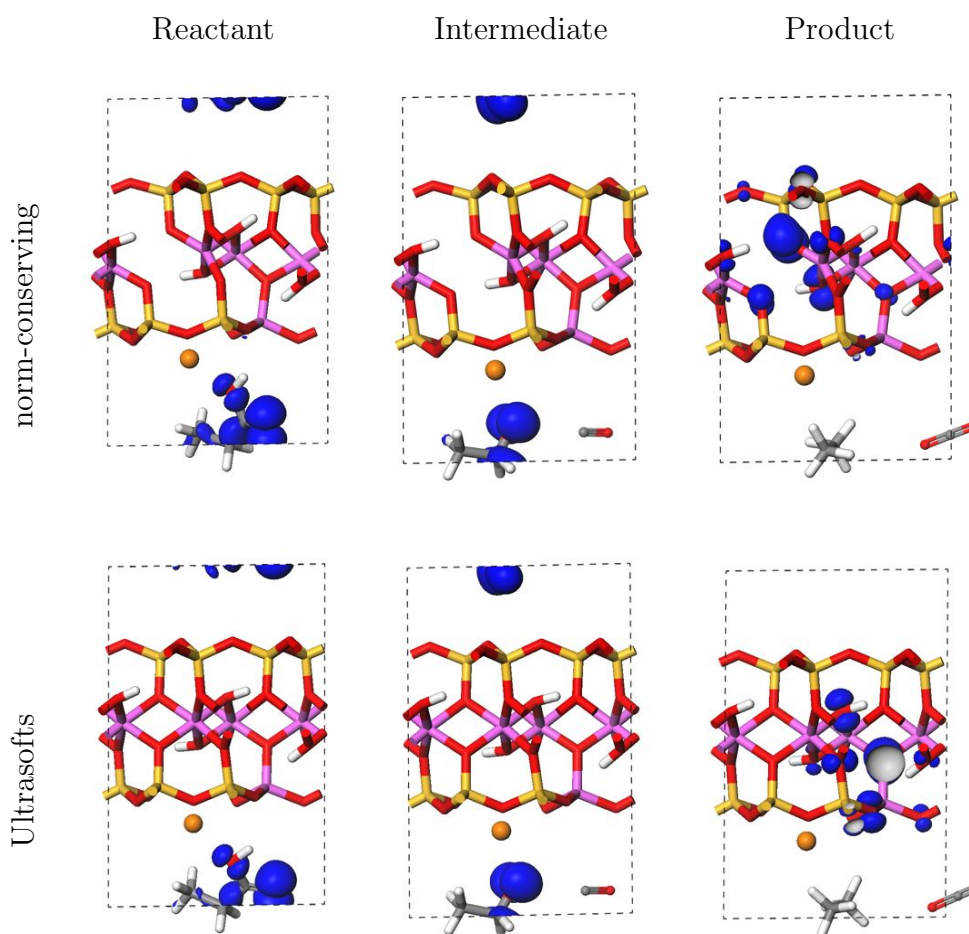
Figure 4.16: Fermi-level orbitals shown in blue where the upper row models use the norm-conserving pseudopotentials and the lower row the ultrasofts.

These Mulliken charges show that the two approximations have resulted in different charge distributions within the clay layers which suggests that where Fermi level orbitals exist within this layer, their distribution may differ depending on the

PP approximation. This is indeed the case in the product model (see Figure 4.16) where there is clay layer involvement of the Fermi level orbitals. The two PP approximations display different Fermi level orbital distributions particularly around the aluminium and oxygen atoms discussed above. However, to what extent have the Mulliken charges and the Fermi level orbitals of the interlayer species been affected by the clay layer distortion?

The Mulliken charges [46] of the reactant atoms (Figure 4.17) show that it has been allocated a relative charge of $-0.31e$ and $-0.30e$ in the norm-conserving and ultrasoft approximations. An examination of the highest occupied molecular orbitals (HOMO) or Fermi level orbitals (Figure 4.16) shows that the electrons most likely to react are those on the fatty acid in both PP cases.

The Mulliken charges on the ethanol of the intermediate model give its overall relative charge of $-0.22e$ and $-0.17e$ in the norm-conserving and ultrasoft approximations. A closer examination of the charges of the oxygen and hydrogen atoms of the hydroxyl bond shows a difference of $0.01e$ between the two approximations and the Fermi-level orbitals in both cases are situated on the ethanol, including this bond. This is consistent with the analysis of the imaginary vibrational mode which showed a joint vibration between the hydroxyl bond of the ethanol and the carbon monoxide and hence the supposition that an application of energy would most probably cause the Fermi level electrons to react, decreasing the overall energy of the system by interacting with CO to form the product.

The overall Mulliken charge on the alkane in the product model is $-0.34e$ and $-0.30e$ in the norm-conserving and ultrasoft approximations. This slightly larger negative charge on the alkane in the norm-conserving approximation together with the positive charge of $1.56e$ on the sodium could be creating a dipole interaction. This dipole may be responsible for the imaginary frequency of the product and those seen in the product's dispersion curves, due to the creation of an instability in the bulk system. It seems coincidental that the imaginary frequency of the product
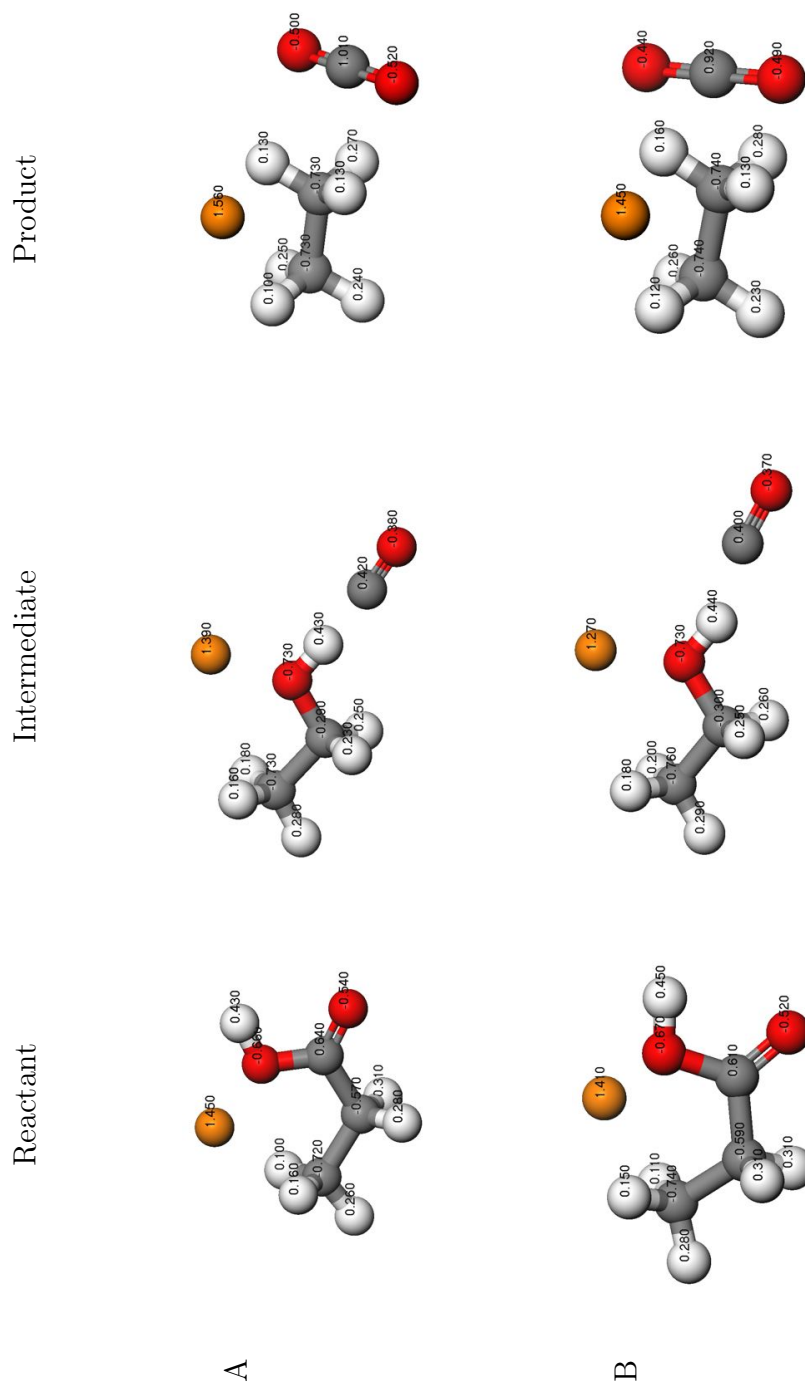
Figure 4.17: Mulliken charges on the interlayer species where set A is with norm-conserving pseudopotentials and B with ultrasofts. For display purposes, the relative positions of the molecules to each other are scaled, see Figure 4.10 for the accurate representation of relative geometries.

model, at the commensurate point, displays a vibration towards the sodium and the distortion in the clay layer. Could it be that the imposed lattice constraints *and* the position of the alkane within the interlayer, have conspired to produce the imaginary frequency of the product? One way to test this would be to swap the positions of the alkane and CO_2, re-optimise and redo the DFPT calculations.

The Fermi-level orbitals in both approximations show dissipation within the clay layer only, but differ in their distributions as commented on in the previous paragraphs. There are no Fermi-level orbitals in either PP approximation on the alkane, which is evidence that this configuration is relatively stable and is not in transition. Thus, the concluding assertions are that the imaginary frequency of the alkane model is a secondary effect of the imposed lattice constraint, i.e. it is not a genuine transition state and that the intermediate of ethanol plus CO_2 has been correctly identified as a genuine transition state.

4.5   Conclusion

Here, for the first time, are presented *ab initio* transition state search calculations with DFT methods to probe potential reaction pathways in decarboxylation reactions in smectite clay minerals. Such reactions are believed to be responsible for crude oil formation under reservoir conditions [10] and are increasingly of interest in biomass-biofuel conversions [68].

Conceptually, low order layered organo-mineral structures are amongst the most difficult to accurately characterise with only limited information available from analytical methods. As such, computer simulation has become an essential adjunct to experiment to characterise the structure of such systems fully [60], [142]. The situation is even more challenging if reaction mechanisms are to be studied, the sheer complexity of a mineral matrix, organic material, water, and applied external conditions make the study of reaction mechanisms in such systems inherently difficult.

In this study some advances have been made in the application of computational methods to address this challenge.

In order to be able to address this topic on a meaningful computational time scale, lattice constraints were enforced on the PP switch. Changing PP could affect the lattice dimensions, but full relaxation is more computationally expensive than the relaxation of atomic positions only. For example, full cell relaxation including lattice parameters as well as atomic positions of one model, processed for one week across 64 nodes; relaxation of the atomic positions only for one model took 17 hours across 128 nodes and a DFPT computation of one model took two weeks to process across 64 nodes, all of which were processed by HECToR.

The lattice constraint was prompted by the structure of the unit cell. The decision regarding the constraints was justified, to a certain extent in the results. The molecular configuration of the intermediate was the same in both PP approximations. Also, forces were well converged and only two distinct imaginary frequencies were computed at the $\mathbf{q} = \mathbf{0}$ point, one each for the intermediate and product (excluding the small imaginary frequencies of the lattice translation). The assertion that the vacuum of the interlayers would protect the gallery guests from any effects of the constraints also appeared to be justified as the distortion due to these constraints appeared in the clay layers only.

The question of 'accuracy' of results is interesting, perhaps a more appropriate word is 'relevance'. In the context of this study, what is the relevance of the results? Comparisons between models ameliorates the computational inaccuracies, which may have been introduced by the imposed constraint. This argument has been used here to, in part, justify this constraint. And, as a result (or in spite) of this, a transition state has been found and identified. Within a computational environment, a new result has been obtained. However, the moment this is exposed to comparison with experiment, 'accuracy'/'relevance' transforms its meaning. Compared to Almon's and Johns' experiment, the simulated transition state does not

exist and hence could be said to be 'completely irrelevant'. So, there are two separate issues here, the computational aspect and the chemical and experimental. At this early stage of this type of investigation, is there any common ground between them?

This pioneering study began with basic models, which by virtue of their simplicity are unrepresentative of experimental environments. Such simplicity allows the artefactual results (e.g. the clay-layer distortion due to constrained lattice parameters and possibly the imaginary frequency of the product) to be distinct from the genuine results (e.g. the transition state identified by its imaginary eigenfrequency and occupied Fermi level electrons). The results are relevant in two ways, firstly they inform future modelling practice, and secondly they suggest the revisions required to increase the complexity of the models and hence increase their experimental relevance. For example, with regard to modelling practice, one development would be to increase the number of q points in the coarse grid in the z-direction. An example of making the models more complex would be for the transition state to be used as a new Reactant or Product and a transition state search re-run.

In summary, this study is evolving to capture the fundamental elements of modelling catalysis in complex mineral systems. Through using an *ab initio* approach, no conditions or assumptions are imposed *a priori* on the system of interest. Through the chosen DFT methodology, information regarding the electronic structure of the system at potentially critical stages along the reaction coordinate has been obtained and, the spectroscopic data even at this early modelling stage, may aid in the interpretation of experimental analytical data.

Such an approach presents a powerful tool to elucidate reaction mechanisms in complex systems. The key to success lies in marrying computational efficiency and methodology, together with experimental conditions and environments, which this study has achieved within the limitations previously discussed.

Although there are several paths this study could take, for now it has reached

a conclusion. The next step in this foray into the electronic structure modelling of clay minerals, was prompted by a question asked at a Clay-Mineral Conference. The point of query was the mechanism of the reduction of iron within clay-minerals and it is this investigation that comprises the following chapter.

5

Ab initio Reduction in Ferruginous Smectite

5.1 Synopsis

This chapter addresses the question of reduction within iron-bearing clay minerals. It opens with a description of the motivation and background for the study, proceeding to examine how reduction should be optimally modelled and the modelling considerations involved. It progresses by presenting the range of models; computations and the results followed by analyses of the Mulliken charges and Fermi level occupancies. While these results produced a firm conclusion of reduction in the octahedral sheet, a further, small adjunct study was required to cultivate a definitive answer concerning reduction in the tetrahedral sheet. Finally, this chapter draws to a close with an overall conclusion discussing reduction in the context of the models

and methods used. However, before the story ends, it begins with the Introduction.

5.2   Introduction

In December 2009 at the FuturoClays: Clay Minerals Group Annual Meeting, this question was raised: 'Could DFT answer the question where and how does reduction in nontronite occur? Is it predominantly at edge sites or at the basal surfaces?' This gauntlet could not be ignored and the attempt to answer these questions forms the investigation presented in this chapter.

Nontronite is a dioctahedral 2:1 ferruginous, smectite clay, similar to pyrophillite described in the previous chapters but with the substitution of Fe^{3+} and/or Mg^{2+} in the octahedral sheet and, more rarely, Fe^{3+} in the tetrahedral sheet. The categories of nontronite depend on their composition for instance, both Fe^{3+} and Mg^{2+} substitution for Al^{3+} cations in the octahedral sheet together with Al^{3+} present in the tetrahedral sheet constitute Garfield nontronites. The smectites with solely Fe^{3+} in the ocatahedral sheet and about 20% [143] substitution in the tetrahedral sheet constitute the NG-1 nontronites. This latter type together with ideal nontronite — an all-Fe^{3+} octahedra and an Al^{3+} substitution in the tetrahedra — are the focus of this investigation into reduction.

The state of oxidation versus reduction in phyllosilicate clays determines many of the chemical and physical properties of clays, such as: specific surface area, cation exchange capacity, magnetic exchange interactions [144], mineral availability, the degree of swelling in water, reactivity with organic chemicals and pesticides and the potential for mineral dissolution and transformation [145]. This direct effect on the smectite layers has consequences for the local environment of the clay as clay is one of the key ingredients of soil. For example, a change in specific surface area of the smectite sheets causes a collapse in the clay layers, reducing the interlayer spacing and trapping some of the interlayer cations making them less available for uptake by

plants. The layer collapse causes an increase in the thickness and size of the smectite particles which determines the settling properties of clays, their permeability to water and hydraulic conductivity [146]. Studies in to the bacterial reduction of smectites [145] have shown that the reaction of the clay with organic chemicals and pesticides increases insofar as the reduced smectites alter and degrade these chemicals to a greater degree than either non-reduced (i.e. oxidized) or reduced re-oxidized smectites. These examples illustrate how the reduction of ferruginous smectites has industrial, environmental and agricultural implications and although these extensive changes have been studied experimentally (and reviewed in reference [147]) to date, the exact mechanism of reduction in ferruginous smectites has not been studied at the level of molecular structure [148].

An element is reduced by gaining electrons, therefore, if an environment is created where electrons are available, an element will be reduced if this is the optimal electronic structure response. In this study, reduction is presented in the form of a series of models with an increasing number of added sodium atoms or charge, which act as the reducing agents. The justification for the modelling method is described in Section 5.3.2, where various artefacts of the models due to their constituents and structure are considered.

This chapter proceeds with a Method section describing the models and the process of reduction, followed by the Results and an in-depth Discussion of the findings, and finally a Conclusion where the investigation is summarised and implications are drawn for future studies. For the purposes of reducing tediousness of language, in the remainder of this chapter, the octahedral sheet will be known as 'OS' and the tetrahedral sheet 'TS'.

5.3   Methods and Modelling Considerations

Chemical reduction is the acquisition of electrons by one atom or molecule which computationally can be achieved, within the current *ab initio* methods, in two ways either by the inclusion of a source of electrons in the simulation, such as an increasing number of sodium atoms, or by the addition of charge to the input file. Both methods have been chosen for investigation, in order to determine if one is more suitable than the other to study this type of reaction. The precedent for this was set in the first results chapter where the conclusion was that the presence of sodium was enabling electron transfer from the organic guest molecule to the clay surface and therefore a necessary inclusion for the investigation of decarboxylation. This investigation is the first step in examining reduction within clay minerals, so the unphysical step of excluding interlayer guest molecules has been taken. Even without this complicating factor, there are many other considerations such as the effect of adding an increasing number of sodium atoms to a unit cell, which potentially introduces Coulombic effects between their periodic images in the x-y plane and dipole effects between Na ions and an uncharged basal surface in the z-direction. The charge-only models could remove these potential problems but may well introduce a different one, that of the change in the density of the background charge as the number of unit cells are increased, as will be explained shortly. A further modelling consideration for these iron-containing simulations, is the effect of spin and the interactions between the unpaired electrons on different Fe atoms and how this affects the process of reduction, if at all. The methods subsequently described are attempts to separate out these modelling effects in order to answer the original question with confidence.

5.3.1   Models

The pyrophillite models from the first results chapter are the template models for this chapter. The interlayer guests and Na were removed and two types of nontronite were made, Ideal and NG-1. Ideal has an all-Fe OS plus a substitution of Al^{3+}

for an Si^{4+} in the TS. NG-1 is the same as Ideal but with an Fe^{3+} substitution in the TS, see Figure 5.1. Both types have an overall layer charge of $-1e$ due to the substitutions in the TSs. The motivation for using two types of nontronite which differ only in their TS, is to gauge the relative effects of reduction in both sheets, for example, would reduction be less pronounced in the OS when there is Fe^{3+} in the TS?

Ideal   NG-1
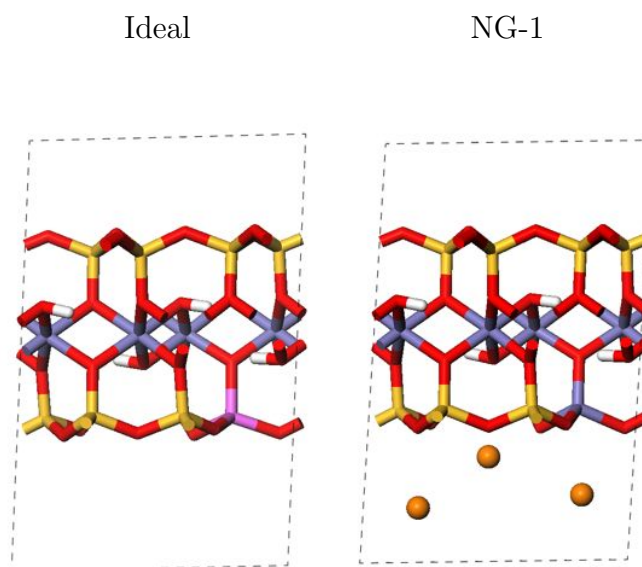
Figure 5.1: On the left is a single unit cell of Ideal (id0-c1) containing no sodiums; on the right is a single unit cell of NG-1 (ng3-c1) containing 3 sodiums. The following colour scheme is used throughout this chapter: Oxygen: red; hydrogen: white; aluminium: pink; silicon: yellow; iron: blue; sodium: orange. The dashed line is the periodic boundary of a unit cell.

Convergence of template models

The introduction of a new pseudopotential in the guise of Fe species necessitated re-testing of the cut-off energy. As described in previous chapters the cut-off energy convergence test involved making two identical models of nontronite with the inclusion of a Na atom in each with slightly different coordinates. A range of single point energy calculations were performed from 450 to 1000eV cut-off energy. The energy differences between the two models converged to 4meV at a cut-off of 550eV hence this was used as the cut-off energy for this study. Ideal and NG-1 — both without

Na were then allowed to fully relax, including atomic positions and lattice parameters using the following criteria: electronic energy tolerance: $\leq 10^{-6}$ eV; geometry optimisation:- energy change per ion: $dE/\text{ion} \leq 10^{-5}$eV; maximum force: $|F|\text{max} \leq 0.04$ eV/$\mathring{A}$; change in distance: $|dR| \leq 0.001\mathring{A}$; external isotropic pressure of 0.05GPa. As previously described, the generalized gradient approximation (GGA) density functional, specifically Perdew, Burke and Ernzerhof (PBE) [21] was used, as this describes molecular bonding to a greater accuracy than does the local density approximation (LDA). PBE ultrasoft pseudopotentials [29] were used as these are consistent with the PBE exchange functional. The pseudopotential for Fe was PBE with non-linear core corrections, a type of pseudopotential described in Chapter 2, Section 2.3 [28]. The (geometry) optimizer was Broyden-Fletcher-Goldfarb-Shanno (BFGS) and the electronic method was ensemble density functional theory (EDFT) [41] although an attempt to use density mixing as the electronic minimizer was made and is described in section 5.3.2.

The results of this relaxation can be seen in Table 5.1 together with the parameters of the template cell. The similarity of the results suggested that repeating the k-point test was unnecessary so the previously optimised 2 k-points for the Brillouin zone integration were used throughout this study.

Model	Lattice length			Angle		
	a	b	c	α	β	γ
Ideal	5.20	9.09	9.82	93.80	101.73	89.65
NG-1	5.21	9.04	9.86	94.29	101.86	89.64
Template	5.22	9.07	9.73	90.87	100.00	89.65

Table 5.1: Lattice parameters of a unit cell of smectite. Lengths are in $\mathring{A}$ and angles in degrees.

Post relaxation, the c-length was increased to 14.5$\mathring{A}$ to accommodate the inclusion of sodium atoms. These cell dimensions were then fixed for the remainder of this study.

Before proceeding with the computational details, there follows a description of

the particular properties of these models and the potential artefacts produced in the results. The question of how to represent the conditions for reduction based on the template models, Ideal and NG-1 and the nature of the reducing agent are considered, followed by a description and justification of the models used for this study.

5.3.2 Modelling considerations — Electrostatic interactions

Electrostatic interactions due to electron charge density and point charges in periodic lattices have been examined extensively since the beginning of the twentieth century with the resulting creation of an increasingly complex model of interacting elements. In this section, the fundamental electrostatic relations will be examined and considered in the context of the reduction models.

Charge density

In 1928, Lennard-Jones [149] illustrated how to calculate the electrostatic potential outside a crystal surface by assuming that a variation in charge density (including that from electrons and nuclei) across the surface could be simplified into an average density across the surface $\sigma(z)$ [14] plus a density dependent on the point in the surface $\delta n(\mathbf{r})$, as shown in Figure 5.2. The calculations showed that the variations in planar density, $\delta n(\mathbf{r})$ gave rise to potentials that decay exponentially with $|z|$ — see the original work for details, whereas the average charge density, $\sigma(z)$, gave rise to potentials which had long-ranging effects. The following sections examine these long-range interactions in detail.

Multipole interactions

The longest range interaction is due to the Coulomb force between charges, whose magnitude in a vacuum is given by :
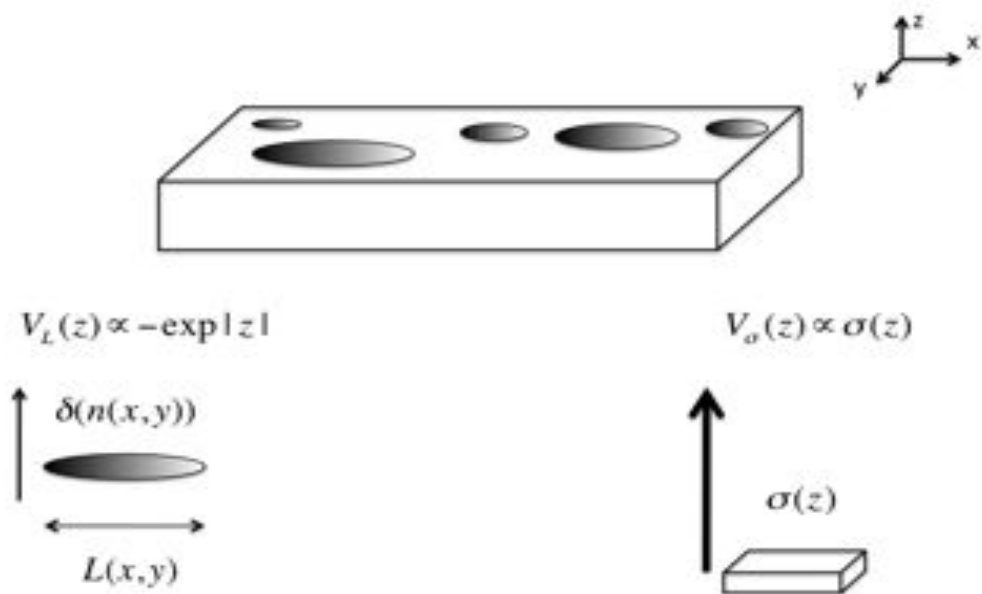
Figure 5.2: Decay length of the potential due to the variation in local density (LHS) is proportional to L, the length over which $\delta n(x, y)$ varies, whereas that due to the average planar density (RHS) is long-ranging and has decay length $\frac{1}{z^N}$ where N is the multipole factor e.g. Coulomb potential, $N = 1$.

$$F_c = \frac{1}{4\pi\varepsilon_0} \frac{q_1 q_2}{r^2} \quad , \tag{5.1}$$

where ε_0 is the permittivity constant of free space, q_1, q_2 are the charges and r is the separation between them. This relation was derived from experimental data and observation, somewhat in the manner of an ansatz. The electrostatic potential, $V(r)$ of this interaction decreases as $1/r$ and is the dominant artefact potential in periodic cell calculations on systems containing charged species. For example, consider a system containing a charged defect modelled with periodic boundary conditions (as opposed to an isolated cluster model), the charge on the defect will interact with its periodic images. In 'reality' i.e. in the physical system, the defect will probably be an isolated effect in terms of atomistic simulation, therefore, the charge defect interaction is artificial, affecting the charge density resulting in errors in the total energy and forces on the atoms. A careful consideration of the factors affecting convergence and hence reliability of results in defect vacancies in silicon [150], concluded that even the symmetry of the initial cell must be carefully considered. Clearly, the Coulomb interaction is potentially very problematic!

One method of determining the strength of the Coulomb interaction between charged species is by consideration of the Madelung energy (E_m), i.e. the Coulomb energy per cell of an array with charged defects: [151], [152]

$$E_m = -\frac{\alpha Q^2}{2\varepsilon L} \quad , \tag{5.2}$$

where Q is the charge on the unit cell, L is the lattice parameter of the periodic array (occupying a cubic volume) i.e. the distance between the charges and α is the Madelung constant whose value for simple cubic, body centred cubic and face centred cubic arrays can be read from a table [152]. Here, ε represents the dielectric permittivity of the background neutralising charge, or jellium [20] which is applied to charged cells to enforce neutrality. Charged periodic cells would lead to infinitely charged systems and divergent Coulomb energies.

Within this study, the charged 'defects' are simply sodium atoms that become charged due to the donation of electrons to the clay layer. They have long-range interactions in the x-y plane across cell boundaries. Therefore, by increasing the distance, L between periodic images, the artificial interaction should decrease, albeit slowly. This could be achieved by using a range (in the x-y plane) of supercell sizes to determine the optimum cell size. The z-direction is less of a consideration for this interaction because the slab layer screens the sodium atoms from each other in this direction. Equation 5.2 could be used to determine the optimum cell size to minimise the charged particle interaction energy, E_m, by plotting $\frac{1}{L}$ and total energy (E_{tot}) and extrapolating to where $E_{\text{tot}} = 0$. However, as reduction is effected by adding an increasing number of sodium atoms or charge, the optimum cell size for a model set containing one sodium atom will not be the same as that containing three. Therefore, the idea of using a single size model to simulate reduction does not seem feasible.

The models in this study have two basal surfaces with varying charge density in the periodic plane due to the range of atoms comprising the clay layers, but as described previously, this will have no effect on the convergence of total energy with cell size as the z-length is larger than the length over which $\delta n(\mathbf{r})$ varies. One of the more significant effects on convergence will be from the difference in $\sigma(z)$ on the basal surfaces due to the substitution of Al^{3+} for Si^{4+} creating a dipole across the aperiodic cell boundary. This is the source of the second electrostatic interaction i.e. the dipole electric field across the cells in the aperiodic, z-direction as shown in Figure 5.3.

A dipole electric field is given by:

$$\mathbf{E}_{\text{dipole}} = \frac{1}{4\pi\varepsilon_0} \frac{\mathbf{p}}{R^3} \quad , \qquad (5.3)$$

where $\mathbf{p} = q\mathbf{d}$ is the dipole moment, (q is the charge and $\mathbf{d}$ the distance (d) and direction of the moment) and R is the distance from the dipole where $R >> d$. There
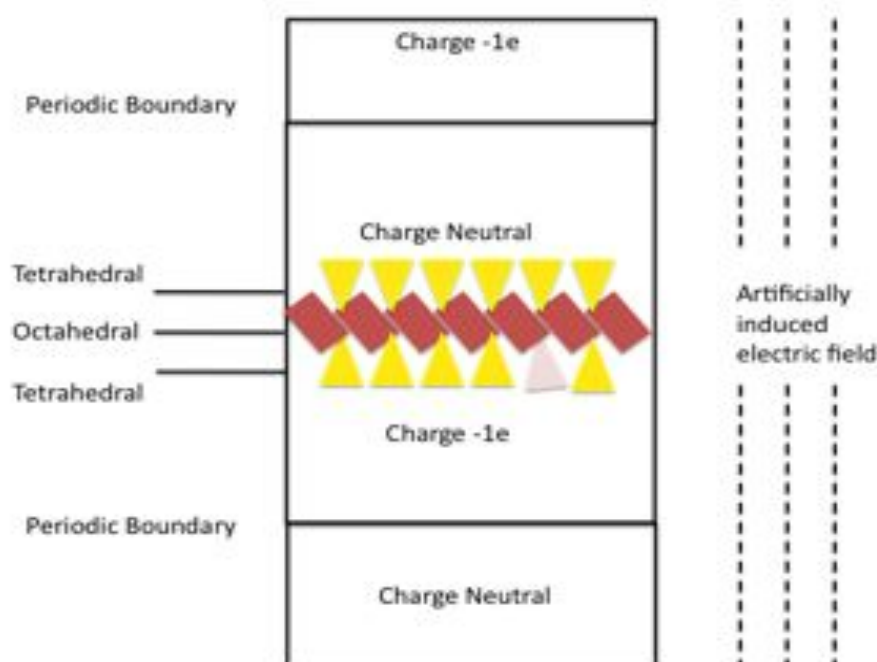
Figure 5.3: Schematic of the origins of an artificial electric field in the aperiodic direction, due to the substitution of an Al^{3+} or Fe^{3+} for Si^{4+} in the TS. The yellow triangles represent Si and the pink, Al.

will also be a dipolar effect arising from the relatively higher charged Na atoms which donate their electrons to the clay layer and the opposite TS. The dipole field is not a physical phenomenon as the clay layers are separated by water, organic molecules and cations. However, in simulated bulk, hence periodic systems, the dipole fields interact with all cell contents and with periodic images of themselves with the consequent introduction of an error in the true charge density. An illustration of the long-ranging interactions is shown in Figures 5.3 and 5.4

Although $\mathbf{E}_{\text{dipole}}$ decreases with $\frac{1}{R^3}$ or, in terms of lattice parameters, $\frac{1}{L^3}$ where the cell volume, $V_c \propto L^3$ and so dies quicker than the Coulomb electric field ($\frac{1}{R^2}$), it can, after cell-size convergence, result in supercells with a vacuum space (between slabs) twice that of the original model [153], which can become computationally expensive. For example, a short test of z-length versus total energy using single point energy (SPE) calculations showed no convergence even on a four-fold increase in c- length (results not shown here). One method of counteracting this effect is
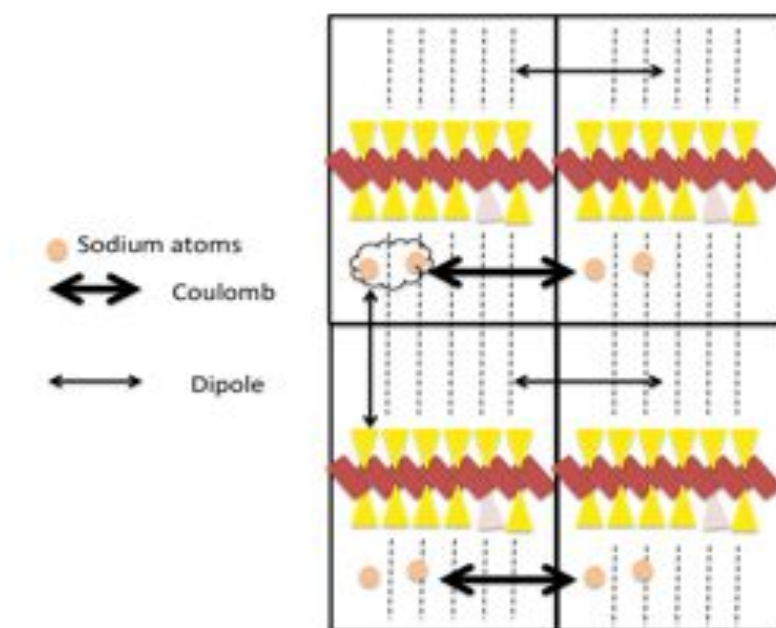
Figure 5.4: Schematic of some of the multipole interactions showing Coulomb interaction between periodic images of Na^+, dipole effect between Na^+ and the opposite basal surface and dipole-dipole interactions of the artificial electric field.

to use a Coulomb cut-off where, if 'slab-thickness' is taken to be the distance between zero charge densities on opposite surfaces, then using a supercell of twice this distance should result in convergence of energies and forces [153]. The tests on c-lengths referred to earlier make this an infeasible approach for this study as the computational efficiency is too low to achieve a sufficient body of results within the six months spent on this investigation.

Another method of counter-acting the electric field due to the difference in charges on the slab surfaces, is to introduce a planar dipole layer in the middle of the vacuum region [154], effectively cancelling the difference in charges across periodic boundaries. By introducing a compensating potential and an energy correction term [155] that compensates for an error in the energy on the introduction of an external field, the dipole moment of the slab is embedded in a periodic supercell. Unfortunately, this method is not available within CASTEP so the artificial interactions cannot be 'modelled out' in this way.

Makov and Payne [156], theorised a method of correcting for artificial multipole interactions in charged systems involving the formulation of an equation for the error in the total energy due to the Coulomb and dipole interactions, which can be subtracted *a posteriori* from calculations involving a charged, aperiodic, cubic system. This is given by:

$$E = E_0 - \frac{\alpha q^2}{2\varepsilon L} - \frac{2\pi qQ}{3L^3\varepsilon} + O(L^{-5}) \quad , \tag{5.4}$$

where E_0 is the electrostatic energy of the uncharged, periodic system, ε and Q are parameters representing properties of the periodic and aperiodic densities respectively. The second term is the Coulomb interaction, the third the dipole and the fourth the interaction of the compensating background jellium charge with cell contents and itself [20]. The jellium background is a monopole comprised of a compensating background charge per unit volume i.e. z_c/V. It interacts with the charge density of the cell and itself but has been shown to converge to $O(L^{-5})$ [156], although, changing the cell size will of course change the density of the background charge and hence its interactions with the environment and itself leading to an error term in the energy which may not have the same convergent property, $O(L^{-5})$. This could prove a way to converge the cell size, but, Makov and Payne applied it successfully to cubic systems and the reduction template models are not cubic. So the search for a suitable method to counteract the artificial interactions continues.

Schultz [157] treated the multipole interactions in an *a priori* manner — altering the potential rather than a post-calculated energy — by splitting the charge density in two parts, one which has no moments and one which represents all of the moments but which are localized in a supercell and hence the potentials are unable to overlap and interact in aperiodic directions. This is applicable to models containing vacuum rather than crystalline bulk systems because the vacuum space allows for a simpler interpretation of the multipole interactions compared to bulk systems where short range interactions dominate. In principle this sounds feasible

for the reduction models, but the dipole is constructed with a 1-D Gaussian in a jellium-free environment and hence is an infeasible method for implementation in the planewave code, CASTEP.

In another attempt to reduce the multipole interactions, Kantorovich [158] re-examined the work by Makov and Payne, extending it to include any Bravais lattice, not just cubic, by explicitly removing dipole-dipole interactions between cells. This was achieved by calculating the energy of interaction of dipoles within the same lattice and subtracting this from the total energy. The obvious difficulty here is the calculation of the energy of the dipole-dipole interaction as there would need to be a way of calculating the strength of the electric field, which is not implemented in CASTEP to date. Although, this could be done manually by taking the average potential across the x-y plane with varying z; the gradient of this potential then gives the electric field and hence a measure of its strength. In this study there are varying numbers of sodium atoms, which will affect the strength of the dipole interactions in the z-direction, hence multiple dipole strength calculations would be required.

Higher multipole interactions such as quadrupole-quadrupole decay as L^{-5} according to Makov and Payne [156] and hence have a negligible effect on systems as large as those studied here. Van der Waals interactions are comprised of three contributions, London dispersion forces where the movement of electrons causes a fluctuation of the charge density, inducing temporary dipole moments. The second force is the Keesom force which describes the attraction between molecules with permanent dipoles and the third is the Debye force describing the induction of a temporary dipole by a permanent dipole. The mathematical description of the energy of the van der Waals interaction (E_{vdw}) is given proportional to the sum of these terms i.e.

$$E_{vdw} \propto \frac{a}{R^6} + \frac{b}{R^8} + \frac{c}{R^{10}} \quad , \tag{5.5}$$

where a, b and c represent the collection of the multipole moments and associated constants and R is the distance between the multipoles.

To date, the calculation of well validated van der Waals forces is not available in CASTEP, so, although these forces exist in a physical clay system and are one of the important forces in producing the layered structure [4], the energy of these interactions (E_{vdw}) is not available to the results. However, their rate of decrease suggests they would not contribute significantly to total energy calculations.

A study into semiconductor point defect errors in supercell approximations, [159] showed Makov and Payne's correction method to be insufficient compared to the method of total potential realignment in real-space and finite scaling. However, this method involves parameter fitting and it is difficult to determine how this could be applied to the reduction models. The method of Freysoldt [160] shows the greatest potential for applicability to the reduction models, as it involves using 'a rigorous analysis of electrostatics in dielectric media' [160], accomplished by deriving exact expressions for the electrostatic interaction of periodic charged defects, in an *ab initio* way rather than fitting parameters. However, this is not currently functionalised in CASTEP and hence cannot be used for the reduction scenario, although it does 'propose a new correction scheme, which is easily implemented in existing codes' [160].

In theory, Kantorivich's approach, together with the method concerning Madelung energy for extrapolating an optimum distance to reduce Coulomb effects, could be used in equation 5.4, to produce a converged cell size, i.e. a cell with minimised artificial electrostatic interactions. But, what would the convergence criteria mean when, in order to allow reduction to occur, an increasing number of sodiums are added to a cell? An increase in the number of sodiums will increase the strength of the multipole interactions, so, the cell size would need re-converging to minimise the electrostatic interactions. But, by converging cell size with respect to energy, say, how can there be any certainty that the reduction effect being examined remains unaffected by the convergence criteria, that is, how can an accurate comparison of reduction effects be made on varying cell sizes? The following section describes the method and models used to try and overcome these potential problems, to investi-

gate reduction in a consistent way.

Model Sets
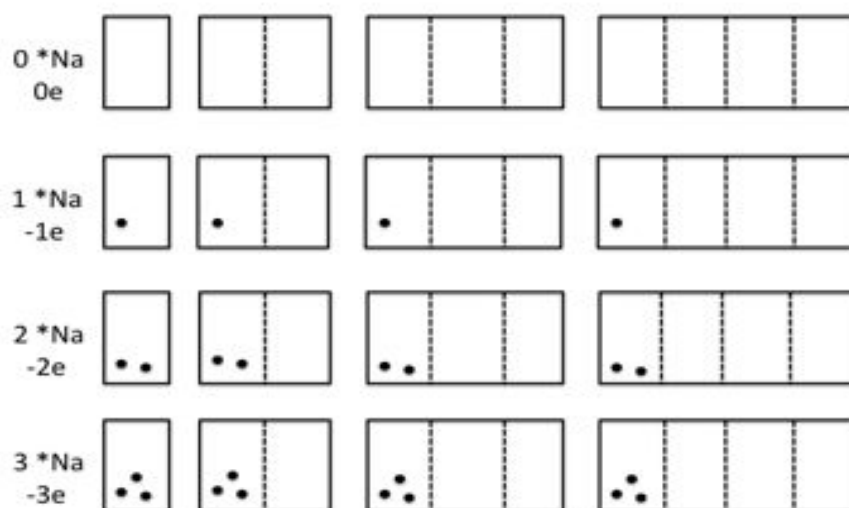
Figure 5.5: Schematic showing the model sets used in this study. Along the horizontal, the cell sizes increase to a maximum of 4 unit cells wide — the dashed line indicates a single unit cell and the black dots, sodium atoms located in the 'first' unit cell. The positions of the sodium atoms are illustrative only, they are identically positioned in all sets of models and are unrelaxed throughout the investigation. The added background charge is dispersed throughout the cells. Down the vertical, the number of added Na atoms or added charge increases. Both Ideal and NG-1 were investigated using both sodium and added charge scenarios resulting in 64 models in total.

The solution to this cyclical problem appeared to be in comparing models of the same size with an increasing number of sodiums and, separately, charge. This method produced sixty-four models to examine but suggested the means by which reduction could be identified with confidence as a physical phenomenon, from the many artificial, periodic interactions discussed at length in this section.

The Coulomb effect of Na on periodic images was tested by making supercells in the x-direction ranging from the original unit cell to four unit cells wide (supercells larger than this proved computationally time-consuming and produced results which

added nothing to the conclusions). Calculating the binding energy of these supercells determines the relationship between periodic images, for example, a Coulomb effect would result in a $\frac{1}{x}$ cell-length vs binding energy curve [152] whereas a non-periodic image relationship would produce a monotonic decrease in the binding energy with increasing supercell length.

The reduction effect was tested by adding an increasing number of Na atoms (0 to 3) to each unit cell in both Ideal and NG-1 model sets. Na $(1s^22s^22p^63s^1)$ acts as an electron donor due to the sole electron in the 3s shell; increasing the number of electrons within a unit cell represents an opportunity for an increasing degree of reduction within the cell. Comparisons of the Mulliken charges between sets of cells indicates the extent of reduction specific to each atomic species. An examination of Mulliken charges is valid when considering the relative changes in charges between model sets [52] and not absolute charges for the determination of, for example, the nature of chemical bonds [53]. A relative comparison of charge does not rely on the spread of the plane wave basis set as this will be the same in each model set as it is the ground state of the electronic structure under examination, whereas, identifying the nature of a chemical bond is determined by the localisation of electron density.

The effect of the presence of the Na atoms was tested by including a uniform background charge rather than the Na atoms themselves, where a charge of $-1e$ represented 1 Na atom and the charge addition ranged from 0e to $-3e$, mirroring the sodium models.

The Coulomb effect of the Na is tested in two ways, first by the increasing supercell size and second by comparison with no-sodium, charge-only models. The electrostatic, z-direction dipole interactions were also effectively cancelled out by using increasing supercells of the same c-length, that is, results could be compared across the rows where the number of Na or charge is constant.

Each of the sixty-four models underwent a single point energy calculation with

fixed atomic coordinates throughout, hence the position of each Na was the same in each Na-model and all of the Na atoms were placed in the same unit cell. This ensured that any Coulomb effect seen when increasing the cell sizes from one to four should be identifiable as all other relationships would remain constant.

Nomenclature

For shorthand the following labels are assigned to the models according to type: Ideal represents id; NG-1 represents ng; followed by the number of added sodium atoms or charge (this distinction will be made clear where applicable) ranging from 0 to 3, e.g. id0 means Ideal with no Na/charge, ng3 means NG-1 with 3 added Na/charge; followed by the size of the (super)cell ranging from 1 to 4 e.g. id0-c3 is a 3-unit cell supercell of Ideal with no Na/charge; ng2-c1 is a unit cell of NG-1 with 2 added Na/charge. This system will be used throughout the remainder of this chapter.

5.3.3 Computational details

Single Point Energy (SPE) Calculations

The SPE calculations were performed using cut-off energy 550eV and two k-points as previously described, with the GGA-PBE exchange functional and ultrasoft pseudopotential approximations as justified in preceding chapters. The configurations of the pseudopotentials are the same as those in Chapter 3, Table 3.1, and that of iron is $3d^64s^2$. The fine grid scale was 2.00, the electronic energy minimiser EDFT and electric energy tolerance $\leq 10^{-6}$eV.[1]

---

[1]An extra facility available in CASTEP was employed for all of the calculations over two unit cells in size, viz, the wave dumping option. The smallest unit cell contained forty atoms, the largest, one hundred and sixty-three and using EDFT for these larger models required more time for an SPE than was available in a single session on HECToR, hence it was necessary to restart the calculations from the previous deposit of wave functions.

Electronic Minimizers

The energy calculations were carried out using the electronic minimiser EDFT as it proved to be completely reliable for these models. The theory behind EDFT was described in Chapter 2 so will not be repeated here. An attempt at using the density mixing minimiser was made but proved to be totally unreliable, as described in the following section.

Density Mixing

Density Mixing (DM) is an electronic minimiser which, in theory, can reach the ground state up to ten times faster than EDFT and so would reduce the computational expense considerably. For the single point energy calculations of sixty-four models. Another advantage over EDFT is the facility to initialise spin which would control the magnetic state of the irons enabling the comparison of like-models, which might otherwise prove difficult due to the differences in energy resulting from whether a material is in a magnetic, ferrimagnetic or antiferromagnetic state.

The DM minimiser begins by calculating the initial electron density from the pseudoatomic orbitals, which allows for the initialisation of spin density; the Kohn-Sham wave functions are then calculated. Contrast this with EDFT where the wave functions are randomly initialised and the electron density is *then* calculated, thus not allowing for any spin density initialisation as the density is calculated from the randomly selected wave functions.

In the DM scheme, the local potential is calculated from the sum of the local eigenvalues for each energy band. If this leads to a 'low' potential, there will be a migration of electrons into this region, creating an area of high electron density, higher than befits the 'low' potential. The Hamiltonian is re-calculated resulting in a higher potential due to the higher electron density just mentioned, and so electrons migrate out of the higher potential region due to electron-electron Coulomb repulsion (V_H). The overall effect of this sloshing of electron density is charge sloshing

and is symptomatic of poor convergence. There is an analogous artefact of DM with spin sloshing. Both types of sloshing can be controlled by eight different parameters in total and what follows is a description of how some of them can be used to dampen oscillatory behaviour to induce convergence to the groundstate.

The Hartree term V_H describing the electron Coulomb interaction is proportional to the size of the reciprocal lattice vector i.e.

$$V_H \propto \frac{n(G)}{|G|^2} \quad , \tag{5.6}$$

where G is a reciprocal lattice vector and $n(G)$ is the electron density. As the real space simulation cell increases in size, the magnitude of the reciprocal space lattice vector decreases and hence any error in electron density is magnified by factor $1/|G|^2$ where $|G| << 1$, hence V_H has a greater effect on the Hamiltonian and the subsequent calculation of electron density with a consequent effect on charge and the degree of its sloshing. One way to dampen this effect is to increase the number of density histories[2] included in the mixing while at the same time reducing the change in the density due to the small Gs which is achieved in the manner of Kerker preconditioning [161], by scaling the Gs: $(|G|^2)/(|G|^2 + c^2)$ where c is a real constant. The value of c is a controllable parameter which affects the Kerker preconditioning of the residual density [162], which is an indicator of the reliability of convergence when it occurs, that is, if the norm of the density residual is $O(E^{-4})$ then convergence is reliable within the convergence criteria. This is a useful test when the energy oscillates and then appears to converge, as it removes any doubt that, on the next iteration, the energy would oscillate away from convergence.

The same scenario is repeated for spin and spin density and the method of control is the same as that above, via the spin parameter equivalent. The sixty-four models examined in this investigation varied in cell size (and therefore the size of $|G|$) and spin due to the number of Fe atoms. Where a single unit cell converged in its single

---

[2]This is one of the controllable parameters where previously iterated densities are mixed together to produce the next successive density.

point energy calculation, a supercell three times its size did not. After numerous attempts to achieve convergence by systematically changing all of the parameters, no consistency was found in the type of model, the parameters used and its likelihood of convergence. It could be posited that, as DM can be up to ten times faster computationally than EDFT, time should have been spent setting correct parameters for each model to achieve convergence, however, this variation in parameters is surely a cause of concern in that one cannot be certain that modelling artefacts — introduced by comparing different size models — skew the results. Therefore, the reliable EDFT method was chosen for all of the calculations in this chapter. This justification was deemed necessary given the potential difference in computational efficiency between the two minimisers.

Spin Polarisation

Initial trial calculations showed that spin polarisation had to be taken in to account as the difference between spin polarised and non-spin polarised calculations was 0.6eV, two orders of magnitude greater than the cut-off energy convergence tolerance of 0.004eV. The difference in energy between the two types of calculations arises from the energy of the exchange interaction as shown in Figure 5.6. In these models the spin polarised calculations are necessary probably due to the electrons in the d-orbitals of Fe. During the convergence of the electronic structure, electrons are 'placed' in an attempt to find the ground state for a particular arrangement of atoms. However, there is a difference in the exchange energy between two electrons with the same spin and two with opposite spins and further, the difference in the exchange energy of symmetric electrons depends on the distance between them. By requesting spin-polarised calculations, CASTEP performs two calculations based on the symmetry of the spins and produces the average of these. Unfortunately, spin-polarised calculations take twice as long as non-spin polarised.
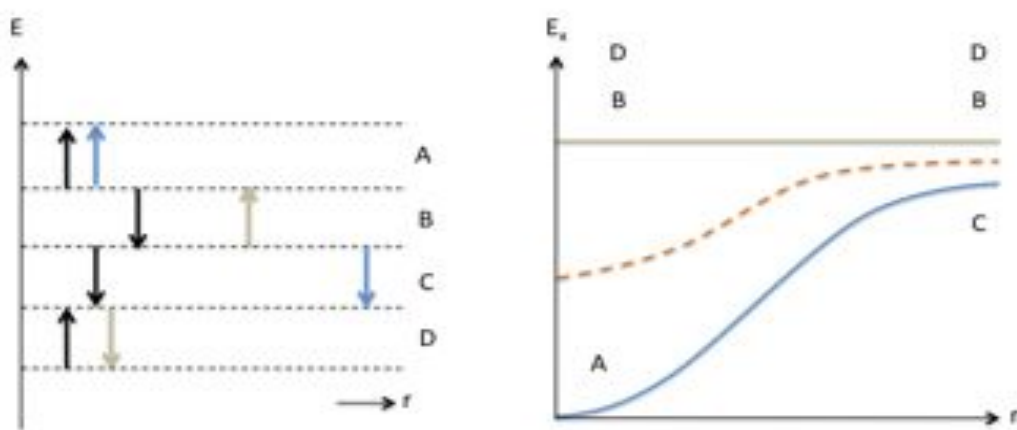
Figure 5.6: Schematic of the origins of the difference between spin and non-spin po-larised energy calculations. The LHS diagram shows energy levels (E) and distance between electrons (r) where the black arrows are the electrons in their energy levels and the coloured arrows the electrons allocated during an SCF cycle. Blue arrows are symmetric to the black and the brown arrows, antisymmetric. The labels A, B, C, D correspond to the labels shown on the RHS diagram where E_x is the exchange energy, r is distance between electrons, the blue line represents the energy curve for symmetrically allocated electrons and the brown, antisymmetrically allocated electrons, the orange dashed line is the average of these.

Binding Energy

Binding energy for the purpose of this work adopts a specific definition in that it describes the energy change on computational relaxation of the electronic structure in a supercell, compared to the sum of the computational energy of each unit cell of the supercell. The electrostatic effects, such as those between periodic images of sodium, are also included in the computations. Figure 5.7 shows a schematic explanation.
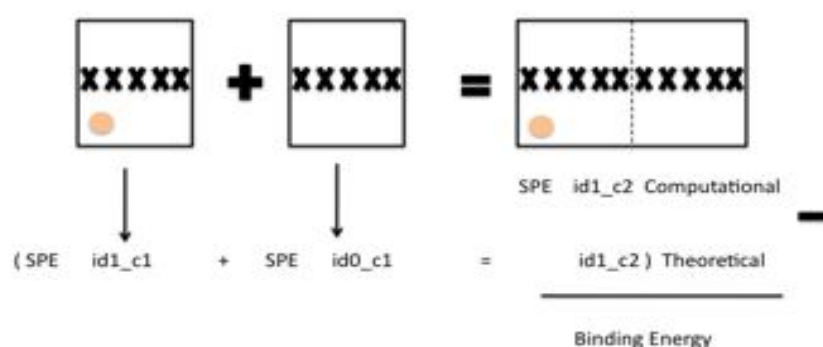
Figure 5.7: Schematic showing the calculation of the binding energy of a 2-unit cell supercell. The black crosses represents the smectite layer and the orange circle a sodium atom.

The relationship between the total energy (in this study from SPE calculations) and supercell size indicates the type of relationship that exists between periodic images such as Coulombic between charged species, dipolar or higher order multipoles as described in section 5.3.2. This information can be used in several ways, such as to determine the effect these interactions might have on the results and hence the conclusions that can be drawn; the validity of supercell comparisons and possibly the identification of an optimum model to simulate reduction.

This concludes consideration of the modelling method and justification of the choices made and the following section proceeds with the results obtained as a con-

sequence of these choices.

5.4 Results and Discussion

5.4.1 Binding Energy

Ideal

Figure 5.8 shows the binding energy for model sets id0-c2 to id0-c4, id1-c2 to id1-c4, id2-c2 to id2-c4 and id3-c2 to id3-c4 where Na atoms were included together with the same sets where Na was replaced with charge. In the case of no sodium (and no charge) there is no significant (in relation to the other trends on the graph) change in energy as would be expected. That is, there is no Na hence no Coulomb interactions between periodic images. There will be an electric field due to the difference in charge density on the basal surfaces which may be interacting with itself via a dipole-dipole interaction in the z-direction, which could explain why, with increasing supercell size, the binding energy does not plateau as the c-length for all models is the same.

With one Na, the binding energies show a monotonic decrease characteristic of Coulomb interactions, which is different to the trend with a charge of -1e; in this case the binding energy parallels that of the case with no Na and is to be expected as again, there is no Na causing Coulomb interactions. There is, however, a compensating, neutralising, background charge which is screening the electric field from its periodic images.

In the case of two and three sodium atoms, there is a dominant Coulomb relationship, that is, the effect of the dipole field interactions seen with zero Na, is masked by the strength of the Coulomb interaction. What is interesting here, is that the Coulomb effect is not enhanced by a third sodium atom which suggests that two sodiums are sufficient for reduction in this system, i.e. the sodiums have become
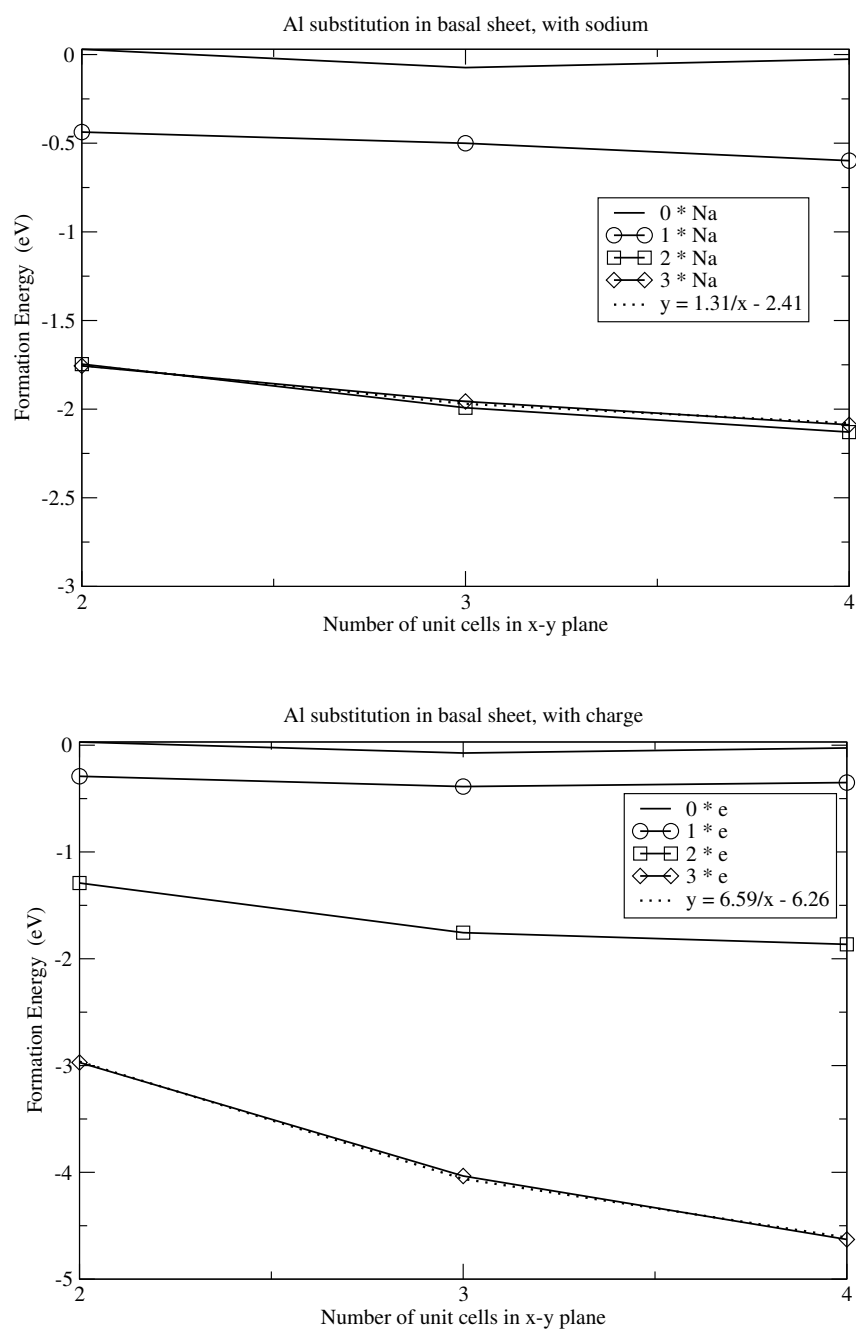
Figure 5.8: Binding energies of Ideal models with sodium and with charge only.

maximally charged, whatever the number of Fe in the OS. The sodium atoms are localised within the first cell in every model hence this effect might change if the sodium atoms were distributed between neighbouring unit cells, but this would make the calculation of binding energies more difficult as the configurations would not be comparable.

In contrast to the near-identical nature of the two and three sodium atom Coulomb trends, the charge models of $-2e$ and $-3e$ are different to each other although the binding energies indicate a Coulomb relationship within the models. The gradient of the curve of the $-2e$ set is steeper than those of the sodium, id2, id3 sets but shows more positive binding energy. For the $-3e$ set, the gradient is steeper again and the binding energy the lowest of all models. What appears to be happening here, is that the background charge is interacting with itself. As the number of unit cells in the supercells increases, the jellium density decreases, which is the same for $-1e$, $-2e$ and $-3e$ and yet, the $-3e$ models show a pronounced Coulomb interaction, so, perhaps as the screening effect decreases, the 'areas of charge' begin to interact with one another.

A closer examination reveals that what is actually happening is less worrying in terms of modelling as it is due to the way the binding energies were calculated rather than to an inherent quality of the models, that is, for the theoretical energies, all of the charge was assumed to be within the first unit cell which was then 'padded' out with charge-empty cells as shown in Figure 5.9.

Contrast this with the computational energies that involve charge distribution throughout the supercell. The latter has a lower energy than the former. What has effectively been created is a theoretical Coulomb interaction between charges contained within one cell and its periodic images. A solution to this might be to calculate the energies of cells with fractional charge and use these in the theoretical calculations which might produce more accurate binding energies. However, the true binding energies will follow the same trend as that for a charge of $-1e$, as, even when this charge was distributed over four unit cells, hence the compensating jellium had
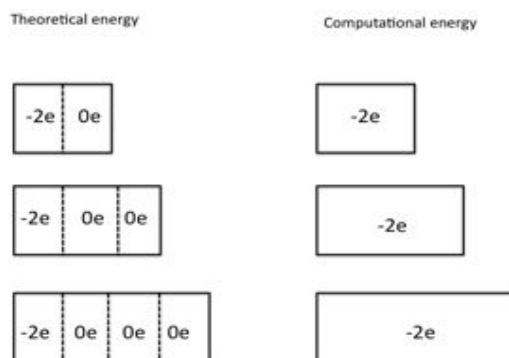
Figure 5.9: Schematic showing how the binding energies were calculated for the charge models.

the smallest possible charge density of all models, the electric field dipoles did not significantly affect the binding energy.

In conclusion, the dominant multipole interaction is Coulomb between sodium ions and their periodic images. This can be eliminated by using charge rather than Na as the reducing agents. The extent to which the Coulomb interactions affect reduction is examined in section 5.5.

NG-1

The results of the binding energy of the NG-1 models indicate that an examination of the spins is required to interpret any meaning from them. Figure 5.10 shows the binding energies for the sodium and Figure 5.11, the charge model sets ng0-c2 to ng0-c4, ng1-c2 to ng1-c4, ng2-c2 to ng2-c4 and ng3-c2 to ng3-c4 together with the dominant spins per model on the tetrahedral Fe. In the case of zero Na, there is a decrease in binding energy with increasing supercell size, as expected. The spin on the Fe in ng0-c4 is separated from its neighbouring spin by three spin-free unit cells hence shows ferrimagnetism at maximum separation which should not affect the binding energy.
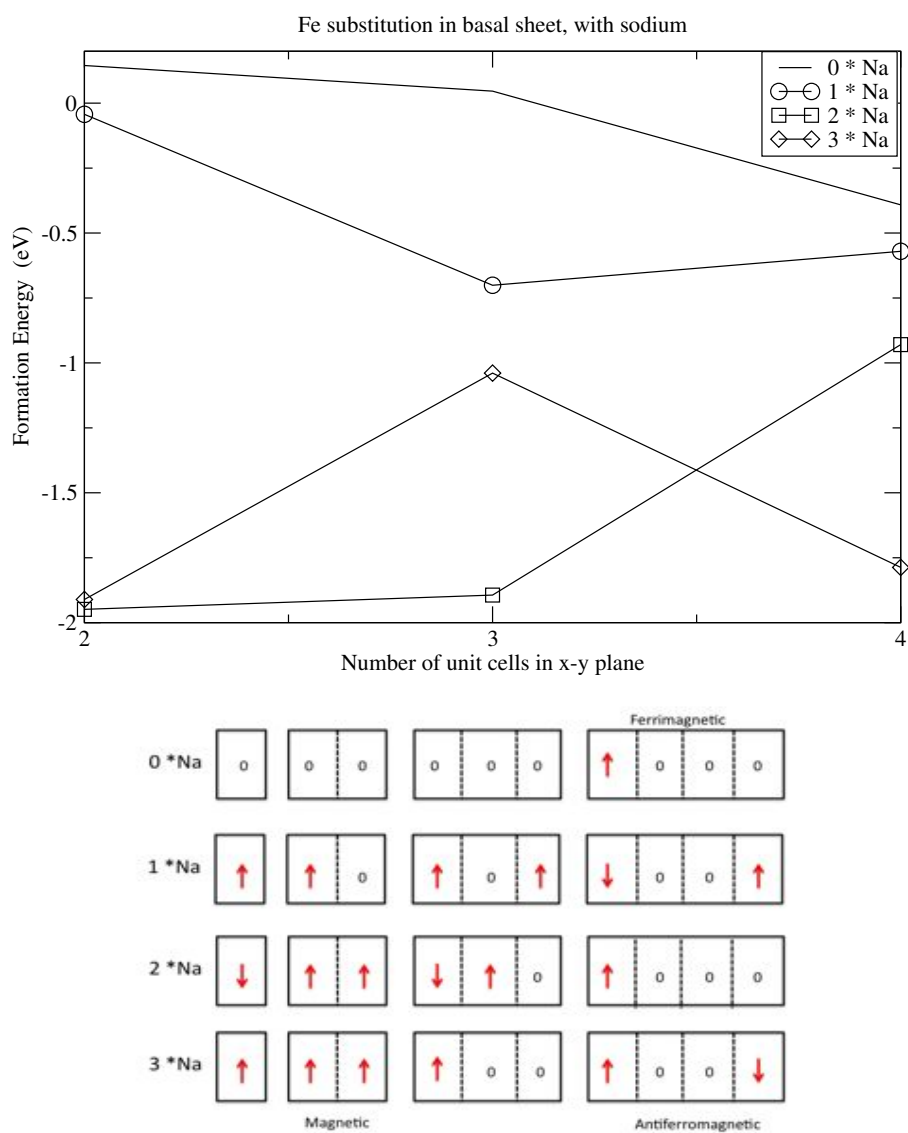
Figure 5.10: With sodium atoms — binding energies of NG-1 models (top) and a schematic of the spin states of Fe in the TS (bottom), where a red arrow represents a spin of magnitude approximately 3 and zero is relative to this.

The graphs for one, two and three sodiums show trends related to how the binding energy was calculated. For example, all theoretical binding energies assumed a ferrimagnetic model — explained shortly — but this is true for the computational models only in cases ng0-c4, ng1-c2, ng2-c4 and ng3-c3. Figure 5.12 shows some of the differences possible between the theoretical and computed spin states and Table 5.2 shows the computed magnetic states and describes the abbreviations AFoM, FiM, FoM and NM.
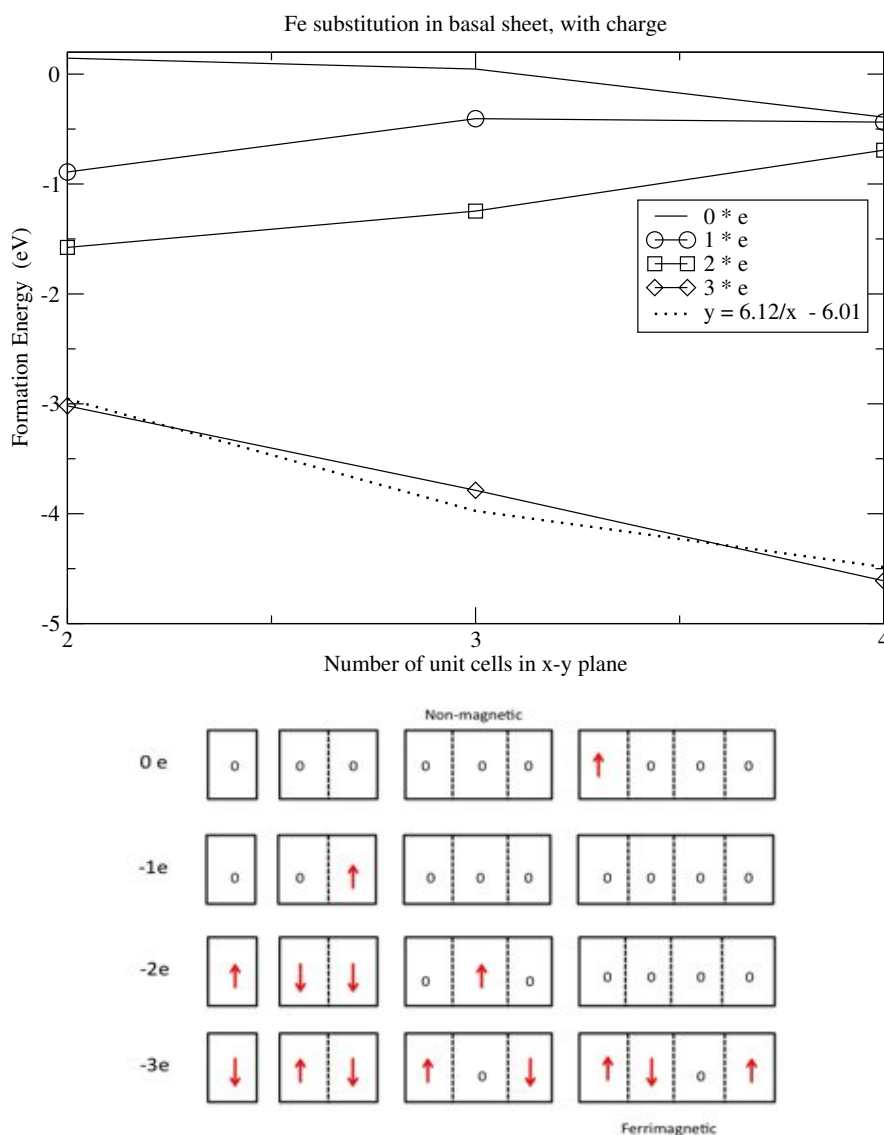
Figure 5.11: Charge only models — binding energies of NG-1 models (top) and a schematic of the spin states of Fe in the TS (bottom), where a red arrow represents a spin of magnitude approximately 3 and zero is relative to this.
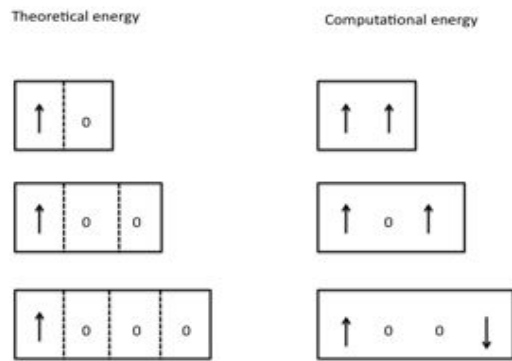
Figure 5.12: Schematic showing the difference in magnetic state between the theoretical and computational models when calculating binding energies.

	With sodium (N * Na)			Charge (N * −e)		
N	c2	c3	c4	c2	c3	c4
1	FiM	FiM	AFoM	FiM	NM	NM
2	FoM	AFoM	FiM	FoM	FiM	NM
3	FoM	FiM	AFoM	AFoM	AFoM	FiM

Table 5.2: Computed magnetic states of the supercells used in the binding energy calculations where AFoM is antiferromagnetic; FiM, ferrimagnetic; FoM ferromagnetic and NM non-magnetic. (All theoretical models were ferrimagnetic.)

Na	Ideal				NG-1			
	c1	c2	c3	c4	c1	c2	c3	c4
1	0	0	0	0	0	0	0	0
2	0.58	0	0	0	0.28	0.02	0	0
3	0.50	0.94	0.84	0.84	0.66	0.86	0.76	0.72

Table 5.3: Spins ($\hbar$) on the sodium atoms after relaxation of the electronic structure

Assuming that, in terms of lowering the energy of a system, NM < AFoM < FiM < FoM and that the computational energy will be lower than the theoretical energy for exactly the same spin state due to the relaxation of the electronic structure, then, relative to the theoretical FiM state FiM_T, it should be that the computational state, FiM_C will be lower, hence $FiM_T-NM_C < FiM_T-AFoM_C < FiM_T-FiM_C < FiM_T-FoM_C$. So, comparison of this progression with Figure 5.10 should help to explain the erratic nature of the binding energies and it does, to some extent. But, there is an added complication in that the energy of, for example, a FiM state will depend on the distribution of spins, that is a ↑ 0 ↑ may have higher energy than ↑ 00 due to the interaction of the spins. Consequently, there is no guarantee that, in every instance, $FiM_T-FiM_C < FiM_T-AFoM_C$ which is indeed the case in Figure 5.10 — one sodium and Table 5.2, row one.

There is one other effect to consider, which is the presence of sodium itself. Table 5.3 shows that the spins on the sodiums in Ideal and NG-1 are practically the same, hence the only way in which this is contributing to the oscillating nature of the binding energies is if the sodium atoms are affecting the spins on the tetrahedral Fe. This is supported by Figure 5.11 where the binding energies for the charge models display monotonic relationships. Also, there are fewer magnetic states of the supercells and there is possibly greater coincidence between the like-for-like energies of, for example, FiM_T and FiM_C states.

There is no numerical analysis of the aforementioned scenarios as it is rather futile, that is, the binding energies for the sodium models of NG-1 are erratic compared with the uncharged models and those of Ideal. It is clear from the above analysis that the spins on the TS iron are affecting these energies and that sodium

may be affecting these results but that replacing Na with charge is not guaranteed to produce more consistent results. So far it has been learnt that there are Coulomb interactions between periodic sodiums, periodic dipole interactions between electric fields and interacting spins in the TS. All of which suggests it is not a simple matter to create an optimum model to investigate reduction. However, using this range of supercells and number of sodium or charge, allows for a thorough investigation of reduction and the distinction between modelling artefacts and reliable results, especially on the examination of charge which comprises the next section.

5.5 Charges-Octahedral Sheet

In this section the effect on the charge on the octahedral irons is examined for Ideal and NG-1 where the model sets for the same sized cell but with an increasing number of sodiums/charge are compared, i.e. down the columns in Figure 5.5 and across where explicitly described.

5.5.1 Ideal

Table 5.4 shows that the greatest decrease in charge occurs in the charged model set, c1 with a reduction of 0.78e and the smallest decrease is 0.36e in the sodium model set, c1. The decrease in the charged models is, per set, greater than that in the sodium models. Table 5.5 shows the increase in total charge on the sodiums, which, in the case of set c1 is 0.52e, from 1.07e to 1.59e and yet, if three sodiums were donating their 3s electrons, they would have a total charge of 3e. This implies that the application of charge ensures it is more available to the system than are the 3s electrons of sodium because, in the latter case, the sodium atoms are localised within the first unit cell whereas in the case of charge, this is evenly distributed throughout the supercells. This 'localisation effect' is discussed further in section 5.6.1.

	Sodium							
	Ideal				NG-1			
	c1	**c2**	**c3**	**c4**	**c1**	**c2**	**c3**	**c4**
0	4.54	9.07	13.58	18.12	4.37	8.75	13.07	17.50
1	4.34	8.87	13.41	17.95	4.26	8.62	13.02	17.41
2	4.23	8.69	13.17	17.76	4.18	8.54	12.92	17.25
3	4.18	8.63	13.19	17.71	4.18	8.50	12.87	17.23
$(\Delta_0 - \Delta_3)$	0.36	0.44	0.39	0.41	0.19	0.25	0.20	0.27

	Charge							
	Ideal				NG-1			
	c1	**c2**	**c3**	**c4**	**c1**	**c2**	**c3**	**c4**
0	4.54	9.07	13.58	18.12	4.37	8.75	13.07	17.50
1	4.31	8.85	13.37	17.92	4.18	8.57	12.90	17.24
2	4.05	8.63	13.25	17.71	3.98	8.40	12.71	17.05
3	3.76	8.35	12.89	17.43	3.73	8.17	12.53	16.98
$(\Delta_0 - \Delta_3)$	0.78	0.72	0.69	0.69	0.68	0.58	0.54	0.52

Table 5.4: Total charges of octahedral Fe following a single point energy calculation. On the LHS, 0 to 3 is the number of added Na or charge and the labels c_1, c_2 etc. represent the size of the (super)cell. Comparison down the columns is examining the effect of the addition of reducing agent to the same size (super)cell, whereas comparison across the rows is examining the effect of changing the (super)cell size.

	Ideal				NG-1			
Na	c1	c2	c3	c4	c1	c2	c3	c4
1	1.07	1.09	1.10	1.10	1.06	1.08	1.08	1.08
2	1.49	2.07	2.08	2.09	1.65	2.05	2.05	2.05
3	1.59	2.12	2.30	2.29	1.58	2.19	2.25	2.28

Table 5.5: Total charges on the sodium ions after relaxation of the electronic structure

The maximum change in total charge of the sodiums occurs in c3 and c4 sets (Table 5.5) with total charges of 2.30e and 2.29e respectively, where the larger cells allow the electronic structure to relax with a reduced Coulomb interaction between periodic sodiums. However, this does not correspond with an increase in reduction in the OS iron, where it peaks at -0.44e for c2 and decreases to -0.41e for c4. So, despite the greater number of Fe atoms within the OS of the larger c4, reduction does not increase but this could be due to the presence of tetrahedral Al which is also being reduced (discussed in section 5.6). There is a similar trend with the charge models, where in c3 and c4 the reduction is -0.69e and the same explanation applies as there is also Al in the TS.

5.5.2   NG-1

The maximum reduction in the NG-1 models occurs in the charge set, c1 (see Table 5.4) of -0.68e and the minimum occurs in the sodium set c1, of -0.19e. As the number of cells increases, the reduction in the charge sets decreases, which is the same trend as in the Ideal models. Therefore, the discussion of this in the last section applies to the charge, NG-1 models. Similarly, the trend for the Na sets is the same as that discussed for the Ideal models and, as the OS constituent atoms are identical in Ideal and NG-1, the same implications can be drawn.

Comparison of Ideal and NG-1

In both sodium and charge sets, the total octahedral charge is higher in Ideal than in NG-1 suggesting a difference due to the presence of Fe in the TS of NG-1. In

both Ideal and NG-1, the total charge of the OS Fe is higher in the sodium models than the charge models, suggesting a difference due to the distribution of the charge 'donated' by the reducing agents. The conclusion at this point is that reduction is occurring in the octahedral irons of all four model sets. The following section examines the effect of the reducing agents on the tetrahedral sheet.

5.6 Charges — Tetrahedral Sheet

In this section the effect on the charge of the tetrahedral Al/Fe substituted atom is examined for Ideal and NG-1 where the model sets for the same sized cell but with an increasing number of sodiums/charge are compared, i.e. down the columns in Figure 5.5 and across where explicitly described.

5.6.1 Ideal

The largest reduction occurs in the sodium sets, c2, c3 and c4 of $-0.21e$ and the smallest in the charge sets c2 and c4 of $-0.08e$ — see Table 5.6 and is the reverse pattern of the OS reduction. Across Table 5.6, from c1 to c4, there is an increase in reduction in the sodium models from $-0.18e$ which stabilizes from c2 onwards to $-0.21e$, which suggests that reduction occurs local to the position of the sodium atoms. A closer comparison of the charges on each of the Al within the models, (results not shown for brevity) shows that the Al in the cell containing the sodiums is reduced more than any other Al, for example, in c2, the c1-Al decreases form 1.96e to 1.79e on addition of three sodiums, whereas the c2-Al decreases from 1.96e to 1.92e. Further scrutiny shows that on the addition of two Na, the maximum reduction effect is achieved for all models c1 to c4.

The smaller reduction effect seen in the charge models could be due to the distribution of charge throughout the cells together with the larger reducing capacity of the OS Fe compared to Al. The local effect of charge is given further credence

	Sodium							
	Ideal				NG-1			
	c1	**c2**	**c3**	**c4**	**c1**	**c2**	**c3**	**c4**
0	1.96	3.92	5.88	7.84	1.23	2.44	3.67	5.05
1	1.89	3.85	5.81	7.77	1.26	2.48	3.85	5.09
2	1.80	3.71	5.67	7.64	1.10	2.43	3.63	4.69
3	1.78	3.71	5.67	7.63	1.14	2.45	3.46	4.88
$(\Delta_0 - \Delta_3)$	0.18	0.21	0.21	0.21	0.09	−0.01	0.21	0.17

	Charge							
	Ideal				NG-1			
	c1	**c2**	**c3**	**c4**	**c1**	**c2**	**c3**	**c4**
0	1.96	3.92	5.88	7.84	1.23	2.44	3.67	5.05
1	1.93	3.90	5.85	7.84	1.17	2.55	3.61	4.85
2	1.90	3.86	5.82	7.80	1.29	2.66	3.73	4.78
3	1.83	3.84	5.79	7.76	1.20	2.62	3.83	5.20
$(\Delta_0 - \Delta_3)$	0.13	0.08	0.09	0.08	0.03	−0.18	−0.16	−0.15

Table 5.6: Total charges of tetrahedral Al (Ideal) or Fe (NG-1) following a single point energy calculation. On the LHS, 0 to 3 is the number of added Na or charge and the labels c_1, c_2 etc. represent the size of the (super)cell. Comparison down the columns is examining the effect of the addition of reducing agent to the same size (super)cell, whereas comparison across the rows is examining the effect of changing the (super)cell size.

by the results from these charge models, where the greatest reduction occurs in c1 compared to c4 where the reduction is less, that is, the charge is concentrated in c1 thereby reducing the local Al, whereas in the supercells, the charge is distributed and hence its effect on the TS Al is diminished. For example in c1, Al decreases from 1.96e to 1.83e on addition of -3e, whereas in c2, the Al in c1 and c2 decrease from 1.96e to 1.92e and in the c4 models the decrease for all four Al is 1.96e to 1.94e. In contrast to the sodium models where reduction stabilised on the addition of two Na, the reduction of Al continues beyond the addition of -2e. Also, all Al reduce to the same extent in the charge models whereas with Na, the effect is localised. This 'localisation effect' is discussed further in the following section where the orbital occupancy of the TS Al is analysed.

Orbital occupancy

Figure 5.13 shows an example of increasing occupancy of the s and p orbitals of the aluminium atoms in the TS on addition of sodium and/or charge. The largest occupancy increase is seen in the π-orbital of Al in the c1 cell containing the sodiums, which explains the localisation effect on reduction described in the previous section. Also, there is further evidence for this seen in the c4 models (full results not shown) where the values for the Al in c1 (s1 and p1) are 0.45 and 0.77 respectively decreasing to 0.41 and 0.64 for the three subsequent s and p orbitals of Al. Compare this with the charge set where all four s and p orbitals have values 0.42 and 0.64 respectively.

5.6.2   NG-1

In this case the greatest reduction effect is seen in c3 of the sodium models and the least in c2 of the charge models where Fe in the TS is oxidized. Oxidation also occurs in c2, c3 and c4 of the charge models; closer inspection of the pattern down the columns reveals that in all three cases, there is both reduction and oxidation. In c1 of the sodium models, there is less oxidation but within the column there is both re-
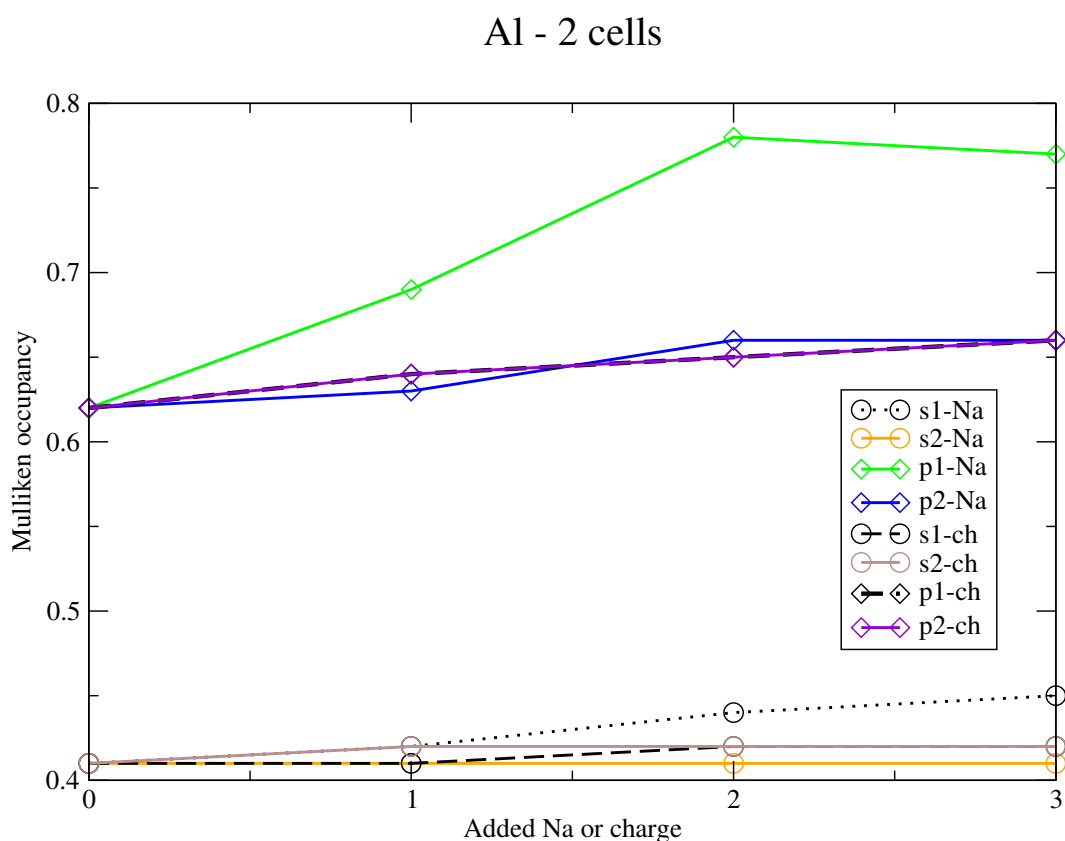
Figure 5.13: Orbital occupancies of Al in the tetrahedral sheet in the 2-cell models where labels s1-Na and s2-Na refer to the s-orbitals of Al in the original unit cell and the second cell respectively, of the sodium sets and similarly for p1-ch and p2-ch referring to the $\pi-$orbitals of the charge sets. This labelling convention also applies to Figures 5.14, 5.15 and 5.19.

duction and oxidation. In fact, examining all NG-1 models down the columns shows that in every case there is both oxidation and reduction, but there is no obvious pattern to predict whether the Na*3 or $-3e$ model is reduced or oxidised relative to the 0*Na or 0e models. This is clearly an effect of the Fe in the TS as there is consistent reduction seen in the Ideal models where the substitution is Al in the TS. There appears to be an interaction between neighbouring Fe's, possibly also Na and the distributed $-e$ charge. Again, as the latter is more diffuse throughout the models and hence spread out over all TS irons, the effect is greater than in the Na models where sodium is localised within the first unit cell. An examination of the orbital occupancy might elucidate the cause of the oscillatory oxidation/reduction behaviour.

Orbital occupancy

Figures 5.14 and 5.15 show the orbital occupancies of Fe in the tetrahedral sheet and, similar to the Ideal case, the p-orbital of the Fe in the first unit cell is occupied to the largest extent in both the 2- and 3-cell sets, which is evidence of a localisation effect. That is, the presence of the sodium atoms in the first unit cell is affecting the occupancy of the p-orbital of the TS Fe. This effect is not present in the charged models or seen in the p-orbitals of the Fe in the sodium set in the cells without the sodium atoms.

An examination of the graphs of the d-orbitals shows erratic occupancy where the number of added electrons or charge appears to have no correlation with the level of d-orbital occupancy. Closer inspection of the graphs shows that the occupancy oscillates between about 6.10 and 6.40 although there are possibly fewer oscillations in the 2-cell sets, which could be a result of fewer interactions between the TS Fe as the 2-cell models contain two Fe in the TS whereas the 3-cell sets contain three. This suggests a possible model which might clarify the effect of sodium/charge addition on the TS Fe and such a model is described in section 5.7.

The conclusion from this analysis is that the nature and location of the reducing agent affects the occupancy of the p-orbitals in particular, of the TS Fe in c1, but is irrelevant to the occupancy of the d-orbitals. Therefore, it seems reasonable to hypothesise that the largest interactions are due to those between neighbouring Fe and that if these were reduced, by decreasing the number of irons per supercell, a conclusion as to the behaviour of TS Fe on the addition of a reducing agent, could be drawn. This idea is pursued in section 5.7.

Fe - 2 cells: s and p

Fe - 2 cells: d
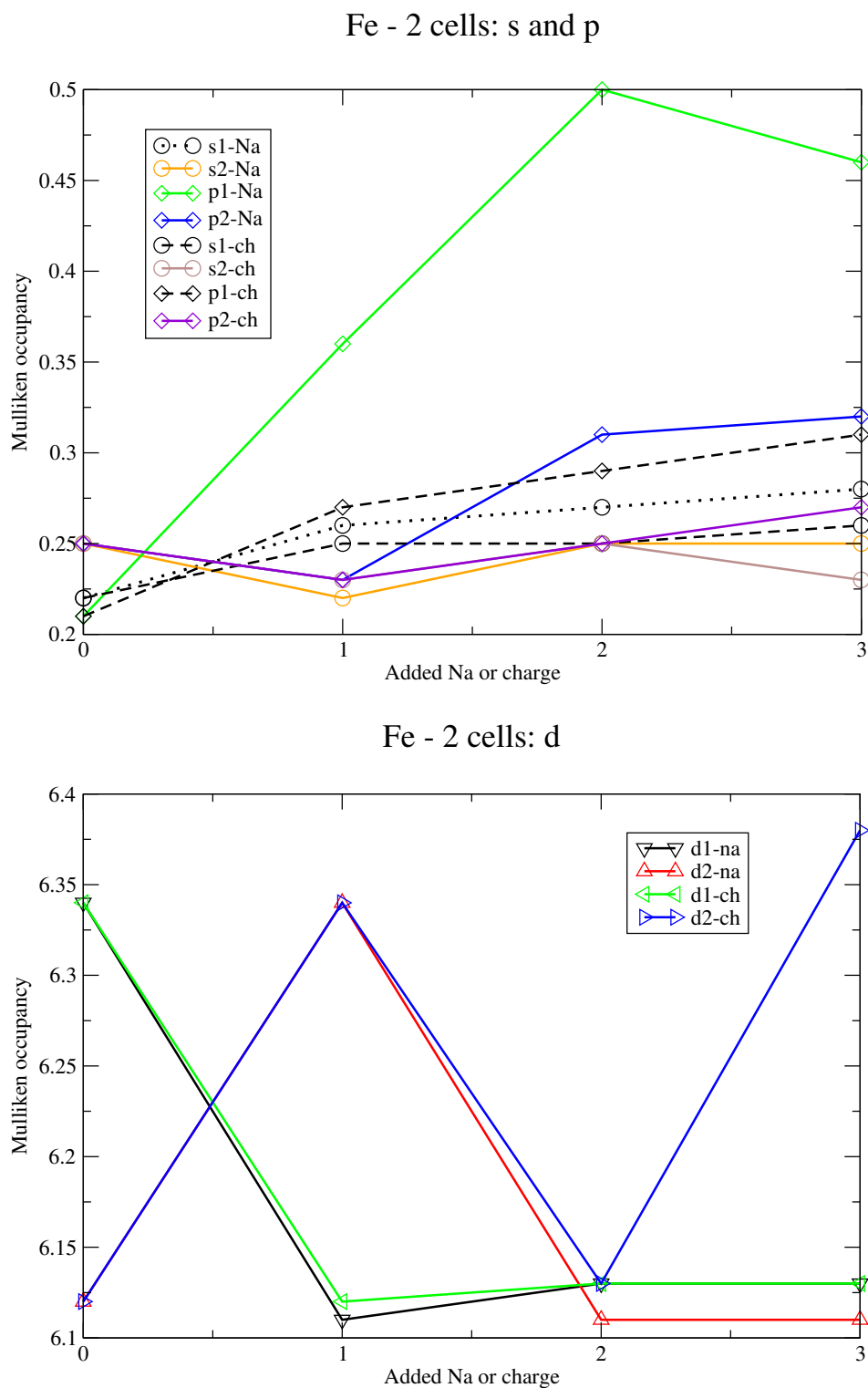
Figure 5.14: Orbital occupancies of iron in the tetrahedral sheet.
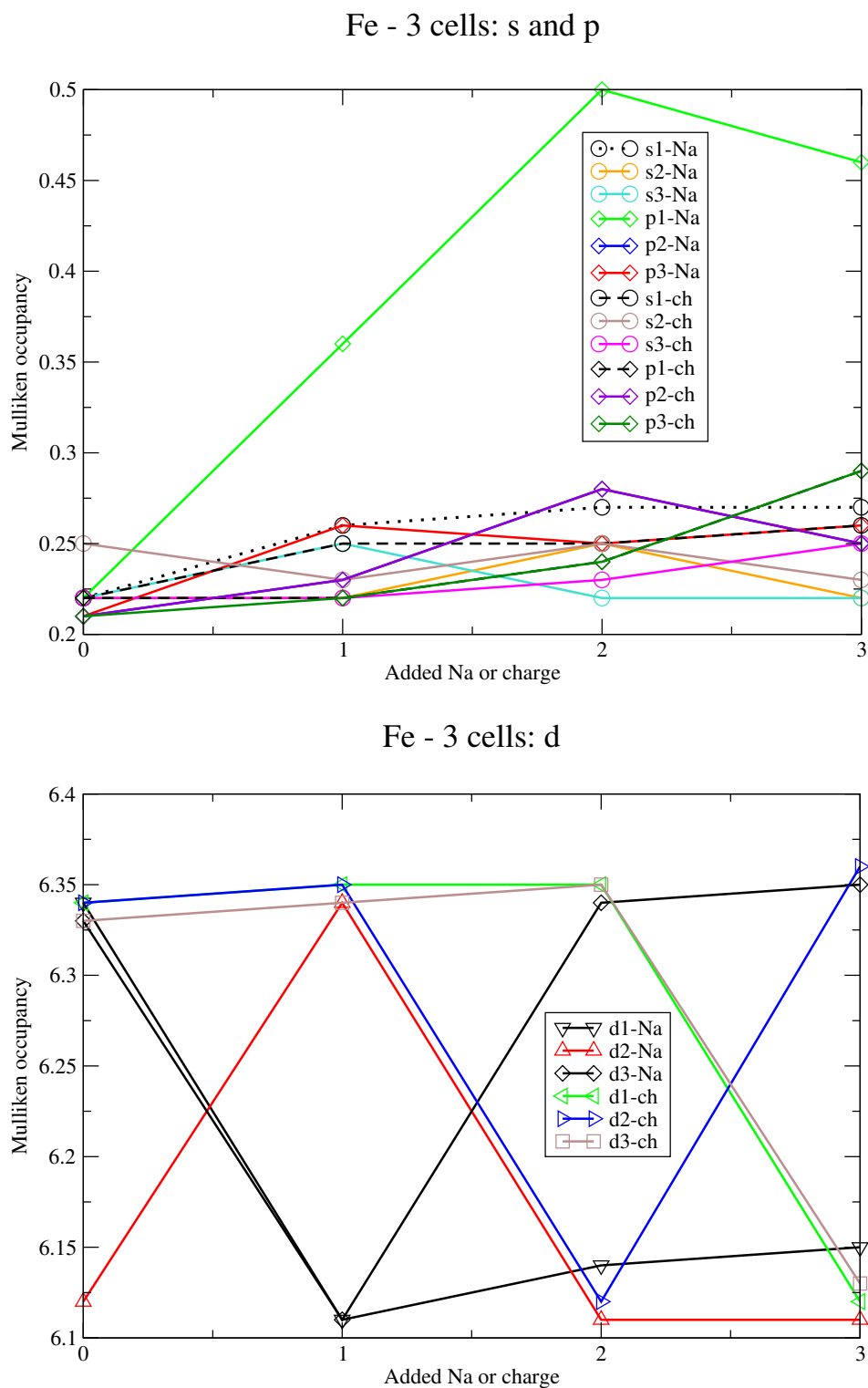
Figure 5.15: Orbital occupancies of iron in the tetrahedral sheet.

	Ideal							
	Oxygen				Silicon			
	With Na		With Charge		With Na		With Charge	
Cells	Max	Species	Max	Species	Max	Species	Max	Species
1	-0.09	6	-0.09	6	-0.16	4	-0.16	4
2	-0.11	6	-0.11	6	-0.12	11	-0.12	11
3	-0.11	6	-0.11	6	-0.13	11	-0.13	11
4	-0.11	6	-0.11	6	-0.13	11	-0.13	11

Table 5.7: Change in charge of the oxygen and silicon atoms from no sodiums/no charge in the Ideal models to 3 sodiums/charge of $-3e$. Max means maximum reduction and species refers to the atoms shown in Figure 5.16.

5.6.3 Oxygen and Silicon

Ideal

The reduction of oxygen and silicon occurs to the same degree in both Na and charge models, see Table 5.7. Silicon is reduced more than oxygen with a maximum of $-0.16e$ compared to $-0.11e$. As can be seen in Figure 5.16, the silicons and oxygens most reduced are closest to the aluminium in the TS, i.e. in c1.

NG-1

The reduction of oxygen and silicon occurs to varying degrees in the Na and charge models; oxygen is reduced more than silicon with a maximum of $-0.20e$ in the charge set compared to a maximum of $-0.15e$ for silicon in the Na set. The reduction of oxygen in the charge set has maxima spread throughout the supercell, whereas the maximum in the Na set is adjacent to, or within the cell containing the sodiums, i.e. c1. The magnitude of reduction of silicon is greater in the Na sets than in the charge sets. Although in both cases the silicons in the first cell are more strongly reduced than any others.
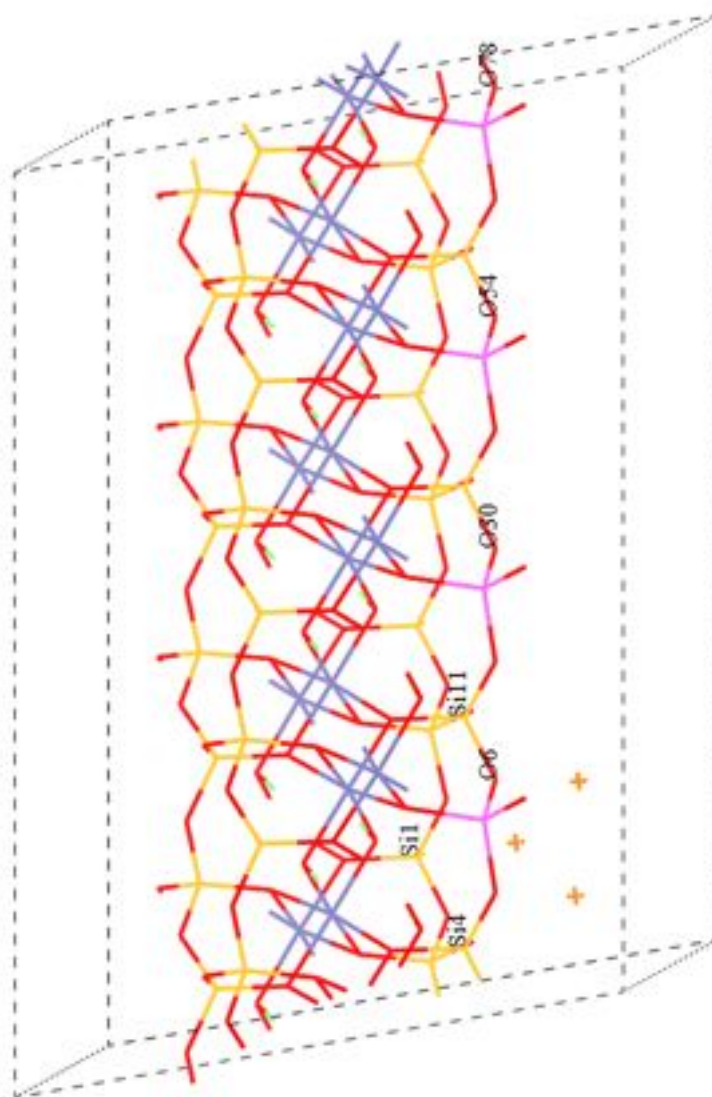
Figure 5.16: Id3-c4 showing the species referred to in Tables 5.7 and 5.8 For clarity of display, hydrogen is green in this model only.

	NG-1							
	Oxygen				Silicon			
	With Na		With Charge		With Na		With Charge	
Cells	Max	Species	Max	Species	Max	Species	Max	Species
1	-0.18	6	-0.20	6	-0.15	4	-0.09	4
2	-0.19	6	-0.15	6	-0.11	1	-0.05	4
3	-0.18	6	-0.13	54	-0.11	1	-0.04	4
4	-0.13	78	-0.11	30	-0.11	1	-0.03	4

Table 5.8: Change in charge of the oxygen and silicon atoms from no sodiums/no charge in the NG-1 models to 3 sodiums/charge of $-3e$. Max means maximum reduction and species refers to the atoms shown in Figure 5.16.

5.6.4 Comparing Ideal and NG-1

A brief summary is that in the Ideal models, if one wants to minimise the reduction effect on the oxygens and silicons and hence maximise the effect on the iron atoms, the optimum model would be a 2-cell set using either Na or charge as the reducing agent. In the NG-1 models, using a 4-cell charge set would achieve this aim.
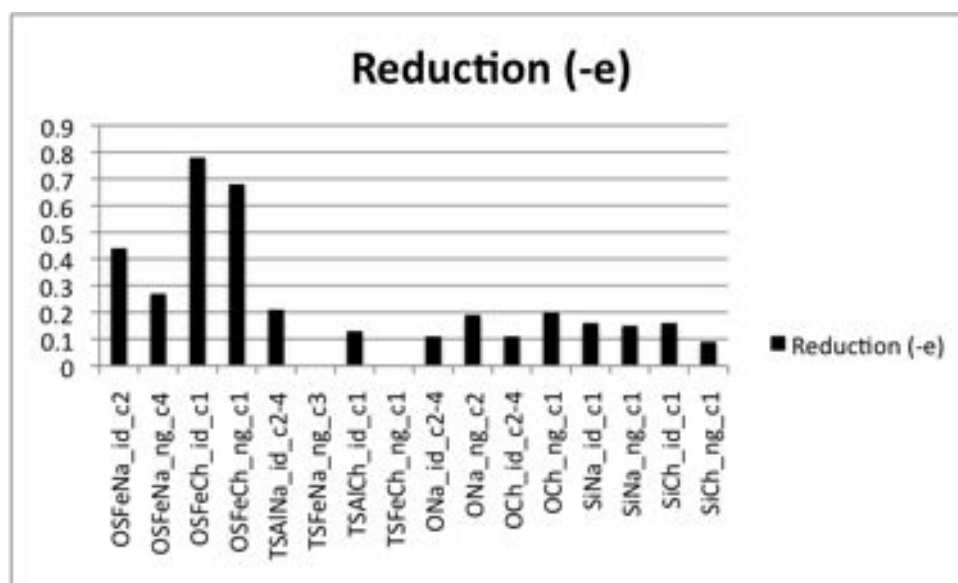
Figure 5.17: Bar chart summarising the maximum charge changes per model set where the first 8 names are comprised of, sheet, species, reducing agent — sodium (Na) or charge (Ch) and then model. The second set of 8 names are comprised of species, reducing agent — sodium (Na) or charge (Ch) and then model.

5.6.5   Conclusion

Figure 5.17 clearly shows that there is reduction of the OS Fe in both Ideal and NG-1 models and that the magnitude of reduction is greater in the charge than the Na sets for reasons previously discussed.

The magnitude of reduction of Al, Si and O in the TS is the same with variations in maxima between Na and charge sets.

The question of whether Fe in the TS reduces is not clear. The interactions between Fe produce results which are too inconsistent to draw any firm conclusions. However, the results discussed in section 5.6.2 suggest that reducing the number of Fe in the TS might lead to reduced interaction between Fe and hence to results which lend themselves to interpretation.

5.7   A further investigation

5.7.1   Introduction

This small, additional study is an attempt to determine the effect on the TS iron upon the addition of a reducing agent. The conclusion from the main body of the study was that the TS Fe are interacting and that this interaction is obscuring interpretation of the results. Therefore, if the TS irons were isolated to the extent that interactions were minimised, a conclusion could be drawn about the behaviour of iron in TS on the addition of sodium or charge.

5.7.2   Method

To test this hypothesis, the model shown in Figure 5.18 was constructed with a single Fe atom in the TS, separated by Si atoms within a supercell the size of three single cells. This is somewhat along the lines of a 'thought experiment' for several

reasons. Substitution of Fe for Si has not been followed by any relaxation of the structure; the charge deficit of $-1e$ caused by this substitution is less than that required for the attraction of a counterbalancing charge of three sodiums or a charge of $-3e$. However, following the same procedure as in the main study, the replication of environments with either the addition of sodium or charge and comparison of these results, ensures the cancellation of errors caused by lack of convergence of the geometry. As in the method of the main study, the models were made ranging from zero Na/0e to three Na/$-3e$. A single point energy calculation was carried out with the convergence criteria as previously described.
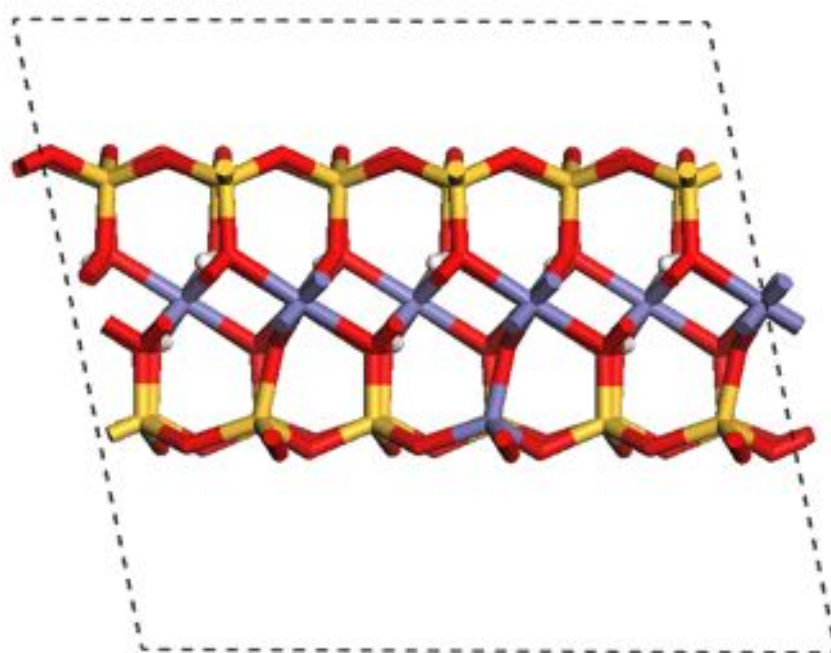
Figure 5.18: Fe isolated in the tetrahedral sheet from neighbouring Fe atoms.

5.7.3 Results and Discussion

Table 5.9 shows that in both sets of models, with sodium or with charge, there is reduction of the iron in the octahedral sheet and that the greater effect is seen in the charge models. This is explained by examining the charge of the sodiums, that is, their charge increases by only 0.05eV on increasing from two to three Na imply-

	Sodium			Charge	
	Na	OS	TS	OS	TS
0	0.00	13.14	1.24	13.14	1.24
1	1.09	13.09	1.37	13.03	1.22
2	2.00	12.92	1.37	12.78	1.19
3	2.05	12.90	1.36	12.60	1.34
$\delta_0 - \delta_3$	-	0.24	−0.12	0.54	−0.10

Table 5.9: Total charge of sodiums and of Fe in OS and TS sheets after a single point energy calculation of the model shown in Figure 5.18.

	With sodium		Charge
	Na	TS	TS
0	-	0.06	0.06
1	0.00	3.46	0.02
2	0.00	−3.56	0.14
3	−1.00	3.54	3.58

Table 5.10: Total spins of Na and Fe in TS after a single point energy calculation of the model shown in Figure 5.18.

ing that their oxidising potential has peaked in this system. Contrast this with the background charge which is wholly available to effect reduction, as commented on previously.

In the tetrahedral sheet there is overall oxidation of the iron in both scenarios although within the charge set, there is some reduction followed by a larger oxidation effect. This is explained later in this section. In Table 5.9 the overall oxidation trend in the Na set is mirrored by an increase in charge on the TS Fe from 0-Na to 1-Na and then its stabilisation through 2-Na and 3-Na. In the charge set, this trend is almost reversed where 0e, −1e and −2e result in approximately zero spin on the TS Fe and have similar charge (1.24, 1.22, 1.19 respectively) and then in the −3e set, the spin on TS Fe increases to 3.58 with a consequent increase in charge to 1.34e.

As can be seen in Table 5.10, spin induction of the sodium appears to occur when the number of sodiums increases which is perhaps a proximity effect such that, the third sodium is closer to the TS Fe and thus adopts some degree of spin which is then transmitted to the second and first sodiums due to their proximity to this third,

spin-induced sodium.

Orbital occupancy

Figure 5.19 shows the s, p and d-orbital occupancy of the single Fe in the TS. In this case, the largest increase in occupancy is of the p-orbital in the charged set although it is only very slightly greater than the increase in the p-orbital of the sodium set. This suggests the localised effects described previously are not important here but, as can be seen in Figure 5.18 the TS Fe is in the position of the second TS Fe in the NG-1 models for supercells of 3 unit cells and hence the sodium is not 'local' to the TS Fe anyway.

The d-orbital graphs in Figure 5.19 do not oscillate in the way the graphs in Figures 5.14 and 5.15 do, which indicates there is less interaction between neighbouring/periodic Fe atoms. Within the parameters of this study, i.e. for the addition of up to three sodium atoms or a charge of $-3e$, and by the removal of the interactions between neighbouring Fe, it can be seen that the s and p orbitals increase in occupancy whereas the d-orbitals decrease in occupancy and their is no difference seen whether charge or sodium atoms are employed as the reducing agents.

Table 5.10 shows that, in the sodium set, the iron in the model where there is no sodium has no spin and hence is Fe^{2+} whereas in each subsequent model, Fe is magnetic and hence could be either Fe^{2+} or Fe^{3+}. This can be deduced from the electronic configuration of these ions, i.e. Fe^{2+} is $[Ar]4s^2 3d^4$ with the d-orbitals occupied thus: $[\uparrow\downarrow] [\uparrow] [\uparrow]$ or $[\uparrow\downarrow] [\uparrow] [\downarrow]$ where the brackets indicate different d-orbitals; Fe^{3+} is: $[Ar]4s^2 3d^3$ with d-orbital occupancy of $[\uparrow\downarrow] [\uparrow]$, that must involve spin and hence magnetism due to the odd number of electrons.

The implications are that, when the iron in the TS is in a state close to Fe^{2+} i.e. close to zero spin — it has been established that Fe^{3+} cannot have zero spin — addition of electrons results in oxidation of the ferrous iron to a state close to ferric,

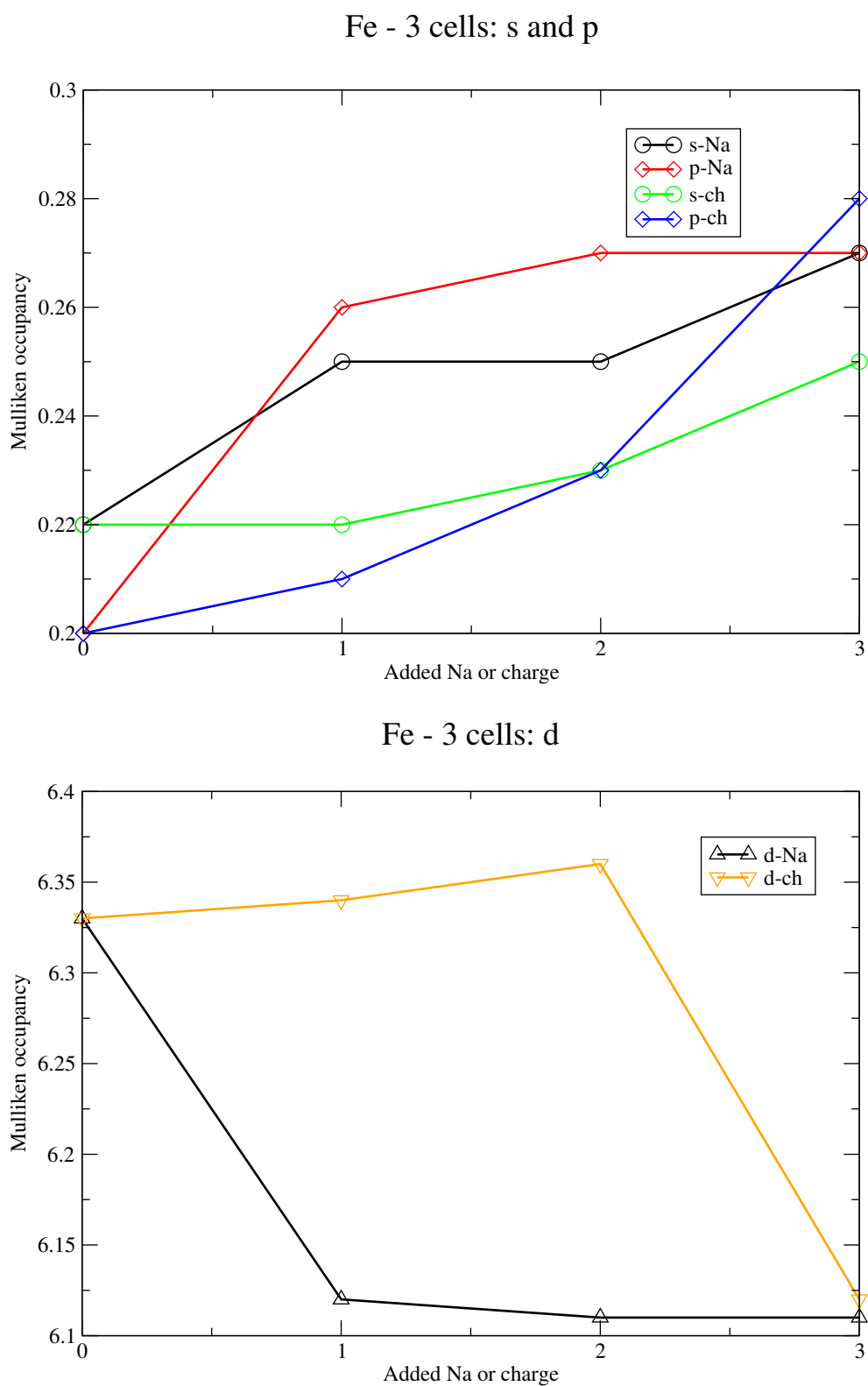Fe - 3 cells: s and p

Fe - 3 cells: d

Figure 5.19: Orbital occupancies of Fe in the TS where s-Na refers to the s-orbital of the Na models and p-ch the p-orbital of the charge models; similarly for d-Na and d-ch.

Fe^{3+} with a spin close to $|3.54|$.

5.7.4   Conclusion

This supplementary study has removed the interactions between neighbouring iron atoms in the TS, which were obscuring the effect of reducing agents on TS Fe. By decreasing the number of Fe atoms in the TS, a clearer picture of the effect of sodiums and charge on TS Fe has emerged. Within the environments described in this last section, TS iron is oxidised and not reduced. When Fe^{3+} exists within this environment, addition of a reducing agent will not cause reduction.

5.8   Overall Conclusions

Reduction *in vivo* has been investigated experimentally as a dynamic process [144] and has been seen to occur via a reduction front mechanism from edge sites and with the irregular development of reduced domains in the octahedral sheet. The study described in this chapter is an attempt to simulate such a reduction scenario, but with two notable differences from the experiments. The computational models are structurally and dynamically different. That is to say, the simulation of clay edges has not yet been widely reported, the edges are themselves not easily identifiable in their structure and constituents and so this study has concentrated on basal surface models. Indeed, it is conceivable that the modelling of edge sites could constitute a PhD in its own right! In spite of this simulation deficit, the results from this study apply to atomic environments and are therefore, theoretically transferable, i.e. if an edge site contains a local environment which is the same as a basal surface, then the same conclusions about the local effects of reduction can be drawn.

The difference in dynamics between experiment and theory is that experimentally, reduction is a continuous reaction whereas computationally, it is static and represented by adding and then increasing the concentration of the reducing agent

(sodium atoms or charge). This introduced modelling considerations such as the increase in Coulomb potential between sodium ions in unit cells containing one, two or three sodiums. To work around this potential problem, supercells were created to test the Coulomb effect. The addition of uniform charge rather than sodium atoms themselves, was another method of determining Coulomb strength, which also tested locality, that is, the proximity of the sodium atoms to the clay layer affected the relative orbital occupancies of the nearest atoms to a greater extent than the more distant atoms of the same species. The electrostatic interactions were tested by calculating the binding energies of the supercells, but their formulation proved more complicated than initially thought and highlighted several considerations specific to these models.

Firstly, the distribution of charge in the theoretical calculations of binding energy. The correct calculation would be to have fractional charge occupancy for the additional cells in a theoretical calculation, e.g. for the binding energy of three cells with an overall charge of $-2e$, each theoretical cell should have a fractional charge of $-\frac{2}{3}e$. A brief calculation for the $-2e$ and $-3e$ sets of Ideal for two and three cells respectively, gave positive binding energies of 0.0739eV and 0.0215eV respectively. Therefore, the nature of the dominant interactions between charge cells has not been correctly identified but is unlikely to be the Coulomb reaction calculated.

Secondly, the binding energies for the NG-1 models displayed an erratic nature belying the interplay between spins on the tetrahedral sheet iron and the overall magnetic nature of the (super)cell, which lead to incorrect comparisons between different magnetic states, when considering the same size model and number of sodium atoms or charge. The ability to fix the spin of the tetrahedral sheet iron would have been very useful, but, as explained in the body of this chapter, was not possible. Consequently, the results from the binding energy calculations acted more as a warning of the potential pitfalls inherent with the models than as useful results in their own right.

Armed with the knowledge that the tetrahedral irons were interacting, the single point energy calculations yielded results which reflected this. For the Ideal models, the conclusions were simple, that iron in the octahedral sheet was reducing and to a greater extent in the charge than the sodium models. In the tetrahedral sheet, aluminium also reduced, to a lesser degree than the irons and more so in the sodium than the charge models due to the localisation of sodium. Similarly, the octahedral sheet irons of the NG-1 models reduced to a greater extent in the charge than the sodium models. The effect on the tetrahedral sheet iron was clarified by creating supercells with fewer neighbouring irons in the tetrahedral sheet. These models clearly showed that tetrahedral sheet iron was oxidising and not reducing.

The conclusions drawn about the octahedral sheet irons are robust as the same results appeared four times, for the sodium and charge cases of Ideal and NG-1 and hence are transferable, that is, where there is an octahedral sheet of iron, the irons will reduce. The results regarding the tetrahedral species agree within themselves, that is, aluminium, $[Ne]3s^2 3p^1$ reduces towards $[Ne]3s^2 3p^2$, i.e. towards silicon's electronic configuration, which has four vacancies in 3p and Fe2+, $[Ar]4s^2 3d^4$ oxidises towards Fe3+, $[Ar]4s^2 3d^3$ i.e. towards four completely empty d-orbitals. This occurs for both reducing agents tested. However, a problem arises in the lack of connection between one model set and that containing an increased amount of reducing agent. There is no guarantee that two consecutive single point energy calculations on the same (super)cell will result in the appearance of the same spin state of iron in the tetrahedral sheet, as the spin polarised calculations may choose different spin states on each occasion. If, however, the local environment determines the nature of the tetrahedral iron spin state, then there is a connection between subsequent (super)cells and the reduction reaction is represented as dynamically as it could be. As both the sodium and charge models of the supplementary study resulted in the same conclusion about tetrahedral iron, the dynamic connection is promising but not guaranteed as the statistical significance of two results agreeing is not high. However, further evidence for the transferability of the results exists within NG-1, where there are oscillations in the graphs of the d-orbital occupancy between

the same values as for the supplementary study between 6.1 and 6.4. As there is an increased number of irons, then, the connection between same size supercells is undermined, as, on each single point energy calculation, the same spin per iron has to be duplicated. The probability of this is much lower than in the supplementary study case, which could explain the oxidation/reduction/oxidation oscillations seen in the main study, as artefacts of the modelling method. Thus, it can be said with confidence that, where there are clay mineral edge site environments containing irons separated by more than three silicon-oxygen bonds, oxidation will occur.

This study could be continued by examining the effect of using the GGA+U functional for the reasons described in Chapter 3 and by creating various environments in the tetrahedral sheet using the results from several cluster model studies [163], [164], which may reproduce in part at least, portions of clay edges.

6

Concluding Remarks

The studies described in this thesis began with an investigation of decarboxylation within an aluminosilicate clay mineral, motivated by the potential to inform the production of biofuels. The study was based on the experimental work done by Almon and Johns [10], which was used as a guide to produce feasible models of the reaction pathway within a DFT, planewave and pseudopotential approximation. An optimum modelling environment was determined although no intermediates in the reaction pathway were found. This prompted a re-examination of the same process but using iron-bearing clay minerals, based on Almon's and Johns' hypothesis that decarboxylation could proceed via a radical mechanism. It was found that the GGA $+U$ functional was required to model the ferruginous clay minerals and that potential intermediates were found, but that the employment of this functional required further testing before the new intermediates could be accepted as genuine results, and not merely artefacts of the modelling process.

193

The second study continued with the optimum aluminosilicate environment found in the first study, using these reactant and product models to carry out an *ab initio* transition state search. An intermediate in the decarboxylation pathway was determined and the identification of its status as a transition state required the employment of lattice dynamics. This in turn highlighted several modelling considerations, which were addressed and analysed for their impact on the results of the phonon calculation, which identified both the product and the intermediate as transition states. In-depth analysis of the Mulliken charges, dispersion curves along two paths through the Brillouin zone and the Fermi level occupancies, showed that only the intermediate model was a genuine transition state.

The final study considered reduction within ferruginous clay minerals and where it occurs within the clay layers. This simple question uncovered a multitude of modelling considerations such as how to best represent reduction and how can this be achieved consistently while decreasing the potential for artefacts in the results. In spite of the modelling complications, analysis of several aspects of the electronic structure lead to satisfactory conclusions about the site of reduction within clay minerals.

These studies have explored modelling techniques specific to clay minerals and highlight that the approach depends on the aspect of investigation. One of the main themes running throughout the investigations is the employment of multiple models, which has informed analysis by enabling comparison between like-models. This has proved an invaluable technique in the absence of similar DFT studies on clay minerals and especially so when identifying a transition state, as, to date, this is the first study of its kind in these types of systems. These studies also serve to highlight that analysing several aspects of the electronic structure enables firm conclusions to be drawn from the results, in the context of the modelling environment.

The next challenge lies in relating these theoretical results to those obtained

experimentally, i.e. to re-creating the relevant experimental environments within a DFT, planewave, pseudopotential approximation, which would require the presentation of more complex systems than those used in this thesis. However, in modelling, complexity is built on simplicity and so the model systems created for the purposes of the investigations recorded here, provide the foundation on which the process of complexification can begin.

A

Lattice Dimensions and Atomic Coordinates of a Unit Cell of Pyrophillite

The lattice dimensions and angles and atomic positions of the initial pyrophillite cell used to create the Model Sets in Chapter 3 with appropriate substitutions and/or the addition of a sodium atom as outlined in the main body of the chapter. This initial cell of pyrophyllite has composition $(Al_2Si_4O_{10}(OH)_2)_2$ and space group $P\bar{1}$.

$a = 5.150$	$\alpha = 90.500$
$b = 8.930$	$\beta = 99.200$
$c = 13.170$	$\gamma = 89.700$

Table A.1: Lattice parameters of a unit cell of pyrophillite: lengths are in Angstroms and angles in degrees.

H	1.2632	0.4194	0.3918	O	0.0636	0.5924	0.0301
H	0.4711	0.6622	0.2328	O	0.2250	0.8700	0.0354
H	0.9814	0.9183	0.4611	O	0.8707	0.2400	0.3880
H	0.1832	0.0389	0.1821	O	0.9512	-0.0704	0.3846
O	0.5246	0.9429	0.2206	O	0.9057	0.3989	0.5648
O	0.6074	0.2465	0.2179	O	0.7443	0.1213	0.5595
O	0.5269	0.5568	0.2213	O	0.9534	0.5510	0.3913
O	0.5724	0.0875	0.0411	O	0.7398	0.6883	0.5447
O	0.7382	0.8056	0.0672	Al	0.7376	0.0768	0.3013
O	0.7337	0.3651	0.0464	Al	0.2317	0.9145	0.2936
O	0.4447	0.0484	0.3743	Al	0.2288	0.5816	0.2903
O	0.3619	0.7447	0.3770	Al	0.7405	0.4096	0.3046
O	0.4424	0.4345	0.3736	Si	0.5193	0.9274	0.0947
O	0.3969	0.9037	0.5538	Si	0.5340	0.2513	0.0912
O	0.2311	0.1857	0.5277	Si	0.4500	0.0639	0.5002
O	0.2356	0.6262	0.5485	Si	0.4353	0.7400	0.5037
O	0.0159	0.4403	0.2037	Si	0.0106	0.4248	0.0777
O	0.2294	0.3030	0.0502	Si	0.0252	0.7562	0.0802
O	0.0986	0.7514	0.2069	Si	0.9441	0.2351	0.5147
O	0.0181	1.0616	0.2103	Si	0.9587	0.5665	0.5172

Table A.2: Atomic positions: fractional.

Notes and References

[1] North M. *Principles and Applications of Stereochemistry*. Stanley Thornes Ltd., first edition, 1998.

[2] Yu C-H.; Newton S. Q.; Miller D. M.; Teppen B. J.; Schäfer L. *Ab initio* study of the non-equivalence of adsorption of D- and L- peptides on clay mineral surfaces. *Structural Chemistry*, 12:393–398, 2001.

[3] Siffert B.; Naidja A. Stereoselectivity of montmorillonite in the adsorption and deamination of some amino acids. *Clay Minerals*, 27:109–118, 1992.

[4] Schoonheydt R. A.; Pinnavaia Y.; Lagaly G.; Gangas N. Pillared clays and pillared layered solids. *Pure Appl. Chem.*, 71:2367–2371, 1999.

[5] Greenwood N. N.; Earnshaw A. *Chemistry of the elements*. Pergamon Press: Oxford, 1994.

[6] Yarnell A. Kitty litter. *Science and Technology*, 82:26, 2004.

[7] Adamis Z.; Fodor J.; Williams R. B. Environmental health criteria 231 bentonite, kaolin and selected clay minerals. Technical report, Inter-Organization Programme for the Sound Management of Chemicals, 2005.

[8] Lahav N.; White D.; Chang S. Peptide formation in the prebiotic era: Thermal condensation of glycine in fluctuating clay environments. *Science*, 201:67–69, 1978.

[9] Kolb V.; Zhang S.; Xu Y.; Arrhenius G. Mineral induced phosphorylation of glycolate ion - a metaphor in chemical evolution. *Orig. Life Evol. Biosphere*, 27:485–503, 1997.

[10] Almon W. R.; Johns W. D. Petroleum forming reactions: the mechanism and rate of clay catalyzed fatty acid decarboxilation. In *7th International meeting on organic geochemistry*, volume 7th, pages 157–171, Chichester, September 1975. Wiley.

[11] Boulet P.; Greenwell H. C.; Stackhouse S.; Coveney P. V. Recent advances in understanding the structure and reactivity of clays using electronic structure calculations. *Journal of Molecular Structure - Theochem*, 762:33–48, 2005.

[12] Payne M. C.; Teter M. P.; Allan D. C.; Arias T. A.; Joannopoulos J. D. Iterative minimization techniques for *ab initio* total-energy calculations: molecular dynamics and conjugate gradients. *Reviews of Modern Physics*, 64:1045–1097, 1992.

[13] Mattsson A. E.; Schultz P. A.; Desjarlais M. P.; Mattsson T. R.; Leung K. Designing meaningful density functional theory calculations in materials science - a primer. *Modelling Simul. Mater. Sci. Eng.*, 13:R1–R31, 2005.

[14] Martin R. M. *Electronic Structure Basic Theory and Practical Methods*. Cambridge University Press, 2005.

[15] Ashcroft N. W.; Mermin N. D. *Solid state Physics*. Brooks/Cole Thomson Learning Inc., 1976.

[16] Royal Society of London Series A - Containing papers of a mathematical and physical character. *Quantum mechanics of many electron systems*, volume 123, April 1929.

[17] Hohenberg P.; Kohn W. Inhomogeneous electron gas. *Phys. Rev.*, 136:864–871, 1964.

[18] Kohn W.; Sham L. J. Self-consistent equations including exchange and correlation effects. *Phys. Rev.*, 140(4A):A1133–A1138, 1965.

[19] Perdew J. P.; Zunger A. Self-interaction correction to density-functional approximations for many-electron systems. *Phys. Rev. B.*, 23:5048–5079, 1981.

[20] Ceperley D. M.; Alder B. J. Ground state of the electron gas by a stochastic method. *Physical Review Letters*, 45(7):566–569, 1980.

[21] Perdew J. P.; Burke K.; Ernzerhof M. Generalized gradient approximation made simple. *Physical Review Letters*, 77(18):3865–3868, 1996.

[22] Koch W.; Holthausen M. C. *A Chemist's Guide to Density Functional Theory*. Wiley-VCH Verlag GmbH, second edition, 2001.

[23] Kurth S.; Perdew J. P.; Blaha P. Molecular and solid state tests of density functional approximations: LSD, GGAs, and meta-GGAs. *International Journal of Quantum Chemistry*, 75:889–909, 1999.

[24] Kittel C. *Introduction to Solid State Physics*. John Wiley and Sons, Inc., seventh edition, 1996.

[25] Hamann D. R.; Schlüter M.; Chiang C. Norm-conserving pseudopotentials. *Physical Review Letters*, 43:1494–1497, 1979.

[26] Kleinman L.; Bylander D. M. Efficacious form for model pseudopotentials. *Physical Review Letters*, 48:1425–1428, 1982.

[27] Goedecker S.; Maschke K. Transferability of pseudopotentials. *Phys. Rev. A.*, 45:88–93, 1992.

[28] Louie S. G.; Froyen S.; Cohen M. L. Nonlinear ionic pseudopotentials in spin-density-functional calculations. *Phys. Rev. B.*, 26:1738–1742, 1982.

[29] Vanderbilt D. Soft self-consistent pseudopotentials in a generalized eigenvalue formalism. *Physical Review B*, 41(11):7892–7895, 1990.

[30] Laasonen K.; Car R.; Lee C.; Vanderbilt D. Implementation of ultrasoft pseudopotentials in *ab initio* molecular dynamics. *Phys. Rev. B.*, 43:6796–6799, 1991.

[31] Accelrys. Materials studio v4.4. Software application, 2009.

[32] Hasnip P. J.; Pickard C. J. Electronic energy minimisation with ultrasoft pseudopotentials. *Computer Physics Communications*, 174:24–29, 2006.

[33] Gonze X.; Stumpf R.; Scheffler M. Analysis of separable potentials. *Phys. Rev. B.*, 44:8503–8513, 1991.

[34] Yin M. T.; Cohen M. L. Theory of static structural properties, crystal stability, and phase-transformations - applications to Si and Ge. *Phys. Rev. B.*, 26:5668–5687, 1982.

[35] Clark S. J.; Segall M. D.; Pickard C. J.; Hasnip P. J.; Probert M. J.; Refson K.; Payne M. C. Castep v5.0. *Zeitschrift für Kristallographie*, 220(5-):567–570, 2005.

[36] Clark S. J. http://cmt.dur.ac.uk/sjc/thesis/thesis/, 1996.

[37] Chadi D. J.; Cohen M. L. Special points in the Brillouin zone. *Phys. Rev. B.*, 8:5747–5753, 1973.

[38] Monkhorst H. J.; Pack J. D. Special points for Brilluoin-zone integrations*. *Phys. Rev. B.*, 13:5188–5192, 1976.

[39] Teter M. P.; Payne M. C.; Allan D. C. Solution of Schrödinger's equation for large systems. *Phys. Rev. B.*, 40:12255–12263, 1989.

[40] Kresse G.; Furthmüller J. Efficient schemes for *ab initio* total-energy calculations using a plane-wave basis set. *Phys. Rev. B.*, 54:11169–11186, 1996.

[41] Mazari N.; Vanderbilt D.; Payne M. C. Ensemble density functional theory for *ab initio* molecular dynamics of metals and finite-temperature insulators. *Physical Review Letters*, 79(7):1337–1340, 1997.

[42] Feynman R. P. Forces in molecules. *Physical Review*, 56:340–343, 1939.

[43] Scheffler M.; Vigneron J. P.; Bachelet G. B. Total-energy gradients and lattice distortions at point defects in semiconductors. *Phys. Rev. B.*, 31:6541–6551, 1985.

[44] Probert M. I. J. http://www.castep.org/castep-talks-07/probert1.pdf. Castep Workshop, 2007.

[45] Pfrommer B. G.; Côté M.; Louie S. G.; Cohen M. L. Relaxation of crystals with the Quasi-Newton Method. *J. Comput. Phys.*, 131:233–240, 1997.

[46] Mulliken R. S. Electronic population analysis on LCAO-MO molecular wave-functions * 1. *J. Chem. Phys.*, 23(10):1833–1840, 1955.

[47] Mulliken R. S. Electronic population analysis on LCAO-MO molecular wave functions. II. overlap populations, bond orders, and covalent bond energies*. *J. Chem. Phys.*, 23(10):1841–1846, 1955.

[48] Mulliken R. S. Electronic population analysis on LCAO-MO molecular wave functions. III. effects of hybridization on overlap and gross AO populations*. *J. Chem. Phys.*, 23(12):2338–2342, 1955.

[49] Mulliken R. S. Electronic population analysis on LCAO-MO molecular wave functions. IV. bonding and antibonding in LCAO and valence-bond theories*. *J. Chem. Phys.*, 23(12):2343–2346, 1955.

[50] Segall M. D.; Pickard C. J.; Shah R.; Payne M. C. Population analysis in plane wave electronic structure calculations. *Molecular Physics*, 89(2):571–577, 1996.

[51] Sanchez-Portal. D.; Artacho E.; Soler J. M. Projection of plane-wave calculations into atomic orbitals. *Solid State Communications*, 95(10):685–690, 1995.

[52] Segall M. D.; Shah R.; Pickard C. J.; Payne M. C. Population analysis of plane-wave electronic structure calculations of bulk materials. *Physical Review B*, 54(23):16317–16320, 1996.

[53] Guerra C. F.; Handgraaf J-W.; Baerends E. J.; Bickelhaupt F. M. Voronoi deformation density (VDD) charges: Assessment of the Mulliken, Bader, Hirshfeld, Weinhold, and (VDD) methods for charge analysis. *J. Comput. Chem.*, 25:189–210, 2004.

[54] Hirshfeld F. L. Bonded-atom fragments for describing molecular charge-densities. *Theor. Chim. Acta.*, 44:129–138, 1977.

[55] http://www.sedlecky-kaolin.cz/en/vyrobky-a-sluzby/kaolin-sedlec-ia.htm. Website, 2010.

[56] http://pubs.usgs.gov/of/2001/of01-041/htmldocs/clays/kaogr.htm. Website, 2010.

[57] Grim R. E. Clay mineralogy. *Science, New Series*, 135:890–898, 1962.

[58] McCabe R. W. *Inorganic Materials.* Wiley New York, 1992.

[59] Kloprogge J. T. Synthesis of smectites and porous pillared clay catalysts: A Review. *Journal of Porous Materials*, 5:5–41, 1998.

[60] Greenwell H. C.; Jones W.; Coveney P. V.; Stackhouse S. On the application of computer simulation techniques to anionic and cationic clays: A materials chemistry perspective. *Journal of Materials Chemistry*, 16:708–723, 2006.

[61] Stackhouse S.; Coveney P. V.; Sandre E. Plane-wave density functional theoretic study of formation of clay-polymer nanocomposite materials by self-catalyzed in situ intercalative polymerization. *J. Am. Chem. Soc.*, 123:11764–11774, 2001.

[62] Churakov S. V. Ab initio study of sorption on pyrophyllite: Structure and acidity of the edge sites. *J. Phys. Chem. B*, 110:4135–4146, 2006.

[63] Johns W. D. Clay mineral catalysis and petroleum generation. *Annual review of Earth and planetary sciences*, 7:183–198, 1979.

[64] Liu D.; Yang X. F.; Wang H. M.; Li J. H.; Su N. A. Impact of montmorillonite and calcite on release and adsorption of cyanobacterial fatty acids at ambient temperatures. *Journal of China University of Geosciences*, 19(5):526–533, 2008.

[65] Russell W. L. *Principles of Petroleum Geology.* McGraw-Hill Book Company Inc., second edition, 1960.

[66] Breger I. A. Diagenesis of metabolites and a discussion of the origin of petroleum hydrocarbons. *Geochimica et Cosmochimica Acta*, 19:297–308, 1960.

[67] Cooper J. E.; Bray E. E. A postulated role of fatty acids in petroleum formation. *Geochimica et Cosmochimica Acta*, 27:1113–1127, 1963.

[68] Smith B.; Greenwell H. C.; Whiting A. Catalytic upgrading of tri-glycerides and fatty acids to transport biofuels. *Energy and Environmental Science*, 2:262–271, 2009.

[69] Worldwatch Institute. *Biofuels for Transport: Global Potential and Implications for Energy and Agriculture.* Earthscan, London, second edition, 2006.

[70] Institution of Chemical Engineers (IChemE) Energy Conversion Technology Subject Group. A biofuels compendium. Rugby, Warwickshire, 2009.

[71] Kalnes T.; Marker T.; Shonnard D. R. Green diesel : A second generation biofuel. *International Journal of Chemical Reactor Engineering*, 5:A48, 2007.

[72] Donnis B.; Egeberg R. G.; Blom P.; Knudsen K. G. Hydroprocessing of bio-oils and oxygenates to hydrocarbons. understanding the reaction routes. *Topics in Catalysis*, 52(3):229–240, 2009.

[73] Do P. T.; Chiappero M.; Lobban L. L.; Resasco D. E. Catalytic deoxygenation of methyl-octanoate and methyl-stearate on Pt/Al_2O_3. *Catalysis Letters*, 130:9–18, 2009.

[74] Quirino R. L.; Tavares A. P.; Rubim J. C.; Suarez P. A. Z. Studying the influence of alumina catalysts doped with tin and zinc oxides in the soybean oil pyrolysis reaction. *Journal of the American Oil Chemists' Society*, 86:167–172, 2009.

[75] Yang T.; Wen X. D.; Li J. F.; Yang L. M. Theoretical and experimental investigations on the structures of purified clay and acid-activated clay. *Applied Surface Science*, 252(18):6154–6161, 2006.

[76] Greenwell H. C.; Stackhouse S.; Coveney P. V.; Jones W. A density functional theory study of catalytic *trans*-Esterification by *tert*-Butoxide MgAl anionic clays. *J. Phys. Chem. B*, 107:3476–3485, 2003.

[77] Oakes R. E.; Beattie J. R.; Moss B. W.; Bell S. E. J. DFT studies of long-chain FAMEs: theoretical justification for determining chain length and unsaturation from experimental raman spectra. *Journal of Molecular Structure - Theochem*, 626:27–45, 2003.

[78] Wang J. G.; Selloni A. First principles study of fatty acid monolayers on Au(111). *J. Phys. Chem. C*, 113(20):8895–8900, 2009.

[79] Hayes C. J.; Burgess Jr D. R. Exploring the oxidative decompositions of methyl esters: Methyl butanoate and methyl pentanoate as model compounds for biodiesel. *Proceedings of the Combustion Institute*, 32:263–270, 2009.

[80] Clausen P.; Andreoni W.; Curioni A.; Hughes E.; Plummer C. J. G. Adsorption of low-molecular-weight molecules on a dry clay surface: An ab initio study. *J. Phys. Chem. C*, 113:12293–12300, 2009.

[81] Rimola A.; Tosoni S.; Sodupe M.; Ugliengo P. Does silica surface catalyse peptide bond formation? New insights from first-principles calculations. *Chem. Phys. Chem.*, 7:157–163, 2006.

[82] Rimola A.; Sodupe M.; Ugliengo P. Aluminosilicate surfaces as promoters for peptide bond formation: An assessment of Bernal's Hypothesis by *ab initio* methods. *J. Am. Chem. Soc.*, 129:8333–8344, 2007.

[83] Rimola A.; Sodupe M.; Tosoni S.; Civalleri B.; Ugliengo P. Interaction of glycine with isolated hydroxyl groups at the silica surface: First principles B3LYP periodic simulation. *Langmuir*, 22:6593–6604, 2006.

[84] Anisimov V. I.; Aryasetiawan F.; Lichtenstein A. I. First-principles calculations of the electronic structure and spectra of strongly correlated systems: the LDA + U method. *J. Phys.: Condens. Matter*, 9:767–808, 1997.

[85] Solomon D. H. Clay minerals as electron acceptors and/or electron donors in organic reactions. *Clays and Clay Minerals*, 16:31–39, 1968.

[86] Kohn W.; Sham L. J. Quantum density oscillations in an inhomogeneous electron gas. *J. Phys. Rev.*, 137(6A):A1697–A1705, 1965.

[87] Lestari S.; Mäki-Arvela P.; Simakova I.; Beltramini J.; Lu G. Q. M.; Murzin D. Y. Catalytic deoxygenation of stearic acid and palmitic acid in semibatch mode. *Catalysis Letters*, 130:48–51, 2009.

[88] Simakova I.; Simakova O.; Mäki-Arvela P.; Simakov A.; Estrada M.; Murzin D. Y. Deoxygenation of palmitic and stearic acid over supported Pd catalysts: Effect of metal dispersion. *Applied Catalysis A: General*, 355:100–108, 2008.

[89] Suter J. L.; Boek E. S.; Sprik M. Adsorption of a sodium ion on a smectite clay from constrained *ab initio* molecular dynamics simulations. *J. Phys. Chem. C*, 112(48):18832–18839, 2008.

[90] Kim J. S.; Lee S.; Cho S. J.; Mhin B. J.; Kim K. S. Structures, energetics and spectra of aqua sodium (1): Thermodynamic effects and nonadditive interactions. *J. Chem. Phys.*, 102:839–849, 1995.

[91] Bridgeman C. H.; Buckingham A. D.; Skipper N. T.; Payne M. C. Ab-initio total energy study of uncharged 2:1 clays and their interaction with water. *Molecular Physics*, 89(3):879–888, 1996.

[92] Wyckoff R. W. G. *Crystal Structures*, volume 4. John Wiley and Sons, 1968.

[93] Larentzos J. P.; Greathouse J. A.; Cygan R. T. An *ab initio* and classical molecular dynamics investigation of the structural and vibrational properties of talc and pyrophillite. *J. Phys. Chem. C*, 111(34):12752–12759, 2007.

[94] Yates Jr J. T.; Madey T. E., editor. *Vibrational spectroscopy of molecules on surfaces*. Plenum Press New York and London, 1987.

[95] Chatterjee A.; Iwasaki T.; Ebina T.; Hayashi H. Relationship between infrared spectra and isomorphous substitution in smectities: A computer simulation study. *Journal of Molecular Graphics*, 14:302–305, 1996.

[96] Govind N.; Petersen M.; Fitzgerald G.; King-Smith D.; Andzelm J. A generalized synchronous transit method for transition state location. *Computational Materials Science*, 28:250–258, 2003.

[97] Zhang X.; Wu F.; Deng N.; et al. Evidence of the hydroxyl radical formation upon the photolysis of an iron-rich clay in aqueous solutions. *React. Kinet. Catal. Lett.*, 94:207–218, 2008.

[98] Gournis G.; Karakassides M. A.; Petridis D. Formation of hydroxyl radicals catalyzed by clay surfaces. *Phys. Chem. Minerals*, 29:155–158, 2002.

[99] Fang Z.; Solovyev I. V.; Sawada H.; Terakura K. First-principles study on electronic structures and phase stability of MnO and FeO under high pressure. *Phys. Rev. B.*, 59:763–773, 1999.

[100] Pickett W. E.; Erwin S. C.; Ethridge E. C. Reformulation of the LDA + U method for a local-orbital basis. *Phys. Rev. B.*, 58:1201–1209, 1998.

[101] Gramsch S. A.; Cohen R. E.; Savrasov S. Y. Structure, metal-insulator transitions, and magnetic properties of FeO at high pressures. *American Mineralogist*, 88:257–261, 2003.

[102] Roth W. L. Magnetic structures of MnO, FeO, CoO, and NiO. *Phys. Rev.*, 110:1333–1341, 1958.

[103] Battle P. D.; Cheetham A. K. The magnetic structure of non-stoichiometric ferrous oxide. *J. Phys. C: Solid State Phys.*, 12:337–345, 1979.

[104] Fujimori A.; Kimizuka N.; Taniguchi M.; Suga S. Electronic structure of Fe_xO. *Phys. Rev. B.*, 36:6691–6694, 1987.

[105] Alvarez-Ramírez F. First principles studies of Fe-containing aluminosilicate and aluminogermanate nanotubes. *J. Chem. Theory Comput*, 5:3224–3231, 2009.

[106] Prat-Resina X.; González-Lafont À.; Lluch J. M. How important is the refinement of transition state structures in enzymatic reactions? *Journal of Molecular Structure - Theochem*, 632:297–307, 2003.

[107] Gao J.; Truhlar D. Quantum mechanical methods for enzyme kinetics. *Annu. Rev. Phys. Chem.*, 53:467–507, 2002.

[108] Raab M.; Kozmon S.; Tvaroska I. Potential transition-state analogs for glycosyltransferases. Design and DFT calculations of conformational behavior. *Carbohydrate Research*, 340:1051–1057, 2005.

[109] Ali M. A.; Rajakumar B. Rate coefficients for the reaction of OH with $CF_3CH_2CH_3$ (HFC-263fb) between 200 and 400 K: *Ab Initio*, DFT, and transition state theory calculations. *J. Comput. Chem.*, 31:500–509, 2010.

[110] Simons J.; Jørgensen P.; Taylor H.; Ozment J. Walking on potential energy surfaces. *J. Phys. Chem.*, 87:2745–2753, 1983.

[111] Elber R.; Karplus M. A method for determining reaction paths in large molecules - application to myoglobin. *Chem. Phys. Lett.*, 139:375–380, 1987.

[112] E W. N.; Ren W. Q.; Vanden-Eijnden E. String method for the sudy of rare events. *Phys. Rev. B.*, 66:052301–4, 2002.

[113] Dellago C.; Bolhuis P. G.; Csajka F. S.; Chandler D. Transition path sampling and the calculation of rate constants. *J. Chem. Phys.*, 108:1964–1977, 1997.

[114] Koslover E. S.; Wales D. J. Comparison of double-ended transition state search methods. *J. Chem. Phys.*, 127:134102–12, 2007.

[115] Sinclair J. E.; Fletcher R. A new method of saddle-point migration energies. *J. Phys. Chem. C: Solid State Phys.*, 7:864–870, 1974.

[116] Dance I. A pragmatic method for location of transition states and calculation of reaction paths. *Molecular Simulation*, 34:923–929, 2008.

[117] Pokidova T. S.; Denisov E. T.; Shestakov A. F. Kinetic parameters and geometry of the transition state of decarboxylation reactions of carboxyl and formyl radicals. *Petroleum Chemistry*, 48:174–185, 2008.

[118] Kakkar R.; Pathak M.; Radhika N. P. A DFT study of the structures of pyruvic acid isomers and their decarboxylation. *Org. Biomol. Chem.*, 4:886–895, 2006.

[119] Li J.; Brill T. B. Spectroscopy of hydrothermal reactions 20: Experimental and DFT computational comparison of decarboxylation of dicarboxylic acids connected by single, double, and triple bonds. *J. Phys. Chem. A*, 106:9491–9498, 2002.

[120] Tietze L. F.; Kinzel T.; Schmatz S. Determination of the origin of stereoselectivity in multiple-transition-state reactions using DFT calculations: Enantioselective synthesis of homoallylic alcohols from aliphatic methyl ketones via an auxiliary-mediated allylation. *J. Am. Chem. Soc.*, 130:4386–4395, 2008.

[121] Meheut M.; Lazzeri M.; Balan E.; Mauri F. Equilibrium isotopic fractionation in the kaolinite, quartz, water system: Prediction from first-principles density-functional theory. *Geochimica et Cosmochimica Acta*, 71:3170–3181, 2007.

[122] Rignanese G. M.; Gonze X.; Pasquarello A. First-principles study of structural, electronic, dynamical, and dielectric properties of zircon. *Phys. Rev. B.*, 63:1043051–1043057, 2001.

[123] Gonze X.; Charlier J.-C.; Allan D. C.; Teter M. P. Interatomic force constants from first principles: The case of α-quartz. *Phys. Rev. B.*, 50:13035–13038, 1994.

[124] Geatches D. L.; Clark S. J.; Greenwell H. C. Role of clay minerals in oil-forming reactions. *J. Phys. Chem. A*, 114:3569–3575, 2010.

[125] Ehrenson S. Analysis of least motion paths for molecular deformations. *Journal of the American Chemical Society*, 96(12):3778–3784, June 1974.

[126] Halgren T. A.; Lipscomb W. N. The synchronous-transit method for determining reaction pathways and locating molecular transition states. *Chemical Physical Letters*, 49(2):225–232, 1977.

[127] Woodward L. A. *Introduction to the theory of molecular vibrations and vibrational spectroscopy.* Oxford University Press, 1972.

[128] Williams D. H.; Fleming I. *Spectroscopic methods in organic chemistry.* McGraw-Hill Book Company (UK) Limited, 3rd edition, 1980.

[129] Baroni S.; De Gironcoli S.; Dal Corso A.; Giannozzi P. Phonons and related crystal properties from density-functional perturbation theory. *Reviews of Modern Physics*, 73:515–562, 2001.

[130] Gonze X. First-principles responses of solids to atomic displacements and homogeneous electric fields: Implementation of a conjugate-gradient algorithm. *Phys. Rev. B.*, 55:10337–10354, 1997.

[131] Refson K.; Tulip P. R.; Clark S. J. Variational density-functional perturbation theory for dielectrics and lattice dynamics. *Phys. Rev. B.*, 73:1–12, 2006.

[132] Refson K. Vibrational spectroscopy methods. CASTEP workshop, Oxford, 2009.

[133] Tulip P. R. *Dielectric and lattice dynamical properties of molecular crystals via density functional perturbation theory: Implementation within a first principles code.* PhD thesis, University of Durham; Department of Physics, 2004.

[134] Lin J. S.; Qteish A.; Payne M. C.; Heine V. Optimized and transferable nonlocal separable *ab initio* pseudopotentials. *Phys. Rev. B.*, 47:4174–4180, 1993.

[135] de Jong G. T.; Geerke D. P.; Diefenbach A.; Bickelhaupt F. M. DFT benchmark study for the oxidative addition of CH_4 to Pd. Performance of various density functionals. *Chemical Physics*, 313:261–270, 2005.

[136] Zhang A.; Ma Q.; Wang K.; Tang Y.; Goddard W. A. Improved processes to re-
move naphthenic acids. Final Technical Report DE-FC26-02NT15383, Califor-
nia Institute of Technology, 1200 East California Blvd., Pasadena, CA91125,
2005.

[137] Şenol O. İ.; Viljava T. R.; Krause A. O. I. Hydrodeoxygenation of methyl
esters on sulphided NiMo/γ-Al$_2$O$_3$ and CoMo/γ-Al$_2$O$_3$ catalysts. *Catalysis
Today*, 100:331–335, 2005.

[138] Fukui K. The path of chemical reactions - the IRC approach. *Accounts of
Chemical Research*, 14:363–368, 1981.

[139] Kraka E.; Cremer D. Computational analysis of the mechanism of chemi-
cal reactions in terms of reaction phases: Hidden intermediates and hidden
transition states. *Accounts of Chemical Rsesearch*, 43:591–601, 2010.

[140] Farmer V. C. *The Infrared Spectra of Minerals*. Mineralogical Society, 1974.

[141] Sainz-Diaz C. L.; Escamilla-Roa E.; Hernandez-Laguna A. Pyrophyllite de-
hydroxylation process by first principles calculations. *American Mineralogist*,
89:1092–1100, 2004.

[142] Suter J. L.; Anderson R. L.; Greenwell H. C.; Coveney P. V. Recent advances
in large-scale atomistic and coarse-grained molecular dynamics simulation of
clay minerals. *J. Mater. Chem*, 19:2482–2493, 2009.

[143] Manceau A.; Lanson B.; Drits V. A.; Chateigner D.; Gates W. P.; Wu J.;
Huo D.; Stucki J. W. Oxidation-reduction mechanism of iron in dioctahedral
smectites: 1. Crystal chemistry of oxidized reference nontronites. *American
Mineralogist*, 85:133–152, 2000.

[144] Komadel P.; Madejová J.; Stucki J. W. Structural Fe(III) reduction in smec-
tites. *Applied Clay Science*, 34:88–94, 2006.

[145] Stucki J. W.; Kostka J. E. Microbial reduction of iron in smectite. *Comptes
Rendus Geoscience*, 338:468–475, 2006.

[146] Stucki J. W.; Shen S. Effects of structural iron reduction on the hydraulic conductivity of Na-smectite. *Clays and Clay Minerals*, 40:381–386, 1992.

[147] Komadel P.; Madejová J.; Bujdák J. Preparation and properties of reduced-charge smectites- A review. *Clays and Clay Minerals*, 53:313–334, 2005.

[148] Stucki J. W.; Lee K.; Zhang L. Z.; Larson R. A. Effects of iron oxidation state on the surface and structural properties of smectites. *Pure Appl. Chem.*, 74:2145–2158, 2002.

[149] Lennard-Jones J. E.; Dent B. M. Cohesion at a crystal surface. *Transactions of the Faraday Society*, 24:92–107, 1928.

[150] Probert M. I. J.; Payne M. C. Improving the convergence of defect calculations in supercells: An *ab initio* study of the neutral silicon vacancy. *Phys. Rev. B.*, 67:1–11, 2003.

[151] Born M.; Huang K. *Dynamical Theory of Crystal Lattices.* Oxford University Press, Amen House, London. EC4, first edition, 1954.

[152] Leslie M.; Gillan M. J. The energy and elastic dipole tensor of defects in ionic crystals calculated by the supercell method. *Journal of Physics C- Solid State Physics*, 18:973–982, 1985.

[153] Yu L. P.; Ranjan V.; Lu W.; Bernholc J.; Nardelli B. M. Equivalence of dipole correction and coulomb cutoff techniques in supercell calculations. *Phys. Rev. B.*, 77:1–6, 2008.

[154] Neugebauer J.; Scheffler M. Adsorbate-substrate and adsorbate-adsorbate interactions of Na and K adlayers on Al(111). *Phys. Rev. B.*, 46:16067–16083, 1992.

[155] Bengtsson L. Dipole correction for surface supercell calculation. *Phys. Rev. B.*, 59:301–304, 1999.

[156] Makov G.; Payne M. C. Periodic boundary conditions in *ab initio* calculations. *Phys. Rev. B.*, 51(4014-4022), 1995.

[157] Schultz P. A. Local electrostatic moments and periodic boundary conditions. *Phys. Rev. B.*, 60:1551–1554, 1999.

[158] Kantorovich L. N. Elimination of long-range dipole interaction in calculations with periodic boundary conditions. *Phys. Rev. B.*, 60:476–479, 1999.

[159] Castleton C. W.; Höglund A.; Mirbt S. Managing the supercell approximation for charged defects in semiconductors: Finite-size scaling, charge correction factors, the band-gap problem, and the *ab initio* dielectric constant. *Phys. Rev. B.*, 73:(035215)1–11, 2006.

[160] Freysoldt C.; Neugebauer J. Fully *ab initio* finite-size corrections for charged-defect supercell calculations. *Phys. Rev. Lett.*, 102:(016402)1–4, 2009.

[161] CASTEP Forum. https://www.jiscmail.ac.uk/cgi-bin/webadmin?a0=castep, 2010.

[162] Kerker G. P. Efficient iteration scheme for self-consistent pseudopotential calculations. *Phys. Rev. B.*, 23:3082–3084, 1981.

[163] Ortega-Castro J.; Hernández-Haro N.; Dove M. T.; Hernández-Laguna A.; Sainz-Díaz C. I. Density functional theory and Monte Carlo study of octahedral cation ordering of Al/Fe/Mg cations in dioctahedral 2:1 phyllosilicates. *American Mineralogist*, 95:209–220, 2010.

[164] Hernández-Laguna A.; Escamilla-Roa E.; Timón V.; Dove M. T.; Sainz-Díaz C. I. DFT study of the cation arrangements in the octahedral and tetrahedral sheets of dioctahedral 2:1 phyllosilicates. *Phys. Chem. Minerals*, 33:655–666, 2006.